uOttawa

L'Université canadienne
Canada's university

FACULTÉ DES ÉTUDES SUPÉRIEURES ET POSTOCTORALES

uOttawa

L'Université canadienne
Canada's university

FACULTY OF GRADUATE AND POSDOCTORAL STUDIES

Sunida Awirothananon
AUTEUR DE LA THÈSE / AUTHOR OF THESIS

Ph.D. (Physics)
GRADE / DEGREE

Department of Physics
FACULTÉ, ÉCOLE, DÉPARTEMENT / FACULTY, SCHOOL, DEPARTMENT

The Electronic Structure of InAs/GaAs Self-assembled Quantum Dots in a High Magnetic Field

TITRE DE LA THÈSE / TITLE OF THESIS

Simon Fafard
DIRECTEUR (DIRECTRICE) DE LA THÈSE / THESIS SUPERVISOR

CO-DIRECTEUR (CO-DIRECTRICE) DE LA THÈSE / THESIS CO-SUPERVISOR

EXAMINATEURS (EXAMINATRICES) DE LA THÈSE / THESIS EXAMINERS

Xiaoyi Bao

Rod Taylor

Patricia Kalyniak

Michael Robertson

Gary W. Slater
Le Doyen de la Faculté des études supérieures et postdoctorales / Dean of the Faculty of Graduate and Postdoctoral Studies

The Electronic Structure of InAs/GaAs Self-Assembled Quantum Dots in a High Magnetic Field

Sunida Awirothananon

Thesis submitted to the Faculty of Graduate and Postdoctoral Studies
in partial fulfillment of the requirements
for the PhD degree in Physics

Physics Department
Faculty of Science
University of Ottawa

Your file Votre référence
ISBN: 978-0-494-41602-0
Our file Notre référence
ISBN: 978-0-494-41602-0

Abstract

The electronic energy levels of dome-shape InAs self-assembled quantum dots (SAQD) grown by the Stranski-Krastanow mode on GaAs substrates are similar to those obtained from a two-dimensional harmonic-oscillator. A simple selection rule allows transitions only that preserve angular momentum, depicted with atomic-like orbital labels s, p, d, f, etc. This electronic structure was examined with photoluminescence (PL) and photoluminescence excitation (PLE) techniques. As well, in magnetic fields up to 28 Tesla applied parallel to the growth direction, SAQD energy-level degeneracies were lifted. The number of branches observed is correlated to the angular momentum. The ground state (GS) level at zero angular momentum is shifted quadratically under the magnetic field and the behavior could be explained with the Fock-Darwin (F-D) spectral model.

The effect of annealing at temperatures from 825 °C to 900 °C in 25 °C steps on the SAQD electronic structure was also examined with the PL technique combined with an applied magnetic field in the Faraday configuration. The PL lines were similar to the F-D spectral lines with their degeneracy lifted by the applied magnetic field. These lines exhibited ten (anti)crossings: three each at 10 T and 28 T, four at 18 T, while the inter-level spacing and the FWHM were reduced with increasing annealing temperature. Thus an increase in the observed (anti-)crossings resulted for the higher anneal temperatures.

The in-plane excitonic reduced-mass was inferred from the systematic splitting of the PL p-branches in a magnetic field. The reduced-mass for all the annealed QD samples was about $0.066\,m_0 \pm 0.012\,m_0$ which decreased slightly with anneal temperature. An 8-band k*p model predicted a similar reduced-mass at low alloying of gallium, but an incorrect trend was observed as the alloying increased with annealing temperature. Unrealistic reduced-masses at 50 percent gallium content were reached. This discrepancy is explained assuming the F-D model is a single (independent) bulk particle picture neglecting many-body effects, and also the k*p model assumes identical disks before and after annealing. The SAQDs were in fact inhomogeneous shallow domes whose height is reduced with annealing temperatures.

It is an attempt to reduce the effect of many-body interactions such as exchange, configuration and screened coulomb interactions dominant in the PL technique, the PLE technique was use. In this technique, a single level in a collection or 'ensemble' of dots is excited with tuned laser-light and only the Coulomb interactions are assumed to be important. The PLE peaks were found to be blue-shifted relative to PL peaks. Furthermore, under the influence of a magnetic field, two PLE peaks were observed that corresponded to the p and d energy states. However, three 'd' lines were expected and is hypothesized that one of the d lines remained degenerate. Moreover, the carrier dynamics observed in PLE spectra are much more difficult to interpret than that of the PL spectra.

Applying the same method, the analysis of the p-branch peaks suggested an in-plane reduced-mass of $\sim 0.084\,m_0 \pm 0.002\,m_0$, higher than obtained from PL measurement. Since the effective mass is normally associated with the mobility of the carriers, this would imply that the excitons in the PLE measurement are *less* mobile than in PL. This is despite the

reduced many-body effects, suggesting that some extra interactions in the PL excitation may actually *enhance* the carrier mobility.

Given the current interest in devices such as QD infrared photo-detectors and the necessary controls on the number of charge carriers in these devices, a single-layer and 25-layer SAQD samples with doping in the top cap layer were compared to un-doped sample using PLE at various detection energies. No absorption signatures appeared for the doped single layer, whereas they were recovered in the 25-layer doped sample. Evidently either dopants or injected carriers diffused into the QD layers beneath the cap. This diffusion and its influence is expected to be decreasing with depth.

Finally, the number of injected charge-carriers in doped GaAs barriers interleaving 50 SAQD layers was studied in order to understand the influence on their electronic structure. From the relation between the dot density and the dopant dose, two to twenty-two charge carriers were estimated to be present in the barriers of each QD. The PLE results indicated that as this number was increased, direct radiative recombination from the higher levels decreased. In addition to Auger scattering and multi-phonon scattering, the enhanced scattering by the dopants impurities appears to add further decay channels toward the lower-energy recombination. This suggests that the PLE technique is sensitive for characterizing the doping effects in SAQD materials.

Some fundamental questions regarding the optical and electronic properties of InAs/GaAs SAQD have been answered in this dissertation and the results can be used to support the future development of opto-electronic devices at the nano-scale level.

Life is a journey.

Along the way, there were many challenges in completing my thesis and

I would like to express my deep appreciation to

Mom and Dad in Thailand, and

J. Hurst.

I am grateful for all the love they've given me since I was young.
They're the ones who first taught me the importance of always
being myself and
they are the reason I am here today.

Statement of Originality

The analysis in this thesis was completed by the author during her doctoral research project under the supervision of Dr. Simon Fafard, except where otherwise stated. All of the data presented in Chapters 5, 7 and 8 were solely obtained by the author at the National Research Council of Canada (NRC). The results presented in Chapter 6 were obtained by the author along with her colleague, Dr. Adam Babinski, at the Grenoble High Magnetic Field Laboratory (GHMFL) in France. The raw data presented in Chapter 4 was obtained by Dr. Sylvain Raymond at GHMFL during the first year of the author's study. Nevertheless, the analysis was performed solely by the author. The modeling results from the eight k*p approximation calculations were performed by Dr. Wei-Dong Sheng at NRC. To the best of the author's knowledge, the original results include:

1. Fock-Darwin-like emission for a single InAs QD layer grown on a GaAs substrate,
2. A reduced in-plane effective mass obtained from a single InAs QD layer at different annealing temperatures,
3. Magneto-photoluminescence excitation for a single-layer InAs SAQD sample,
4. The electronic structure of doped and undoped InAs/GaAs SAQDs,
5. The electronic energy levels of SAQDs with various doping doses in the GaAs barrier were determined.

All samples were grown by Dr. Fafard at the Institute for Microstructural Science, National Research Council of Canada, Ottawa, Ontario over the period from 1998 to 2001.

Publications:

1. ***S. Awirothananon*** *et al.*, "Single Exciton Energy Shell Structure in InAs/GaAs Quantum Dots," to be published in Physical Review B.
2. ***S. Awirothananon***, W. D. Sheng, A. Babinski, S. Studenikin, S. Raymond, A. Sachrajda, M. Potemski, S. Fafard, G. Ortner and M. Bayer. "Electronic and Structural Properties of Interdiffused Self-assembled Quantum Dots from Magneto-Photoluminescence", Japanese Journal of Applied Physics ***43*** (4B), 2088 (2004).

3. A. Babinski, ***S. Awirothananon***, S. Raymond, S. Studenikin, P. Hawrylak, S.-J. Cheng, W. Sheng, Z. Wasilewski, M. Potemski and A. Sachrajda. "Photoluminescence Excitation Spectroscopy of InAs/GaAs Quantum Dots in High Magnetic Field" Physica E ***22***, 603 (2004).

4. A. Babinski, ***S. Awirothananon***, J. Lapointe, Z. Wasilewski, S. Raymond, M. Potemski. "Single-dot Spectroscopy in High Magnetic Fields" Physica E: Low-dimensional Systems and Nanostructures ***26***, 190 (2005).

5. S. Raymond, C. Allen, ***S. Awirothananon*** and C. Dion. "Benefits associated with 'tunable'artificial atoms' Nanotechnology Forum, McGill University, Montreal, Canada (2004).

Articles contributed to but not related to thesis.

6. S. Raymond, D. Labrie, J.-F. Girarad, S. Poirier, ***S. Awirothananon***, P.J. Poole, H. Marchand, P. Desjardins and R.A. Masut "Tuning of the Electronic Properties of Self-Assembled InAs/InP Quantum Dots by Rapid Thermal Annealing," Materials Research Society Symposium – Proceedings, 642, J9.6.1 (2001).

Conference Presentations:

1. ***S. Awirothananon***, S. Raymond, A. Babinski, S. Studenikin, A. Sachrajda, S. Fafard, W.D. Sheng, P. Hawrylak and M. Potemski. "Excitonic Shell Structure in Self-Assembled Quantum Dots from Magneto-Luminescence Spectroscopy," Oral presentation: Quantum Dot 2004. Banff, Canada (May 2004).

2. ***S. Awirothananon***, S. Raymond, S. Studenikin, W. Render, A. Sachrajda, W. Sheng, P. Hawrylak, S. Fafard. "Magneto-Photoluminescence Excitation Spectroscopy of InAs/GaAs Self-Assembled Quantum Dots," Oral Presentation: Photonic North Conference, Ottawa, Canada (September 26th – 29th 2004).

3. ***S. Awirothananon***, W. Sheng, A. Babinski, S. Studenikin, S. Raymond, P. Hawrylak, A. Sachrajda, M. Potemski. : "Magneto-Luminescence of Interdiffused Self-Assembled Quantum Dots," Oral presentation: International Conference on Solid State Devices and Materials, Tokyo, Japan (September 16th – 18th 2003).

4. ***S. Awirothananon***, K. Rananratanatumapan and S. Raymond. "Intermixing Coefficients and Residual Damage in InGaAs/InP Heterostructures," Poster presentation: 4th Development and Promotion of Science and Technology, Ambassador Hotel, Bangkok, Thailand (November 30th 2001 – December 1st 2001).

5. ***S. Awirothananon***, J. E. Haysom, G. C. Aers, P. J. Poole, T. Simpson, I. V. Mitchell, S. Raymond. "Intermixing Properties for $In_{1-x}Ga_xAs_{1-y}P_y$/InP Quantum Well Structures with Varying Initial Composition and Strain Profiles," Poster presentation: Photonic's North International Conference on the Application of Photonic Technology (ICAPT), Quebec, Canada (June 2000).

Conference Participation:

1. "OSA leadership meeting for young scientist," Rochester, NY, USA, (October 7th – 11th, 2006).
2. "OSA leadership program for young scientist," Hilton Tucson, Arizona, USA (October 16th – 20th, 2005).

3. "International Women in Engineering and Science (ICWES 13th)," South Korea (August 26th – 30th, 2005).
4. "International Conference on Solid State Devices and Materials," Tokyo, Japan (September 16th -18th 2003).
5. "Eleventh Canadian Semiconductor Technology conference," Ottawa, Canada (August 18th-22th, 2003).
6. "Opto Canada, Optoelectronics, Photonics and Imaging," Ottawa, Canada (May 2002).

Acknowledgements

The time I spent at the University of Ottawa working on my doctoral research was an experience that will continue to mold me for the rest of my life. I am immensely grateful to Dr. Bela Joos, for his generosity, patience and support, even during the tough times of my program. I would like to acknowledge Dr. Babinski, Dr. Marek Potemski, Dr. Raymond, Dr. Fafard, Dr. Pawel Hawrylak and Dr. Sheng for providing guidance, suggestions, discussions and funding for this work.

Thank you to the Grenoble High Magnetic Field Laboratory in Grenoble, France for providing the facilities for the measurement and collection of data. Also, thanks to the National Research Council of Canada for providing research facilities. It was also my great privilege to have worked with Dr. Babinski, Dr. Potemski and Ms. Basia Chwalisz-Pietka during my time at the Grenoble High Magnetic Laboratory.

I would like to express my boundless gratitude to my husband, James, who has nourished and supported me throughout my graduate study. We have shared problems, joys, and hopes that punctuated our journey. He has been my blessed sensibility. In addition, this thesis is dedicated to my parents who, even though they are not able to read and understand this thesis, have been a great support throughout my education.

I would like to thank Dr. Monique Frize, who has been my mentor during my doctoral program. She has been a fantastic mentor. Her patient guidance has made this thesis possible. I would like to express my gratitude to Ms. Danielle Plouffe and Ms. Catherine Stanford for all of their support during the hard times along my way to complete the thesis.

I would like to thank all of my friends for their support (Claudine, Winnie, Dang, May, Panitee and the ones that have not been mentioned whom I have met along the way at the University of Ottawa). It has been an amazing experience working with them on many projects.

Many thanks are to Susan Hurst for proof-reading and her support all the way along the completion of my thesis. I am greatly appreciative to Dr. Gary Knight for his critical copy-editing of this thesis.

Thank you Murielle and all of my friends in the Department of Physics at the University of Ottawa

Table of Contents

List of Figures

List of Tables

List of Abbreviations

BEC	-	Bound Exciton Complex
BF	-	Bright Field
BZ	-	Brillouin Zone
DF	-	Dark Field
DOS	-	Density of States
E_e	-	Electron Energy
E_g	-	Energy Gap
FCC	-	Face-Center Cubic
F-D	-	Fock-Darwin
FWHM	-	Full-Width-at-Half-Maximum
GS	-	Ground State
LA	-	Longitudinal Acoustic
LO	-	Longitudinal Optical
LED	-	Light Emitting Diode
LN	-	Liquid Nitrogen
m_0	-	Electron Rest Mass
MBE	-	Molecular Beam Epitaxy
M-PL	-	Magneto-Photoluminescence
M-PLE	-	Magneto-Photoluminescence Excitation
PL	-	Photo-Luminescence
PLE	-	Photo-Luminescence Excitation
QD	-	Quantum Dot
QDIP	-	Quantum Dot Infrared Photo-Detector
QW	-	Quantum Well
Qwire	-	Quantum Wire
RTA	-	Rapid Thermal Annealing
SAQD	-	Self-Assembled Quantum Dot
SPPh	-	Surface Plasmon-Phonon
S-K	-	Stranski-Krastanow
TEM	-	Transmission Electron Microscope
TA	-	Transverse Acoustic
TO	-	Transverse Optical
WL	-	Wetting Layer

Chapter 1

Introduction

Technological development and increased physical understanding of semiconductor heterostructures have resulted in remarkable changes in everyday lives throughout the world. It is increasingly difficult to envisage life as it was formerly lived without semiconductor technology such as fiber-optic telecommunication systems [1-6] or light emitting diodes (LED) [1-7]. The need for smaller and faster electronic devices has created the new field of nanotechnology, where microelectronics may be complemented by the promise of quantum-effect devices. The underlying principles for nano-scale devices [14] are remarkably different from micro-electronic ones because, in the nano-scale, quantum as well as semi-classical size effects govern their behaviour.

Progressive improvement in fabrication techniques has helped scientists to produce nano-semiconductors with stricter dimensional confinements. In the 1960s, Hayashi and Anish [15] started to fabricate nano-devices by confining carriers to narrower band-gap materials sandwiched in between wider band-gap materials [16]. As a result, carriers (electrons and holes) were restricted from moving in the one dimension, which was typically the growth direction, but were free to move within the orthogonal plane. This type of confinement is called a quantum well (QW). Research activities were then extended to the study of quantum properties of carriers restricted from moving in two and three directions. When restricting movement in two dimensions, carriers are confined to one dimension, the axis of a quantum wire (Qwire). By adding confinement in this remaining degree of freedom, carriers are limited in three directions. This limit is called a quantum dot (QD).

The properties of semiconductor structures with carriers sufficiently confined in one, two and three directions are very different from those of the bulk material. QD semiconductors, with properties that are analogous to individual atoms even though one QD may contain tens of thousands of atoms, have attracted particular interest. A QD is thus an atom-like structure with an optical response distinct from Qwires or QWs.

There are many techniques to fabricate QDs: lithography, interface fluctuations [17] and self-organization [18]. The lithographic technique has been used to produce many types of QD, including free-standing QDs[1], [19-20], and QDs grown on patterned substrates [21-25]. The interface (potential) fluctuation techniques [26-27] on a QW generally induce fluctuation of the gallium or the indium content. This effect produces efficient localization centers for excitons, which act as QDs. In the case of the self-organized technique [28-31], QDs are formed spontaneously during the fabrication process due to lattice mismatch at the interface between two different types of semiconductors. Generally producing randomly positioned QDs in a layer, this technique is relatively easy, fast, inexpensive and reliable. All samples studied in this dissertation were InAs dots grown by the self-organized technique via the Stranski-Krastanow (S-K) mode on GaAs substrates.

[1] This type of QD requires patterning by either positive or negative resists and dry etching process.

The optical characteristics of self-assembled QDs (SAQD) are quite distinctive, especially in III-V compounds. Dome–shaped or hemispherical capped SAQDs have simple energy levels similar to the two-dimensional harmonic-oscillator, and are depicted with atomic-like orbital labels – s, p, d, and f with the principal levels represented with quantum numbers $|n_+, n_-\rangle$. The selection rule $\Delta n_\pm = 0$ determined in previous studies and discussed in Chapter 2 determines the excitonic recombination energy at each level of the QD.

Variation in dot dimensions and composition causes Gaussian broadening in the PL emission due to emission lines of individual dots. Rapid thermal annealing (RTA) is a post-growth method used to reduce this broadening [31-34] and to somewhat tailor the inter-level spacing. The RTA technique is described in Chapter 3.

There are many challenges for meaningful optical characterization including the many steps required to prepare a single SAQD sample, such as a 'mesa mask' [35]. Thereafter, PL measurement (using laser illuminaTheretion) is readily performed, but it probes many QDs at the same and with many interacting excited carriers. Many-body effects such as exchange, screened coulomb and configuration interactions are then involved in the carrier dynamics.

These uncontrolled many-body interactions are alternatively reduced by using the PL excitation (PLE) technique. In the PLE technique, only a single energy level in a collection of dots is 'activated' by absorption of tuned laser light. The experimental setup for both techniques is described in Chapter 3. Fundamental electronic properties of the QDs such as the energy level structure, level offset and effective masses were examined with these two techniques.

The focus of this dissertation is to examine these fundamental optical and electronic properties of GaAs-based SAQDs. The knowledge contributed will help to control the QD properties. For example, the optical characterization results might allow setting or adjusting a growth parameter suited to a fabrication process.

Chapter 2 focuses on the fundamental characteristics of a SAQD by reviewing the density of states for an idealized quantum confinement structure (Qwire, QW and QD), and then emphasizes the electronic energy levels of a dome-shaped QD. The electronic structure is examined under the influence of an applied external magnetic field and a Fock-Darwin spectral model of independent (single) electron-hole pairs is illustrated. The carrier dynamics including recombination processes in a SAQD are described at the end of the chapter, including phonon emission/absorption, multi-phonon emission/absorption and Auger effects.

The experimental set-up for PL and PLE optical characterization of SAQDs is described in Chapter 3. The optical path and instrument configurations, including magneto-PL and magneto-PLE techniques, are illustrated and explained in detail in this chapter. Some RTA results (or technique overview) are briefly discussed at the end of the chapter.

In Chapter 4, experiments that optically explore the electronic properties of InAs/GaAs SAQDs with increasing In-Ga intermixing across the QD-barrier interface are reported. A set of InAs/GaAs SAQDs samples annealed at various temperatures for 30 seconds was examined under magnetic fields in Faraday configuration up to 28 Tesla. The PL spectra

with increasing field-strength showed evidence of a Fock-Darwin [36-37] (F-D)-like line pattern, indicating that the level structure may be understood in terms of two-dimensional harmonic oscillators. An estimate of the exciton reduced-mass in QDs with varying RTA treatment was obtained. An 8 band k*p calculation including valence-band mixing and a Bir-Pikus Hamiltonian coupling to strain was employed to estimate the Ga content in the InAs QDs after deposition and after RTA-promoted interdiffusion.

A single particle picture of excitons in these SAQDs is the central discussionpresented in Chapter 5. The complexity of many-body interactions, including direct and screened coulomb, exchange, and configuration coupling energies, was expected to be diminished for the results obtained from the PLE technique. A blue shift in the PLE spectra was observed. The experiment was performed on an InAs QD sample annealed at 825 °C for 30 seconds, instead of the as-grown QD, in order to shift the discrete energy levels of the QD into the tunable range of the excitation laser. As well, the electronic structure in the F-D picture was examined by applying an external magnetic field in the Faraday configuration. A comparison between the optical luminescence from PL and PLE experiments is discussed in Chapter 6.

In order to produce practical devices for applications such as quantum dot lasers [38-44], gates for quantum computing [45-47], memory devices [48-50], and quantum dot infrared photo detectors (QDIP) [51-52], a great deal of fundamental scientific research is required. There is especially a significant interest in quantum dot infrared photo-detectors and the ability to modify and control the number of charge carriers in such QD devices. Thus, the fundamental effects of positive and negative charges in the QD were examined. In Chapter 7, the electronic structure of single layer InAs/GaAs SAQDs as affected by dopants in a capping layer is examined and the influence of dopants in capping layers on top of 50 SAQD layers is also studied. Subsequently, the influence of various dopant doses in the barrier GaAs layer sandwiched in between 50 layers of QD is studied in Chapter 8 in order to examine the QD electronic structure and carrier relaxation. Since the available carrier relaxation mechanisms and rates are related to the energy levels of the SAQD, the influence of the different size of dots (and the density of the dots) at different doping levels is discussed.

The experimental research reported in this dissertation contributes to answering some fundamental questions concerning QDs and their optical and electronic models. The author anticipates that this contribution will also eventually enhance applications of nano-scale opto-electronic devices themselves.

Chapter 2

Fundamental Characteristics of the Quantum Dot

The purpose of this Chapter is to provide sufficient background about GaAs-based SAQDs in order to discuss the experimental results presented in Chapters 4 - 8. The structure of III-V semiconductors is briefly reviewed, especially InAs and GaAs, followed by the description of the fabrication of SAQDs which utilizes the lattice mismatch between these two semiconductors. The QD density of states is then discussed along with single-carrier energy levels with and without an applied external magnetic field. A description of the selection rules for radiative recombination and the various recombination processes – both radiative and non-radiative – concludes the Chapter.

2.1 Structure of III-V Semiconductors

In atoms, the energy levels of bound electrons are discrete and precisely defined within the limit of Heisenberg's uncertainty relation ($\Delta x \Delta p \leq \hbar$) and the same fact applies to SAQDs. The length scale of bulk semiconductors is on the order of centimeters, whereas for a waveguide it is in the scale of micrometers, which is in the wavelength range of visible light (0.4 – 0.7 μm). This relationship is illustrated in the unscaled cartoon presented in Figure 2.1.

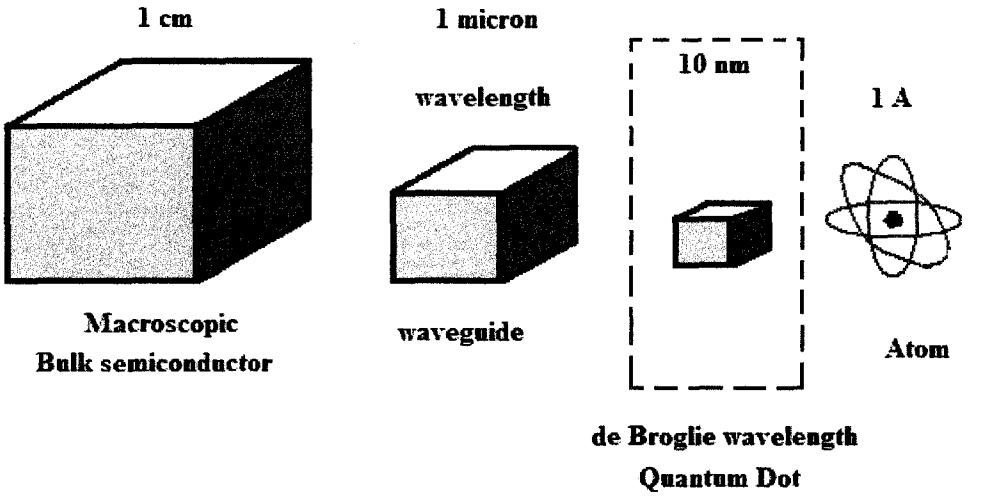

Figure 2.1: Comparing dimensions of bulk material, waveguides for visible light, a QD and atoms[2]

When charge carriers move within a semiconductor and the mean free path is on the order of the de Broglie wavelengths [53], the effects of size quantization can be observed. In a highly non-degenerate semiconductor like GaAs, the de Broglie wavelength λ depends on

[2] Adapted from "Introduction to Semiconductor Optics" by cf. N. Peyghambarian [75].

the relationship between momentum and wavelength through temperature and effective mass[3], m_{eff}, of the carriers as [54]

$$\lambda = \frac{h}{p} = \frac{h}{\sqrt{3m_{eff}k_B T}} \quad , \qquad \text{[EQ 2.1]}$$

where the momentum[4], p, is based on the assumption of a free electron gas colliding in three dimensions - $\frac{1}{2}m_{eff}v^2 = \frac{3}{2}k_B T$ and $p = m_{eff}v$. Since the effective mass of such a semiconductor, m_{eff}, is much smaller than the electron rest mass, m_0, the wavelength in the semiconductor, λ_{eff}, is larger than that of the free electron, λ_e.

In SAQDs, the effective mass is also reflected in flattened 'bands' where size quantization flattens them ten to several hundred times. This is due to the strength of confining potentials, strains, and barrier height.

Quantization effects in semiconductors have been a popular topic of study since the late 1950s, especially energy quantization in ultra-thin layers of silicon [55]. By the end of the 1980s the main properties of QWs and super-lattices were rather well understood, and interest shifted toward structures of reduced dimensionality: the Qwire [56] and QD [57-59]. Studying low dimensional confinement over the past two decades, various research groups produced QD applications such as photo-detectors [60-61] and QD lasers [62-63]. To the present date, advances in fabrication and characterization techniques have expanded the opportunities to study various optical, electronic and structural properties of QDs.

Knowledge of the basic properties of bulk III-V semiconductors like indium arsenide (InAs) and Gallium Arsenide (GaAs) are required to grasp those of QDs. Both GaAs and InAs have the zinc-blende structure with a face-centered cubic (FCC) translational symmetry, and a basis of one GaAs (InAs) molecule, where one atom is at 000 and the other is at $\frac{1}{4}\frac{1}{4}\frac{1}{4}$ of the (non-primitive) FCC unit cube. Figure 2.2 is a schematic of this structure for III-V semiconductors.

[3] Effective mass is an important parameter in studies of III-V hetero-structure confinement.

[4] For highly non-degenerate semiconductors, an ideal-gas Maxwellian distribution holds as an approximation to the Fermi distribution and possible relativistic corrections in high B fields.

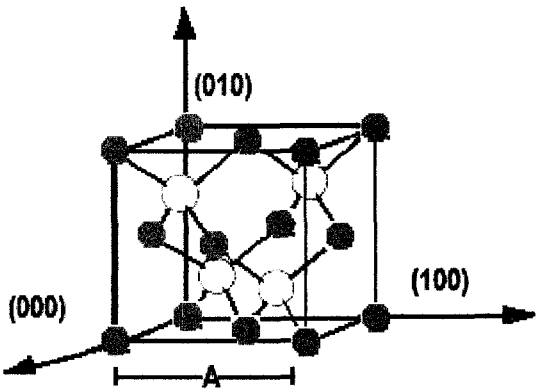

Figure 2.2: GaAs and InAs zinc-blende structure; the volume of a few cubic Å*s* is four primitive cells. (after Waugh [76])

The lattice constant for GaAs, InAs and their alloys ranges from 5.6 Å to 6.1 Å as shown in Figure 2.3. The mismatch between InAs and GaAs lattice constants is important[5] in promoting growth of SAQDs.

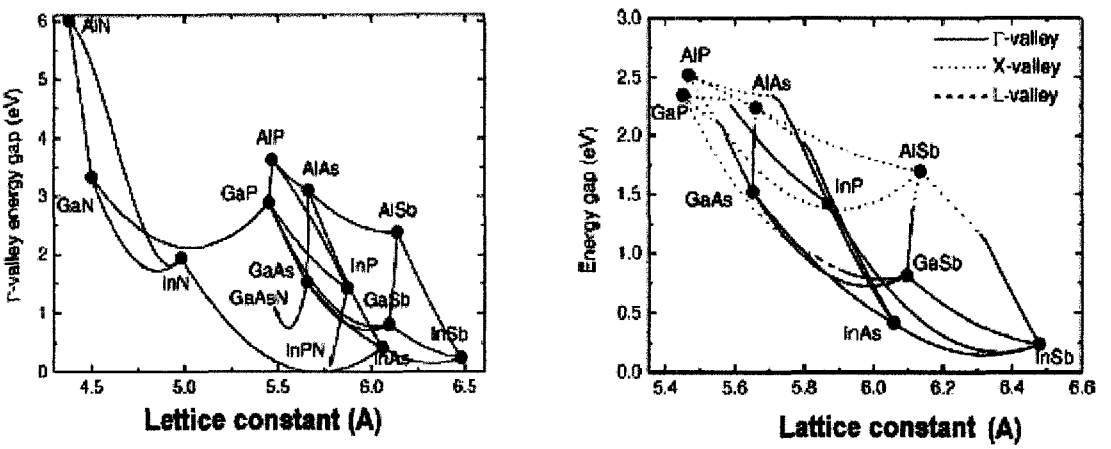

Figure 2.3: The energy gap and lattice constant for III-V semiconductors at T=0 K. (after Vurgaftman [64])

Figure 2.3 above depicts the Γ vertical energy gap as a function of a lattice constant for the zinc-blende III-V binary compounds (left) and the lowest energy gap as a function of a lattice constant for non-nitride III-V compound semiconductors (points) and their random ternary alloys (lines) at a zero temperature (right).

At appropriate temperature and pressure, InAs dots grow after deposition on GaAs of a few monolayers, due to the strain between these two layers since the InAs lattice

[5]Other well defined conditions are required for S-K growth such as GaAs substrate temperature, pressure and the rate of injection of gallium, arsenic, and indium atoms.

constant is 6.7 percent larger than that of GaAs[6]. This type of growth is called Stranski-Krastanow (S-K) and this type of dot is called a SAQD[7]. A TEM picture of a SAQD is shown in Figure 2.4.

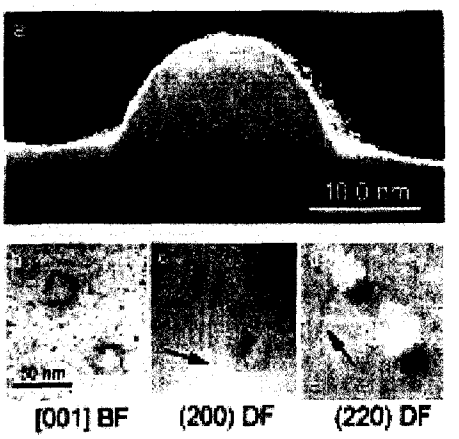

Figure 2.4: TEM images of InAs/GaAs SAQDs (a) cross section; (b), (c), (d) plan view, in bright (BF) and dark field (DF) imaging conditions [65]

2.2 Density of States for Idealized Structures

The optical response and density of states of low-dimensional semiconductors can be studied by PL and PLE experiments. The density of states $g(\varepsilon)$ is the number of available energy states per energy interval $d\varepsilon$ per spin orientation per unit volume in real space as given by

$$g(\varepsilon)=\frac{\vec{k}^2}{\pi^2}\left(\frac{d\varepsilon}{dk}\right)^{-1}, \qquad \text{[EQ 2.2]}$$

where k is the wave-vector space. Quantitatively, modification of the band structure can be expressed through the effective mass in the density of states. For instance, the band structure of GaAs as shown in Figure 2.5 has a parabolic energy band at the Γ center (center of the Brillouin zone[8]).

---

[6] The lattice constants for GaAs and InAs are 5.65 Å and 6.06 Å, respectively.

[7] Sometimes, this type of dot is called a self-organized QD.

[8] The Brillouin zone is the primitive cell in reciprocal lattice space ($\vec{k}$). It is defined on a Wigner-Seitz primitive cell, based on a geometrical interpretation of $2k \bullet G = G^2$. The first Brillouin zone is symbolized by Γ. More detail is found in Cf. Kittel [225].

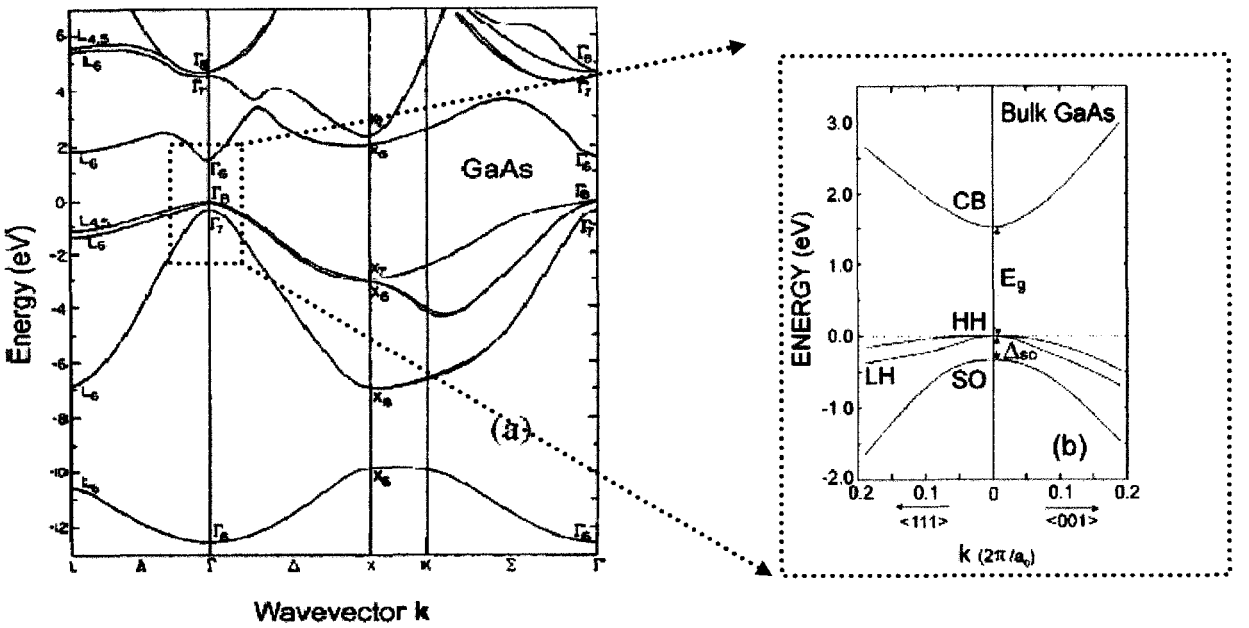

Figure 2.5: Band structure in the vicinity of energy gap of GaAs [64]

The change in curvature of the parabolic energy is associated with the effective mass value. Often such an extremum occurs for $\bar{k} = 0$ at the Γ point, at the center of the Brillouin zone. In the case of bulk semiconductors, the conduction-band density of states is generally given through the dispersion relation - $\varepsilon_{Bulk} = \frac{\hbar^2}{2m^*}\left[k_x^2 + k_y^2 + k_z^2\right]$[9]- by

$$g_{Bulk}(\varepsilon_{bulk}) = \frac{1}{2\pi^2}\left(\frac{2m^*}{\hbar^2}\right)^{3/2} \varepsilon_{bulk}^{1/2}, \qquad \text{[EQ. 2.3]}$$

where m^* is the carrier effective mass of the bulk semiconductor.

On the other hand, if the carriers are free to move in two dimensions (x, y) but are confined in one dimension (z-direction), the dispersion relation needs to be modified. For example, if the carriers are confined in the z-direction by an infinite finite square well potential, the dispersion relation[10] will be

$$\varepsilon_{QWell} = \sum_{n_z=0} \varepsilon_{n_z} = \frac{\hbar^2}{2m_\perp^*}k_\perp^2 + \frac{\hbar^2}{2m_z^*}\left(\frac{n_z\pi}{L_z}\right)^2, \qquad \text{[EQ. 2.4]}$$
$$\{n_z \in 1,2,3,...\}$$

where L_z is the physical length in the z-direction. Typically L_z is measured with respect to the bounding semiconductor with a larger 'infinite' energy gap, and $m_\perp^*$ and m_z^* are in-plane and z-direction projected effective masses, respectively. As a result, the density-of-states[11] for the QW is defined as

[9] Details for obtaining these energy levels can be found in cf. Peyghambarian [75] p 40-44.

[10] Energy levels for QW with infinite square well potential can be found in cf. Peyghambarian [75] p 190-197.

[11] The density of states for QW can be found in cf. Peyghambarian [75] p 205-209.

$$g_{QW}(\varepsilon) = g_{\perp}(\varepsilon) + g_{z}(\varepsilon),$$

$$g_{QW}(\varepsilon) = \frac{1}{2\pi^2}\left(\frac{2m_{\perp}^{*}}{\hbar^2}\right)^{3/2}\varepsilon_{\perp}^{1/2} + \frac{m_z^{*}}{\pi\hbar^2}\sum_{n_z=1}\Theta\left(\varepsilon_{QW} - \varepsilon_{n_z}\right). \qquad \text{[EQ 2.5]}$$

Similarly, the energy dispersion relation and the density-of-states[12] for the quantum wire and the quantum-dot semiconductors, with two and three dimensional confinement are given by

{Quantum wire}

$$\varepsilon_{Qwire} = \varepsilon_{n_z,n_x} = \frac{\hbar^2}{2m_x^{*}}\left(\frac{n_x\pi}{L_x}\right)^2 + \frac{\hbar^2}{2m_z^{*}}\left(\frac{n_z\pi}{L_z}\right)^2 + \frac{\hbar^2 k_y^{\,2}}{2m_y^{*}}, \qquad \text{[EQ 2.6]}$$

$$g_{Qwire}(\varepsilon) = g_{y}(\varepsilon) + g_{x,z}(\varepsilon),$$

$$g_{Qwire}(\varepsilon) = \frac{1}{2\pi^2}\left(\frac{2m_y^{*}}{\hbar^2}\right)^{3/2}\varepsilon_{\perp}^{1/2} + \frac{1}{\pi}\left(\frac{m_{(x,z)}^{*}}{2\hbar^2}\right)^{\frac{1}{2}}\frac{1}{\sqrt{\varepsilon - \varepsilon_{n_z,n_x}}}, \qquad \text{[EQ 2.7]}$$

{Quantum dot}

$$\varepsilon_{Qdot} = \varepsilon_{n_y,n_z,n_x} = \frac{\hbar^2}{2m_x^{*}}\left(\frac{n_x\pi}{L_x}\right)^2 + \frac{\hbar^2}{2m_z^{*}}\left(\frac{n_z\pi}{L_z}\right)^2 + \frac{\hbar^2}{2m_y^{*}}\left(\frac{n_y\pi}{L_y}\right)^2, \qquad \text{[EQ 2.8]}$$

$$g_{Qdot}(\varepsilon) = 2\sum_{n_x,n_y,n_z}\delta\left(\varepsilon - \varepsilon_{n_x,n_y,n_z}\right), \qquad \text{[EQ 2.9]}$$

where $n_x, n_y, n_z \in \{0,1,2,3,...\}$.

The energy dispersion relations and DOS for all of the quantized dimensionalities are illustrated in Figure 2.6.

[12] ε_{QWire} and g_{QWire} can be found cf. Peyghambarian [75] p 235-238, and ε_{QD} and ε_{QD} from p 244 - 245.

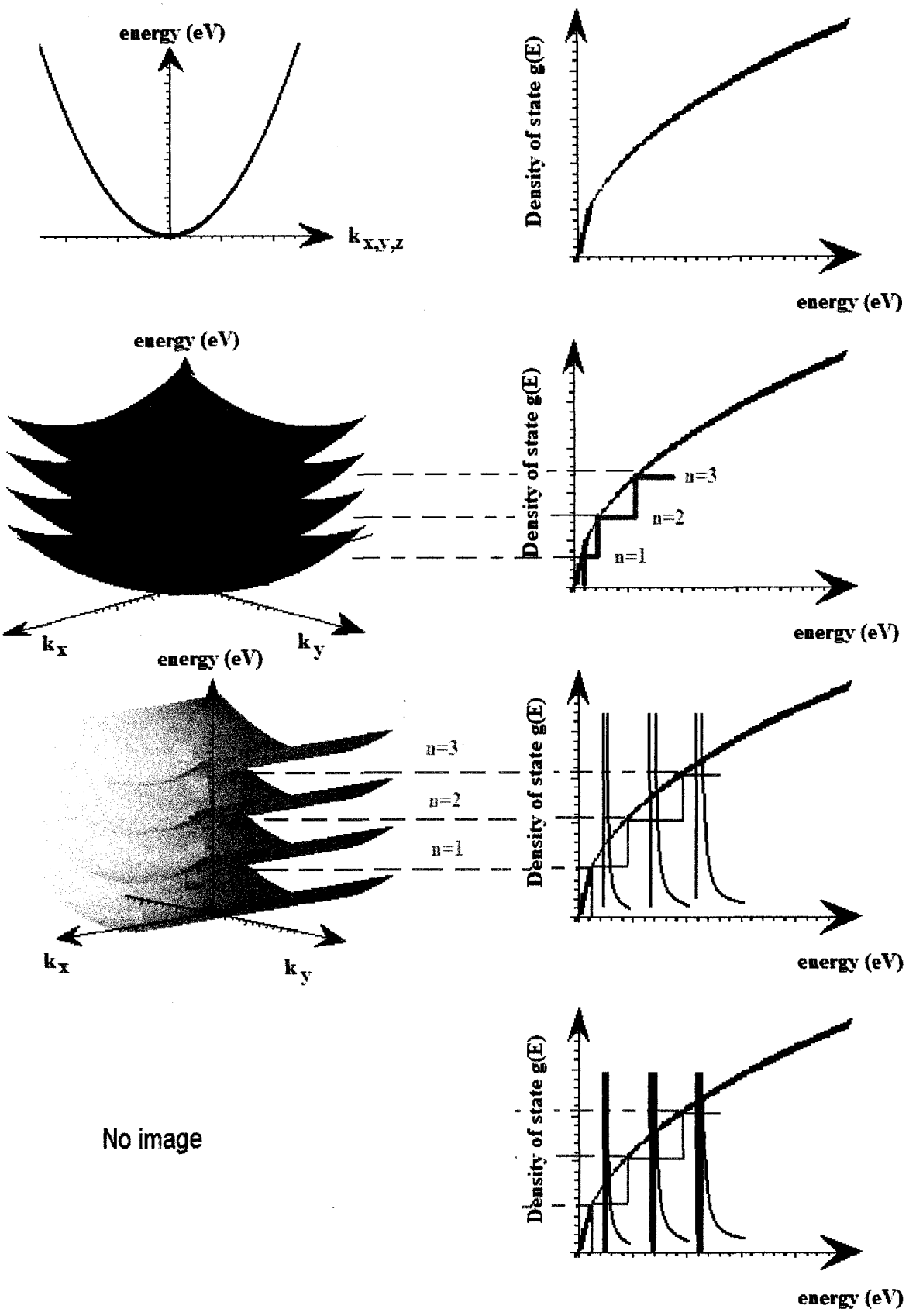

Figure 2.6: Energy dispersion (left) and DOS (right) for bulk, QW, quantum wire and QD structures with carriers confined by infinite barriers

2.3 Electronic Energy Levels of a- Lens-Shaped QD

The growth of SAQDs by the S-K mode produces islands or dots after a few mono-layers of a larger lattice constant material are deposited on a smaller lattice constant material. These preliminary layers are labeled the wetting layer (WL). Although greater than this WL thickness, the dot height is 3-4 times less than lateral diameter, giving the dots a flat-dome shape [66]. The vertically confining potentials for such a dot and its WL are modeled as two finite square-wells even though the WL has a narrower square well than the height of QD. Carriers are localized within the QD rather than the WL because the dot ground-state energy level is below the wetting layer's. The domed potential[13] is thus a combination of lateral $V(x,y)$ and vertical $V(z)$ confinements. An ideal dome-shaped SAQD on a WL of thickness t_w is modeled as a part of a sphere with fixed height ℓ_0 and basal radius r in Figure 2.7.

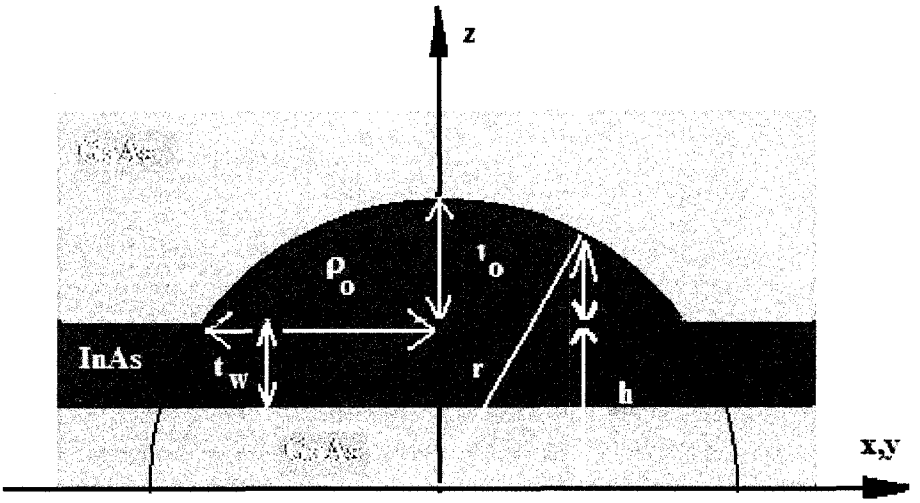

Figure 2.7: Cross-section[14] of an ideal dome-shaped quantum dot. The lighter shaded regions depicts a semiconductor with larger band gap than the darker shaded regions

The effective Hamiltonian for the free electron-hole pairs[15] within a SAQD confined in three dimensions is given by

$$H = \left[\frac{p_e^2}{2m_e^*} + V(\vec{r}_e)\right] + \left[\frac{p_h^2}{2m_h^*} + V(\vec{r}_h)\right] - \frac{e^2}{\varepsilon|\vec{r}_e - \vec{r}_h|}, \qquad \text{[EQ. 2.10]}$$

where $V(\vec{r}_e)$ and $V(\vec{r}_h)$ are the electron and hole confining potentials, respectively, due to the dot shape (height and diameter)[16]. $m^*_{e(h)}$ represents the electron (hole) effective mass[17], which is

[13] The formal model is from "Zero-dimensional properties of self-assembled Islands" (Ph.D. dissertation, Sylvain Raymond, University of Ottawa, 1997).

[14] This cross-section is adapted from "Zero-dimensional properties of self-assembled Islands" (Ph.D. dissertation, Sylvain Raymond, University of Ottawa, 1997).

[15] SAQD energy levels are described by the flat-disk model in Woj's article [67].

effected by strain and variations in QD composition. The last term is associated with the Coulomb interaction between electrons and holes inside the dot, where ε is the phenomenological dielectric constant of the QD.

The (screened) Coulomb interaction, the intrinsic attraction between conduction electron and valence hole is small. Therefore, when the dot radius, r, is on the order of an excitonic Bohr[18] radius, $a_B = \frac{\varepsilon\hbar^2}{m_e^* e^2}$[19], the lateral confinement potential has *more* influence than the Coulomb interaction, which may be treated as a perturbation. For simplicity this perturbation is neglected at the moment. The Schrödinger equation for the effective Hamiltonian then reduces to

$$\left\{\left[\frac{p_e^2}{2m_e^*}+V(\vec{r}_e)\right]+\left[\frac{p_h^2}{2m_h^*}+V(\vec{r}_h)\right]\right\}\Psi(\vec{r})=(E_e+E_h)\Psi(\vec{r}). \qquad \text{[EQ2.11]}$$

In this approximation, the effective Hamiltonian for the electron and hole are independent, and the Schrödinger equation [EQ2.11] reduces to a one-particle form:

$$\left[\frac{p^2}{2m_e^*}+V(\vec{r})\right]\Psi(\vec{r})=E\Psi(\vec{r}). \qquad \text{[EQ 2.12]}$$

The electron or hole subscript is henceforth dropped in order to simplify notation. As above, the potential $V(\vec{r})$ separates into two components, restricting carriers to the growth direction (z-axis) and the lateral confinement (XY plane):

$$V(\vec{r})=V(\rho)+V(z), \qquad \text{[EQ 2.13]}$$

where $V(z)$ is the ground-state potential profile of a QW with the vertical height of the QD, and $V(\rho)$ is the QD lateral confinement potential. An adiabatic approximation[20] [67] is adopted in this formulation. $V(\rho)$ is the lateral potential energy at any point in the XY plane defined by the net ground-state-QW energy at physical height, $\ell(x,y)$, relative to the height at the center of the dot, $\ell_0(x,y)$. In other words, the carriers in the QD feel the potential difference at each point in x-y plane as the ground state energy of a QW of equivalent thickness, $\ell(\rho)$, relative to the initial energy $V(\rho_0)$thus:

---

[16] In three dimensions, unresolved as yet in the vertical QW, lateral confinement presented in [EQ 2.13].

[17] Effective mass is first associated with intrinsic crystallographic periodicity then strain and confinement.

[18] In III-V semiconductors with high dielectric constant (weak screened Coulomb attraction), Mott-Wannier excitons form at radii much larger than a lattice constant. Mott-Wannier excitons are neutral and free to move through out the crystal unless confined as in a QD.

[19] Bohr radius is ~ 0.6 Å where $\varepsilon = 8.85x10^{-12}C^2/Jm, m_e^* = 0.0662m_0$.

[20] The adiabatic approximation follows from ion core mass being three to five orders of magnitude greater than the electron mass with therefore much lower resonance frequencies. This results in separable wave functions for ion cores and electrons (cf. Klingshirn [229], pp 129-130).

$$V(\rho) = E_{QW}(\ell(\rho)) - E_{QW}(\ell_0)\,, \qquad \text{[EQ 2.14]}$$

where the ground-state energy of the QW is given by

$$E_{QW} = \frac{\hbar^2\pi^2}{2m^*\ell^2}\,. \qquad \text{[EQ 2.15]}$$

Substituting [EQ 2.15] into [EQ 2.14], the lateral confining potential can be expressed as

$$V(\rho) = \frac{\hbar^2\pi^2}{2m_\perp^*}\left[\frac{1}{\ell^2(\rho)} - \frac{1}{\ell_0^2}\right],$$

$$V(\rho) = \frac{\hbar^2\pi^2}{2m_\perp^*}\left[\frac{1}{\left[\left(r^2-\rho^2\right)^{1/2} - h\right]^2} - \frac{1}{\ell_0^2}\right],$$

$$= \frac{\hbar^2\pi^2}{2m_\perp^* r^2}\left[\frac{1}{\left[\left(1-\left(\frac{\rho}{r}\right)^2\right)^{1/2} - \frac{h}{r}\right]^2} - \left(\frac{r}{\ell_0}\right)^2\right],$$

$$V(\rho) = \frac{\hbar^2\pi^2}{2m_\perp^* r^2}\left[\frac{1}{\left(\left(1-\left(\frac{h}{r}\right)\right) - \frac{1}{2}\left(\frac{\rho}{r}\right)^2\right)^2} - \left(\frac{r}{\ell_0}\right)^2\right]. \qquad \text{[EQ 2.16]}$$

By using a Taylor series expansion about $V(\rho = 0)$, $V(\rho)$ becomes

$$V(\rho) = \frac{\hbar^2\pi^2}{2m_\perp^* r^2}\left[\frac{1}{\left(1-\left(\frac{h}{r}\right)\right)^3}\left(\frac{\rho}{r}\right)^2 + \frac{1}{4}\frac{4-\left(\frac{h}{r}\right)}{\left(1-\left(\frac{h}{r}\right)\right)^4}\left(\frac{\rho}{r}\right)^4 + O\left(\rho^6\right)\right]. \qquad \text{[EQ 2.17]}$$

Most dome-shaped SAQDs fabricated by S-K mode growth have a height ℓ_0 to radius ρ_0 ratio of ~0.2: $A = \frac{\ell_0}{\rho_0} \approx 0.2$ [65]. Therefore, it is useful to introduce this parameter into [EQ 2.17]

$$V(\rho) = \frac{\hbar^2\pi^2}{2m_\perp^*}\left\{\frac{2}{\left(1+A^2\right)\rho_0^2}\frac{\rho^2}{\rho_0^2}\left(1 + \frac{A^2\left(3+5A^2\right)}{2\left(1+A^2\right)^2}\frac{\rho^2}{\rho_0^2}\right)\right\}. \qquad \text{[EQ 2.18]}$$

The term $\frac{A^2(3+5A^2)}{2(1+A^2)^2}\frac{\rho^2}{{\rho_0}^2} << 1$ and is neglected. Substituting [EQ 2.18] into [EQ 2.13] gives

$$V(\vec{r}) = \frac{\hbar^2\pi^2}{2m_\perp^*}\left\{\frac{2}{(1+A^2)}\frac{\rho^2}{\rho_0^2}\right\} + V(z). \qquad \text{[EQ 2.19]}$$

Then inserting [EQ 2.19] into [EQ 2.12], the Schrödinger equation becomes

$$-\frac{\hbar^2}{2m^*}\nabla^2\psi(\vec{r}) + \left\{V(z) + \frac{1}{2}m_\perp^*\,\omega^2\rho^2\right\}\psi(\vec{r}) = E\psi(\vec{r}), \qquad \text{[EQ 2.20]}$$

where $\omega^2 = \frac{4}{(1+A^2)}\frac{\pi^2\hbar^2}{(m^*)^2{\rho_0}^4}$. The second potential term in [EQ 2.20] is an effective centripetal confining potential affecting carrier motion in the x-y plane within a circular section[21], but is independent of the motion in the vertical direction (first potential term). Therefore the Schrödinger equation separates:

$$-\frac{\hbar^2}{2m_z^*}\frac{\partial^2}{\partial z^2}Z(z) + V_z Z(z) = E_z Z(z), \qquad \text{[EQ 2.21]}$$

and

$$-\frac{\hbar^2}{2m_\perp^*}{\nabla_\perp}^2\phi(\rho) + \frac{1}{2}m_\perp^*\omega_\perp^2\,\rho^2\phi(\rho) = E_\perp\phi(\rho). \qquad \text{[EQ 2.22]}$$

The first equation [EQ 2.21] describes energy in the vertical confinement (z-direction). Typically $V(Z)$ is taken as zero inside the QD, but V_z in the barrier and WL regions. Hence, the energy in the vertical direction (z-direction) is simply the ground state energy of a finite square well:

$$E_z = \frac{\hbar^2\pi^2}{2m_z^*{\ell_0}^2}. \qquad \text{[EQ 2.23]}$$

The second equation [EQ 2.22] describes motional energy within an effective central confinement potential due to a circular QD cross-section within a cylindrical geometry (i.e. in a plane). This generates not the standard atomic spherical harmonics, but two-dimensional oscillator wave functions. Therefore, it is convenient to approach this problem using annihilation (a,b) and creation operators (a^+,b^+) as given by[22]

$$a = \sqrt{\frac{m\omega_\perp^*}{2\hbar}}\left(x + i\frac{p_x}{m\omega_\perp^*}\right), \quad a^+ = \sqrt{\frac{m\omega_\perp^*}{2\hbar}}\left(x - i\frac{p_x}{m\omega_\perp^*}\right), \qquad \text{[EQ 2.24]}$$

[21] The 'circular' or central confinement potential -- due to the circular QD cross-section -- is (being in a plane) intrinsic to cylindrical geometry, not the spherical harmonics of the standard atom.

[22] These annihilation and creation operators are defined in Cf. Claude Cohen-Tannodji [68] p 731–732.

$$b=\sqrt{\frac{m\omega_{\perp}^{*}}{2\hbar}}\left(y+i\frac{p_y}{m\omega_{\perp}^{*}}\right),\qquad b^{+}=\sqrt{\frac{m\omega_{\perp}^{*}}{2\hbar}}\left(y-i\frac{p_y}{m\omega_{\perp}^{*}}\right). \qquad \text{[EQ 2.25]}$$

Since (a,b) act in different spaces, E_x and E_y, the only non-zero commutators between the four operators a,b,a^{+},b^{+} are $\lfloor a,a^{+}\rfloor=\lfloor b,b^{+}\rfloor=1$. The N_x,N_y operators are defined as $N_x=a^{+}a$ and $N_y=b^{+}b$. On substituting, the Schrödinger equation transforms into

$$\left\{\hbar\omega\left(a^{+}a+b^{+}b+1\right)\right\}\left|n_x,n_y\right\rangle=E_{\perp}\left|n_x,n_y\right\rangle,$$

$$\left\{\hbar\omega\left(N_x+N_y+1\right)\right\}\left|n_x,n_y\right\rangle=E_{\perp}\left|n_x,n_y\right\rangle. \qquad \text{[EQ 2.26]}$$

This equation means in the x-y plane wave function modes are counted by operators N_x,N_y: N_x referring to modes in the x-axis and N_y in the y-axis. Since the state energy is invariant under rotation about the z-axis, another good quantum operator is angular momentum L_z along the z-axis: $L_z=XP_y-YP_x=i\hbar\left(ab^{+}-a^{+}b\right)$. Introducing two new operators in replacing a,b with $a_{+}=\frac{1}{\sqrt{2}}(a-ib)$ and $a_{-}=\frac{1}{\sqrt{2}}(a+ib)$, whose non-vanishing commutators are $\lfloor a_{+},a_{+}^{+}\rfloor=\lfloor a_{-},a_{-}^{+}\rfloor=1$, the Hamiltonian in [EQ 2.26] and L_z become $\left\{\hbar\omega\left(a_{+}^{+}a_{+}+a_{-}^{+}a_{-}+1\right)\right\}\left|n\right\rangle=E_{\perp}\left|n\right\rangle$ and $L_z=\hbar\left(a_{+}^{+}a_{+}-a_{-}^{+}a_{-}\right)$. The combinations $a_{+}^{+}a_{+}$ and $a_{-}^{+}a_{-}$ are number operators N_{+},N_{-} (the number of right and left circular modes) rendering [EQ 2.26], $\left\{\hbar\omega\left(N_{+}+N_{-}+1\right)\right\}\left|n_{+},n_{-}\right\rangle=E_{\perp}\left|n_{+},n_{-}\right\rangle$. These signed number operators are associated with an orbital motion, or oscillation, of the electrons or the holes. If $N_{+}\rangle N_{-}$, the motion is clock-wise, but counter-clockwise if $N_{+}<N_{-}$[23]. The in-plane energy spectrum[24] (eigenvalues of [EQ 2.26]) for an electron or hole is thus

$$E_{\perp}=\hbar\omega\left(n_{+}+n_{-}+1\right), \qquad \text{[EQ 2.28]}$$

where $n_{+},n_{-}\in\{0,1,2,3,...\}$. The energy levels for an electron or hole are presented in Figure 2.8. In the case of the lens-shaped QD, the electron and the hole move circularly with an associated angular momentum along the symmetric axis (z-direction) given by

$$\ell_z=(n_{+}-n_{-})\hbar. \qquad \text{[EQ 2.29]}$$

[23] When $N_{+}=N_{-}$, the carriers are in a standing wave mode.

[24] Details of the formalism for a simple harmonic oscillator are found in Cf. Sakurai [72] p. 92-107.

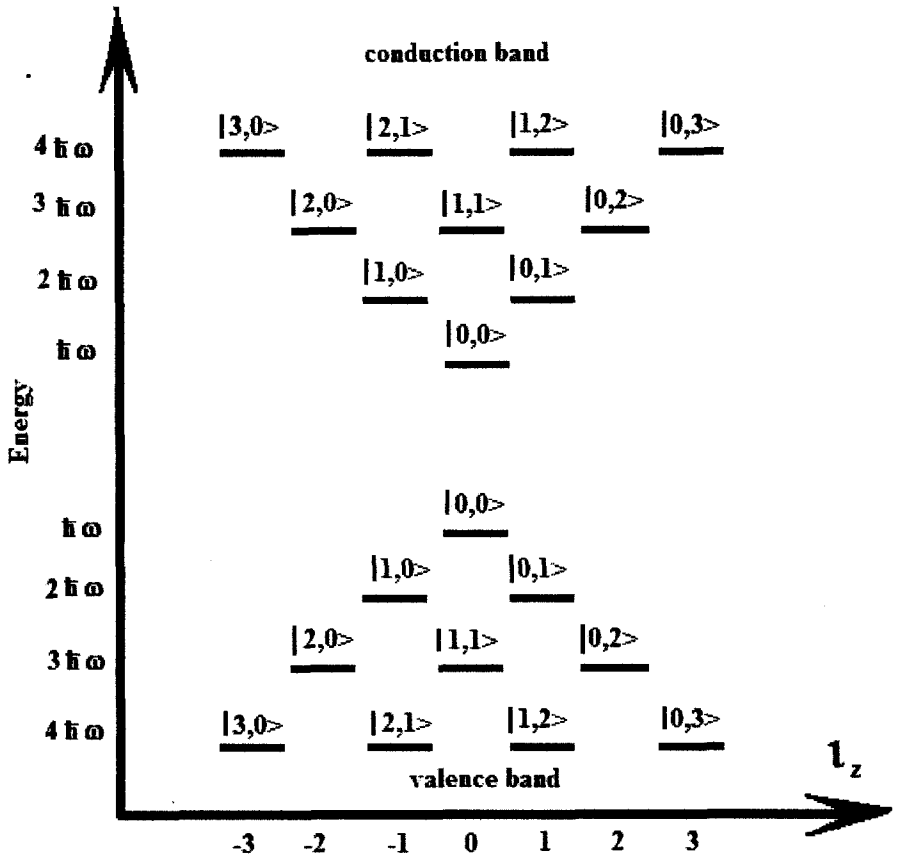

Figure 2.8: Energy levels $|n_+, n_-\rangle$ for an electron-hole pair, labeled by orbital angular momentum

This idealization of harmonic oscillators is accurate only for the lower QD energy levels because the wave-function at higher energy levels tends to penetrate the finite barriers. The motion of an electron-hole pair introduced in this section (not involving magnetic fields) strongly involves the lateral confinement potential. This potential has a shape close to a parabolic curve, similar to the center zone (Γ), for a dome-shaped SAQD.

2.4 The Influence of a Magnetic Field on a Free Electron-Hole Pair

The degeneracy of the SAQD excited states as shown in Figure 2.8 is lifted by applying a magnetic field in Faraday configuration (parallel to the growth direction). Fock [36] and Darwin [37] developed the single-particle "Fock-Darwin (F-D) spectrum model" describing the influence of the magnetic field strength.

A magnetic field significantly influences the motion of electrons and holes in the XY plane, particularly in the case when both bands have a two-dimensional parabolic well (i.e. self-organized InAs/GaAs QD). Weak magnetic fields have only minor influence on the

motional freedom already limited by lateral confinement, by shifting the energy levels diamagnetically". But in strong fields[25], the carrier orbits are more confined by the field than by the barrier potential, and the energy levels are shifted toward the Landau level[26] where cyclotron energy is larger than either the exciton binding or the lateral confinement energy.

In such a magnetic field, the carrier motion in the x-y plane is modified to the new "effective Hamiltonian" [68] given by

$$H = \frac{1}{2m_{\perp}^{*}}\left(\vec{p}_{\perp} - \frac{e}{c}\vec{A}\right)^{2} + \frac{1}{2}m_{\perp}^{*}\omega_{\perp}^{2}\,\rho^{2}\,, \qquad \text{[EQ. 2.30]}$$

where $\vec{A}$ is the vector potential of the magnetic field. In the case of $B//z$, the vector potential $\vec{A}$ is defined as $\frac{1}{2}B(y\hat{i} - x\hat{j})$. The electrons and holes are subjected to a combined 'squeezing' from magnetomotive force and centripetal confinement in the plane, reducing the radial motion. By expanding [EQ. 2.30], with the definition of $\vec{A}$:

$$\begin{aligned} H &= \frac{1}{2m_{\perp}^{*}}\vec{p}_{\perp}^{2} + \frac{1}{2m_{\perp}^{*}}\left(\frac{e}{c}\vec{A}\right)^{2} - \frac{e}{2m_{\perp}^{*}c}\left(\vec{p}\cdot\vec{A} + \vec{A}\cdot\vec{p}\right) + \frac{1}{2}m_{\perp}^{*}\omega_{\perp}^{2}\rho^{2}, \\ &= \frac{1}{2m_{\perp}^{*}}\vec{p}_{\perp}^{2} + \frac{1}{2m_{\perp}^{*}}\left(\frac{eB}{2c}\right)^{2}\left(x^{2}+y^{2}\right) - \frac{eB}{4m_{\perp}^{*}c}\left(p_{x}y - p_{y}x + yp_{x} - xp_{y}\right) + \frac{1}{2}m_{\perp}^{*}\omega_{\perp}^{2}\rho^{2}, \\ &= \frac{1}{2m_{\perp}^{*}}\vec{p}_{\perp}^{2} + \frac{m_{\perp}^{*}}{8}\left(\frac{eB}{m_{\perp}^{*}c}\right)^{2}\rho^{2} - \frac{eB}{2m_{\perp}^{*}c}\left(yp_{x} - xp_{y}\right) + \frac{1}{2}m_{\perp}^{*}\omega_{\perp}^{2}\rho^{2}, \end{aligned}$$

$$H = \frac{1}{2m_{\perp}^{*}}\vec{p}_{\perp}^{2} + \frac{1}{2}m_{\perp}^{*}\left(\left(\frac{\omega_{c}}{2}\right)^{2} + \omega_{\perp}^{2}\right)\rho^{2} + \frac{\omega_{c}}{2}\ell_{z}\,. \qquad \text{[EQ 2.31]}$$

where $\omega_{c} = \frac{eB}{m_{\perp}^{*}c}$ is the cyclotron frequency with the in-plane effective mass $m_{\perp}^{*}$, and ρ is the radial position of a carrier in the XY plane. $\vec{p}_{\perp}$ is the momentum in the XY plane and ℓ_{z} is the

---

[25] The cyclotron frequency $\omega_{c} = \frac{eB}{m^{*}c}$ is greater than the frequency ω where ω is defined by the effective potential, U_{eff}: $\omega = \frac{U_{eff}}{\hbar}$.

[26] Landau levels occur when the carrier orbit becomes smaller than the dot diameter. A sufficient strong field has more influence than the confining potential, quantizing carrier motion in circles in the plane perpendicular to B and quasi one-dimensional sub-bands are produced in a similar fashion to quantum wires. The Landau levels are given by $E = \left(n_{\ell} + \frac{1}{2}\right)\hbar\omega_{c}$, with n_{ℓ} the principal quantum number (Cf. Klingshirn [229] p 406).

angular momentum in the z-direction - $\ell_z = xp_y - yp_x$. Letting Ω stand for $\left(\left(\frac{\omega_c}{2}\right)^2 + \omega_\perp^2\right)^{1/2}$.

[EQ 2.31] reduces to

$$H = \frac{1}{2m_\perp^*}\vec{p}_\perp^{\,2} + \frac{1}{2}m_\perp^*\Omega^2\rho^2 + \frac{\omega_c}{2}\ell_z \,. \qquad \text{[EQ 2.32]}$$

The first two terms of the effective Hamiltonian in [EQ 2.32] are similar to the two-dimensional harmonic oscillator without magnetic field in [EQ 2.22], but with addition of frequency term, Ω. These effective Hamiltonians have similar interpretations, with the difference that the latter includes the influence of magnetic field in Faraday configuration, through its vector potential. The last term of [EQ 2.32] involving the projection of the angular momentum onto the magnetic-field direction amounts to a Zeeman-like interaction.

To obtain the energy states due to magnetic field, note that H commutes with L_z: $[\mathrm{H}, L_z] = 0$[27], and therefore H and L_z form sets of commuting observables; energy states for H are also momentum eigen-states for L_z. Two new annihilation and creation operators are defined as Fock and Darwin suggested [36 - 37]. They are not hermitian and modify those of the simple harmonic oscillator in two dimensions [EQ 2.24] and [EQ 2.25]. F-D combined the complex variable method with the original two-dimensional harmonic oscillator operator [69] to create these operators[28] given here:

$$a_+ = \frac{1}{2}\sqrt{\frac{m_\perp^*\Omega_+}{\hbar}}\left[(x - iy) - \frac{i}{m_\perp^*\Omega_+}(p_x - ip_y)\right], \qquad \text{[EQ 2.33a]}$$

$$a_- = \frac{1}{2}\sqrt{\frac{m_\perp^*\Omega_-}{\hbar}}\left[(x + iy) + \frac{i}{m_\perp^*\Omega_-}(p_x + ip_y)\right] \qquad \text{[EQ 2.33b]}$$

where i denotes the complex $\sqrt{-1}$. As a result, the effective Hamiltonian is transformed to

$$H = \hbar\Omega_+\left(\left(a_+^+ a_+\right) + \frac{1}{2}\right) + \hbar\Omega_-\left(\left(a_-^+ a_-\right) + \frac{1}{2}\right), \qquad \text{[EQ 2.34]}$$

where $\Omega_\pm = \left[\omega_\perp{}^2 + \frac{1}{4}\omega_c^2\right]^{1/2} \pm \frac{\omega_c}{2}$. The carrier (electron or hole) moves circularly in the XY plane when a magnetic field in the Faraday configuration; hence Ω_+ is associated with the clockwise motion while Ω_- refers to counter-clockwise motion.

For this effective Hamiltonian the single-particle energy spectrum is:

$$E(n_+, n_-) = \hbar\Omega_+\left(n_+ + \frac{1}{2}\right) + \hbar\Omega_-\left(n_- + \frac{1}{2}\right), \qquad \text{[EQ 2.35]}$$

---

[27] Details on obtaining the Hamiltonian and z-angular momentum eigenstates are found in cf. Claude Cohen-Tannodji [68] p 734.

[28] The transformation is demonstrated in Appendix B using the ladder operators.

where $n_{\pm} \in \{0, 1, 2, 3, \ldots\}$. Assuming that the electron and hole effective mass are equal to that of the bulk material[29] the energy levels for an electron or hole can be calculated from [EQ2.35] as shown in Figure 2.9.

More realistically, the effective mass is associated with the strain present between the QD and the barrier. As previously noted, electron or hole effective masses are different in QDs than bulk semiconductor. A relationship between the strain and effective mass in InAs/GaAs SAQDs is discussed with experimental results in Chapters 4, 5 and 6.

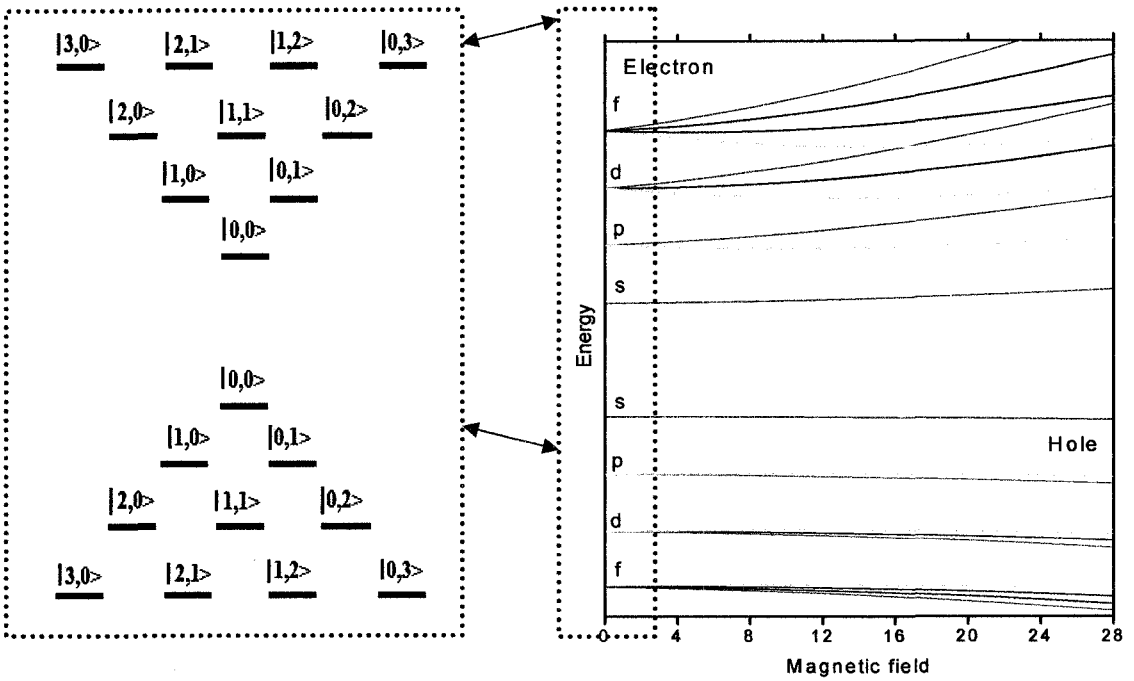

Figure 2.9: Energy levels for a confined electron-hole pair plotted as a function of external magnetic field applied in Faraday configuration

At zero magnetic field, the degenerate shells labeled by p, d ... have 2, 3 and 4 degenerate states, respectively. This degeneracy is gradually lifted as the external magnetic field is increased, without affecting the spin degeneracy. The inter-level spacing between conduction electron and valence hole is also slightly widened in a magnetic field due to the difference in the in-plane effective masses of electron and hole.

Thus far, electrons and holes have been considered as single particles with the Coulomb interactions between them neglected, as these are weak in a Wannier exciton[30]. But this interaction perturbation does affect the optical properties, especially around the band edge. The exciton is somewhat analogous to a positronium atom except that in the atom an electron is bound to a positron through the Coulomb interaction (in the exciton the electron and hole are unbound but correlated). Like an unanchored atom though, an exciton may act as a neutral

[29] i.e. ignoring 'band' or level bending near the confining barriers, strain effects and carrier mobility loss by scattering on alloyed constituents and at rough barriers.

[30] Wannier excitons are the most common type in semiconductors, whose Bohr radius (the mean distance between electron and hole) is large compared to the length of the lattice unit cell.

particle free to move through the crystal. Such excitons in semiconductors are responsible for intense absorption lines below the band gap energy in a region expected to be transparent.

In the case of a small dome-shaped dot, both the e-h interaction and lateral-confinement potential affect the energy spectrum [70,71] but the lateral potential is neglected at the moment (assuming a high magnetic field strength) in order to simplify the problem. Then the effective Hamiltonian in [EQ 2.10] reduces to

$$H = \left[\frac{p_e^2}{2m_e^*} + \frac{p_h^2}{2m_h^*}\right] - \frac{e^2}{\varepsilon|\vec{r}_e - \vec{r}_h|} \quad . \qquad \text{[EQ 2.36]}$$

The effect of the periodic atomic lattice and its periodic potential is incorporated into the electron and hole effective masses. Since the Coulomb interaction is attractive and the magnetic field confines the movement to circular orbits, an electron tends to stay in the vicinity of a hole. This exciton wave function is described as a wave packet[31] contracted from the linear combination of electron and hole Bloch functions.

$$\Psi(\vec{r}_e, \vec{r}_h) = \sum \phi(\vec{k}_e, \vec{k}_h) u_{c\vec{k}_e}(\vec{r}_e) e^{i\vec{k}_e \cdot \vec{r}_e} u_{v\vec{k}_h}(\vec{r}_h) e^{i\vec{k}_h \cdot \vec{r}_h}, \qquad \text{[EQ 2.37]}$$

where $\phi(\vec{k}_e, \vec{k}_h)$ is an expansion coefficient, depending on the electron and hole wave vectors, $\vec{k}_e$ and $\vec{k}_h$, respectively. $u_{c\vec{k}_e}(\vec{r}_e)$ and $u_{v\vec{k}_h}(\vec{r}_h)$ are the Bloch wave functions varying slowing with $\vec{k}_e$ and $\vec{k}_h$. Typically the band extreme is at the center of Brillouin zone where the atomic part of the Bloch wave function is at $\vec{k}_e = \vec{k}_h = 0$. The wave function reduces to

$$\Psi(\vec{r}_e, \vec{r}_h) \approx u_{c0} u_{v0} \sum \phi(\vec{k}_e, \vec{k}_h) e^{i\vec{k}_e \cdot \vec{r}_e} e^{i\vec{k}_h \cdot \vec{r}_h}. \qquad \text{[EQ 2.38]}$$

Adopting this wave function in [EQ 2.36], the energy eigenvalue can be obtained by transforming to a center-of-mass, relative position and momentum formalism:

$$\vec{r}_{CM} = \frac{m_e^* \vec{r}_e + m_h^* \vec{r}_h}{m_e^* + m_h^*}, \qquad \vec{r} = \vec{r}_e - \vec{r}_h \ , \qquad \text{[EQ 2.39a]}$$

$$\vec{p}_{CM} = \frac{m_e^* \vec{p}_e + m_h^* \vec{p}_h}{m_e^* + m_h^*}, \qquad \vec{p} = \vec{p}_e - \vec{p}_h \quad . \qquad \text{[EQ 2.39b]}$$

By using the relation in [EQ 2.37], the Schrödinger equation of [EQ 2.36] is rewritten as

$$\left\{\left(\frac{p_{CM}^2}{2M^*} + \frac{p^2}{2\mu^*}\right) - \frac{e^2}{\varepsilon|\vec{r}_e - \vec{r}_h|}\right\} \Psi(\vec{r}_{CM}, \vec{r}) = E\Psi(\vec{r}_{CM}, \vec{r}) \ , \qquad \text{[EQ 2.40]}$$

[31] The Wannier exciton is defined by Wannier approximation in cf. Peyghambarian [75] p.138-155.

where $M^* = M_e + M_h$ and $\mu = \frac{m_e^* m_h^*}{m_e^* + m_h^*}$. Now $\Psi(\vec{r}_{CM}, \vec{r})$ divides into two separable functions

$$\Psi(\vec{r}_{CM}, \vec{r}) = g(\vec{r}_{CM})\Omega(\vec{r}) , \qquad \text{[EQ 2.41]}$$

and the Schrödinger equation separates into

$$\frac{p_{CM}^2}{2M^*} g(\vec{r}_{CM}) = E_{CM} g(\vec{r}_{CM}), \qquad \text{[EQ2.42a]}$$

and

$$\frac{p^2}{2\mu^*} - \frac{e^2}{\varepsilon|\vec{r}_e - \vec{r}_h|}\Omega(\vec{r}) = E_r \Omega(\vec{r}) . \qquad \text{[EQ 2.42b]}$$

[EQ 2.42b] is referred as the Wannier equation.

The excitonic energy level[32] obtained are:

$$E_n = \frac{\hbar^2 K_{CM}^2}{2M^*} - \frac{\mu e^4}{2\varepsilon_r^2 \hbar} \frac{1}{n^2} , \qquad n = 1,2,3 . \qquad \text{[EQ 2.43]}$$

The first term describes the motion of an electron and hole bound together with the center of mass M^* while the second term gives the relative motion of the electron and hole. The exciton Bohr radius defined as $a_B = \frac{\varepsilon \hbar^2}{\mu e^2}$ specifies the binding energy of the electron-hole pair. The relation of an electron-hole pair and an excitonic picture is illustrated in Figure 2.10.

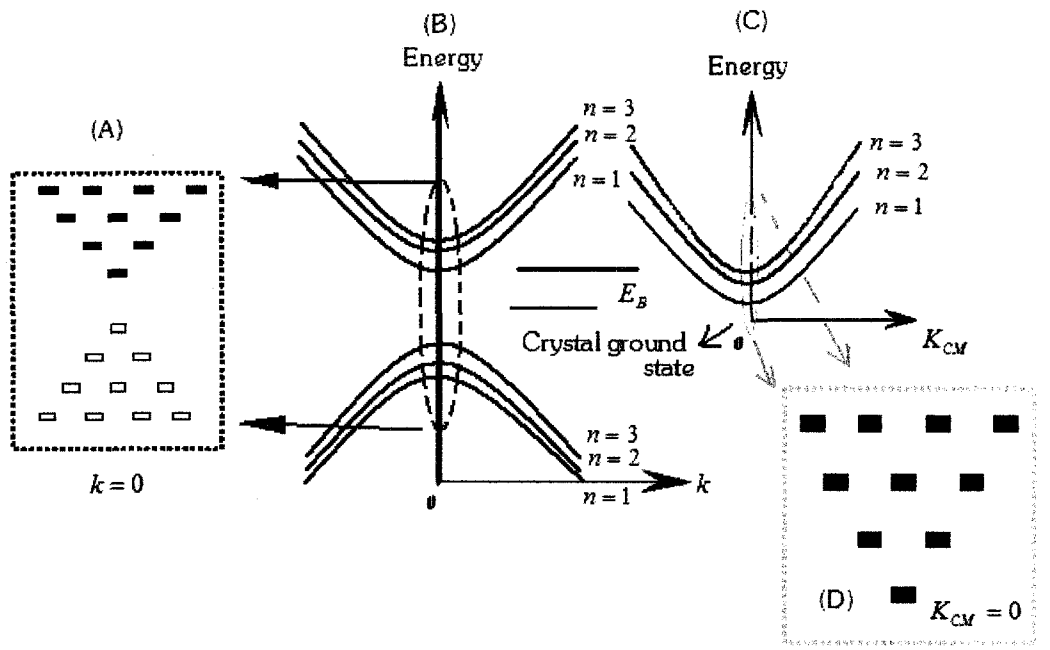

Figure 2.10: Levels for an electron-hole pair and exciton at zero magnetic fields

[32] Note that more details of the derivation are found from the textbook "Quantum Mechanics" by cf. Cohen-Tannodji [68].

A dispersion relation for free electron-hole pairs and excitons is schematized diagram (B) and diagram (C) respectively of Figure 2.10. In diagram (B), the upward and downward curves represent as usual energy levels for conduction electrons and valence holes. At the extremum $\vec{k} = 0$, within the dashed oval the degenerate energy levels with different angular momentum number are projected into diagram (A), where black solid bars represent electron energy states, the open bars holes. In diagram (C), upward curves represent exciton energy levels where the zero of energy ($\vec{K} = 0$) is the crystal ground state, the state without excitons. Here K is the exciton's center of mass wave vector.

The lower exciton resonance occurs within the forbidden gap (of free electron-hole pairs) and is named as the Rydberg exciton, whose energy appears as

$$E_B = \frac{\hbar^2}{2\mu a_B^2} . \qquad \text{[EQ2.44]}$$

The energy-levels for excitons at $\vec{k} = 0$ are detailed in diagram (D), with wave function

$$\Psi(\vec{r}_e, \vec{r}_h) = u_{c0} u_{v0} e^{i\vec{K}_{CM}\cdot\vec{R}} . \qquad \text{[EQ 2.45]}$$

The first two factors of this product wave function contain the character of the atomic orbital forming the valence and conduction bands.

In reality, the lateral confining potential does need to be taken into account even when magnetic fields are applied, involving both confining potential and Coulomb interaction. In a weak magnetic field, the Coulomb interaction term will play a relatively larger role, but still smaller than the lateral confining potential. In order to approach this problem theoretically, the perturbation methods[33] are employed. In contrast, if the applied external magnetic field is strong compared to the confining potential, a variational approach on a periodic QD array may be more suitable (eg. Aschcroft & Mermin, Appendix C). Such a model is outside the scope of this thesis.

2.5 An Electronic Band-to-Band Transition Rule[34]

The foregoing treatment of e-h pairs as confined excitons is made clearer in the context of an inter-level transition rule. Such a selection rule determines the optical properties of a specimen, as manifest in experiments such as PL and PLE. The selection is defined in accordance with Fermi's Golden rule [72] as the probability of a transition per unit time $\tilde{p}_{if}$, which for the transitions from an initial state $|i\rangle$ to final state $|f\rangle$ is given by

[33] cf. Cohen-Tannodji [68], p. 1093-1104.
[34] This section is modified from cf. Bastard [73], p 239-242.

$$\tilde{p}_{if} = \frac{2\pi}{\hbar}\left|\langle f|V|i\rangle\right|^2 \delta\left(\varepsilon_f - \varepsilon_i - \hbar\omega\right); \quad \varepsilon_f > \varepsilon_i \,, \qquad \text{[EQ 2.46]}$$

where V is the potential difference between effective Hamiltonians in the presence and absence of an electromagnetic field, and $\hbar\omega$ is the energy of an absorbed photon. Under typical experimental conditions[35] [73] the electric dipole approximation applies for purely imaginary V:

$$V = \frac{ie\left|\vec{E}\right|}{2m^*_{e(h)}\omega}\vec{\varepsilon}\cdot\vec{p} \quad , \qquad \text{[EQ 2.47]}$$

where e is the elementary charge magnitude, $m^*_{e(h)}$ is the electron (hole) effective mass, $\vec{\varepsilon}$ is the EM polarization vector perpendicular to propagation, and $\vec{E}$ and $\vec{p}$ are electric field and the carrier momentum, respectively.

When the same incident monochromatic light of sufficient energy is absorbed in a QD, electrons are promoted from valence to conduction levels leaving positive holes[36]. Such unbound electrons will tend to recombine with holes of suitable spin, spontaneously emitting photons. A schematic for these processes is presented in Figure 2.11.

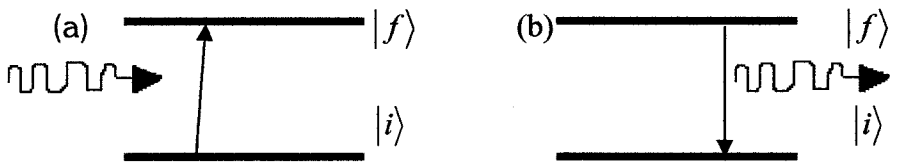

Figure 2.11: Absorption and spontaneous emission processes between states of differing energy

In absorption, the probability per unit time for an electron to make a transition from state $|i\rangle$ to $|f\rangle$ is ruled by the occupation of state $|i\rangle$ and the availability of state $|f\rangle$:

$$P_{if} = \tilde{p}_{if} f(\varepsilon_i)\left[1 - f(\varepsilon_f)\right] \,, \qquad \text{[EQ 2.48]}$$

where[37] $f(\varepsilon_v) = \dfrac{1}{\left(1+\exp\left[\dfrac{1}{k_B T}(\varepsilon_v - \mu)\right]\right)}$ and μ is the chemical potential (Fermi energy) of the electrons. The electromagnetic field then loses energy per unit time according to:

$$\mathrm{P}_{loss} = P_{if}\hbar\omega \,. \qquad \text{[EQ 2.49]}$$

---

[35] cf. Bastard [73], p. 239

[36] The holes are also mobile, not in the sense of movable ions but in the sense of movable ionicity, by the adiabatic exchange of core electrons with other ions.

[37] Now the Fermi distribution is used rather than the Maxwellian used as a first approximation at the outset of this Chapter

In spontaneous emission the probability of creating a photon is

$$P_{fi} = \tilde{p}_{fi} f(\varepsilon_f)[1 - f(\varepsilon_i)], \qquad \text{[EQ2. 50]}$$

where

$$\tilde{p}_{fi} = \frac{2\pi}{\hbar}\left|\langle i|V|f\rangle\right|^2 \delta(\varepsilon_f - \varepsilon_i - \hbar\omega). \qquad \text{[EQ 2.51]}$$

The rate of energy dissipation for the electron system is then:

$$\mathrm{P}_{create} = P_{fi}\hbar\omega. \qquad \text{[EQ 2.52]}$$

The net radiant power loss or intensity attenuation from these processes (absorption *less* spontaneous emission) is

$$\mathrm{P}_{total} = \mathrm{P}_{loss} - \mathrm{P}_{creat} = \hbar\omega(P_{if} - P_{fi}), \qquad \text{[EQ 2.53]}$$

$$\mathrm{P}_{total} = \frac{2\pi}{\hbar}\frac{e^2|\vec{E}|}{4m_0^2(m^*_{e(h)})^2}\hbar\omega\sum_{i,f}\delta[\varepsilon_f - \varepsilon_i - \hbar\omega]\left|\langle f|\vec{\varepsilon}\cdot\vec{p}|i\rangle\right|^2[f(\varepsilon_i) - f(\varepsilon_f)]. \qquad \text{[EQ 2.54]}$$

which is positive when the initial (lower) states are more occupied than the accessible higher ones. $\langle f|\vec{\varepsilon}\cdot\vec{p}|i\rangle$ is the optical matrix element expressing the coupling between the initial and the final states of polarized light. The optical matrix is a key to the selection rules of allowed the optical transitions.

For low dimensional heterostructures, like an idealized SAQD material, the initial and final states can be expressed as the product of a periodic function (Bloch function) and envelope function[38]. The wave function describing such a carrier [73] is given by

$$\langle i|r\rangle = \Psi_i(r) = u_{v_i}(\vec{r})f_i(\vec{r}), \qquad \text{[EQ 2.57]}$$

where u_{v_i} is the periodic part of the Bloch function for band v_i. In III-V semiconductors the periodic function for either electrons or holes is usually expressed at a BZ center or Γ point. Here $f_i(\vec{r})$ is the envelope function associated with the energy state defined in Section 2.3 as $|n_+, n_-\rangle$. Substituting this expression into the optical matrix element $\langle f|\vec{\varepsilon}\cdot\vec{p}|i\rangle$ renders

$$\langle f|\vec{\varepsilon}\cdot\vec{p}|i\rangle = \vec{\varepsilon}\cdot\int_{\Omega}F_i(\vec{r})(\vec{p})F_f(\vec{r})d^3r. \qquad \text{[EQ 2.58a]}$$

Since the Bloch function u_{v_i} varies rapidly, compared to the characteristic of the envelope function[39], [EQ 2.58] can be rewritten as

[38] In reality In/Ga alloying, strain and reconstruction affect dispersion in QDs, and they are not periodic.
[39] cf. Bartard [73], p 64.

$$\langle f|\vec{\varepsilon}\cdot\vec{p}|i\rangle = \langle u_{v_h}|\vec{\varepsilon}\cdot\vec{p}|u_{v_e}\rangle\langle f_{n_h}\|f_{n_e}\rangle + \langle u_{v_h}\|u_{v_e}\rangle\langle f_{n_h}|\vec{\varepsilon}\cdot\vec{p}|f_{n_e}\rangle, \quad \text{[EQ2.58b]}$$

where $\langle f_{n_h}\|f_{n_e}\rangle = \langle n_h\|n_e\rangle = \delta_{n_e,n_h}$. The first term denotes inter-band and the second is intra-band transitions, as all allowed optical transitions are some combinations of these. The latter occur only within the conduction band or valence band and are associated with the Bloch function - $\langle u_{v_h}\|u_{v_e}\rangle$ which implies that both electrons and holes occupy the same zone. Typically, these transitions are non-radiative processes, discussed further in Section 2.6.

The recombination term $\langle u_{v_h}|\vec{\varepsilon}\cdot\vec{p}|u_{v_e}\rangle\langle f_{n_h}\|f_{n_e}\rangle$ has two parts. The $\langle u_{v_h}|\vec{\varepsilon}\cdot\vec{p}|u_{v_e}\rangle$ is related to a polarization effect while $\langle f_{n_h}\|f_{n_e}\rangle$ represents a conduction electron $|n_+,n_-\rangle_e$ recombining with a hole $|n_+,n_-\rangle_h$. $\langle f_{n_h}\|f_{n_e}\rangle$ is illustrated as

$$\langle f_{n_h}\|f_{n_e}\rangle = {}_e\langle n_+,n_-|n_+,n_-\rangle_h . \quad \text{[EQ 2.59]}$$

This relation leads to the transition selection rule:

$$\Delta n_+ = 0 = n_{+,e} - n_{+,h} , \quad \text{[EQ 2.60a]}$$

$$\Delta n_- = 0 = n_{-,e} - n_{-,h} . \quad \text{[EQ2.60b]}$$

In III-V dome-shaped SAQDs then, the selection rule is remarkably simple, and it applies with or without an external magnetic field[40]. A schematic of radiative transitions is given in Figure 2.12 before a magnetic field is applied, showing degeneracy for the excited states (p, d, f, ...). As Figure 2.13 depicts, a Faraday-configured magnetic field lifts the degeneracy, and reveals extra structures in the emission spectra.

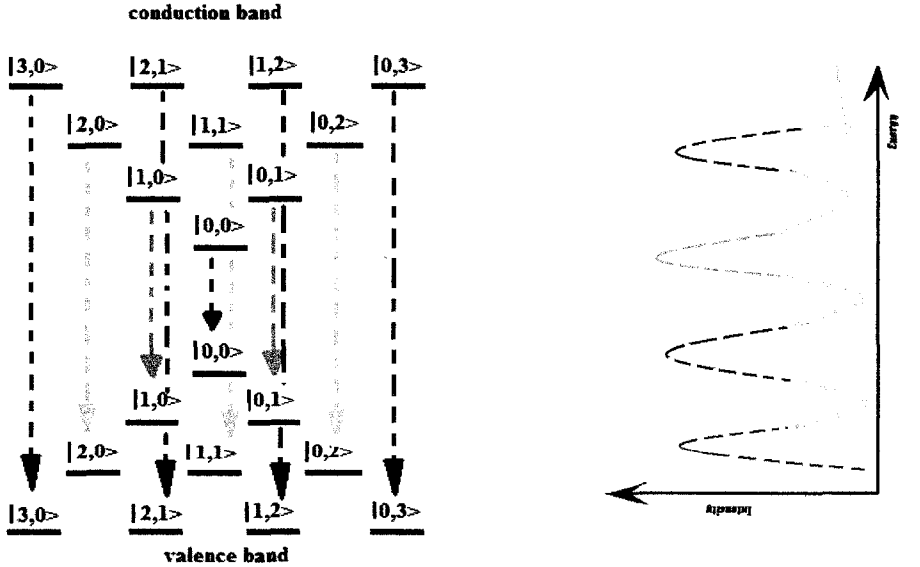

Figure 2.12: Energy-bands involved in SAQD transitions before a magnetic field is applied

[40] A magnetic field only lifts angular momentum degeneracy, without changing principal quantum number.

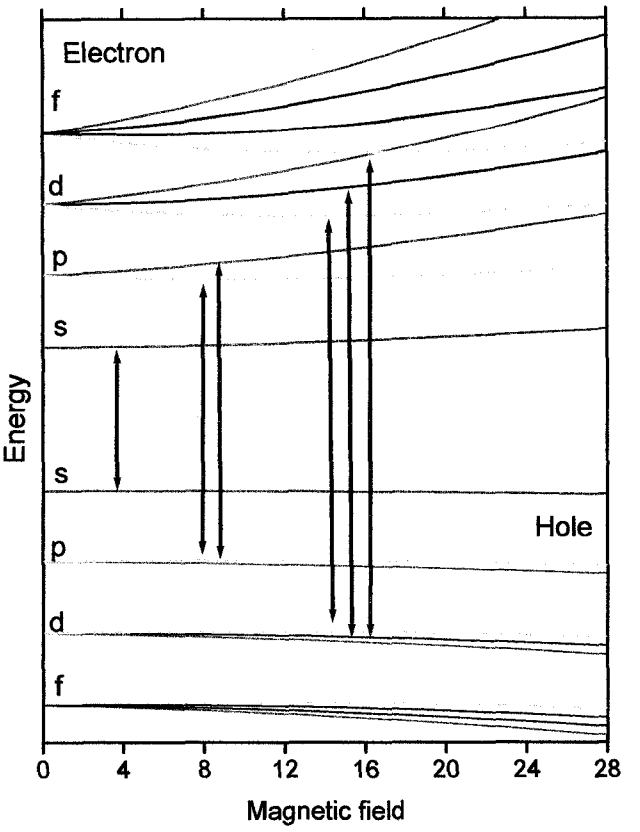

Figure 2.13: Possible energy-transitions in SAQDs in a Faraday-configured magnetic field

2.6 Non-Radiative Recombination[41]

Non-radiative recombination refers to any e-h recombination that does not emit a photon. Such recombination rates can be associated with semiconductor quality, especially in III-V compounds, where for instance impurity states inside the band-gap act as trapping or non-radiative recombination centers. They negatively impact the performance of optoelectronic devices since these processes deplete bands of carriers which would participate in key optical or transport mechanisms on which the device operation depends. Other typical intrinsic non-radiative recombination processes include Auger scattering, phonon and multi-phonon emission.

2.6.1 The Auger effect[42]

The Auger effect[43] is a process whereby the energy released by a recombining electron is immediately taken-up by one or more electrons (auger electrons) which then

[41] Auger scattering, phonon and multi-phonon emission do not depend directly on quality of crystal. They are intrinsic but non-radiative.

[42] This section was adapted from Chapter 7 (cf. Pankove [228]).

[43] Indeed, even without recombining with holes first, energetic electrons can depopulate higher states by emitting phonons.

dissipate the extra energy by emitting phonons. This three-body scattering event involving two electrons and a hole results in no net photon emission.

In SAQD, auger recombination may play a significant role in the inter-level transitions. For example, an electron in the higher state releases energy to another electron and relaxes down to a lower energy level and recombines with a valence hole. Figure 2.14 is a schematic illustration of an example of an Auger process in a band-to-band transition.

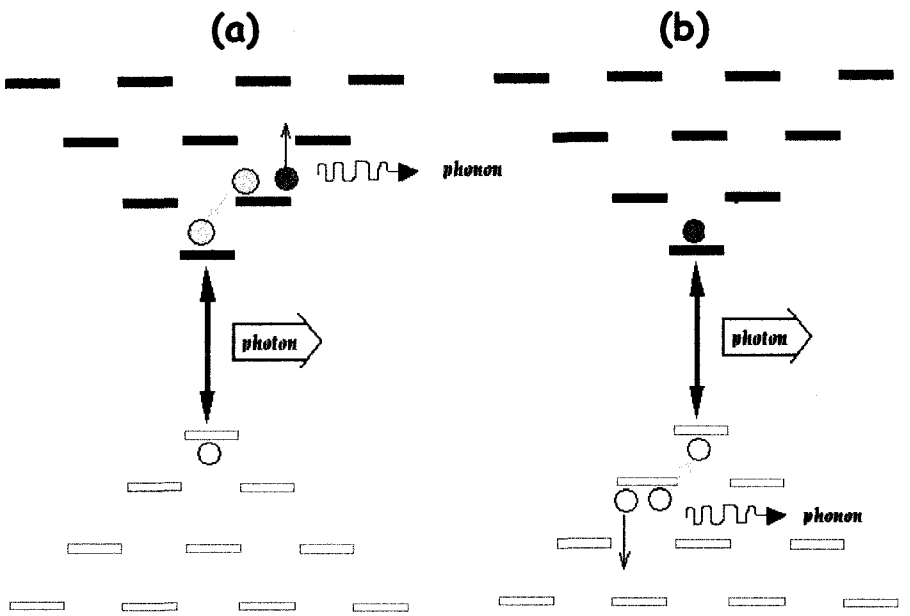

Figure 2.14: The Auger process in a semiconductor during band-to-band recombination for an electron (a) and a hole (b)

The Auger process also occurs in doped semiconductors. In n-type, the transition occurs from a donor to the valence band and the recombination energy can be taken up by either an electron in another donor or a conduction electron if many holes are present. A similar Auger process applies to p-type semiconductors. A schematic of either is shown in Figure 2.15.

In a doped SAQD (i.e. n-doped for example), of two electrons in a donor state the first transfers some of its energy as kinetic to the second and recombines with a hole, while the second is promoted into the QD conduction band. Otherwise just one electron in the donor state transfers its energy to a second already in the QD conduction band and then recombines with a hole.

Uskov *et.al.* [74] reported that, the Auger capture times in QDs could be of the order of 1-100 ps depending on origin of Auger carrier and the dot densities. Two types of Auger capture processes were discussed in this report. First, an electron or hole in the WL collides with another WL electron. One is captured by the SAQD and the other electron was scattered into a higher energy state in WL. Second, a WL hole was captured by the SAQD electron due to Coulomb scattering. A correlated electron with WL hole was excited into a higher state in WL.

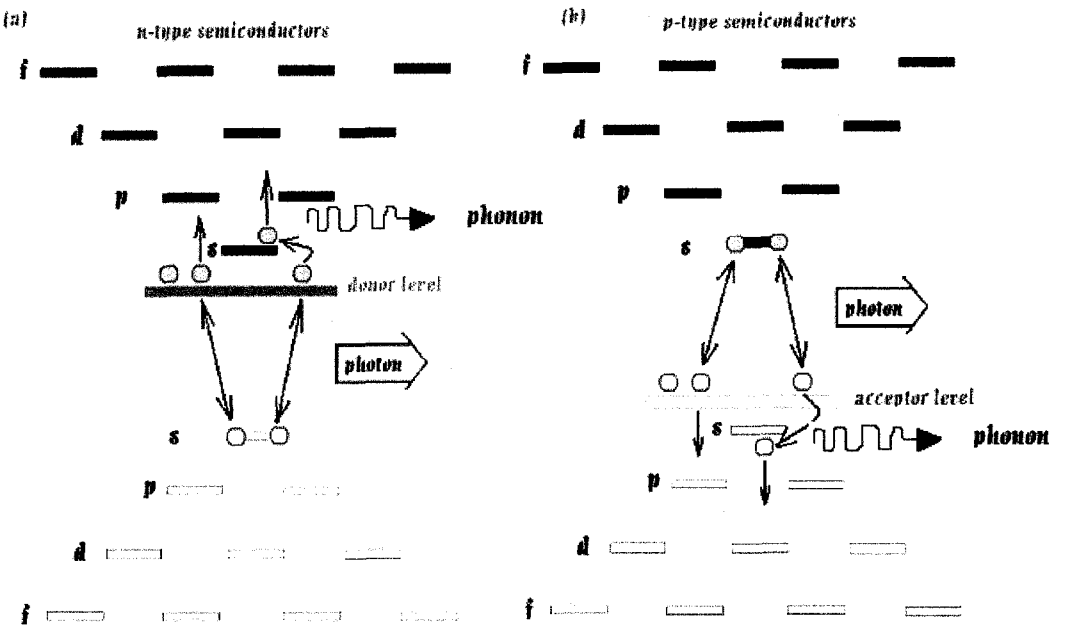

Figure 2.15: The Auger process for doped semiconductors[44]

2.6.2 *Single phonon emission or absorption*[45]

In carrier recombination, momentum and energy must be conserved. Typically, the processes for III-V semiconductors are distinguished as either direct or in-direct. In direct or 'vertical' recombination a phonon is not required to conserve momentum and the invariants are:

{Energy conservation}

$$E_i + \hbar\omega = E_f \ , \qquad \text{[EQ 2.56]}$$

{Momentum conservation}

$$\vec{k}_i = \vec{k}_f \ , \qquad \text{[EQ 2.57]}$$

(the subscripts denoting *initial* and *final* states accordingly). Indirect recombination changes the crystal momentum and requires a conserving phonon to do so, the invariants becoming

{Energy conservation}

$$E_i + \hbar\omega \pm \hbar\Omega = E_f \ , \qquad \text{[EQ 2.58]}$$

{Momentum conservation}

$$\vec{k}_i \pm \vec{K} = \vec{k}_f \ , \qquad \text{[EQ 2.59]}$$

where $\hbar\Omega$ and $\vec{K}$ are phonon energy and wave vector, respectively.

Semiconductors have characteristic band-gaps: either direct or indirect. InAs and GaAs have direct band-gaps while SiC and Ge are indirect. However, direct recombination occurs not only in direct -- nor indirect processes only in indirect -- band-gap semiconductors.

---

[44] Following cf. Pankove [228], Figure 7.1.

[45] This section is adapted from cf. Peyghambarian [75], Chapter 5.

Direct recombination may occur in either material at higher photon energies, and indirect recombination is always possible with some available matching phonons[46]. In short, phonon *emission* or *absorption* may occur in non-radiative recombination; but the more common transition for InAs QDs is direct or vertical and involves no phonon.

Phonons, whether emitted or absorbed during the recombination process, are by definition quantized ('pseudoparticle') mechanical oscillations of the semiconductor lattice atoms with several phonon *modes*. The optical phonon (LO and TO) branches have neighbors oscillating in opposite phase, while in acoustic phonons (LA, TA) they oscillate in phase [75]. The two 1-D longitudinal branches are illustrated in Figure 2.16(a). The diatomic lattice of any III-V semiconductor involves vibrations with three degrees of freedom, which support in each branch three phonon modes (longitudinal and orthogonal transverse modes) as shown in Figure 2.16(b).

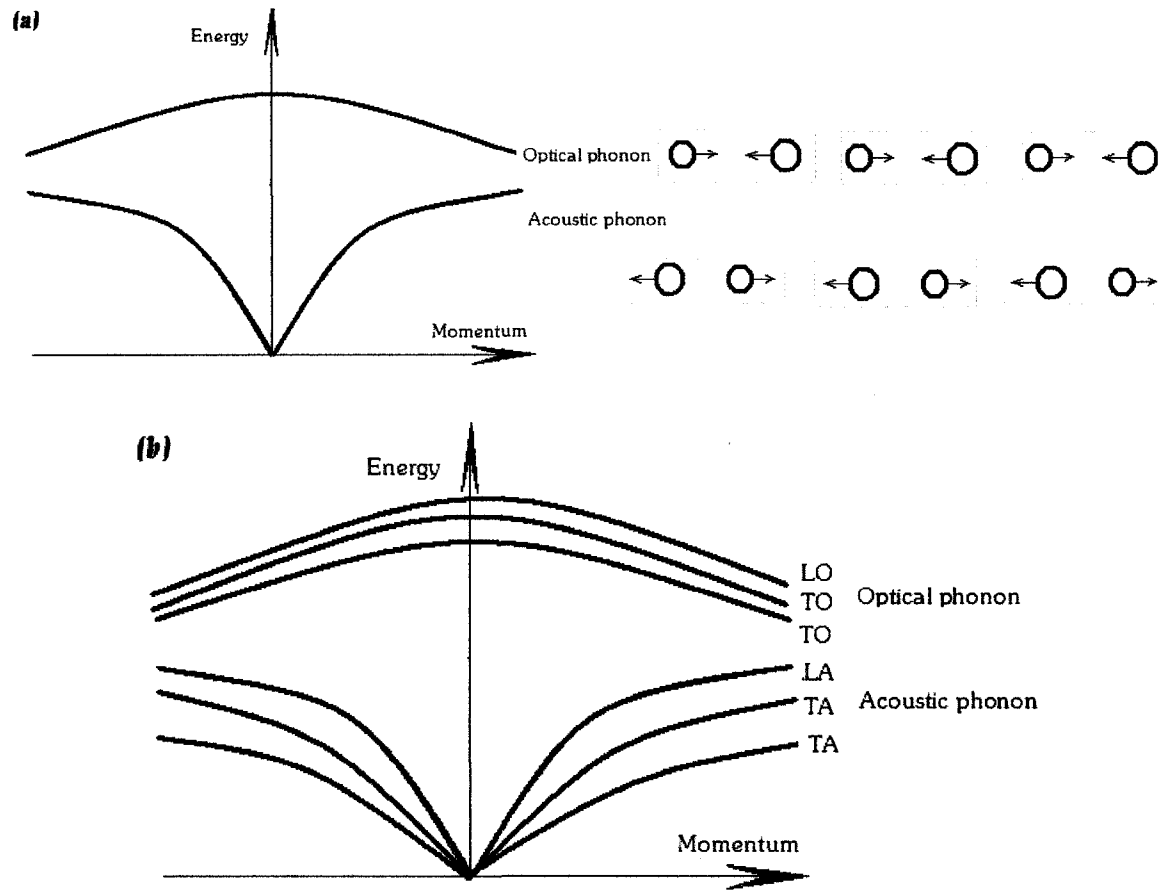

Figure 2.16: Optical and acoustic phonon branches in (a) one and (b) three dimensions[47]

Figure 2.17 gives phonon dispersion curves for GaAs [76, computed model] and the phonon energies of high-symmetry BZ points are collected in Table 2.1.

[46] or surface-acoustic waves (coherent phonons), or even physical gratings.
[47] This figure is adapted from page 87-89 of reference [75].

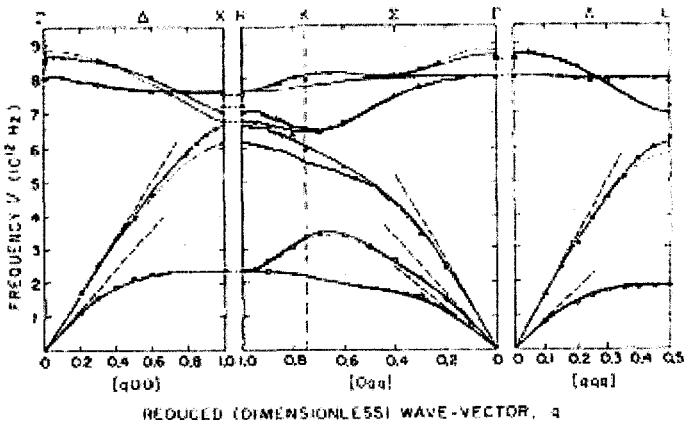

Figure 2.17: Phonon dispersion curves in GaAs at room temperature (after [76])

Table 2.1: Room temperature GaAs phonon energies for high symmetry BZ points [76]

Reciprocal Space location	Phonon mode	Energy (meV)
$\Gamma(000)$	LO	35.4 ± 0.8
	TO	33.2 ± 0.3
$X(100)$	LO	31.3 ± 0.3
	LO	29.9 ± 0.6
$R(0\bar{1}0)$	LA	28.1 ± 0.25
	TA	9.75 ± 0.06
$L\left(\frac{1}{2}\frac{1}{2}\frac{1}{2}\right)$	TO	32.4 ± 0.5
	LO	29.6 ± 0.3
	LA	25.9 ± 0.4
	TA	7.70 ± 0.08
$K\left(0\frac{3}{4}\frac{3}{4}\right)$	$TO_{//}$	32.7 ± 0.6
	$TO_{\perp}$	31.1 ± 0.5
	LO	26.6 ± 0.5
	LA	23.4 ± 0.5
	$TA_{//}$	14.4 ± 0.25
	$LA_{\perp}$	9.58 ± 0.15

2.6.3 Multi-Phonon Emission

A whole cascade of phonons may be emitted during the carrier recombination where the energy of any one phonon is smaller than the recombined carrier energy-loss. One such multi-phonon emission process is illustrated in Figure 2.18. Other types of minor non-radiative recombination processes in a QD are a surface recombination [77] and recombination through defects [78]. These occur when carriers are within a diffusion length or bulk mean-free-

path of a surface or defect, where by scattering they can recombine through a continuum of states[48].

Typically, PL and PLE measurements are associated with three main carrier dynamics: energy absorbed to produce electron-hole pair, relaxation process and recombination process. During the relaxation process, phonon-assisted emissions are likely to be involved during the process. The carrier inside the dot may be coupled to those LO or LA phonon modes during the relaxation process. In particular, PLE spectrum is observed only for those dots for which there is an efficient relaxation mechanism to the ground state for carriers absorbed into an excited state. Hence phonons need to assist during the recombination process, unless the level separation within a band happens to be equal to a single phonon energy (i.e. the so called phonon bottle-neck effect).

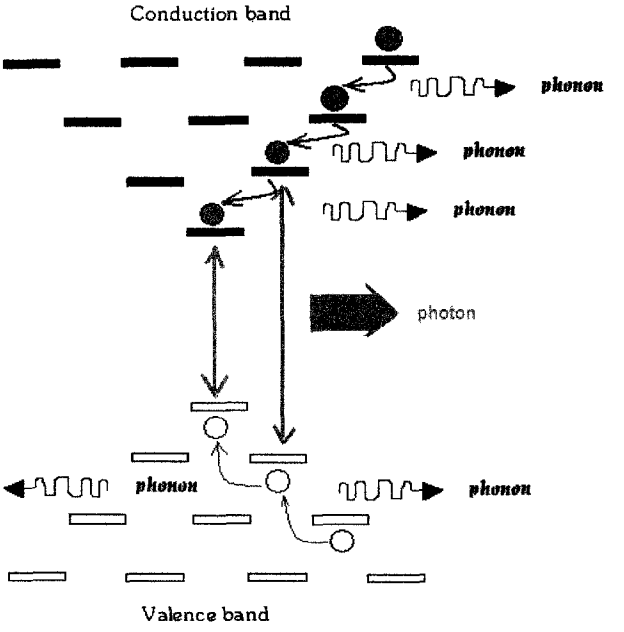

Figure 2.18: Example of multi-phonon emission

[48] Although some surface impurity scattering may be radiative.

Chapter 3

Experimental Setup

Optical characterization techniques are commonly used to probe the structural and electronic properties of semiconductors. There are three main components in any standard optical characterization measurement: an excitation source, a spectrometer and a detector. If the carriers in the semiconductor are excited by laser light, their recombination emission is "photo-luminescence" (PL). If the excitation source is an electron beam or charges injected by electric field or tunneling, the optical emission is called "cathodo-luminescence" [79-81] and electro-luminescence [82-84] respectively. Since PL is a conventional probe of the semiconductor optical properties and is relatively straightforward to perform and analyze, the SAQD samples discussed in this thesis were characterized by this technique as described in Section 3.1.

Further to the PL results described in Section 3.1, photoluminescence excitation (PLE) optical experiments are described in the subsequent section. Beyond these two techniques, some SAQD samples were examined under a Faraday-configured magnetic field in experiments described in Section 3.3 and 3.4.

The PL spectra for InAs/GaAs SAQD samples reveal well-resolved peaks from the s-, p-, d- and f-levels as shown in Figure 3.1. However, each line width is broadened and inter-wavelength separation between the emission peaks is considerable. Fafard and Allen [85] found that a post-growth rapid thermal anneal (RTA) reduces the line width and inter-level emissions. Some details of the RTA process are given in Section 3.5.

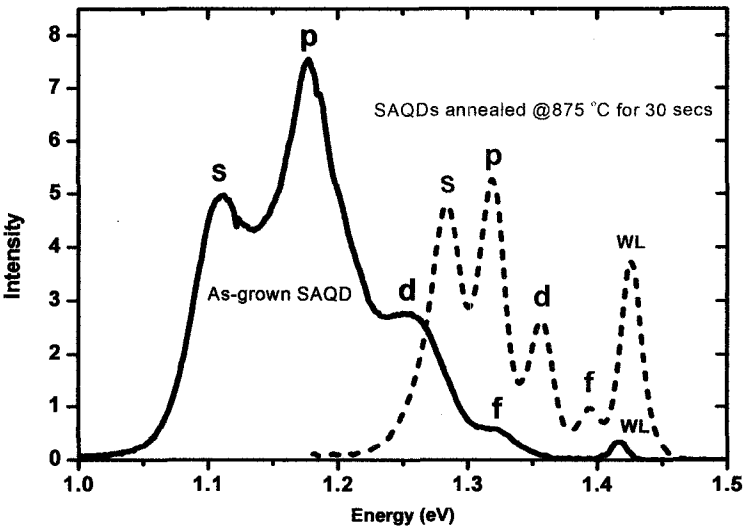

Figure 3.1: PL spectrum of InAs/GaAs SAQD. Experimental uncertainty is ± 1 meV

In Figure 3.1 the solid line marks the spectrum of an as-grown SAQD sample, the dashed line is for the same sample after RTA of 875°C for 30 seconds. The InAs/GaAs QD

layer was grown by MBE combined with indium flush technique [95] and capped by 100 nm of undoped GaAs.

3.1 Photoluminescence (PL)

PL as in Figure 3.1 above is a standard characterization technique for the optical properties of semiconductors, especially III-V compounds. The word "photoluminescence" refers to various mechanisms involved in light emission. In semiconductors there are three main processes: absorption, relaxation and emission.

Consider a piece of InAs cryogenically cooled to 4.2 K (liquid He). At this temperature any conduction electrons have low kinetic energy. When some monochromatic light shines on the sample the electrons in the semiconductor absorb energy. If the absorbed energy is sufficient to overcome the band-gap, the photons promote electrons into the conduction from the valence band.

When electrons are excited to conduction levels, valence holes are created, and as these carriers are not in a low-energy state they tend to release the extra energy by scattering and/or recombining. Thus the non-equilibrium photo-excited ensemble of carriers relaxes via scattering processes from higher energy levels into lower ones, as described in Chapter 2. During this relaxation *phonons* may be emitted before electrons and holes recombine radiatively as described in Section 2.6.

The processes already described are illustrated in Figure 3.2, which presents light absorption and relaxation processes in a semiconductor. The energy bands on the left depict the original states of electrons before the light shines on a cold sample. The middle panel represents absorption, where electron-hole pairs are created. The panel on the right displays relaxation processes in which both photons and phonons are generally emitted.

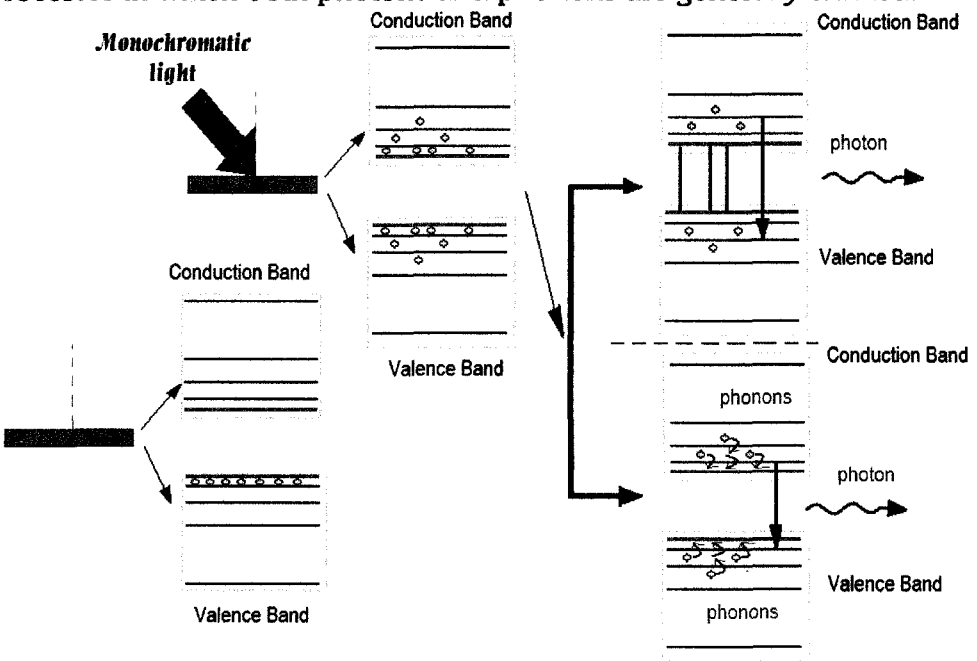

Figure 3.2: A schematic picture of the physical processes involved in the PL technique

In the case of a heterostructure, such as InAs/GaAs forming a random 'fabric' of QDs, similar processes occur when illumined by monochromatic light. Holes are generated in InAs valence levels with the electrons in conduction levels. When the photon energies are much higher than the band-gaps in the WL or GaAs cap layers, electrons are promoted to the continuum state; hence PL emission is called ***non-resonant PL***. If the energy of excitation goes to discrete states within the QD, it is called ***resonant PL***.

Both excitations follow similar relaxation mechanisms whereby the created electron-hole pairs seek to lose energy. Within the limits of exclusion and selection rules, the carriers may relax to lower energy states and/or recombine radiatively emitting photons. If not in the lowest *possible* state (s-shell) electron-hole pairs may also recombine from higher states (p, d, f,..) as described in Chapter 2. The emitted photons are collected with lenses and spectrally dispersed in a spectrometer before being detected as a function of wavelength.

Unrelaxed electrons and holes tend to form hydrogenic orbitals, or excitons of Mott-Wannier type. Such excitons occur in discrete QD energy levels for resonant PL, but also in the continuum state for non-resonant PL. In either case a main emission line is observed corresponding to exciton decay at the s level if the excitation power is low, since then relatively few excitons are created per unit time and the s states do not get saturated.

If a QD is populated with another exciton (i.e. via resonant PL), another line appears from recombination of a single electron-hole pair within the bi-exciton state[49]. An energy shift of this bi-exciton line, compared to the exciton line, is due to Coulomb interaction within the SAQD [86], although the lowest bi-exciton is not easy to distinguish from the single exciton in a PL measurement because a very large number of SAQDs are excited at the same time in macro-PL of a large QD ensemble.

On increasing the number of excitons occupying a QD at any given moment (via blue-shift[50] of the light and/or increased intensity), they occupy the p level and above, as the s level or ground state can accommodate a maximum of two electron-hole pairs in accordance with the Pauli exclusion principle [87]. The p level can support up to four, and further excitons fill higher shells (d, f, etc) as discussed in Section 2.3. PL spectra exhibit a clear level structure as a function of increasing power, corresponding to the increasing exciton occupation of available states. This phenomenon is typically called the "state filling effect" [88 - 90].

An example of some measured PL spectra is shown in Figure 3.3 as a function of illumination intensity. The intensity of the collected luminescence is provided at the peak energies to represent the number of excitons per dot. The energy levels in the panels represent various exciton level occupations: 2 for the s, 4 for the p, 6 for the d, and 6 excitons for a partially filled f level[51]. Each electronic diagram represents a different QD ensemble, since many QDs are probed in PL.

---

[49] Biexciton is two excitons correlated with each other.

[50] Light energy sufficient to promote to higher levels may add cascading or decaying carriers from above a given level and contribute to state-filling.

[51] When a lower level is filled, higher ones are partially filled due to finite lifetime or decay rate: (1) non-uniform or Gaussian excitation profile, (2) statistics of hole generation in different QDs, (3) the different rates of carrier relaxation among different QDs, and (4)finite recombination times (decay rate) in any QD level.

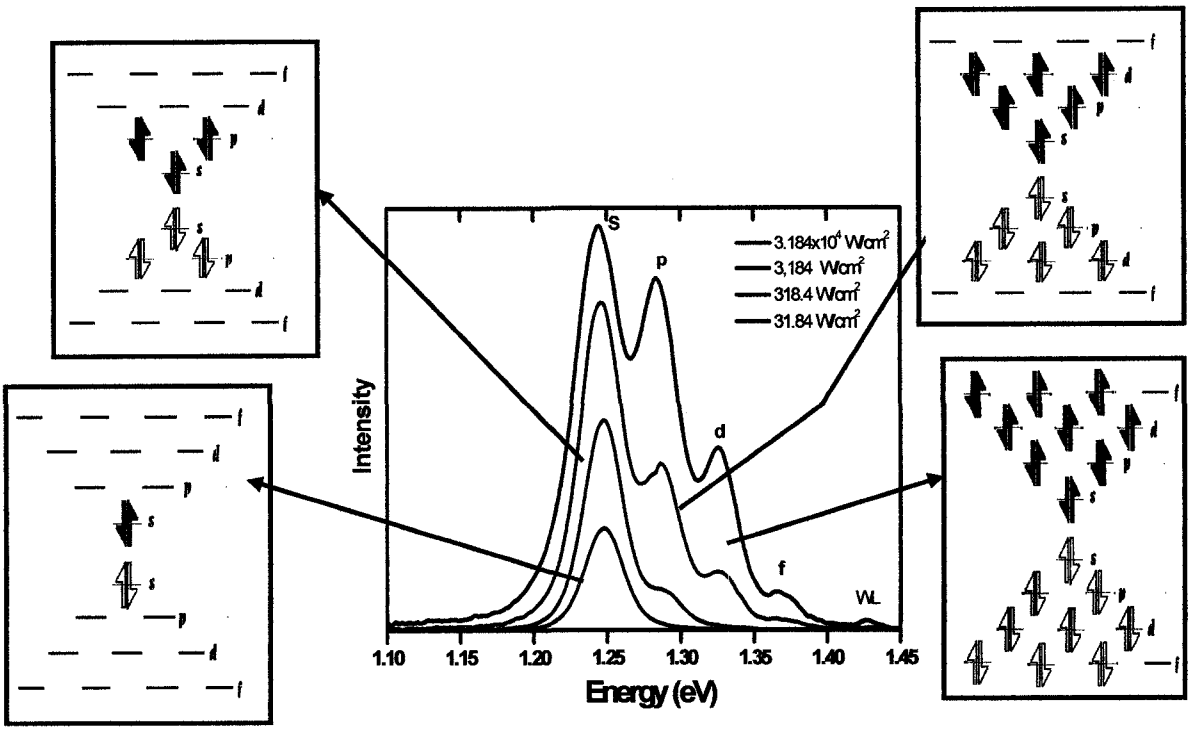

Figure3.3: Evolution of a non-resonant PL spectrum of InAs/GaAs SAQD[52] with ±1 meV experimental uncertainty

The as-grown QDs have somewhat different sizes and alloy composition, which broaden their luminescence peaks. Specifically, exciton decay in differently sized dots of shifted energy levels produces luminescence in a spread of emission energy. Increasing the number of excited dots reduces the visibility of the individual dot fluctuations in the spectrum, as shown in Figure 3.4.

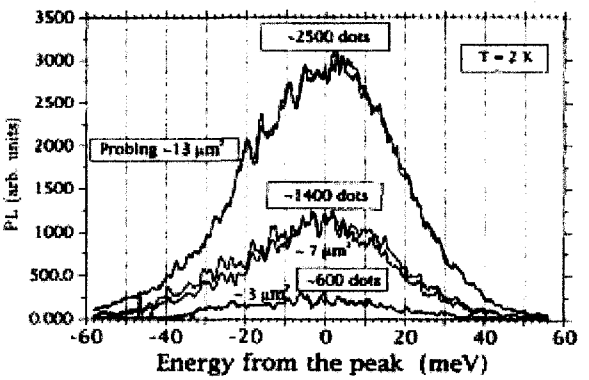

Figure 3.4: PL spectra showing positive correlation between fluctuation and the number of QDs probed (from Fafard [91])

Next, ***resonant PL*** is considered where the laser excitation energy is set in the SAQD discrete energy range ($E_{exc} < E_{Barrier}$). Electron-hole pairs are now created at these discrete energy levels inside the QD. For example, monochromatic wavelength may be set to create excitons just below the WL level at the f state in SAQDs with lateral 20 ± 2 nm diameter

[52] The SAQD sample was annealed at 850 °C for 30 sec.

and 4 ± 0.4 nm height[53] [92-93]. Excitons are created in the f state only in QDs having that energy level (within uncertainty) [94-96] even though the excitation laser illuminates many SAQDs of various diameters and heights. Thus the resonant PL results in a narrower emission line from each level, compared with non-resonance.

Non-resonant PL (dashed line) and resonant PL (solid line) spectra are compared in Figure 3.5 for InAs/GaAs SAQDs[54] using excitation energies of 1.960 and 1.470 eV, respectively. As expected, they are significantly different.

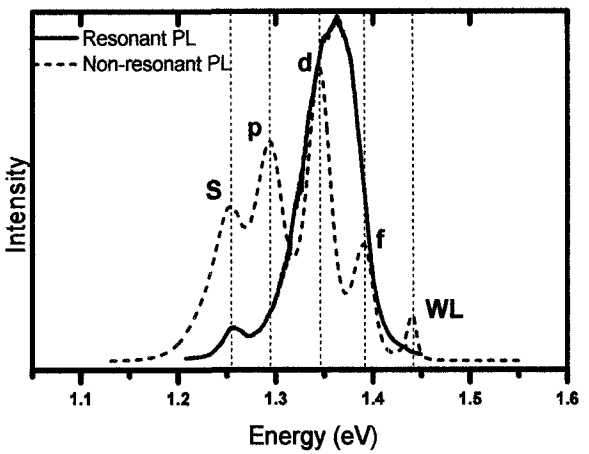

Figure 3.5: Comparing non-resonant and resonant PL spectra[55] with ± 1nm (±1 meV) uncertainty

As detailed in Figure 3.6, the system employed for this research uses coherent light which impinges on a SAQD sample that has been cooled to either 77 K or 4.2 K. The beam passes a chopper and a focusing lens before exciting the sample, whose luminescent response is steered through a beam-splitter and the focusing lens, then onto the grating spectrometer. Normally the slits in front of the spectrometer are opened to a 1 mm wide aperture to control the resolution while obtaining enough signal intensity.

The luminescent light after being dispersed by the grating is sampled by the detector. A long-wavelength pass filter may be placed in front of the spectrometer to allow only the luminescence to reach the grating while rejecting the stray lights from the laser. If necessary, a neutral density filter is placed in the collection path to protect the detector from excess signal intensity. The energy-binned intensity of the emitted luminescence is finally converted to voltages with a lock-in amplifier (to improve the signal-to-noise ratio) and processed by computer.

[53] The diameter and height is quoted from the references. Percentage of error is relied on the InAs deposite rate (0.2nm/sec) and normally QD layer is taken from 24 sec up to 40 sec. TEM pictures [95]

[54] 2138 RTA 825 °C for 30 sec from data "France Nov2003"

[55] The result is from the SAQD studied in France (more results in Chapter 6).

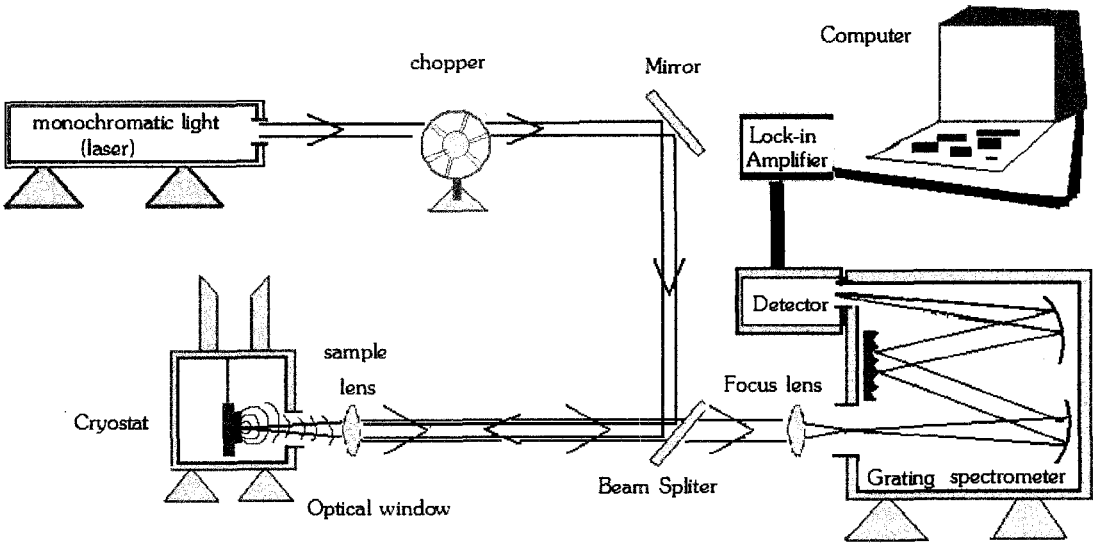

Figure 3.6: A schematic diagram of the PL experimental setup used

The list below outlines the equipment employed:

- ***Excitation Sources***,
  - 532-nm line of a Millennia V Nd:YVO_4 Laser by Spectra-physics
  - 632.8-nm line of He-Ne gas laser
  - Ti-sapphire tunable laser pumped by Ar^+ laser; the laser could tune from ~850 nm (1.4586 eV) to ~1000 nm (1.2398 eV)

- ***Spectrometer:*** an optical monochromator provided with a calibrated scale for the measurement of the wavelength.
  - ***Double grating spectrometer***: an optical device consisting of an assembly of narrow slits with a grooved gating. When the light falls on these grooves, it diffracts and produces the spectra. The spectrometer used in this thesis is CVI DK240 ¼ m double grating equipped with 600 grooves/mm (3.2 nm/mm for dispersion) and 1200 grooves/mm (1.6 nm/mm for dispersion).

- ***Detector***: a device that responds to, and in effect counts photon (the sample PL emission). Two types of detectors are employed for this thesis: position independent and position-based.
  - ***Position independence*** refers to the sensitivity of the position on the surface of a detector to incoming light. A LN_2-cooled Si CCD camera is employed for the work. The CCD camera detects the energy range of the dispersed emission light as a function of a position in the image field in a single exposure. The position on the detection surface of CCD camera has a non-linear relation with the detected energy (or wavelength). This is non-linearity confirmed by performing the calibration at the detected energies before beginning measurement.
  - ***Position base*** refers to the detector that records an incoming photon (emission light) at a particular detected energy (or wavelength). A *Germanium detector* [EO-817L North Coast Scientific Nitrogen-

cooled Ge Photo-detector: 700 - 1800-nm detection wavelength] and *InGaAs 1.3-micron Photo-multiplier tube were use.* For full data-set many exposures are needed at different image positions. The detector can't itself be tuned, but is placed at various angles in the chromatic dispersion of the grating at the exit of the spectrometer.

An example calculation for a non-resonant PL experiment is next considered using the data of Figure 3.3, whose energy levels referenced to the GaAs bulk are given in Figure 3.7. Typically the in-plane density of the InAs/GaAs SAQDs grown by MBE [97-103] is ~ 10^{10}-10^{11} cm^{-2} per layer [93,96]. Their size range is about 25-30 nm in lateral diameter and about 3-5 nm in height. As an estimate of the number of available states for each of the QD energy levels (s, p, d or f) after they are saturated, assume that the density of dots is $5x10^{10}$ cm^{-2}, and that the dot size is monodisperse (all dots are the same). The number of available states helps to check the minimum excitation power to produce enough excitons when a QD is in the saturated condition. The number of available states in SAQD is calculated by multiplying the number of available states (i.e. s, p, d, f, ...) with the density of dot.

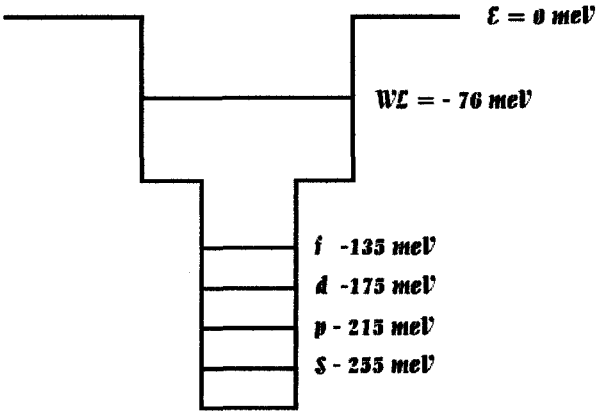

Figure 3.7: Energy levels for an InAs/GaAs SAQD determined from PL spectra

This diagram sets the levels to peak energies of the PL spectrum in Figure 3.3. As seen, the average inter-level energy of the QD is ~40 meV. The total number of available quantized states, N, is the energy integral over the density of states in the SAQD:

$$N(\varepsilon) = \int g(\varepsilon) d\varepsilon \qquad \text{[EQ 3.1]}$$

For a QD sample $g(\varepsilon)$ is given in [EQ 2.9]. Assuming a dot density of $5x10^{11}$ cm^{-2}, the number of available recombination states from a given state of the sample is calculated as $1x10^{12}$ cm^{-2}, $2x10^{12}$ cm^{-2}, $3x10^{12}$ cm^{-2} and $4x10^{12}$ cm^{-2} for s, p, d and f levels, respectively. Appendix D.1 provides the details of this calculation.

In PL experiments, luminescence from the p state is not observed until the s state is completely occupied. Likewise d and f lines are not detected until the lower energy states are filled. To fill the lower levels, sufficient incident intensity is required to produce more excitons per second than are decaying and recombining for them. In these experiments the source intensity is only partly transmitted through the cap layer even at normal incidence to the sample

surface. As discussed in Appendix D.2, only about 33.9 % of the exciting light at 514.5 nm penetrates to the QDs, where it is mostly absorbed, and producing excitons.

The number of created photons (from an incident laser beam) per second per surface area $\Phi(P_{exc})$ generated is given by

$$\phi(P_{exc}) = \frac{P_{exc}}{E_{Photon}} \qquad \text{[EQ 3.2]}$$

where E_{photon} is the energy of each individual photon in the laser beam. Certain proportion of the photons can penetrate to QD layer is expressed through the fraction parameter $f(P_{exc})$ demonstrated in Appendix D.1. The average number of photons getting into the QD layer is $f(P_{exc})\phi(P_{exc}) = \frac{P_{exc}}{E_{Photon}} f(P_{exc})$. Hence, the average number of photons created after the recombination process in the QD σ given as the combination of the created photon in the QD and the recombination lifetime in the QD τ is given by

$$\sigma = \frac{P_{exc}}{E_{Photon}} f(P_{exc})\tau \qquad \text{[EQ 3.3]}$$

Typically the carrier lifetime τ in InAs/GaAs SAQD is ~1 ns [104] and the excitation power required to saturate the various energy levels is

s-shell: $$P_{exc} = \frac{E_{Photon}\sigma}{f(P_{exc})\tau} = \frac{(1.1\text{x}10^{11}\ \text{cm}^{-2})(3.7x10^{-19}\ J/photon)}{0.34(1x10^{-9}\ s)} = 1.1x10^{2}\ \frac{W}{cm^2}$$

p-shell: $$P_{exc} = 1.1x10^{2} + \frac{(2.0\text{x}10^{11}\ \text{cm}^{-2})(3.7x10^{-19}\ J/photon)}{0.34(1x10^{-9}\ s)} = 2.2x10^{2}\ \frac{W}{cm^2}$$

d-shell: $$P_{exc} = 2.2x10^{2} + \frac{(3.0\text{x}10^{11}\ \text{cm}^{-2})(3.7x10^{-19}\ J/photon)}{0.34(1.0x10^{-9}\ s)} = 5.5x10^{2}\ \frac{W}{cm^2}$$

f-shell: $$P_{exc} = 5.5x10^{2} + \frac{(4.0\text{x}10^{11}\ \text{cm}^{-2})(3.7x10^{-19}\ J/photon)}{0.34(1x10^{-9}\ s)} = 9.8x10^{2}\ \frac{W}{cm^2}$$

Intensities required in experiment are only qualitatively close to these calculated. The true dot density might not be very close to that derived from other published TEM pictures[56].

PL spectra represent a spread or distribution within energy levels (s, p, d, f and g) for a very large number of SAQDs that possess variations in diameter and height. Well over a million dots are probed at once at normal laser incidence to the SAQD sample. This is due to a limitation of the equipment in narrowing the laser spot size (~ 50 - 100 microns)[57] and the density of dots grown in a S-K mode [105 - 107] (~1x10^{10} cm^{-2}).

[56] The dot density estimates from TEMs cf. Fafard [95]

[57] This is not the limit in principle. Other methods may be used to reduce the laser waist at incidence

As explained above in Section 3.1, with excitation wavelength fixed at say ~ 2.33 eV in the green, the electron-hole pairs are created in the continuum states or at highly excited states in the QD and then scatter, release phonons, and drop to the discrete levels where they recombine to emit photons. The detected photon energies typically cover the range of WL ~1.42 eV down to the expected emission energy in the energy regime of the QD ~1.0 eV.

3.2 Photoluminescence Excitation (PLE)

In the PLE technique, the detection energy is first set at a particular value in the low energy range of the PL spectrum, usually in the range of ground state energy (s-level). The excitation energy is then tuned from about 6-meV above this GS-detection up to or above the WL energy (~1.42 eV). The excitation source employed for these experiments was an Ar^+-pumped Ti-sapphire laser tunable from ~850 nm (1.459 eV) to ~1 micron (1.240 eV). Figure 3.8 illustrates the process of electron-hole pair generation.

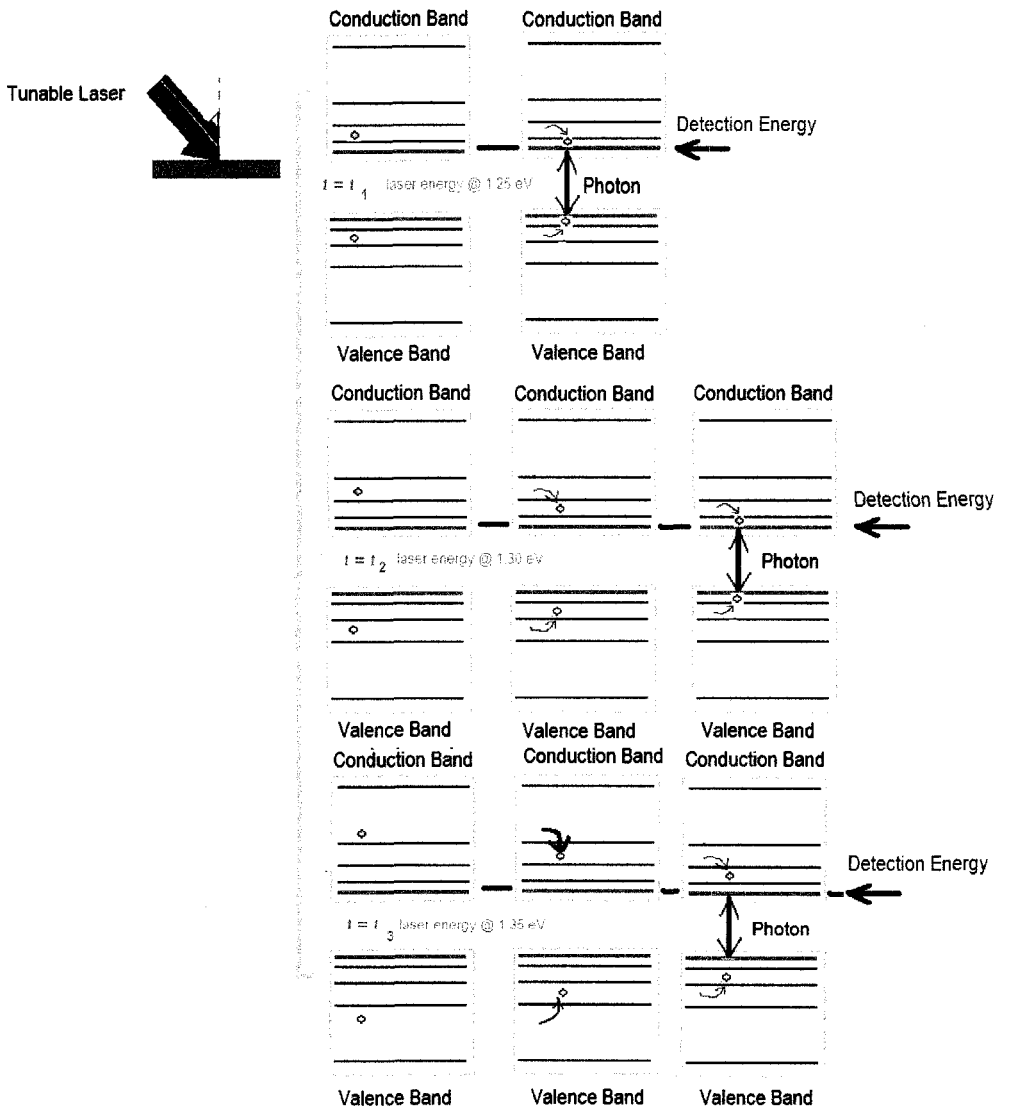

Figure 3.8: Processes of electron-hole pair generation in PLE

As this figure depicts, in the PLE, electron-hole pairs are created at a particular energy in the SAQD and after relaxing to ground state, a pair recombines emitting a photon. Electron-hole pairs are excited at 6-meV above the GS-detection energy up to the WL by tuning the laser.

In this technique, the excited energy is tuned continuously in increments of about 1 meV. When resonant with an excited state, more electron-hole pairs are produced. These pairs are not stable in an excited state. They can either recombine directly and radiatively (without detection in PLE), or the pair may follow non-radiative transitions, decaying to the GS level and there recombine. The emitted GS photon is picked-up by the optical detector. Accordingly, the PLE spectrum features absorption 'signature' lines or peaks of emission at GS which arose from peak absorptions at higher levels corresponding to the density of state of the excited levels.

Another feature which may be observed in the PLE spectra is a phonon resonance, signifying the assistance of decay to the GS detection level – perhaps from a dot with higher s- level – mediated by the resonant phonon. In general, phonons detected by PLE come only from GS emission as seen by the detector at the set angle within the chromatic dispersion of the grating. Besides resonant phonons as mediators, other scattering processes may assist or hinder carrier decay into the GS state, one of which is Auger scattering; another is impurity traps discussed later.

To conclude, direct recombination, phonon emission/absorption and Auger scattering play a role in the eventual GS recombination process in PLE as the excitation energy is tuned up to the WL energy. PLE spectra can be repeated using the same procedure but with the detection energy set at a different wavelength to sample a different ensemble of QDs.

The spectra obtained by PL and PLE have some similar features as indicated in Figure 3.9. But not only do emission intensities differ, the peak positions of the PLE absorption 'signature' are blue-shifted from PL emission peaks.

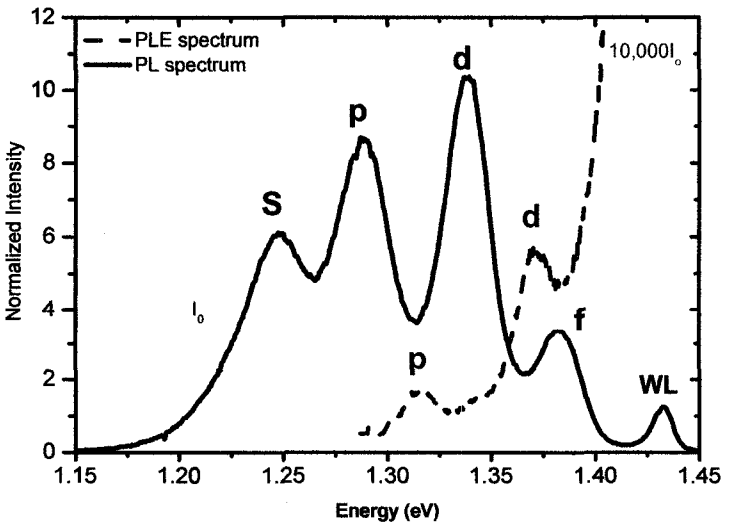

Figure 3.9: Comparison between PL and PLE spectra for a single layer of InAs/GaAs SAQDs

In Figure 3.9, the PL spectrum is plotted as a function of the detection energy while the PLE spectrum is plotted as a function of excitation energy. They both have well-defined lines within a broadened spectrum, but they are shifted with respect to one another.

The PLE experimental setup is similar to the PL system, except that the excitation energy is tunable while the detection energy is fixed. Most of the PLE results to be discussed were detected by a CCD camera. A schematic diagram of the PLE system is shown in Figure 3.10.

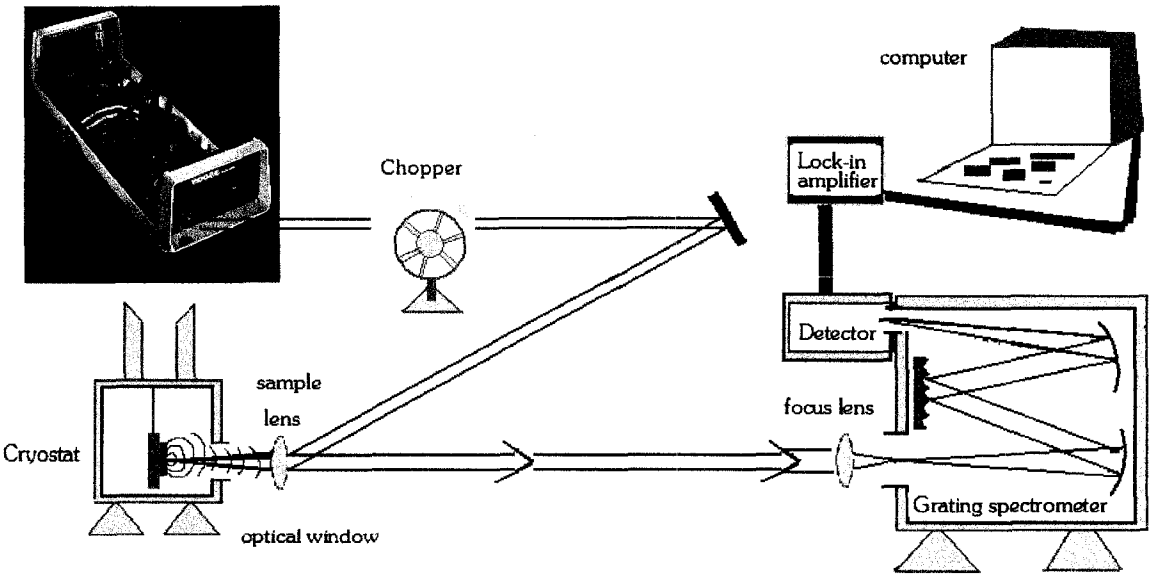

Figure 3.10: A schematic diagram of the PLE system used in this work

The tunable laser light strikes the sample at an angle in order to reduce the background signal (laser scattering at the surface of sample) received by the spectrometer. The photons emitted on recombination of excitons created at the selected energy are dispersed from the spectrometer's diffraction grating and detected at the calibrated GS detected wavelength by a CCD camera. The detected signal is sent through a lock-in amplifier to the computer. The exposure is repeated by tuning the excitation energy until the whole spectrum of interest is recorded.

3.3 Magneto-Photoluminescence and Magneto-Photoluminescence Excitation

PL and PLE spectroscopy are standard techniques for determining the principal electronic eigen-energies of a heterostructure, especially InAs/GaAs SAQD; however, these techniques cannot distinguish the orbital *degeneracy* of electronic sublevels in the 'excited' states[58]. Wang [108] documents that two p-branches occur in PLE, but composition, size and

[58] An electron in the s state is 'excited' above the valence level, but convention is to name only p level excitons and above 'excited'.

strain variations cause energy-level broadening, smearing out the separation. With good process controls the QDs can be produced with about 10 percent size variations, but this may not be tight enough to separate the near degeneracy.

The present research examined this issue by applying an external magnetic field in the growth direction (Faraday configuration), which lifts the level degeneracy at increasing field strengths. Samples with well-resolved spectral lines are essential to facilitate the identification of the principal energy levels (s, p, d and f) before a magnetic field is applied.

In absence of an imposed magnetic field, the in-plane projections of the confined carrier trajectories are clockwise and counter-clockwise with the same frequency[59]. When a magnetic field is applied, electrons and holes are still in essentially a circular motion, but with different frequencies and radii. This Zeeman-like effect is analogous to the influence of a magnetic field on 'hydrogenic' orbits of atomic hydrogen. One difference is that QD extended orbitals are not spherical harmonics, so that frequencies and radii changes have greatest effect when the magnetic field is transverse to a QD dome or parallel to the growth axis.

This Zeeman-like mechanism has similar effects in both PL and PLE, the only difference being the number of energy states of e-h pairs across all dots that are moving either clockwise or counter-clockwise: in the magneto-PL (M-PL) measurement it is many, in M-PLE it is only a few[60]. Consequently, the main contribution of this research work and thesis was to experiment with M-PL and M-PLE on high quality QD ensembles to learn more details about their electronic structure.

When magnetic fields are involved two elements are added to the experimental system. First, multi-mode fibers are added to guide the incident excitation light and to collect the luminescence from the sample and guide it to the spectrometer and detector. Second, the QD sample is mounted in a tube and placed in either a resistive or a superconducting magnet. The remainder of the optical setup is unchanged, except the arrangement for the optical fiber inside the cryostat. A schematic diagram of M-PL and M-PLE setups appears in Figures 3.11.

[59] Pairs cancel angular momentum and resulted in no net torque.

[60] In PLE many excitons *are* involved, across those dots which have electrons excited to the selected laser energy; but that energy bin is only one, and implicitly only an ensemble of dots is activated.

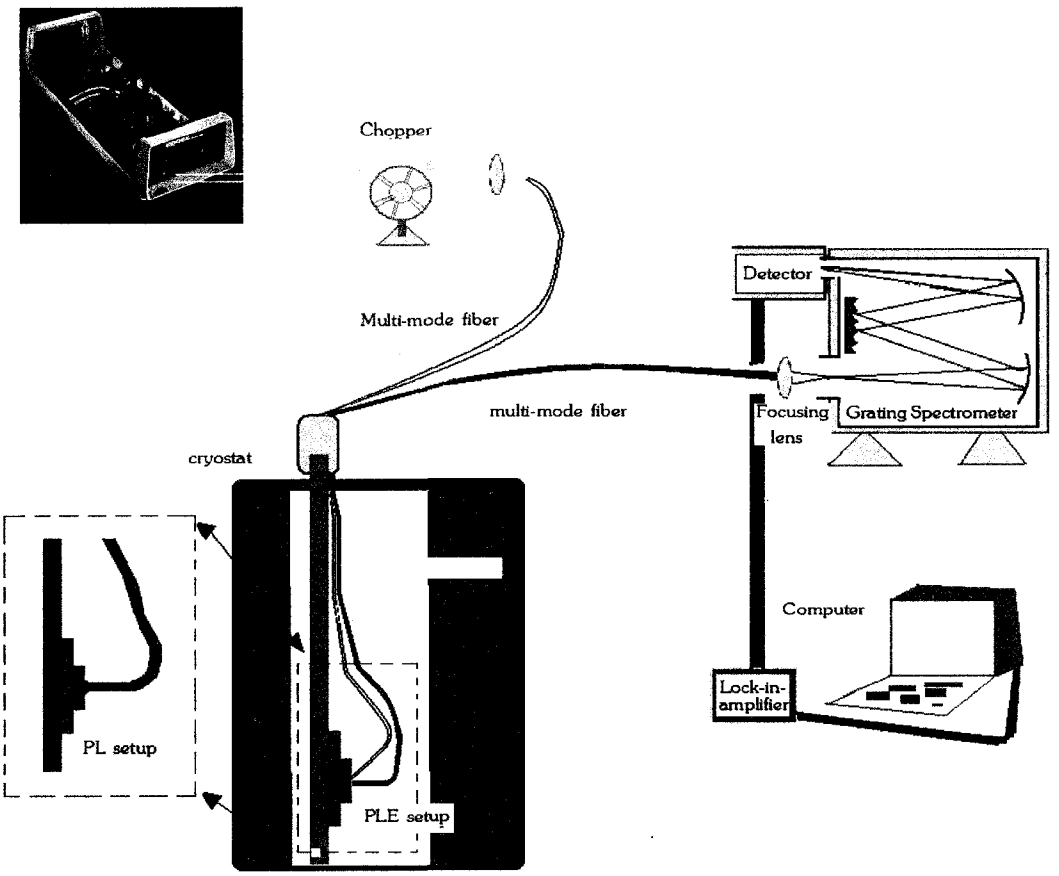

Figure 3.11: The magneto-luminescence (M-PL) and M-PLE experimental system

A resistive electromagnet[61] provided a magnetic field from 0 Tesla to 30 Tesla at a 20-MW power, with 1.4×10^{-3}-cm homogeneity and a 50-mm bore diameter. The bore diameter provides a safety distance between the tube and the magnet/sample mounting to avoid electrical and mechanical contact with the inner wall of the magnet. The superconducting magnet[62] was able to supply fields from 0 to 18 Tesla. Both systems are shown in Figure 3.12.

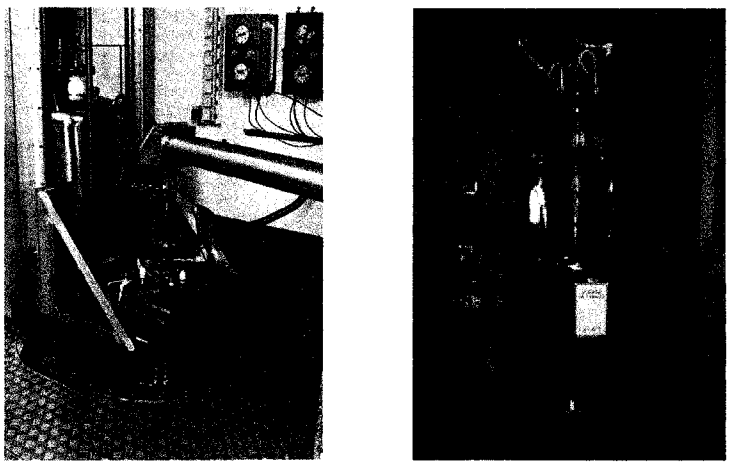

(a) ***(b)***

Figure 3.12: Photographs of both resistive (a) and superconducting (b) magnet systems

[61] The electromagnet used was on-site at High Magnetic Field Laboratory in Grenoble.
[62] This Superconducting magnet was available in the laboratory at NRC, Ottawa Canada.

3.4 Rapid Thermal Annealing Technique (RTA)

Dr. Fafard [95] at the National Research Council of Canada (Ottawa) grew a series of SAQD specimens which produced a well-resolved luminescence spectrum with narrow (small FWHM) s, p, d, f and g lines. Such lines are well suited to study M-PL or M-PLE study. To achieve further line-narrowing, an RTA was applied after growth. RTA is the rapid heating of the QD sample at high temperature over a short period of time to promote inter-diffusion and a more uniform exchange (alloying) of atoms between the QD and the cap layer. Increased 'impurities' might be expected to enhance e-h scattering and thus recombination-rates. However, given the intrinsic partial alloying of in-situ QD during growth, a more uniform alloying in samples after RTA is expected. This can alter the crystal lattice and *reduce* the scattering (increasing lifetimes).[63]

Contaminants such as dust and grease must be cleaned from the SAQD sample before going through the RTA. All of the QD samples were cleaned with three chemicals in the following order: Trichloroethylene, Acetone and Isopropyl alcohol. Samples were then rinsed in de-ionized water and blown dry with a purged gas. Following cleaning, the sample was placed in a small oven manufactured by AG associates to heat radiantly by high-voltage tungsten halogen lamps above and below the sample chamber. The chamber walls were made of high purity quartz, and the sample held in the center of the chamber on a quartz tray. The top of the tray had a silicon wafer with thermocouple (cantilever type[64]) to measure the temperature at the wafer center. The RTA system is depicted in Figure 3.13.

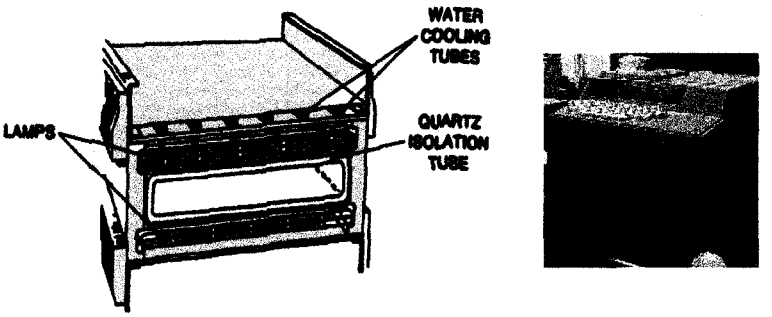

Figure 3.13: Images of the rapid thermal annealing system

Samples were placed at the center of the silicon wafer as shown in Figure 3.14, covered on top and sides with a III-V proximity cap to inhibit QD degradation by minimizing the loss of group V species such as arsenic, which are volatile at high temperature. A GaAs proximity cap was re-used about 10 times or until visible degradation (a white patina of arsenic on the surface). Ordinary non-reactive nitrogen gas ran through the whole system to stabilize temperature or keep the rest of the unit cool.

[63] GD Knight – private communication.

[64] The thermocouple (TC) wires clads in soft-weave ceramic tubing junction-contacted at the bottom of the carrier wafer using the cantilever spring force. This TC measures temperature up to 1050 °C.

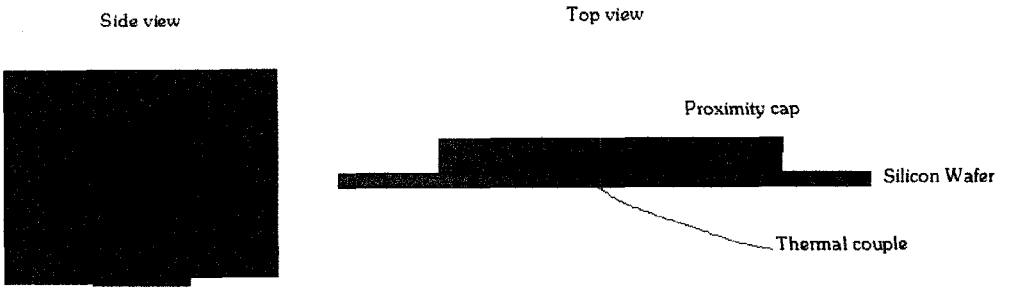

Figure 3.14: Schematic of a proximity gap around the QD sample inside the RTA oven

The first trials of the annealing process were performed without QD samples, to verify the system, and the apparatus was flushed with purged gas before inserting QD samples. With such precautions the RTA technique is reproducible. Besides the RTA method mentioned, there are several alternatives to promote inter-diffusion: annealing with a dielectric cap [109 - 111] and laser-lithography [112 - 114]. In the former, a dielectric cap is placed on top of the QD sample to create group-V vacancies in the barrier, allowing group-III atoms to diffuse across.

3.4 Conclusion

To conclude this chapter, three main components (excitation source, a spectrometer and a detector) were essential for the PL and PLE experiments. RTA played an important part in the experiments by reducing the emission line-widths and making increasingly the ratio of the top peak to the bottom of valley. Since orbital degeneracy of SAQDs can be resolved by applying external magnetic fields, the experimental setups for M-PL and M-PLE were included and constitute the main contribution to this research as discussed in the following chapters.

Chapter 4

Electronic and Structural Properties of InAs/GaAs SAQDs

As mentioned in the previous chapters, the fundamental properties of QDs, whose carriers are confined in three dimensions, are the subject of intense study due to the many related applications such as semiconductor lasers [115], optical switches [116 - 117], optical modulators[118 - 119], optoelectronic devices [120 - 122], QD lasers [123 - 125], quantum computing information [126], single photon sources [127], and single electron transistors [128 - 129]. A QD laser for example can have a higher differential gain [130 -131], a lower threshold current density [132] and higher temperature stability [133 - 134] than a QW laser.

In order to fully exploit the potential of QDs, we need to understand and control their fundamental electronic properties, such as the energy level structure, the band offset and effective masses. Among other advances, the RTA technique [33,135-136] has been shown to provide some control over the emission wavelength, inhomogeneous broadening, and inter-sublevel spacing.

Magneto PL and PLE results have been reported [137 - 139] to characterize the electronic-structure of InAs/GaAs SAQDs. Unlike bulk or QW semiconductors, QD characteristics such as exciton reduced-mass are not readily examined with transport experiments.

Using M-PL, Paskov *et al* [139] obtained the in-plane effective mass and extent of the electron wave function[65] from the p-level splitting of the emission spectrum[66] using a magnetic field applied in Faraday configuration. The evolution of the emission spectrum with magnetic field can be related to the electronic properties, providing useful insight into the energy level structure as discussed in Chapter 2[140].

The PL spectra in the presence of a magnetic field show direct evidence of a Fock-Darwin like (F-D) [36 - 37] emission pattern: the level structure of a two-dimensional harmonic oscillator with turning-points progressively limited by the field. As already described, the magnetic field lifts the degeneracy in the manner of a Zeeman effect on Fock-Darwin states.

The present chapter reports on M-PL studies of a set of InAs/GaAs SAQD samples annealed at various temperatures for 30 seconds, with magnetic fields varying up to 28 Tesla. The first purpose of this study was to monitor the electronic structure of annealed InAs/GaAs SAQDs with increased In-Ga intermixing as the primary effect of RTA.

---

[65] This is represented by in-plane electron-hole separation in a weak confinement limit or extent of the single particle wave functions for electron and hole assume equal in a strong confinement limit.

[66] The spectra were interpreted in terms of single particles or a gas of weakly interacting excitons.

After RTA, the PL spectrum reveals a blue shift in the emission energy as a function of annealing temperature, due to extended alloying from the QD-barrier interface [85, 141]. As well, reduction in the inhomogeneous broadening and the inter-level spacing were observed, suggesting that the alloying homogeneity may reduce a prompt recombination induced by the carrier scattering at 'impurities' [142]. These benefits assist in resolving fine-structure level-(anti)crossing patterns when the external magnetic field is applied.

The second experimental aim was to obtain the in-plane reduced-mass from the splitting of the p line. The p-level splitting energy is inversely proportional to the in-plane reduced-mass when the field is perpendicular to the sample surface. The in-plane reduced-mass was examined as a function of gallium content, and the experimental analysis is compared with 8-band k*p calculations for InAs quantum dots with various levels of gallium content.

4.1 Description of Samples and Optical Measurements

The sample consists of a single layer of InAs QDs grown by MBE on a n-doped GaAs substrate in Stranski-Krastanow (S-K) growth mode [143, 144]. To help minimize the inhomogeneous line-broadening, an "Indium Flush" technique [144] was applied to optimize the height uniformity of the QDs. The dots are capped with a GaAs buffer layer. The average lateral diameter and the QD height are ~25 nm and ~3-3.5 nm, respectively [65].

The as-grown wafer was cleaved into 5x5 mm pieces before applying the RTA. Each piece was annealed for 30 seconds at temperatures varying between 825 ^{0}C and 900 ^{0}C by 25 ^{0}C intervals, under a GaAs proximity cap to stabilize the sample surfaces as described in Chapter 3. After RTA, each piece was mounted in an insert cooled to 4.2 K in liquid He and introduced into the core of either an 18 Tesla superconducting magnet, or a 30 Tesla electromagnet.

The optical luminescence was obtained from laser excitation at normal incidence, at either 532 nm (for the superconducting magnet) or 514.5 nm (for the resistive magnet) through a multi-mode fiber of core size 62.5 μm or 200 μm, respectively. For the superconducting magnet, PL from the InAs QDs was collected back through the excitation fiber, dispersed by a 600 grooves/mm double-grating monochromator with a resolution of ~1 meV. The optical signal was focused onto a LN-cooled germanium detector, and recorded using a lock-in amplifier. For the electromagnet the fiber geometry was the same, but the optical signal was focused onto a 1.3 μm InGaAs photomultiplier detector. The signal was recorded using a lock-in amplifier.

4.2 Results and Discussions

Figure 4.1 shows PL spectra in a 1 Tesla B-field as a function of annealing temperature. Each sample was exposed with varying excitation power, to obtain similar zero-field emission spectra showing s, p, d, f emission lines [137] as well as the WL emission. After the RTA process, the PL spectra from each specimen with different annealing temperature required different excitation intensity to saturate the QD energy levels sufficiently for the s, p, d and f lines to appear.

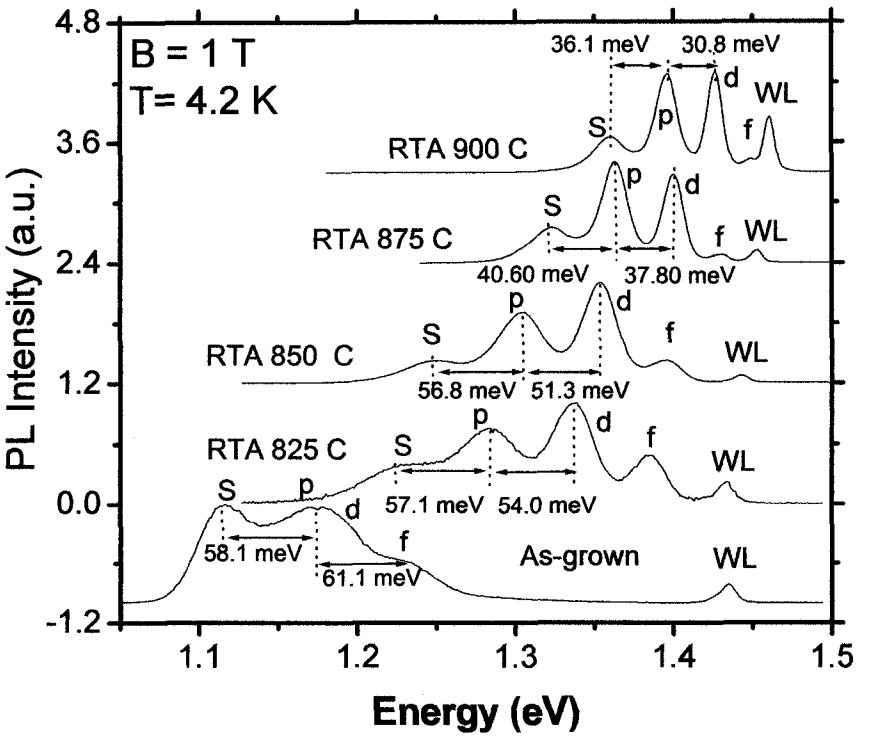

Figure 4.1: Variation of PL emission spectra with annealing temperatures

As this figure shows, all emission lines were blue-shifted. The inter-level spacing between the s and p states decreased from 58.1 meV down to 57.1 meV, 56.8 meV, 40.6 meV and 36.1 meV for QD samples annealed at 825 °C, 850 °C, 875 °C and 900 °C, respectively. A similar decrease is seen for the p-d inter-level spacing. In the figure, the samples are indicated by the annealing temperature; for example, a piece of the QD sample annealed at 825 °C is labeled as RTA825. The FWHMs of the lines is seen to be reduced by an amount proportional to the RTA temperature as shown in Figure 4.2.

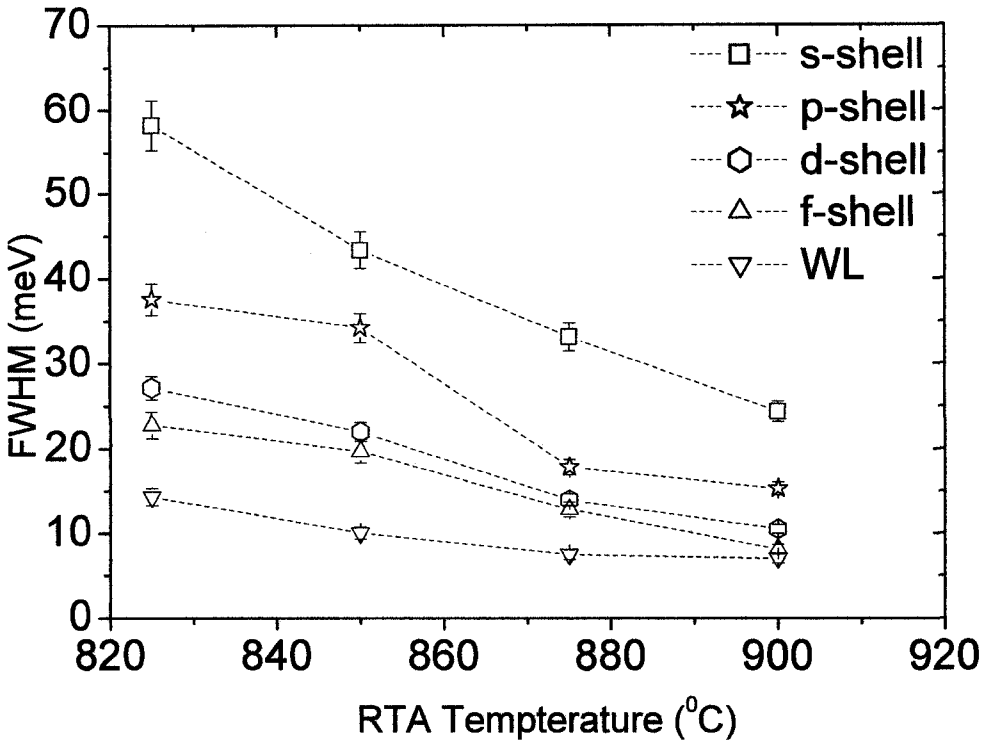

Figure 4. 2: Progression of FWHM (from Fig. 4.1) as a function of annealing temperature

Indeed, in this figure all FWHMs of the emission-lines decrease as a function of the RTA temperature. The s line-width most rapidly decreases with annealing temperature, progressively less-so for d, f and WL lines. The result reveals the increase in uniformity of the transition energies from different dots. Since the QDs are flattened domes occupying very small volume, their atoms have significant opportunity to exchange with neighboring material, resulting in compositional changes (inter-diffusion). For InAs/GaAs QDs annealed at high temperature, gallium atoms move in while indium atoms move out.

From Fick's diffusion law, the diffusion length (D) is expressed as an exponential function of temperature (T) and activation energy[67] (E_a): $D = D_0 \exp\left[-\frac{E_a}{k_B T}\right]$. Fafard and Allen [33] reported that as a function of annealing temperature the diffusion length of InAs/GaAs QDs was 0.26, 0.29, 0.68 and 1.02 nm for RTA 825, 850, 875 and 900, respectively. Notably, for RTA900 the atoms had five times the diffusion length of RTA825. This diffusion helps to establish the QD compositional uniformity.

Accordingly Fafard *et al* attributed the spectral changes to the uniform introduction of gallium into the InAs QDs, more than to variations of shape and size which were also present. [145 - 146] The gradual decrease of inter-level energy spacing of s-p levels and E

[67] E_a is the activation energy required for atoms to hop or diffuse.

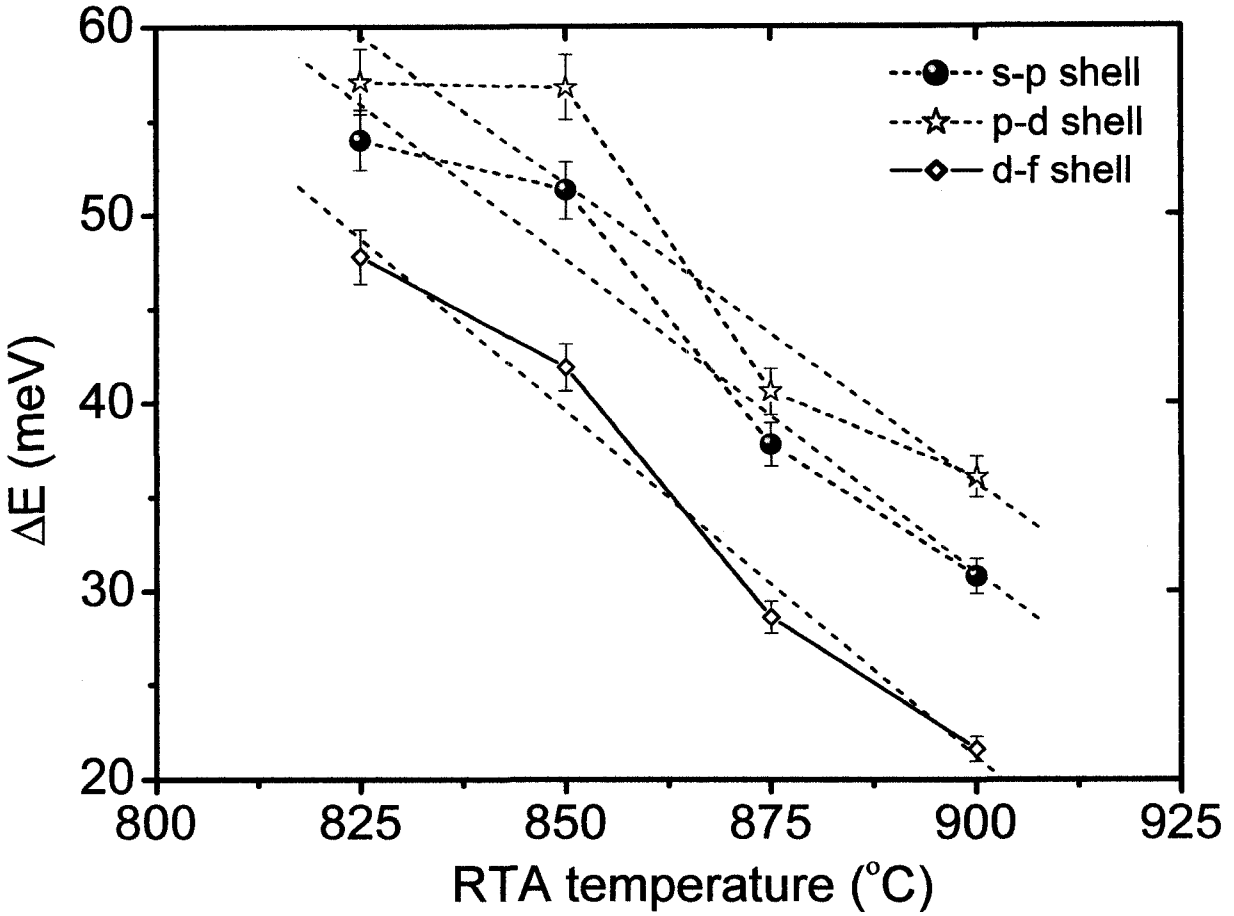

Figure 4.3: Progression of the inter-level energy as a function of annealing temperature

This figure shows that the excitonic inter-level spacing bears an approximate linear negative relation to the anneal temperature. The difference in average SAQD energy-levels declines with this temperature. The solid circles, stars and diamonds represent energy differences between s-p, p-d and d-f levels, respectively. The dashed lines present a linear fit to each set of data. As mentioned, this information helps to identify the electronic energy levels as a function of field-strength, given the narrower peaks.

For M-PL the applied field ranged from 0 to 28 Tesla in steps of 1 Tesla. Figures 4.4 and 4.5 present the results using surface plots of the PL intensity by emission energy and applied field strength. For the RTA825 sample (Figure 4.3a), the s-shell emission at 1.239 eV undergoes a monotonous diamagnetic shift upon application of the external magnetic field, while Zeeman-like splitting can be directly observed from the p (1.289 eV) and d (1.336 eV) emission ($B < \sim 12T$). The p^+ branch shifts to higher energies, and starts to encounter the d^- branch around 14 Tesla. These splitting and crossing behaviors indicate a F-D type evolution for the dipole-allowed transitions of the electron-hole pairs.

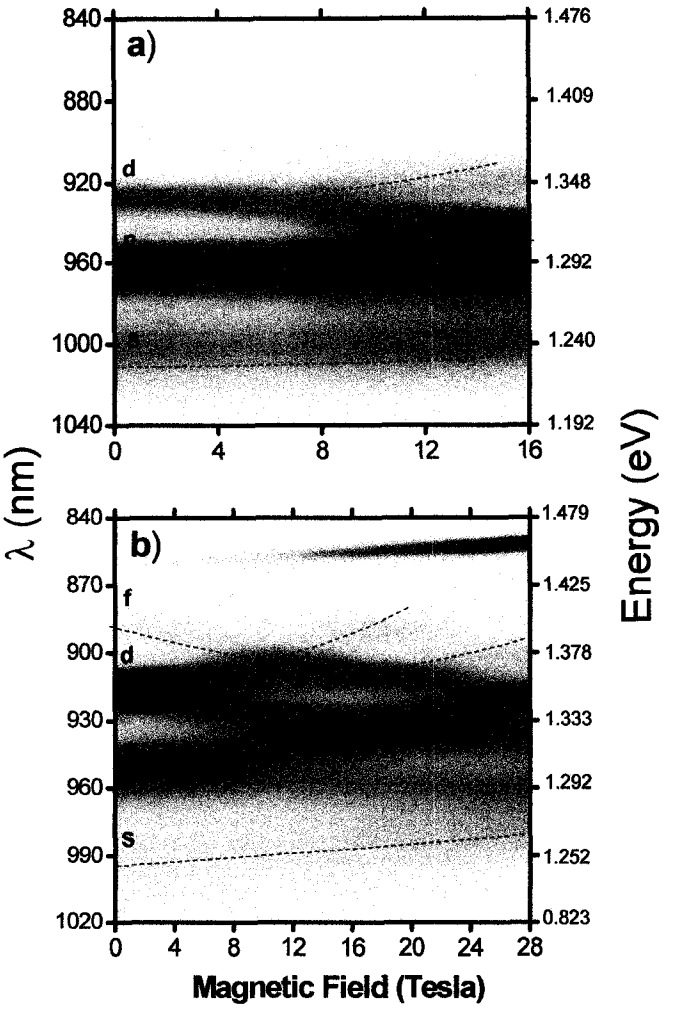

Figure 4.4: M-PL surface plots for samples annealed at a) T=825 °C with $3.3x10^1$ W/cm^2, b) T=850 °C with $6.4x10^2$ W/cm^2

In this figure dark (light) shades represent regions of a high (low) PL intensity. The spectra were recorded at 4.2 K with the Ar^+-ion laser excitation power of: a) $3.3x10^1$ W/cm^2, b) $6.4x10^2$ W/cm^2.[68]

Figure 4.4b shows the spectral evolution as a function of applied field for sample RTA850. The s-line starting at ~ 990 nm (~1.216 eV) shifts quadratically with magnetic field strength, while Zeeman-like splitting is observed for the p, d and f levels. The first (anti)crossing in this sample occurs at ~18 Tesla, lower than the RTA825 result. Such splittings can be expressed in F-D theory as described in Figure 2.9. In that figure the ground state excitonic energy (or s-level) is non-degenerate (aside from spin); while in the p, d and f levels there are two, three and four branches respectively.

The M-PL was also performed on samples RTA875 and RTA900 as shown in Figure 4.5. The results are as above, but with more (anti)crossings. As annealing temperature

[68] A different power is applied to a different annealed sample.

increases, the F-D pattern evolves with a first crossing at respectively 14T or 11T for RTA875 or RTA900: lesser fields due to smaller inter-level energy separations than in Figure 4.4. This clearly demonstrates the inter-level dependence of the magnetic field splitting as indicated by [EQ 2.35] in Chapter 2.

A second (anti)crossing is observed for the RTA875 sample, with a third for the RTA900 sample. For annealed temperature above 825 °C, the number of branches clearly goes in a 1-2-3 sequence for the s-p-d lines, while only the lower branch of the f level can be identified[69]. Still other states become resolved from the continuum at higher fields. For example, after crossing the f branch, the RTA 900 d^+ branch becomes resonant with the lower g branch at the first crossing point. This g branch is then observed to successively cross the d_0 and p^+ branches at 18 T and 25 T respectively.

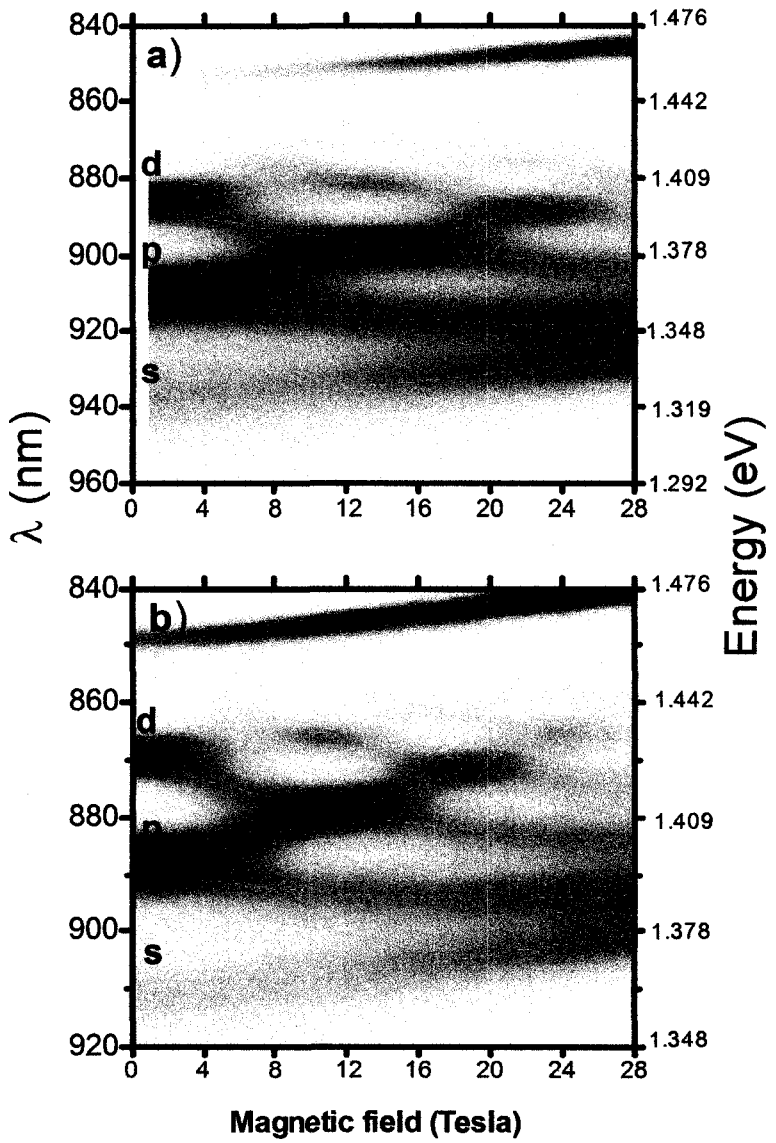

Figure 4.5: PL spectra for samples annealed at a) T=875°C, b) T=900°C

[69] Other f branches may have split off at small magnetic fields to merge with the continuum and go unobserved.

All spectra were recorded at 4.2 K with Ar^+-ion laser excitation power of 3.2×10^2 W/cm^2.

It may seem surprising that the emission spectrum of a large number of electron-hole pairs in confined dots (at a given field) resembles that predicted for independent particles by Fock and Darwin. Raymond *et al* [147] have described degeneracy-lifting in an external magnetic field and how the M-PL results match the F-D spectrum model. In details however, the carrier interactions should be taken into account, as discussed further below.

In the four M-PL results above obtained at different anneals, some aspects of the electronic structure -- particularly the in-plane excitonic reduced-mass -- are manifested in the p-level splitting, ΔE_p. The energy difference is proportional to the out-of-plane magnetic field and is the inverse of the in-plane excitonic reduced-mass $\mu_\perp^*$ of the InAs/GaAs QDs: [139]

$$\Delta E_p = \frac{e\hbar B}{\mu_\perp^*}, \qquad \text{[EQ 4.1]}$$

Note that the heavy-hole band is the uppermost valence band in a strained InAs layer on GaAs [148] so that the expression for an in-plane reduced electron-hole mass will be $\frac{1}{\mu_\perp^*} = \frac{1}{m^*_{e_\perp}} + \frac{1}{m^*_{hh_\perp}}$.

In order to compare theory and experiment, PL spectra were fitted using multiple Gaussian functions to obtain the peak positions as a function of external magnetic field. The following general guidelines were used:

(i) The line widths become narrower as higher energy shells are probed and as the magnetic field is increased,
(ii) The decreasing (increasing) occupation of states as they shift to higher (lower) energies is reflected in their emission intensity,
(iii) Peaks have the same width within a degenerate shell, whether at 0 Tesla, or at a subsequent crossing point.

Assumptions (i) and (ii) are empirical observations. Assumption (iii) depends on the number of excitons occupying the QDs.

As an example, the fitting procedure for sample RTA875 is shown in Figure 4.6 (a), where the experimental curves are shown along with the Gaussians associated with each transition. The procedure fits the s, p and WL lines accurately. For the higher energy levels the number of overlapping Gaussians increases making individual lines difficult to resolve; but the results support a narrowing FWHM of the s and p transitions as the magnetic field is increased as expected from the F-D model.

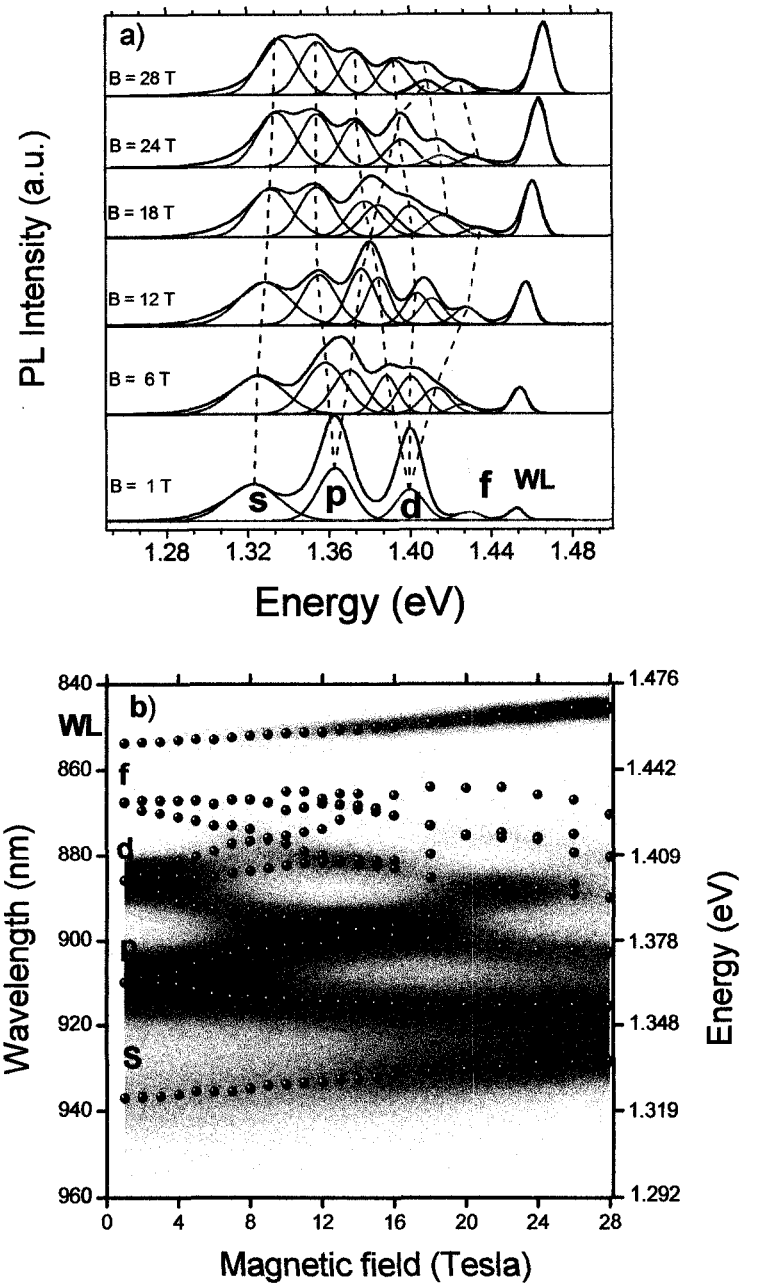

Figure 4.6: M-PL; (a) Gaussian fits to RTA 875; (b) points on the I (B,E) surface

In this figure, the emission spectra (solid lines) and corresponding Gaussian peak de-convolutions represent the evolution of the different transitions for this sample. They are depicted by colors: red, green and violet for s, p and d level transitions, respectively. The overlayed points in part (b) illustrate correspondence of de-convoluted peak positions with the experimental F-D spectra.

Broadening of the p line at 6 Tesla can be clearly observed, indicating splitting of the p^+ and p^- branches. At 12 Tesla, the p^- branch is completely resolved from other transitions, and the p^+ branch has merged with the d^- branch. In the overlay of the peak

positions on the surface plot in Figure 4.6 (b), a clear correspondence is seen, in particular for the s and p lines. All of the annealed samples were analyzed using a similar procedure.

The p-branch energy splittings up to 18 Tesla are plotted in Figure 4.7(a). A linear slope for each sample is fitted by least-squares analysis; with an in-plane reduced-mass as extracted using [EQ.4.1].

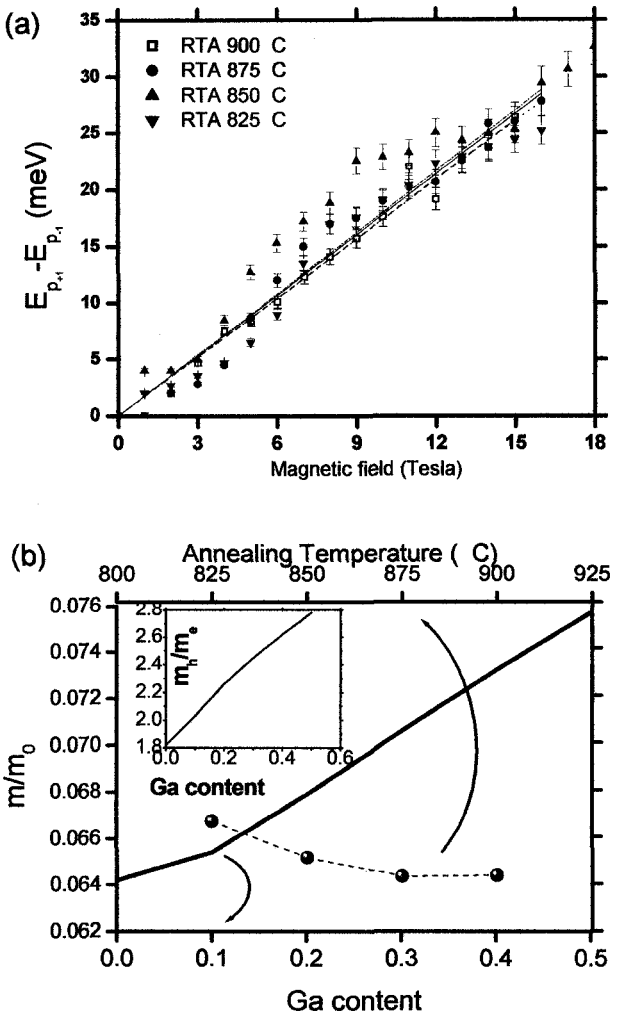

Figure 4.7: (a) p-branch difference as a function of magnetic field; (b) relationship between reduced-mass vs annealing temperature and gallium content from k-p model

In this Figure, panel (a) presents the p-shell energy splitting by the magnetic field strength with various samples annealed at different temperature. The solid lines are the least square fits. In panel (b), the effective masses are plotted as obtained from the slopes of the least square fits (scatter dots) and the 8-band k*p calculation (solid line).

Figure 4.7(b) shows the inferred reduced-mass for each annealing temperature (large dots). It can be seen that effective mass (around $\sim 0.066m_0 \pm 0.012m_0$, in fair agreement with previously reported values of $\sim 0.053m_0$ [139]) does not appreciably change, despite

significant incorporation of gallium implied by the large blue-shift seen in Figures 4.1 and 4.2. The experimental error is ~25% for the effective mass.

The ratio of heavy hole to electron in-plane effective masses (or electron to heavy-hole mobility) is shown in the inset of Figure 4.7(b). This ratio would increase with gallium content and indicates an electron mass ~2 to 3 times lighter (more mobile) than the hole. Consequently the observed experimental evolution in magnetic fields is dominated by the electrons.

To gain insight into the invariance of excitonic mass with gallium content, an 8 band k*p calculation was performed including the valence band mixing, coupled via the Bir-Pikus Hamiltonian to the strain in the dot, calculated using the continuum elasticity theory [148]. The shape of the QD was assumed to be a disk with the thickness of 2.3 nm and radius of 25.4 nm. The model parameters were adjusted to reflect the fact that no significant spin-related splitting can be observed in the experimental results. From an energy comparison of the calculated and measured emission lines, the concentration of gallium in InAs QDs was estimated to be ~50% for the RTA 900 sample. The results of the model, running from 0-50% of gallium content, appear in figure 4.7 (b) as a solid line.

For low gallium content, the model does not disagree strongly with experiment (though its upward trend is apparently wrong); but the model-predicted steeper decrease of mobility with Ga content (or RTA temperature) leaves calculated and experimental values differing more for hotter anneals[70].

The experimental value for the effective mass is ~25 percent different from another research group [139]. Various sources of error are present. For instance the F-D energy evolution described in Chapter 2 assumes an equal extent for electron and hole wave functions. The differences might be important, but the turning points in the QDs are essentially determined by the lateral size -- the same for electrons and holes. In this analysis the many-body interactions in the QDs are neglected.

The model (line) in Figure 4.7(b) would appear to discredit the 8-band k*p model, which indicates increasing effective masses at high alloying, whereas in fact a gentle decrease appears with anneal temperature. There is some possibility of mobility (inverse reduced-mass) decreasing from non-linear scattering with increased inter-diffused 'impurity' content and the as-grown barriers, but the opposite result argues for a homogenizing effect of alloying, with a modified alloy lattice. It seems clear that other models, perhaps of the pseudopotential variety (cf. Williamson [44]), need to be explored in connection with the

[70] The exact shape and composition/strain distribution can play a role in determining in-plane effective masses so that deviations from the QD shape and composition occur in such a way as to keep the reduced-mass practically constant despite injections of gallium into the QDs. But this should be qualified as an improbable rescue for the p-k model, and another model seems required.

reduced-mass, as well as more complete models to interpret the spectra from which it is derived.

4.3. Summary

A progressive reduction of size inhomogeneity, line broadening and inter-level spacing in InAs/GaAs SAQDs is achieved by RTA with raised annealing temperature. These changes are accompanied with diffusion of gallium into the InAs QDs as evidenced by the strong spectral blue-shifts. Clear Fock-Darwin like spectra are obtained for samples annealed at higher temperatures. Using the splitting of the p emission line in increasing magnetic field, the values for the reduced in-plane effective excitonic mass as a function of increasing gallium content are obtained in the range of $0.066\ m_o \pm 0.012 m_o$. The result shows that excitonic reduced-mass is independent of the gallium content up to ~50%. Calculations based on the 8 band k*p model predicts similar values for the low gallium content, but predicts notably higher values for the high gallium content of ~50%.

Identifying the origin of this discrepancy requires further structural studies to monitor the evolution of the size and shape of the QDs with higher annealing temperatures. The significant deviation might be because the F-D energy spectrum model is based a single (independent) particle picture with equal lateral extent for both electron and hole wavefunctions, and only a Coulomb interaction between the electron and the hole is taken into account. Also the 8 band k*p calculation assumed that all QDs are identical disks, and no spin interaction was considered. By all accounts the partly unexplained results invite considerations of alternate models and further experimentation.

Chapter 5

Single Exciton Picture of InAs/GaAs SAQD

Zero-dimensional QDs have a somewhat hydrogenic electronic structure and a comb-like density of states. In the previous chapter, a broad PL emission line from each level was described as representing a superposition of narrow lines of individual QDs at different energies due to variations in the QD dimensions and the extent of gallium diffusion in the growth process [149 - 152] .

Post-growth anneal using an RTA [33] partially narrows the inhomogeneous broadening of the QD ensemble, with the additional result that the inter-level spacing is better-resolved and with a reduced spacing. Further studies undertaken in the present research on the SAQD optical response involved the PLE technique. In PLE, excitons at a particular energy are created, so the individual QDs with a corresponding energy level will be populated with them. In InAs/GaAs SAQDs, the orbital momentum rules then select the recombining electrons and holes with the same quantum numbers.

The study of the electronic structure can be approached through the use of magnetic fields. Raymond *et al* [147] described the electronic structure of the excitons InAs/GaAs SAQD using M-PL and F-D spectrum theory. However, many body interactions of the multiple excitons created in PL complicate the analysis. The PLE technique is a potential simplification as only one exciton energy level is stimulated at a time [153], with therefore reduced many body effects.

In this work, the single (independent) particle picture of InAs/GaAs SAQDs annealed at 825 °C for 30 seconds was examined more closely through PLE measurement and then under a magnetic field in a Faraday configuration to examine the F-D spectrum in a single exciton regime. In this chapter, the F-D spectra of M-PL and M-PLE measurements are compared, and the relationship between the energy-level structures and the process controls (such as gallium content in the QD) is discussed.

5.1 Description of Samples and the Optical Measurements

SAQD samples were cleaved from the same SAQD wafers mentioned in Chapter 4. The RTA temperature in this case was 825 ^{0}C for 30 seconds. Two optical arrangements were employed for these studies. The M-PL setup was described in Chapter 4. For M-PLE, two 62.5-μm core fibers were used as described in Chapter 3. The excitation fiber introduced the light non-normally to the surface in order to reduce background intensity. Laser light tuned through the excited states of the QDs up to WL (from ~1.240 eV to ~1.393 eV) was launched on this fiber and the luminescence was coupled-out through the second fiber oriented normally to the sample surface. The collected luminescence was dispersed by a 600 groove/mm double grating monochromator and sampled by a LN-cooled Ge detector at a position pre-set for picking-out the ground state emission only. The output GS intensity signal was then recorded via a lock-in amplifier.

5.2 Results and Discussion

Figure 5.1 presents the evolution of the PL spectra at 4.2 K in annealed InAs/GaAs QDs as a function of excitation power at zero magnetic field. At very low power only s-level emission is observed from excitons recombining in the ground state. As excitation power increases, excitons occupy higher states (p, d, f and g). When the power reaches ~554 W/cm^2 both s- and p-emission lines are clearly observed at 1.244 eV and 1.290 eV.

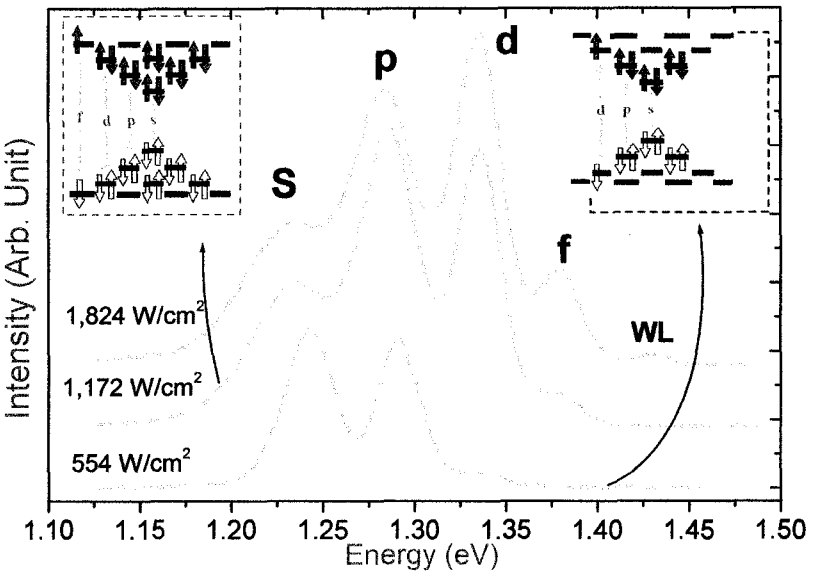

Figure 5.1: PL spectra with increasing excitation power; with 25 percent of vertical offset

Each successive spectrum was offset by 25 percent of the total vertical scale (in arbitrary units). The measurements were excited with laser wavelength at 514 nm (2.41 eV). The two small inset panels in (a) depict the number of excitons filling the energy levels at a particular excitation power.

Further emissions from d- and f- levels appear as the excitation power is increased. At 1,172 W/cm^2, the PL intensity from the p level already *exceeds* that from the s level, and a small f emission peak appears. By 1,824 W/cm^2 the d-emission *exceeds that from the* p. These are evidence that the levels become saturated with excitons as the higher levels continue to be populated. In the latter case, more excitons are then also filling the f-shell and the InAs WL. This progression is simply attributed to state-filling [154] by an increased exciton population in the QDs [154].

As mentioned above, when many excitons populate the QDs, the analysis of PL experiments is complicated by many-body interactions [86]. In order to reduce the impact of the multi-excitons, the PLE [155 - 156] is the technique of choice. Figure 5.2 presents the PLE (red solid line) spectrum with an excitation energy of 1.2399 eV and the PL spectra of that sample at 4.2 K, at zero magnetic field.

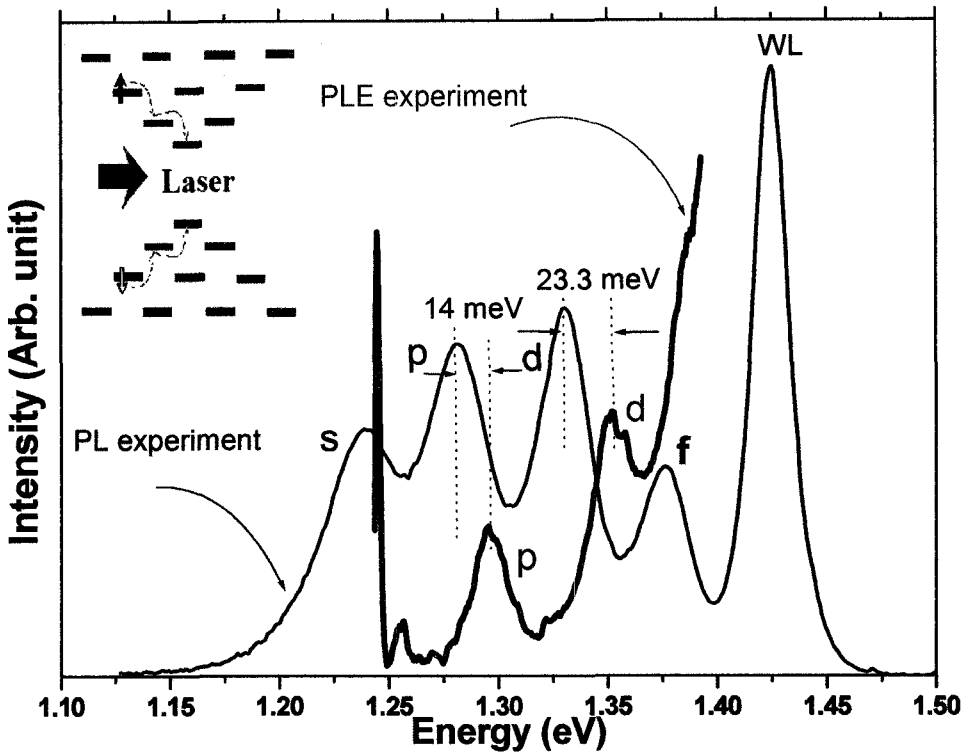

Figure 5.2: Non-resonant PL (black) and PLE (red) spectra

The p and d PL lines are red-shifted by 14 meV and 23.3 meV respectively from the PLE lines. This is attributed to many-body effects as seen in Figure 5.2. Usually in undoped QWs, the low temperature PL emission lines are red shifted with respect to the peaks in absorption or PLE spectra. But Ivchenko [157] described this shift as an excitation spectrum dominated by optical transitions involving extended free-exciton states. In the case of the low temperature PL on SAQDs, it arises from radiative recombination of localized excitons. Thus the red-shifts appearing in QWs as a Stoke-shift at low temperature are irrelevant for QDs which have a unique comb-like density of states and no explicit electric field is present in this experiment. Many-body effects must therefore be involved.

The PL state-filling effect does not occur in PLE[71], as exciton only fill a specific energy level. In the power-dependent PLE measurement shown in Figure 5.3, the p and d emission peaks maintain a nearly constant ratio. The intensity of transitions is proportional to the absorption of the exciting laser, suggesting that the recombination lifetime for p and d are in the same range[72]. Raymond *et al* [104] reported decreasing recombination rates for the higher excited states in PL, but they remained in the same range.

[71] However, excited states can saturate at sufficient power in PLE.

[72] It may be useful to further study the recombination rate of InAs/GaAs SAQDs with time-resolved methods.

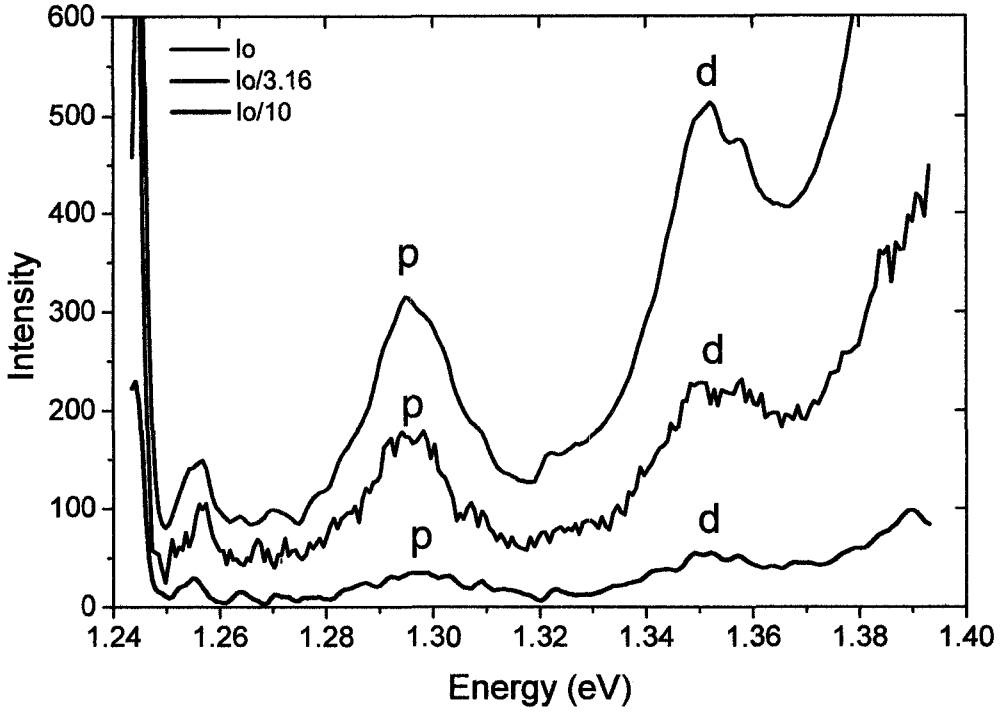

Figure 5.3: Evolution of the PLE spectra as a function of excitation power, $I_0 = 70W/cm^2$

The many body effects in the PL and PLE measurements are further discussed by Raymond *et al* [147]. They described the chemical potential as the energy to remove or add one electron-hole pair in the PL spectrum. It is independent of the number of the electron-hole pairs and the level-filling, and is given by [162 - 163]

$$\mu_N = E_{GS}^N - E_{GS}^{N-1}. \qquad \text{[EQ 5.1]}$$

where E_{GS}^{N-1} is the energy of completed configuration. It is useful to understand the relevant many-body effects. In a non-degenerate N-exciton configuration, neglecting the scattering to higher shells, $\mu_N = E_{GS}^N - E_{GS}^{N-1}$ is

$$\mu_N = E_i^e + E_i^h - V_i^{eh} - \sum_{i \in core} V_i^{N,x} \qquad \text{[EQ 5.2]}$$

where the first two terms are the kinetic energy of electron and hole in the state i, and the third is their direct Coulomb potential. $V_i^{N,x}$ denotes the exchange energy between the topmost particle in state N and one in a lower state i. Beyond this, the configuration energy and scattering should be added to correct the chemical potential. The configuration may be illustrated in the recombination of an exciton as shown in Figure 5.4.

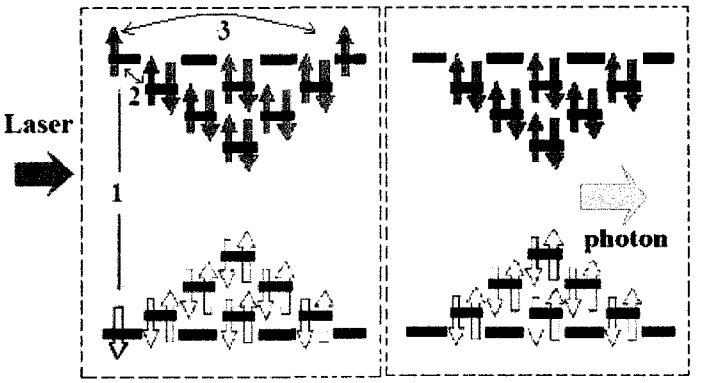

Figure 5.4: Representation of the chemical potential for the PL spectrum

In this figure symbols (1), (2) and (3) denote direct coulomb, exchange, and configuration coupling energy, respectively. For example, a multi-exciton droplet (13X) is created in its ground state (left) when the laser light is incident on the QD. A photon is then emitted through the recombination of the excitons. The emitted photon energy, equal to the chemical potential, is the difference between the 13X and 12X ensemble energies. The emission energy is a combination of contributions 1, 2 and 3: $\mu_{13} = E_k - (E_{coulomb} + E_{exchange} + E_{conf.})$.

By contrast, in PLE only the kinetic and the Coulomb interaction energy are considered for an electron-hole pair, as depicted in Figure 5.5. This is because the QD exciton population is the number of photo-generated excitons at a specific energy. Each such electron-hole pair is presented in a single exciton picture. Upon thermalizing to the ground state configuration a photon is emitted at the energy corresponding to $\Delta\hbar\omega = \Delta E_k + \Delta E_{coulomb}$ with only the direct Coulomb interaction and kinetic energy. Thus the shift between PL and PLE peaks is expected to give quantitative information on the magnitude of exchange and other coupling energy terms.

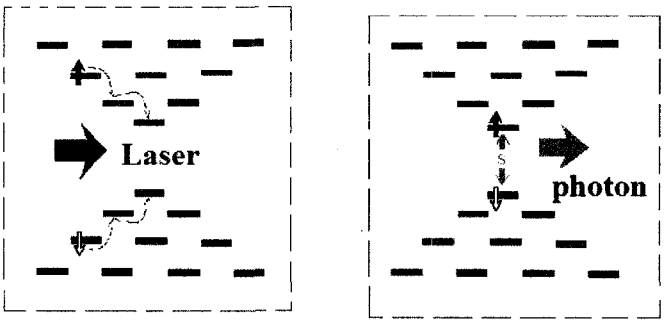

Figure 5.5: Chemical potential energy in the PLE spectrum[73]

The foregoing demonstrates that a number of interactions are involved in PL spectra, while only the kinetic energy and direct (though somewhat screened) Coulomb interaction take place in PLE. The latter situation favors F-D spectral analysis, with only two

[73] Not all excitons 'thermalize' but some can recombine directly from upper levels too.

types of interaction taken into consideration when the magnetic fields are applied. Accordingly, M-PLE experiments were performed in a Faraday configuration, and PLE spectra as a function of magnetic field were observed from 0 to 16 T in increments of one Tesla. Therefore, Figure 5.6 shows a surface plot of the PLE intensity spectra as a function of the external magnetic field.

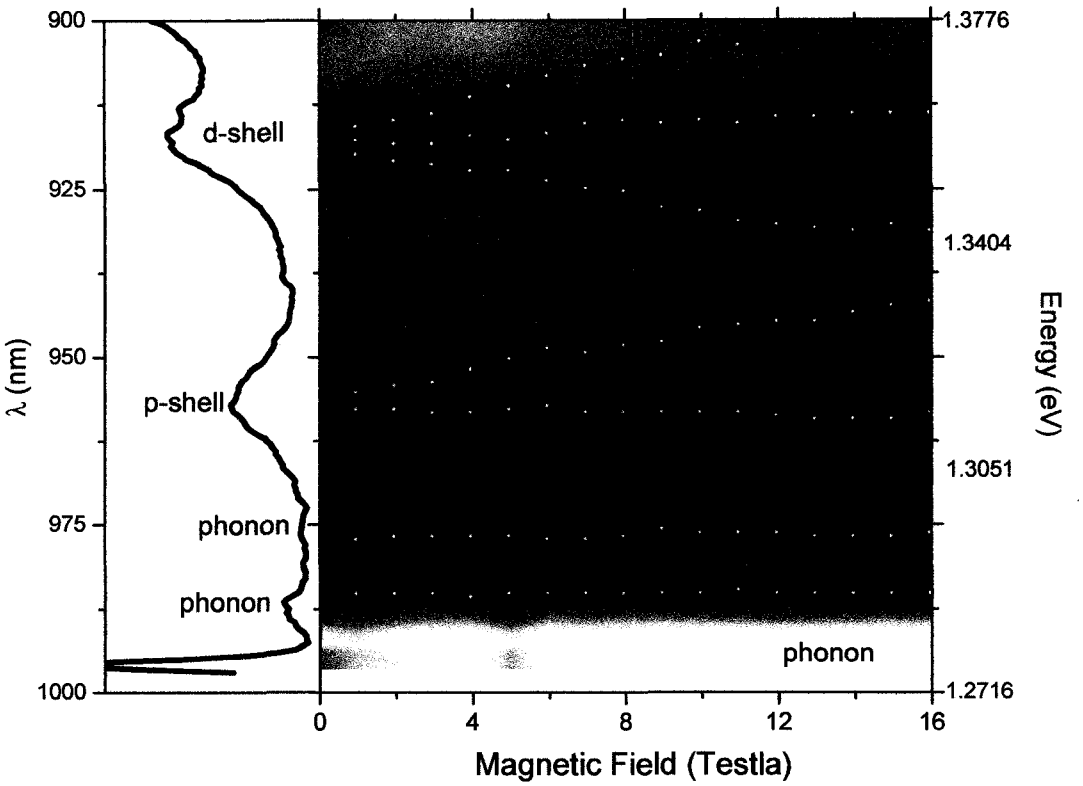

Figure 5.6: Surface plot of PLE spectra, I(B,E), at a detection energy of ~1.238 eV

At zero field, the spectrum recorded at a GS energy of ~1.238 eV (PL peak) has only the p and d lines at 1.296 eV and 1.351 eV, respectively. Two small peaks at 1.257 eV and 1.270 eV also appear, corresponding to the Raman scattering energies at ~19 meV and ~33 meV respectively. These two phonons assist the excitons occupying excited states to relax to detected ground-state energy. The latter value is consistent with LO-phonons for strained InAs quantum dots at 32.6 meV reported by Heitz [158], Fafard [159] and Wilson [160]. The former ~19 meV corresponds to LA InAs phonons at the X point in the crystalline BZ. With emission from the higher s level red-shifted by emitting a resonant phonon. These resonant phonons are used as a convenient signature for the emission peak.

When the magnetic field was applied, various degenerate branches of the p and d levels were observed. The p line clearly split into two branches as the field is increased. Only two branches were observed from the d line in the same field range, whereas the harmonic oscillator model discussed in Chapter 2 would call for three.

Nevertheless, the branching structure of this M-PLE spectrum is analogous to a Fock-Darwin spectrum modeled in a single (independent) particle picture. In M-PLE, an

emission line other than the resonant phonons is understood as an excitonic recombination. Based on energy levels described in (EQ 2.34), the e-h energy is rewritten as:

$$E(n_+,n_-)=E_0+\hbar\left\langle\Omega_+^{electron}(B)+\Omega_+^{hole}(B)\right\rangle\left(n_++\frac{1}{2}\right)+\hbar\left\langle\Omega_-^{electron}(B)+\Omega_-^{hole}(B)\right\rangle\left(n_-+\frac{1}{2}\right), \qquad \text{[EQ5.3]}$$

where E_0 is an offset comprised of semiconductor gap and vertical confinement energies. n_+ and n_- denote quantum numbers $(n_\pm = 0,1,2,3,...)$ and $\Omega_\pm^{(electron,hole)}$ is the corresponding frequency - $\Omega_\pm^{electron,hole}(B)=\left\{\omega^2+\left(\frac{\omega_c}{2}\right)^2\right\}^{1/2}\pm\left|\frac{\omega_c}{2}\right|$, where ω is the harmonic frequency describing the strength of the in-plane parabolic confinement and $\omega_c=\frac{eB}{m_*}$ is the cyclotron frequency. These FD spectra obey:

(i) dipole transitions - only electrons and holes with the same set of quantum numbers can recombine and,

(ii) $\Delta n_+ \bullet\left\langle\Omega_+^{electron}(B)+\Omega_+^{hole}(B)\right\rangle=\Delta n_- \bullet\left\langle\Omega_-^{electron}(B)+\Omega_-^{hole}(B)\right\rangle$.

Then, based on this F-D theory, an independent exciton picture could be simulated as soon as the in-plane reduced-mass is known. This value could be observed through the splitting of the p-shell transition energy ΔE_p as mentioned in [EQ 4.1]. Qualitatively, the M-PLE measurements correspond somewhat to an F-D model, but the peak position and inter-level spacing differ from the model.

Quantitatively, by tracking the PLE peak positions of the degenerate p branches, the energy splitting of the p level is plotted as a function of magnetic field strength in Figure 5.7. The slope fit using least squares is ~1.383 ± 0.030. From this the in-plane reduced-mass can be extracted using [EQ. 4.2], yielding ~ $0.084m_o \pm 0.002m_o$ which only is in qualitative agreement with the result in the previous chapter of $\sim 0.066m_o$ and other results reported of $\sim 0.053m_o$ [139]

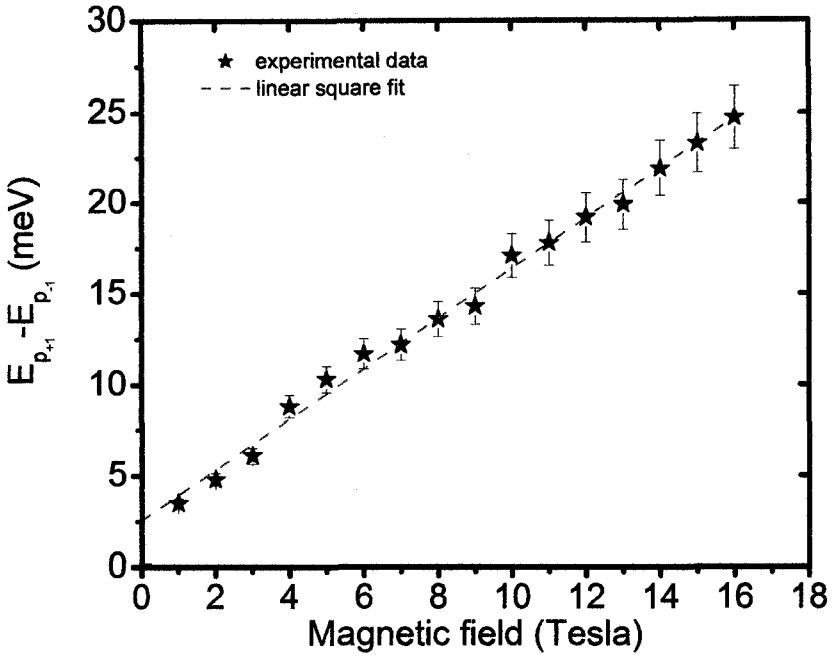

Figure 5.7: Peak energy difference between two p-shell branches as a function of B field

The difference in reduced-mass between the PL and PLE results of about 27 percent is potentially affected by, among other things, some acquisition differences between PL and PLE data or method of excitation. In PLE, the energy states are populated without filling the lower energy states first. It therefore increases the mobility of electrons and phonon scattering effects. Lifetime or recombination rates for each state are other possible factors. The recombination rates for s, p, d and f recombinations differ somewhat: higher states have more phonon-scattering opportunities to decay into unfilled states lower in energy. This means greater probability of a radiative recombination channel from the s level than at higher levels having more decay channels. Raymond *et al* [104] reported that recombination at the ground state was about 10 times faster than from an excited state.

Only the s-s transition (ground-state recombination) is observed in PLE since the detected energy is set in the ground state region, but other (p-p, d-d and f-f) emissions are directly obtained in PL[74]. Many body effects and scattering channels are therefore probably important factors.

The heavy hole in-plane effective mass is generally ~2 to 3 times larger than the electron. Awirothananon *et al* [161] reported ~2.1 for this ratio in InAs/GaAs SAQDs annealed at 825 °C. Using this ratio and the in-plane reduced-mass obtained above, the electron and heavy-hole effective masses are $0.124m_0$ and $0.26m_0$, respectively. The electron effective

[74] This doesn't mean they don't occur in PLE, they're just less likely, therefore less intense if the detection energy were set to their level instead.

mass compares with that obtained by Paskov [139]: $\sim 0.153 m_0$, but the result for the heavy-hole is greater than other researchers' findings [139, 170] by 70 %. Some of the discrepancy may be due to differences in strain, confinement and the nature of carrier relaxation mechanisms among the samples reported in various experiments. The scatter in these results suggests a need for further experiment and modeling.

In fact the interpretation of the PLE results is uncertain and non-trivial. The carrier dynamics involved in the PL spectra are quite different from the PLE for two reasons. The PLE emissions are from no energy levels other then the selected GS and arise from the ground-state recombination from a subset or ensemble of dots with an identical GS energy. Secondly, only those excited excitons which relax either radiatively or non-radiatively to this GS play a role. Thus the carrier dynamic in PLE is dominated not only by spectral absorption, nor by state-filling, but by carrier relaxation channels. It therefore excludes typical PL emissions that ensue from direct radiative recombinations at excited levels.

The GS emission peaks in PLE are therefore an indirect absorption/emission peak 'signature', whose fidelity is an unknown function of the relative rates of relaxation to the GS and of statistically enhanced dispersions in different dot geometry, strain and composition within the GS-selected ensemble. Accordingly, the peaks, their branches, and their inter-level spacing in PLE cannot be interpreted directly as those of PL without detailed models. The trade-off is that while PLE reduces the many-body carrier effects it increases the role of non-radiative channels and physical dispersion.

It follows that the method for extracting the reduced exciton mass from the separation of p-branches is less reliable when carried over to the M-PLE 'p-lines' (so-labeled). In addition the assumed ratio of heavy-hole to electron mass, as derived from an unreliable fit of the k*p model in the PL spectra, gives only a qualitative basis -- albeit surprisingly good quality via other published results -- for even the PL estimates. By using the same ratio in the already questionable reduced-mass from PLE spectra, the electron and heavy-hole masses cannot be expected to be accurate.

5.3. *Summary*

The RTA technique reduces the physical inhomogeneity of InAs/GaAs SAQDs with the effect of reducing the FWHM of the emission-line as well as the inter-level energy spacing. In PLE, the one-exciton energy is effective at a given excitation wavelength. The PLE peak is blue-shifted because only a Coulomb interaction holds. In PL by contrast, many-body effects arise involving exchange and configuration coupling energies in addition to Coulomb-interaction. This is expected to decrease the carrier mobility and diminish the energy gaps, red-shifting the emission as observed in this chapter.

In addition, clear F-D like M-PLE spectra are observed in a progression of magnetic field strengths. Using the p-branch energy-splitting, an effective in-plane reduced-mass of $\sim 0.084 m_o \pm 0.002 m_o$, was obtained. This value is unexpectedly higher (i.e. the electron is less mobile) than that obtained from the M-PL measurements involving more

interactions. This might suggest an improbable view that (coherent) interactions may *enhance* the mobility of carriers in PL measurement. Alternatively, excited frequencies are selected in PLE, while the measurements are made at only one (GS) wavelength. A difficulty of interpretation is that the p-branch separations are not of the p-emission per se, but of GS-level result after relaxation down from the p-branches. This could lead to an erroneously lower inferred mobility while using the PLE technique[75] [142].

The reduced-masses obtained from the QDs (including the M-PL value) are greater than in bulk InAs semiconductors because of strain and confinement effects in the SAQDs. Based on the ratio of the heavy hole to electron effective masses, these masses are estimated as $0.124\,m_o$ and $0.26\,m_o$, respectively. By using the same ratio of heavy-hole effective mass to electron effective mass (~2.1) combined with the PL in-plane mass obtained in Chapter 4 ($0.066\,m_o$ and $0.012\,m_o$), the electron and hole effective mass are respectively estimated as $0.097\,m_o$ and $0.2046\,m_o$.

[75] GD Knight, *personal correspondence.*

Chapter 6

Many Body Excitonic Effects in SAQDs

Relationships between the electronic and the physical properties of SAQDs are of great importance to optimize the fabrication process. Thus optical characterization can help understand better the growth conditions. One measure of the optical quality is the photo-luminescent response in the presence of a magnetic field (M-PL), revealing systematic changes in the electronic structure via degeneracy-lifting and diamagnetic shift at low B-field strength. At stronger magnetic fields, the increased separation of degenerate level branches leads to anti-crossings [162], and finally Landau levels appear at very high magnetic fields[76].

In this chapter the electronic level structure of SAQDs annealed at 825 °C is discussed via PL and PLE data with and without applied magnetic fields. Many-body effects are considered such as the direct Coulomb interactions between a promoted electron and a 'core'[77] of filled states, the configuration energy of electrons or holes, and the exchange energy in degenerate states. The exchange energy between electrons and holes in various levels is omitted in the analysis, but the effective mass is included and largely embodies the net interactions.

A single layer of InAs QDs was grown on n-GaAs substrate using the MBE technique in the S-K growth mode. This SAQD specimen was fabricated in the same conditions as described in Chapters 4 and 5, but cleaved from a different part of the wafer. Due to equipment availability, the optical setup[78] in this study underwent a few changes: a 1.3-micron InGaAs detector and a CCD camera detector were employed in PL and PLE experiments, respectively. A 200-micron diameter multi-mode fiber and a 28-Tesla electromagnet also replaced the smaller fiber and 18-Tesla superconducting magnet used earlier.

PL is first discussed, followed by examination of PLE results. The latter measurements covered a detection wavelength range (not just the lowest PL ground-state but up through the excited states), and both M-PL and M-PLE were performed under external magnetic fields right up to the 28 Tesla available.

6.1 Photoluminescence (PL)

The progression of PL spectra as a function of excitation power at 4.2 K and no magnetic field is shown in Figure 6.1. In this experiment, the number of exited QDs was large: about ten million. Only the ground state emission is observed at a very low excitation (<1.41 W/cm^2), and as the excitation power increases, more excitons occupy the excited energy states

[76] At high magnetic fields, the carrier radius is smaller than that of the QD radius. Thus the confinement effect has less influence.

[77] This is a core configuration of promoted electrons or excitons, not the ionic cores from which they were promoted.

[78] The PL and PLE experiments were performed at High Magnetic Field Laboratory in Grenoble, France.

(p, d, f and g) producing emissions from these higher levels. The s and p emission lines are visible at 1.253 eV and 1.294 eV, respectively, when the excitation power is ~16 W/cm^2.

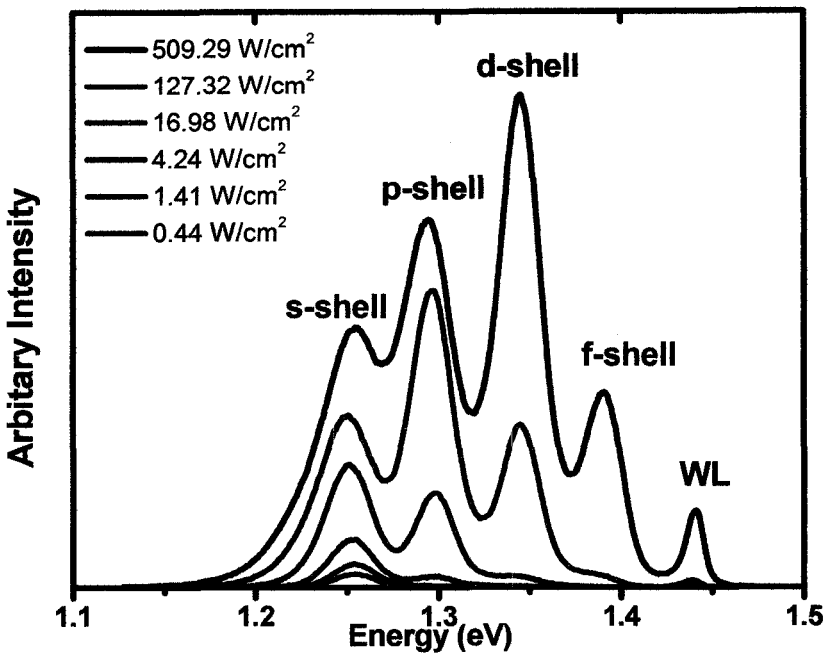

Figure 6.1: PL spectra as a function of excitation power at 77 K, 0 Tesla with undoped InAs/GaAs SAQD sample

The spectra of Figure 6.1 track the increase of exciton level occupation and the state filling effect [90]. As the excitation power rises to 127 W/cm^2, the QD energy states become increasingly populated, but hardly at the WL level. The WL emission (1.441 eV) is observed clearly at well above 127 W/cm^2.

The s emission is from a non-degenerate state (excluding spin) and the first excited p level is doubly degenerate, with degeneracy increasing linearly with the excited state: three and four branches for d and f levels, although these are not visible until a magnetic field is applied. A close inspection of the PL peak positions shows a slight shift with excitation power, suggesting that the mean value of the emission energy depends on the exposed number of dots with different sizes.

Multiple electronic states are excited in PL (but not in PLE). Consider the PL spectrum at ~509 W/cm^2 power in Figure 6.1. The ground and p states are saturated while the higher levels are only partially filled with excitons. The peak intensities (red color) are depicted in the M-PL plot at the zero magnetic field side of Figure 6.2.

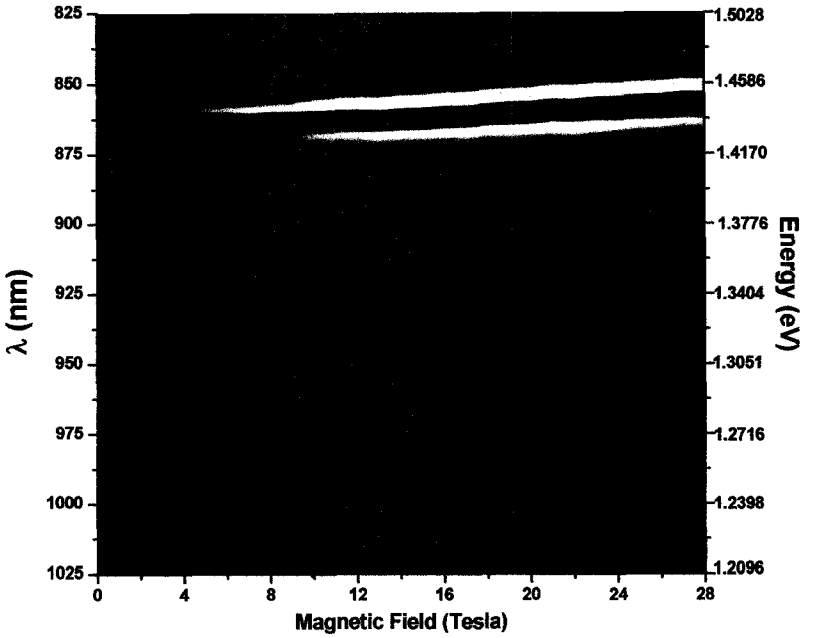

Figure 6.2: M-PL spectra $I(B,E)$ (detected at T= 4.2 K) of InAs/GaAs SAQD annealed at 825 °C for 30 seconds. The emission intensity corresponds to red color saturation (bright (red) = more PL intensity). The vertical line and rectangle box are represented the focus of further study

Figure 6.2 presents an intensity surface plot as a function of emission wavelength (energy) and magnetic field strength for the annealed InAs/GaAs SAQDs. The PL spectra were obtained in a Faraday-configured magnetic field with one-Tesla increments. The second derivatives were taken of the individual spectra to determine their peak positions. The zero-field s peak at around ~990 nm (1.252 eV) progressively blue-shifted with increasing magnetic field.

The two-fold p degeneracy was lifted with the magnetic field, the branch separation is increasing with field-strength at a linear rate, determined by the in-plane exciton reduced-mass. Three and four branches were expected to emerge from d and f lines. While three d branches are clearly seen at ~8-10 Tesla, only three f branches appear in the whole range of B-field. Plausible explanations for this might be that the f level is only partly filled at the highest laser power used (1kW/cm^2) or one of the f branches had split off to the continuum states. A third possibility is that the middle branch is still doubly degenerate and not fully accounted-for in the ordinary F-D theory valid at lower levels[79].

Nine apparent crossings (or anti-crossings [70-71]) appear in Figure 6.2. The upper p branch starts to encounter the lowest d branch at ~ 14 T, and the middle d branch merges with the lowest f branch at 20 T. Two crossings occur around 8-12 Tesla and three at ~16-22 Tesla. Four more might be expected if the magnetic field were to exceed 28 Tesla.

[79] GD Knight, *personal correspondence* .

For PL experiments as above, the following interactions need to be taken into consideration: (1) direct coulomb, (2) QM exchange between the topmost particles in state N and those in the filled lower levels and (3) configuration interactions. As mentioned in the previous chapter, these interactions all contribute to the chemical potential μ. In one QD, this potential corresponds to the energy of adding or removing an exciton. Especially at the energy of the lowest (anti) crossing, the chemical energy is independent of the number of excitons; it equals the energy of that (anti) crossing level plus or minus the electron-hole interaction energy [163].

6.2. The configuration interaction[80]

In M-PL, many-exciton and configuration interactions are involved. In a magnetic field the QD energy states in a single particle picture may be obtained from [EQ 5.3]. If the effective masses and 2-D oscillator frequencies of the electrons and holes satisfy the relationship $m_e^*\omega_e = m_h^*\omega_h$ under the influence of magnetic field, the electron and hole level structure is reconstructed with states crossing or merging with each other [162-163]. The first encounter between upper p and lowest d branch, for example, is outline in the dashed rectangle in Figure 6.2. The QD energy levels at this (anti)crossing are represented in Figure 6.3.

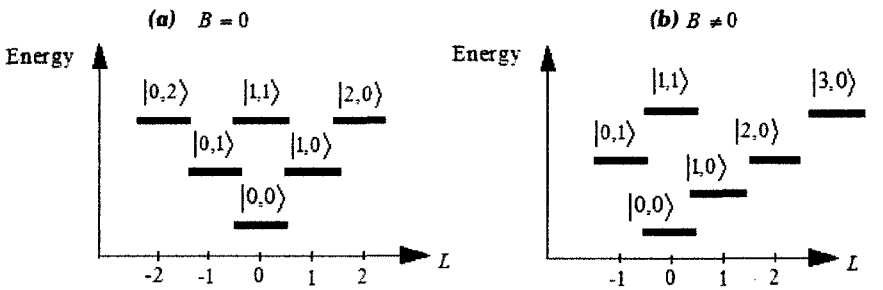

Figure 6. 3: QD energy states at (a) zero magnetic field and (b) lowest first crossing (rectangle in Figure 6.2) in magnetic field. (following Cheng [163])

Cheng *et al* [162-163] developed a theory of excitonic artificial atoms formed by N-electrons and holes confined in a QD. In this model, including for magnetic fields, the valence-band mixing and electron-hole exchange are neglected in treating many-body effects. The many electrons and holes are treated with the configuration interaction (CI) method. The multi-exciton Hamiltonian is a combination of five terms: (i) electron kinetic energy, (ii) hole kinetic energy, (iii) Coulomb-attraction of electrons and holes, (iv) Coulomb repulsion of neighboring electrons and (v) Coulomb repulsion of neighboring holes. The relationship $m_e^*\omega_e = m_h^*\omega_h$ is assumed when the electrons and holes in a state of fixed quantum number have identical envelope wave-functions. Since configurations with different quantum numbers are decoupled, only a subspace spanned by a selected configuration is treated. In this models N is number of excitons, L is total angular momentum, S^e, S^h are the total spin for electron and hole, S_z^h, S_z^e are the z-axis spin for electron and hole; and those are good quantum numbers to represent the excitonic states.

[80] This section is adapted from Cheng [163].

In a magnetic field, the electronic states are reconstructed as shown in Figure 6.3, especially the lowest merging states $|0,1\rangle$ and $|2,0\rangle$ within the rectangle of Figure 6.2. In this case, the multiplicity of excitons states could be 5, 6, 7 or 8, and each may be considered as a subspace; in particular four subspaces are considered here. The case of 5 excitons yields two configurations[81] with the lowest states filled fully by four particles, and the topmost particle in either $|0,1\rangle$ and $|2,0\rangle$. This is illustrated in Figure 6.4.

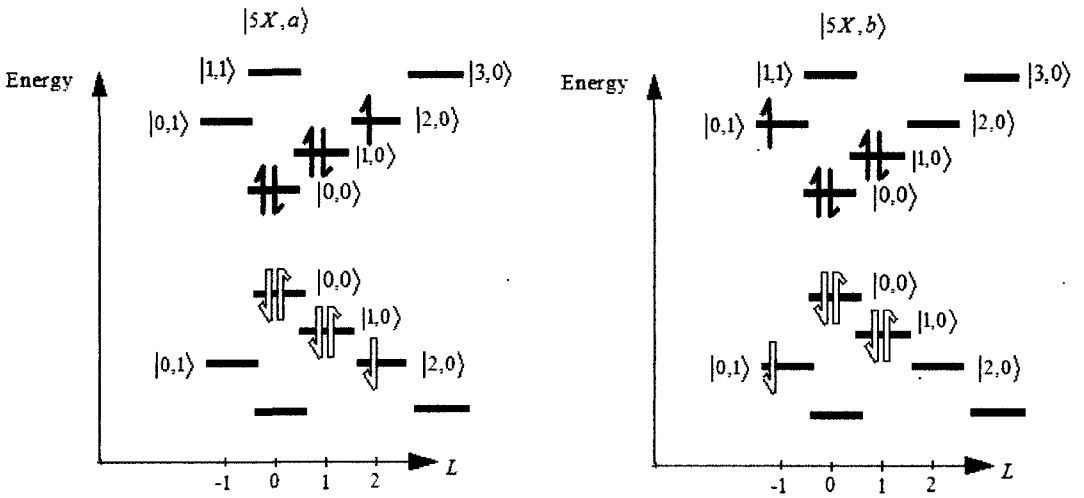

Figure 6.4: Two lowest energy configurations for $N = 5X$, five excitons (following Cheng [163])

The ground configurations for five excitons are a linear combination of these two. By solving for these 'exchange'- coupled states through the Hamiltonian (EQ 5 of reference [163]), including this term in the chemical potential, the degeneracy is lifted as shown in Fig.6.5.

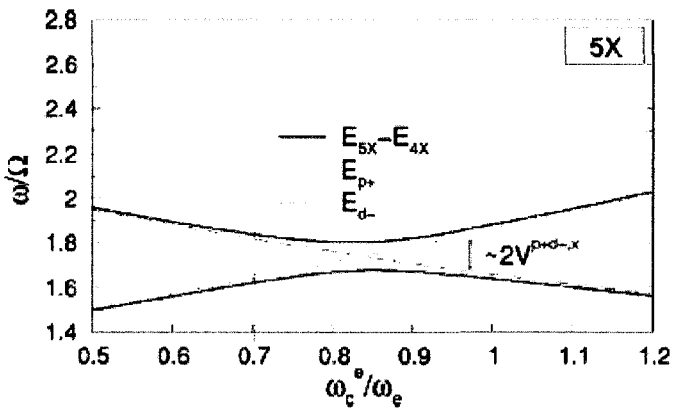

Figure 6.5: Calculated energies of 5X states. The degeneracy is lifted due to the configuration coupling (after Cheng [163]) where $\omega, \omega_c, \omega_e, \Omega$ are frequency, cyclotron frequency, electron frequency and relative electron-hole frequency, respectively

[81] Cheng *et.al* describe an energetic interaction between independent configurations, it is analogous to an exchange interaction between equivalent configurations. This exchange term is non-zero even without accounting for spin-orbit coupling.

In the subspace of 6 excitons, five relevant configurations are classified by the total excitonic spin into singlet-singlet ($S_e = S_h = 0$), triplet-triplet, ($S_e = S_h = 1$) and single-triplet ($S_e = 0, S_h = 1$ or $S_e = 1, S_h = 0$) as shown in Figure 6.6.

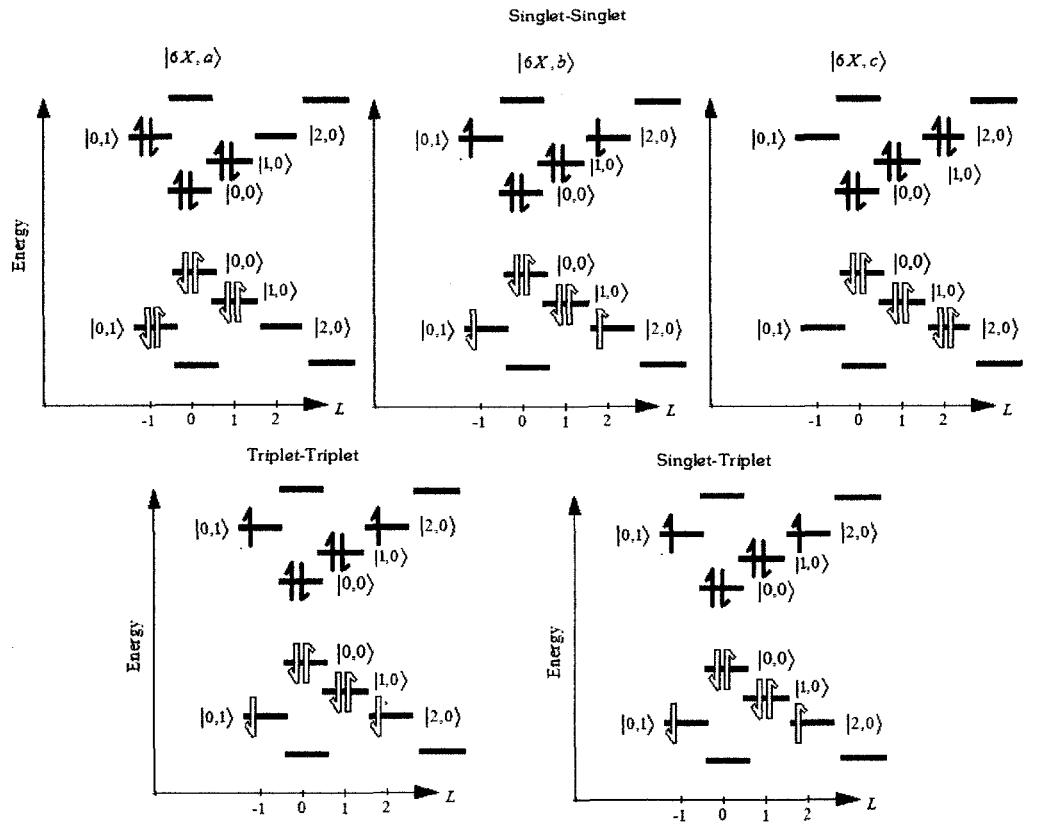

Figure 6. 6: Lowest-energy configurations for 6 excitons (after Cheng [163])

In a relevant basis, the eigen-energies can be solved with the Hamiltonian as given in Reference [163]. Contribution to chemical potential near the $|0,1\rangle$ and $|2,0\rangle$ anti-crossing states is shown in Figure 6.7.

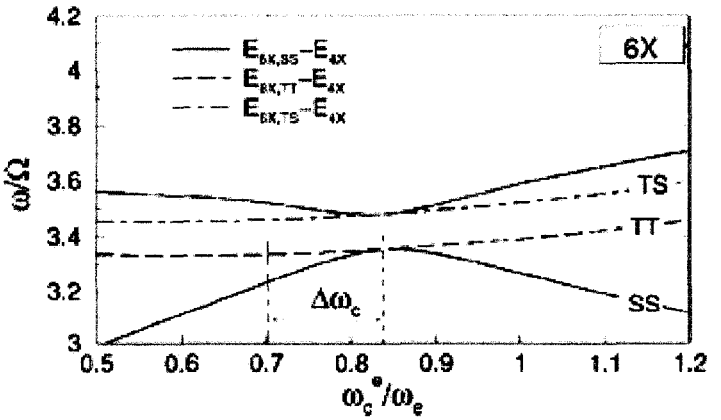

Figure 6.7: Calculated energies of 6 excitons: singlet-singlet (SS), triplet-triplet (TT) and triplet-singlet (TS) states (after Cheng [163])

In this figure, the vertical dotted lines indicate the magnetic field (cyclotron frequency) where the $|0,1\rangle$ and $|2,0\rangle$ states encounter each others. The exchange energy in the field shifts the crossing by $\Delta\omega_c$. Configurations for 7 and 8 excitons are also shown in Figure 6.8 where the 7 exciton configurations are similar to 5. The 8-exciton system has only 1 relevant configuration.

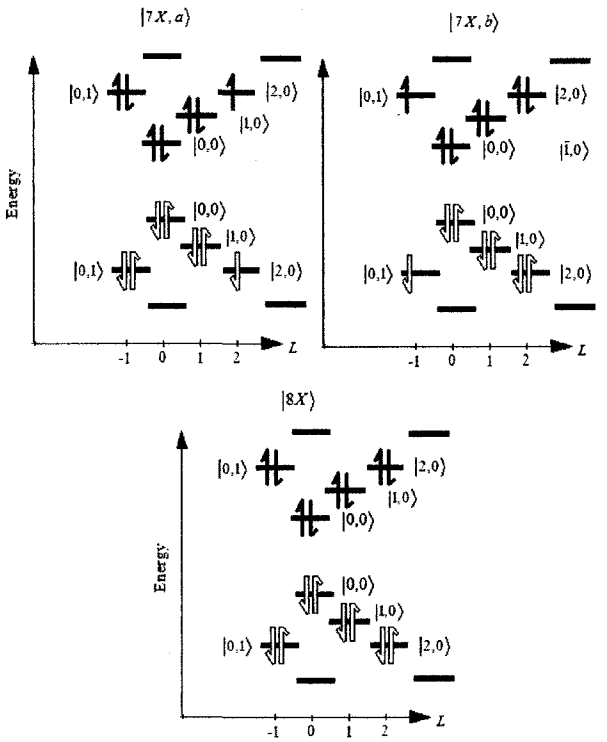

Figure 6. 8: Lowest energy configurations for 7 and 8 excitons (after Cheng [163])

Thus far the effect of many-body (CI) interactions on the energy states was considered on the first (anti)crossing for $|0,1\rangle$ and $|2,0\rangle$ states. In this approach, the PL spectra may be obtained from the configured states taking the many body (CI) effects into account. Cheng [163] assumed a prompt relaxation of the electron-hole pairs so that an N-exciton system relaxes to its ground state before recombination takes place. The emission of a photon during the recombination of one e-h pair involves the process of removing an electron and hole with the same quantum number and opposite spin from the configuration. Without inelastic (eg phonon-producing) interactions, the emitted photon energy is equal to that of the recombined electron-hole at fixed quantum number.

In reality, there are more complicated features in the presence of many excitons and many interactions other than CI need to be considered. Lacking a more realistic model, an appropriately weighted sum of the computed spectra such as those in Figure 6.9 at 9 Tesla may approximate an emission spectrum. This figure shows the emission peak positions when an exciton recombines in a CI system. Due to these configuration interactions, as the initial number of excited excitons increases, the number of luminescence peaks increases and that occur at different positions.

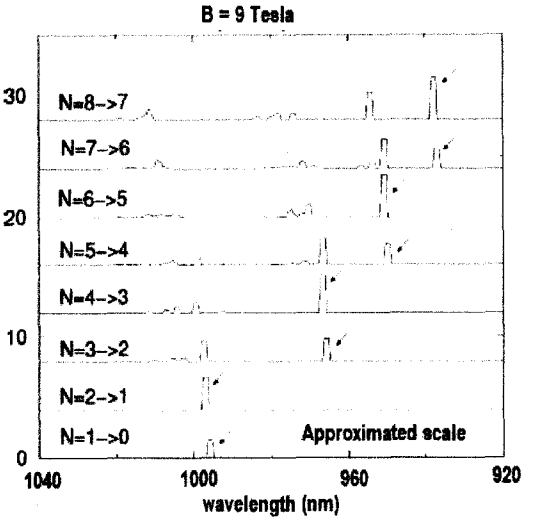

Figure 6.9: Calculated PL spectra from dot with various exciton numbers (after Cheng [163])

6.3 Photoluminescence excitation (PLE)

Figure 6.10 presents PL and PLE spectra taken without a magnetic field. The PL was excited with a 532-nm laser with 509 W/cm^2 of optical power. Different detection wavelengths within a narrow range of the ground state energies can be chosen by setting the grating dispersion angle for the detector. Starting with an excitation at 7 – 8 nm below the detection wavelength, the laser energy is swept up to WL. In Figure 6.10, with a detection wavelength of 1 micron (1.240 eV), the spectrum was excited with an argon laser pumped Ti-sapphire laser tuned from 992.7 nm (1.249 eV) to 850 nm (1.459 eV).

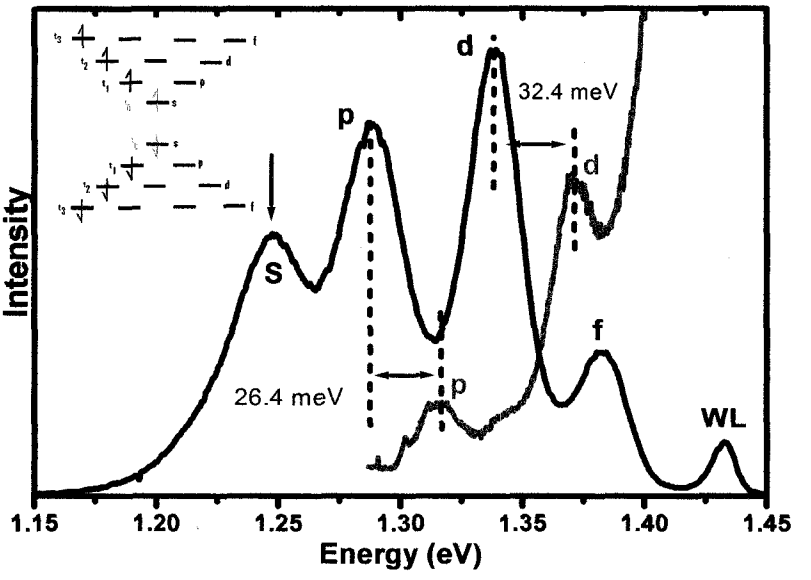

Figure 6.10: PL (black solid line) emission and PLE absorption (gray line) spectra

In the PL spectrum four emission peaks are observed with a 41 meV inter-level spacing between s (1.248 eV) and p (1.289 eV) lines. The energy interval for p-d is 50 meV, and 42 meV for d-f (from 1.339 to 1.381 eV). In the PLE spectrum, only two peaks, p (1.315 eV) and d (1.371 eV) are observed when the detected energy was set at 1.235 eV with energy interval 56 meV: 6 meV greater than that in the PL. These lines are blue-shifted relative to PL by 26 and 32 meV, respectively.

The above spectra are produced at steady-state recombination between electron-hole pairs generated during excitation. In PL, when the excitation power is ~509 W/cm^2, the average number of excitons generated in a QD is between 8 and 20 (the steady number of unrecombined excitons). Looking closely at the absorption range between 1.272 and 1.305 eV, two small peaks can be observed. These two peaks match the two LO phonon assisted emissions near the QD ground states.

To further the PLE study, Figure 6.11 presents spectra taken at 4.2 K at different ground-state detection wavelengths. The resonance spectra for energies from the p and the d levels are prominent when the detection energy is in the range of 1.242 eV to 1.264 eV. Strong resonance peaks at distinct phonon energies are observed when the detection energy reaches 1.253 – 1.259 eV.

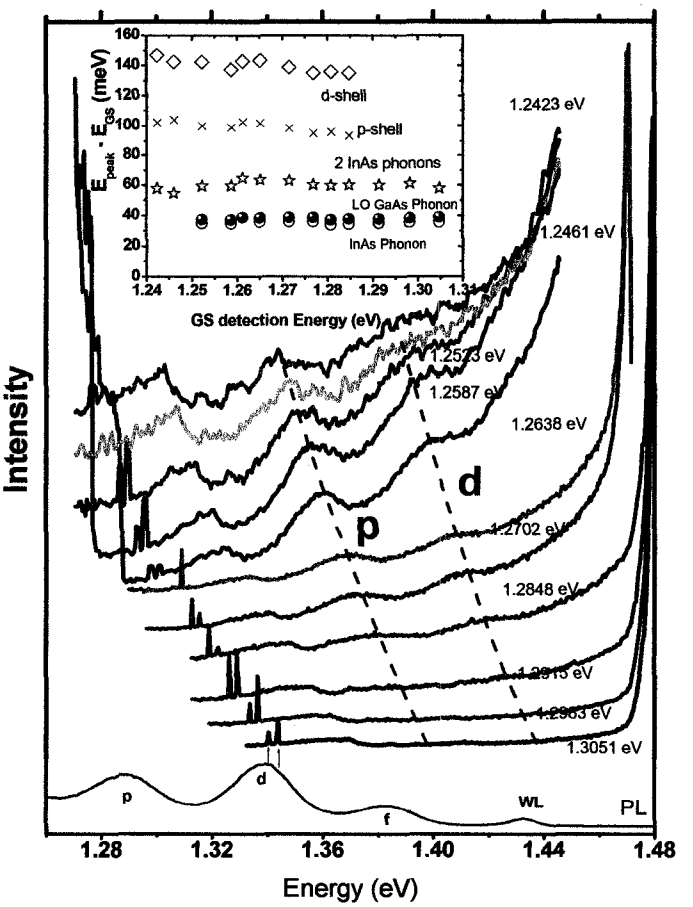

Figure 6.11: PLE spectra as a function of the detection energy in zero magnetic field for InAs/GaAs SAQD taken at 4.2 K

By tracking the two phonon and the p and d peaks, the energy difference between the peak position and the detection energy is plotted as a function of the latter in the inset of the figure. Changing the detection energy selects a different collection or 'ensemble' of QDs from among the various sizes and shapes, having differing energy levels. Small crosses at 100 meV above the GS represent a p absorption signature, while diamonds at 140 meV mark the d peak. All the peaks track horizontally on the plot, meaning that these absorption energies move constantly with the detection energy.

The filled dots mark a phonon-assisted emission[82], probably corresponding to a 36.4-meV GaAs bulk LO-phonon [164]; the circles mark a 31.9-meV InAs QD phonon [165]. The open stars represent two InAs assisted-emission phonons, suggesting a total of four resonant phonons participating directly at the low-energy GS emission: they assist the emission by relaxing carriers to the detection energy for radiative recombination.

6.4 Magneto-Photoluminescence Excitation (M-PLE)

As mentioned, the shallow dome SAQD is electronically analogous to an artificial atom. The discrete energy levels can be meaningfully labeled with angular momenta (s, p, d,...) even if these aren't atomic spherical harmonics but 2-D harmonic oscillator projections, and the spatial extent of a QD electron wave-function is greater than an atom. But like atoms, the QD wave functions are sensitive to strong magnetic fields. This allows the electronic structure of the QDs to be explored with the magnetic fields presently available at research facilities.

Figure 6.12 show some s ground state PL emission peaks as they are quadratically blue-shifted with an increasing magnetic field. This experiment was performed at 1.41 W/cm^2, a very low excitation power to reduce the many-body effects in PL. The inset presents the corresponding intensity spectra as a function of the energy and magnetic field. The peak position shift can be fitted by the relation:

$$E_{GS} = [(1.249 + 7.921(\pm 0.477)B^2] \pm 0.001eV. \qquad \text{(B in mT)} \qquad \text{[EQ 6.1]}$$

Note that the detection energy (set for $B = 0$) is 1.2494 eV. [EQ 6.1] was used to obtain the ground state detection energy for the following M-PLE experiment.

[82] This phonon energy for QD is approximated by the bulk dispersion. In fact, the QD phonon dispersion is quite different than bulk: but to determine precisely how different would require further modeling.

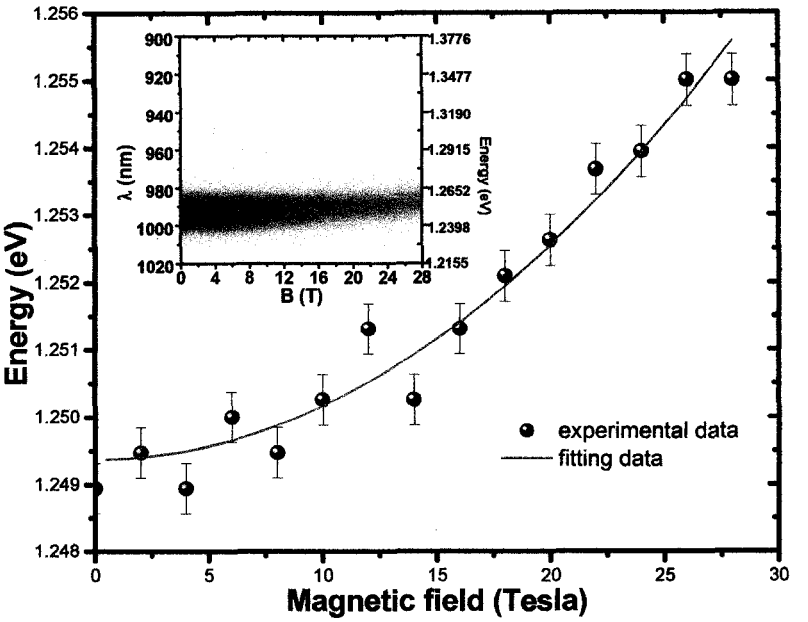

Figure 6.12: Diamagnetic shift of PL emission as a function of applied magnetic field

Figure 6.13 is a surface plot of the PLE intensity as a function of the wavelength and magnetic field. A degeneracy of two is observed for the p and d lines, whereas three is expected for the latter. This indicates that a branch probably remains doubly degenerate with $|2,0\rangle$ and $|1,1\rangle$ being unresolved.

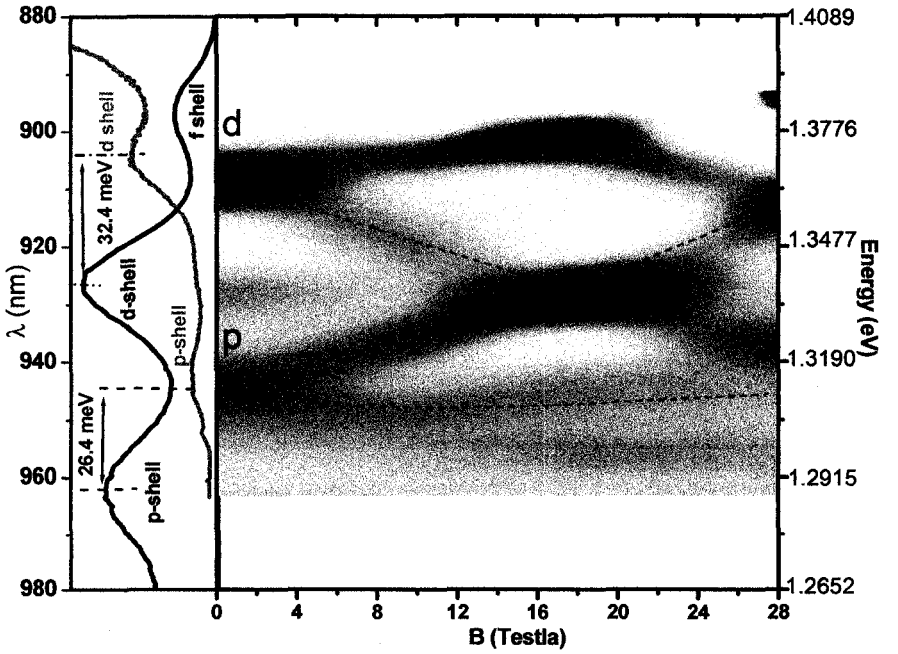

Figure 6.13: PLE spectra of InAs/GaAs SAQD sample plotted as a function of applied magnetic field, $E_{detected} = 1.249eV$ at 4.2 K

In this PLE experiment (again performed at 4.2 K), the spectra were obtained by following the detection energy from [EQ 6.1]. Two (anti)crossings are observed around 14-20 Tesla. The degeneracies are clearly lifted around 8 Tesla and anti-crossings occur near 18 Tesla (i.e. the d-state encounters the f-state). It is useful to examine the spectra at high magnetic fields such as 8 and 18 Tesla in order to test the uniformity of the SAQDs. The electronic structure of this SAQD was obtained at 1.249 eV; the electronic structure at different detection energies would be obtained in a similar fashion[83].

The PLE spectrum at 8 Tesla is shown as a dark gray line in Figure 6.14. The second derivative of that spectrum, represented by the solid black line, was taken to locate the peak positions. The dashed vertical lines indicate the p and d branch positions.

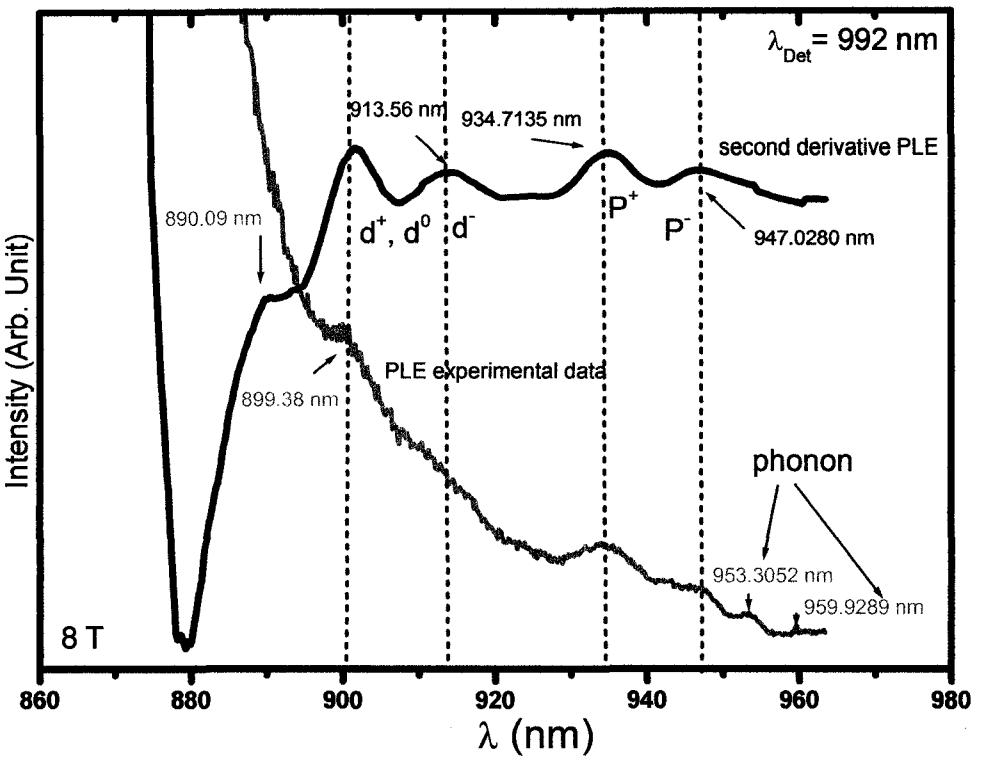

Figure 6.14: PLE spectrum in 8 Tesla magnetic field of InAs/GaAs QD measured at 4.2 K

This spectrum reveals again two phonon-assisted peaks at 953.3 nm (1.301 eV) and 959.9 nm (1.292 eV), which are 50.8 meV and 41.8 meV from the GS energy respectively. Two lifted p branches appear at 934.7 nm (1.326 eV) and 947 nm (1.309 eV) and two (again not three) clear d branches appear at 899.4 nm (1.376eV) and 913.6 nm (1.357 eV). Two degenerate d-states may be unresolved at 913.6 nm. Further experiments were performed as a function of the detection energy, as shown in Figures 6.15 -6.16.

[83] Variations of QD height and lateral size cause variations in the SAQD energy levels. By detecting at various energy settings, different ensembles of dots are probed.

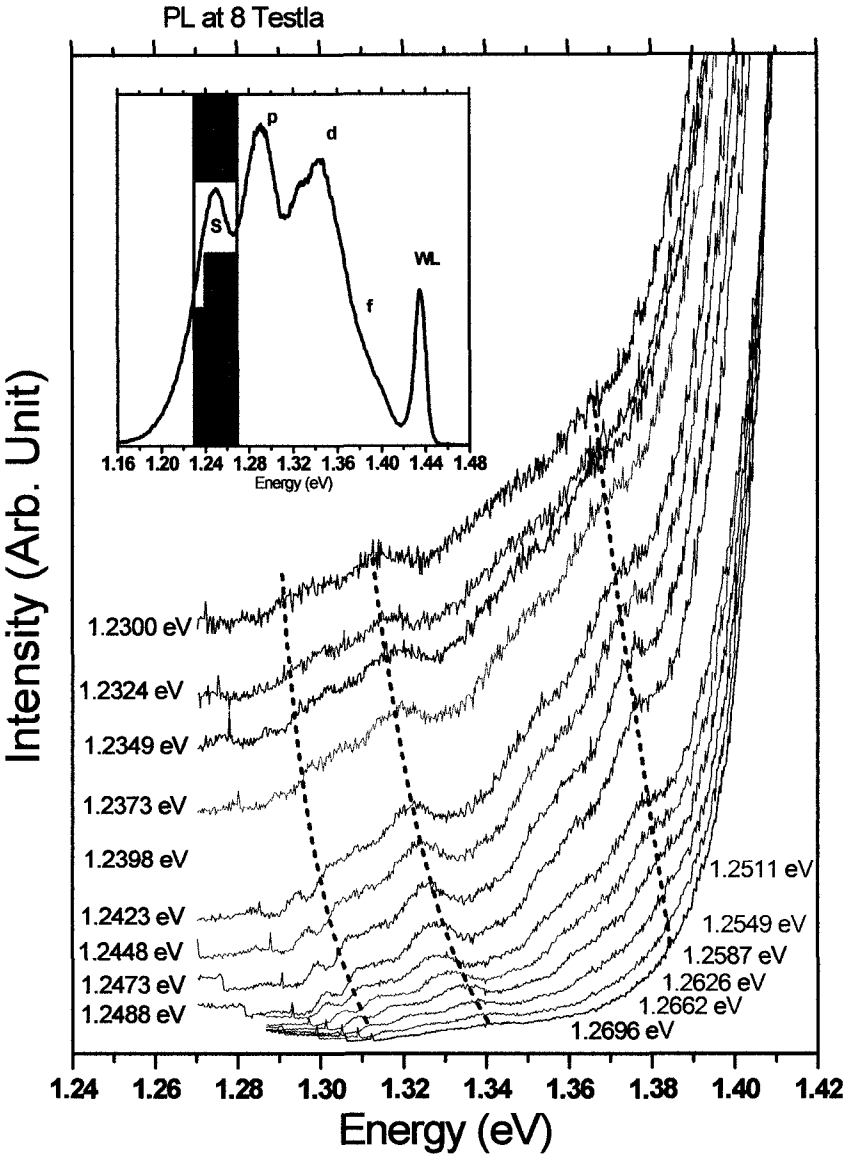

Figure 6.15: PLE spectra at various ground state energies in 8 Tesla B field for InAs/GaAs SAQD measured at 4.2 K. The inset is indicated where the detection energy set (red color)

Figure 6.15 shows the PLE absorption spectra in an 8 Tesla field detected at various detection energies as seen in the red shadow region in the panel. Three clear emission peaks are prominent; with their positions identified by the dashed curves obtained using the second derivatives of the spectrum. Figure 6.16 shows the second derivative of a selection of these PLE spectra. Two and three emission branches respectively from the p and d degeneracies are indicated with blue and olive guide-lines. The additional three resonances indicated with a red line represent the expected phonon-assisted emission lines.

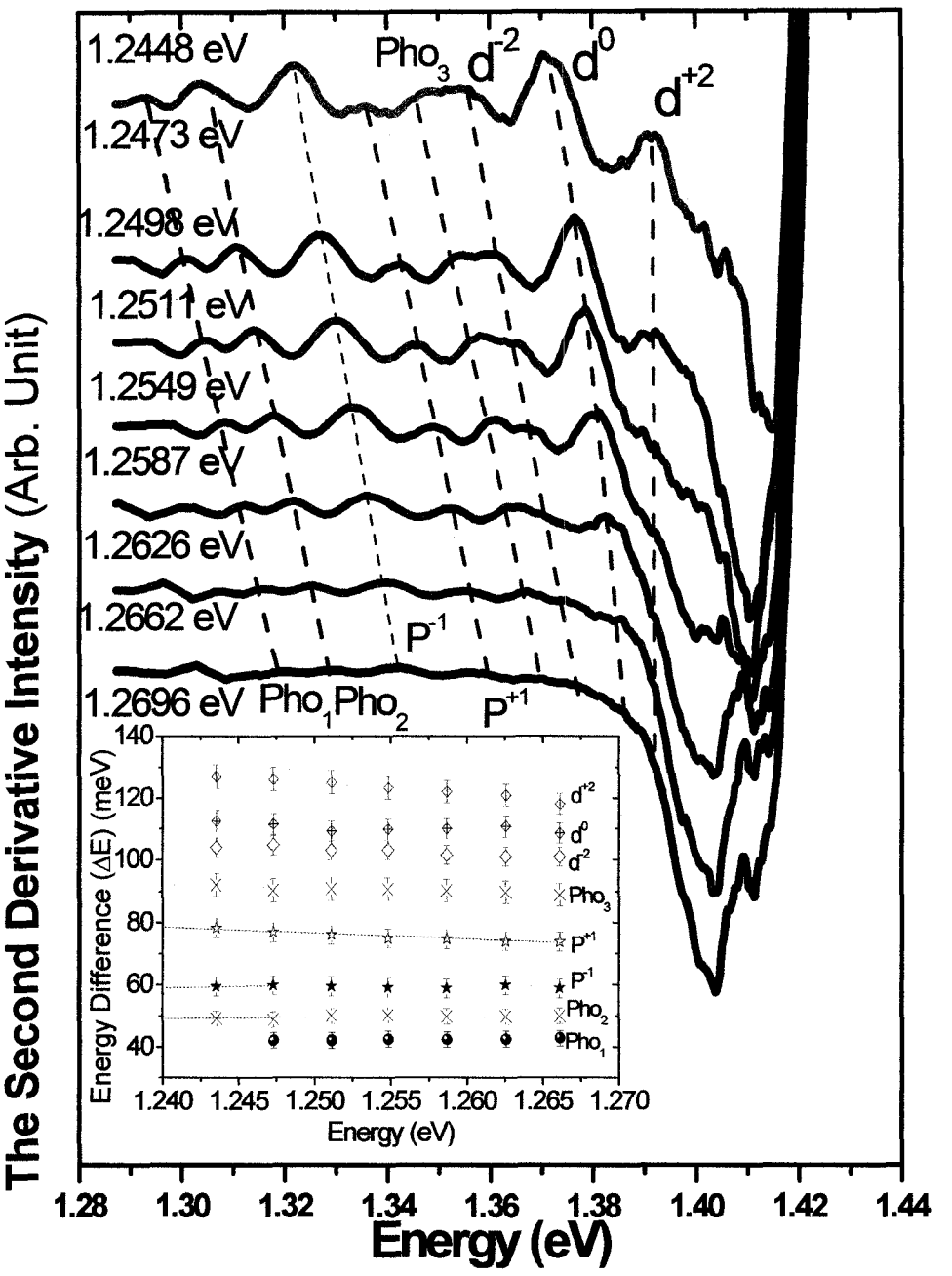

Figure 6.16: Second derivative of several PLE spectra from Figure 6.15. The inset represents the tracking peak position from the figure

The inset of Figure 6.16 plots the energy difference between the peak positions and the ground state (GS) as a function of the latter for the above branches. Two energies, 42.44 meV and 49.75 meV above the detection, correspond to phonon resonances within the expected region for phonons. The (filled and open stars) <1,0> and <0,1> p signatures are respectively at ~ 75 meV and ~ 92 meV. The two lower (<0,2> and <1,1>) d branches (diamonds) at ~ 101 meV, and ~110 meV, are not quite resolved in the detection range. The

higher <2,0> d-branch (hatched diamond) at ~120 meV increases linearly with the detection energy, suggesting a strong non-uniformity across the selected QDs.

To further probe the PLE absorption signature behavior of this SAQD, the 18 Tesla (anti-)crossing region was examined at different detection energies. Figure 6.17 presents the spectra with offset for clarity. The peak position (~1.35 eV) bracketed by the black dashed lines is the merging of one of the p branch <1,0> and the lowest d branch <0,2>. The phonon peak energy positions occur at ~ 1.30 eV as demarcated in red dashes. The high <2,0> d branch (in blue dashes) is observed at ~1.37 eV.

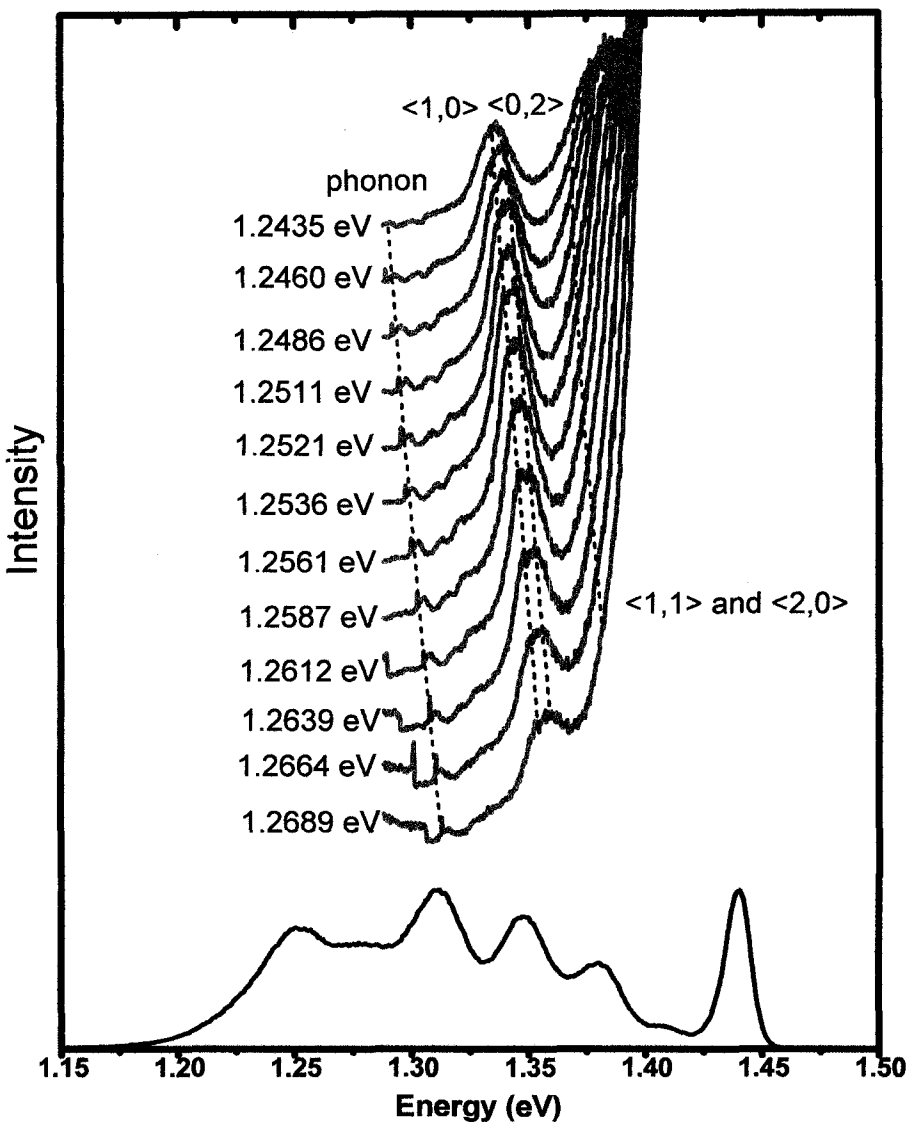

Figure 6.17: PLE spectra in an 18-Tesla magnetic field as a function of detection energy for InAs/GaAs SAQD at T=4.2 K

While tracking these peaks, the energy difference between the peak and the detection energy is again plotted as a function of the latter in Figure 6.18.

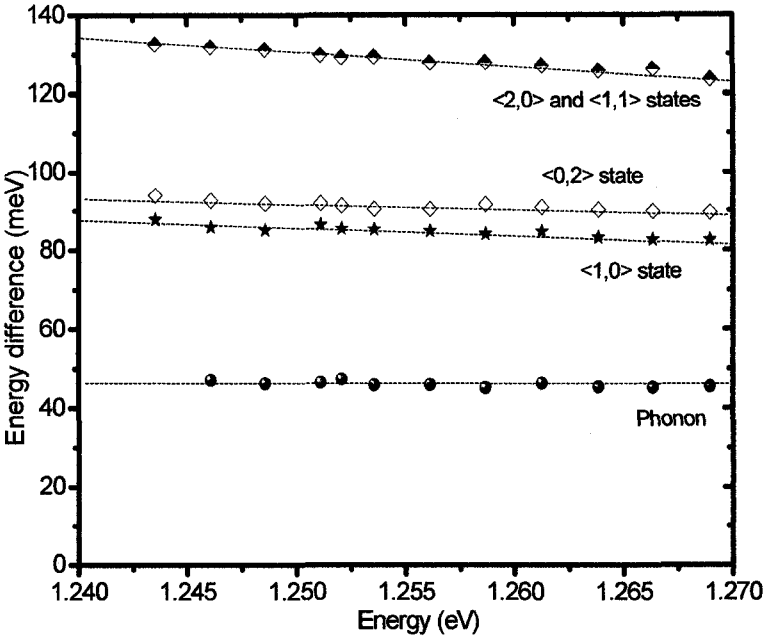

Figure 6.18: Peak-to-detection differences for the PLE spectra in 18 Tesla, from Fig. 6.17

The solid closed circles correspond to a resonant phonon-assisted emission. One possible identity of this phonon peak may be a coupled LO-phonon-plasmon modes L^+ in the heavily-doped GaAs substrate, as reported by Baranov [166]. This could be relevant since these SAQDs were grown on n-doped GaAs. The branches associated with <1,0> and <0,2> shown by solid star and open diamond symbols approach one another at the lower GS energies.

In this QD sample two phonons can be observed: the InAs phonon and the GaAs LO phonon. Also two InAs phonons were observed at 0 Tesla. At 8 Tesla, the electronic structure observed through PLE revealed that the ensemble of the SAQD with the same GS level tended to have similar inter-level spacing as the detection energy was increased. The p-branch for example tended to move up with the detection energy (a horizontal plot). However, the d-branch tended to remain more constant with the increasing detection energy. At 18 Tesla, the encounter of the p^+ and the d^- states moved at about the same separation with detection energy. However, the lifted-degenerate branches d^0 and d^+ remained roughly constant. Still, higher energy states may have merged into QDs as the field strength was increased, and some of the lower states may have shifted toward the continuum states[84]. A detailed model for ensemble of QD states would be helpful to understand these issues, and is worthy of further study.

[84] Such trends may not be observed in PLE due to direct recombinations at other than the detection energy.

6.5 Electronic Structure

QDs can be tailored from their carrier effective masses as they are associated with the electronic structure as determined by the confining potential, geometric shape, alloying and strain. Confinement effects are linked to variations in size, shape and composition of the QDs, while the InAs/GaAs SAQD strain tensor causes a significant change in effective band gap and level spacing. For example, the ground state transition energy is ~ 1.2 eV in the SAQD whereas the band gap energy of InAs is ~0.4 eV.

The in-plane reduced-mass can be obtained from [EQ 4.1]. The p branch energy differences for M-PL and M-PLE in Figures 6.2 and 6.13 are plotted in Figure 6.19 with a least-square linear regression. The M-PL slope is 1.997 ± 0.301 meV/T and implies a reduced-mass of $0.058 m_0 \pm 0.010 m_0$, agreeing with published findings between $0.053 m_0$ [167] and $0.070 m_0$ [168]. The M-PLE slope is 1.602 ± 0.301 meV/T yielding a reduced-mass of $0.072 m_0 \pm 0.010 m_0$, within 8% of the one obtained by Hameau [169] *et al* ($0.067 m_0$).

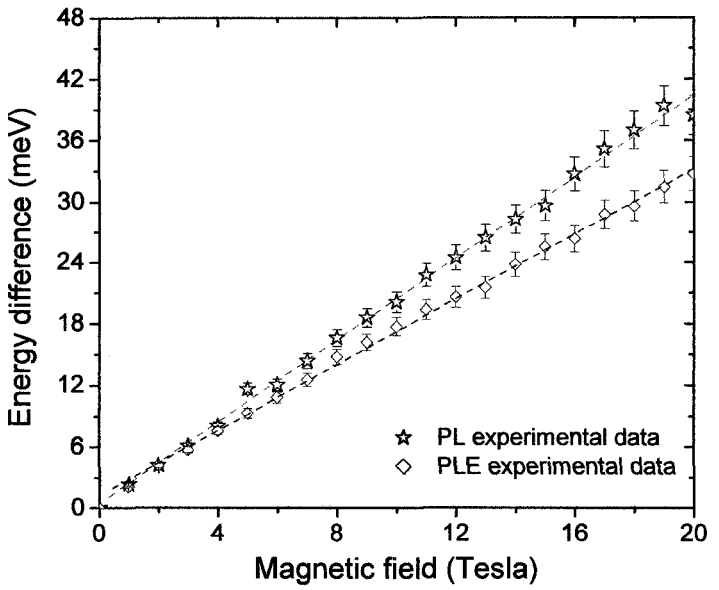

Figure6.19: The energy difference between the p branch-energies as a function of magnetic field

The value of the in-plane reduced-mass, as obtained from the PL spectra is a parameter required in the F-D spectrum model. Details of the model are outlined in Chapter 2.

Recall the F-D expression for an exciton

$$E(n_+, n_-) = E_0 + \hbar\left(\Omega_+^e + \Omega_+^h\right)\left(n_+ + \frac{1}{2}\right) + \hbar\left(\Omega_-^e + \Omega_-^h\right)\left(n_- + \frac{1}{2}\right). \qquad \text{[EQ 6.1]}$$

$$\Omega_\pm^{e(h)}(B) = \left\{\omega^2 + \left(\frac{\omega_c}{2}\right)^2\right\}^{1/2} \pm \frac{\omega_c}{2}, \quad \omega_c = \frac{eB}{m^*}$$

In this model, the electron and h-h 'orbital' (oscillation) frequencies and the in-plane effective masses are required. The latter can be calculated from the in-plane exciton reduced-mass and the h-h to electron mass ratio.

For a dome-shaped SAQD, the confinement energy in the growth direction may be approximated as a QW. Wimbauer [170] *et al* found that the h-h effective mass for $In_xGa_{1-x}As/GaAs$ QW was $\sim 0.143 m_0$, depending on the ratio of indium and gallium composition. This finding may be transferred to the SAQD, modified by the deformation of the confinement potential with strain.

Awirothananon [161] *et al* found 2.1 for the in-plane h-h to electron effective mass ratio, which is related to the ratio of electron to h-h frequency (small electron effective mass raises its frequency). To model the h-h to electron effective mass ratio, the lowest crossing point as indicated by the dash-square in Figure 6.2 is discussed here. This (anti)crossing at 18 Tesla was simulated for different ratios of h-h to electron effective masses, holding three parameters constant: the exciton reduced effective mass of $0.058 m_0$, the crossing point (its energy and magnetic field), and inter-level spacings. Only certain electron and h-h masses were found to be in good agreement with these conditions as shown in Table 6.1 with the simulated results plotted in Figure 6.20.

Table 6.1: The relation between in-plane effective masses and the electron and hole energies.

Color	***In-plane effective masses***			***Electron energy (meV)***	***Heavy-hole energy (meV)***	$\frac{m_{hh}}{m_e}$
	Reduced	***Electron***	***Hole***			
Black	$0.0461 m_0$	$0.06809 m_0$	$0.1430 m_0$	35.22	16.7741	2.1
Red	$0.0435 m_0$	$0.0515 m_0$	$0.2832 m_0$	44	8	5.5
Blue	$0.0421 m_0$	$0.0515 m_0$	$0.23175 m_0$	42.54	9.454	4.5
Green	$0.0394 m_0$	$0.0515 m_0$	$0.42195 m_0$	47.14	4.85	9.7

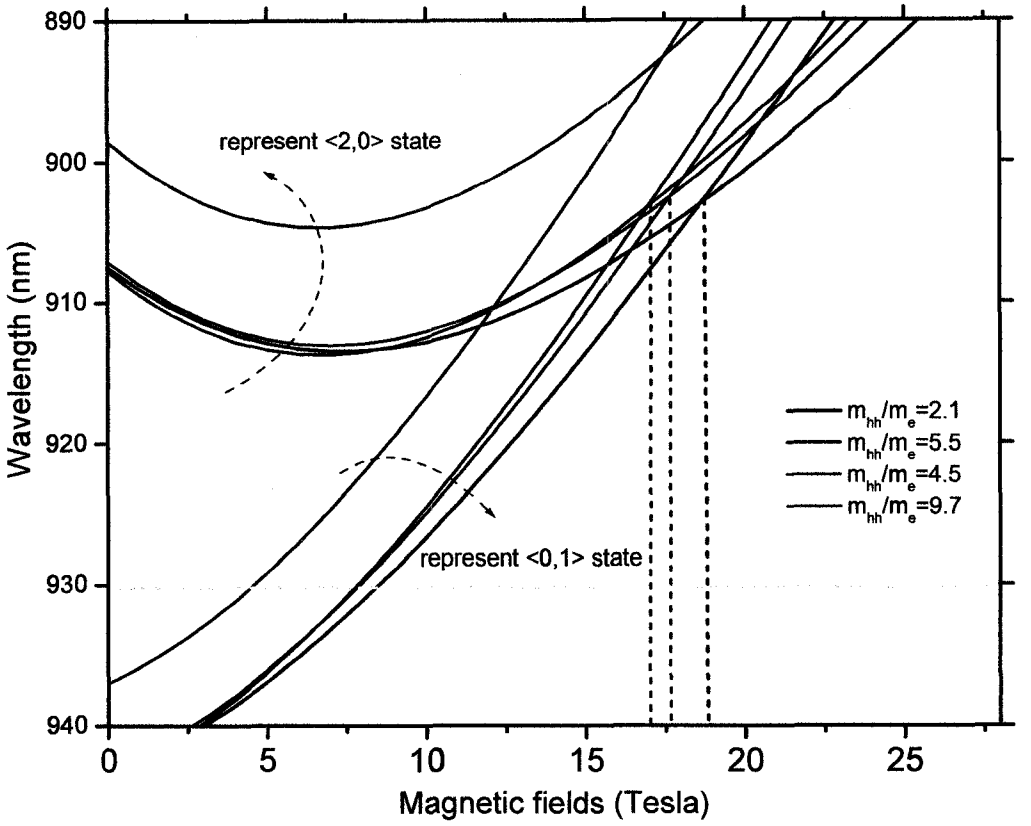

Figure 6.20: Simulated <0,1> and <2,0> branches with variation of the electron and h-h parameters

As the ratio of heavy-hole to electron effective mass increases, the <0,1> and <2,0> branch curvatures are enhanced. Also, the crossing point blue-shifts when the electron effective mass is increased with the effective mass ratio held constant.

The M-PL experimental data in Figure 6.2 may be fitted by using the above relation combined with:

(i) the PL reduced effective mass of $0.058\,m_0 \pm 0.010\,m_0$., where $m^*_{hh} = \dfrac{m^*_e \mu}{m^*_e - \mu}$,

(ii) the relation between electron (hole) in-plane effective mass and electron (hole) frequency at the (anti-)crossing point is:

(iii)

$$m^*_e \omega_e = m^*_h \omega_h, \qquad \text{[EQ 6.3]}$$

(iv) the inter-level energy gap at 0 Tesla is equal to $\hbar$ times $(\omega_h + \omega_e)$.

The oscillation frequency of electrons and holes is associated with the turning-points of the QD confinement potential. From the above relation, the h-h to electron effective mass ratio equals the electron to h-h frequency ratio, which entails that lighter electrons will oscillate at higher angular velocities than holes.

By setting the energy offset E_0 equal to 1.2006 eV, the ground state energy level is separated from the bottom of the potential energy by 45 meV. Also the results reveal that the inter-level spacing are 43 ± 1 meV, 46 ± 2 meV and 46 ± 1 meV for s-p, p-d and d-f, respectively. The electron and hole in-plane effective masses which are found to give the best fit are shown in Figure 6.21.

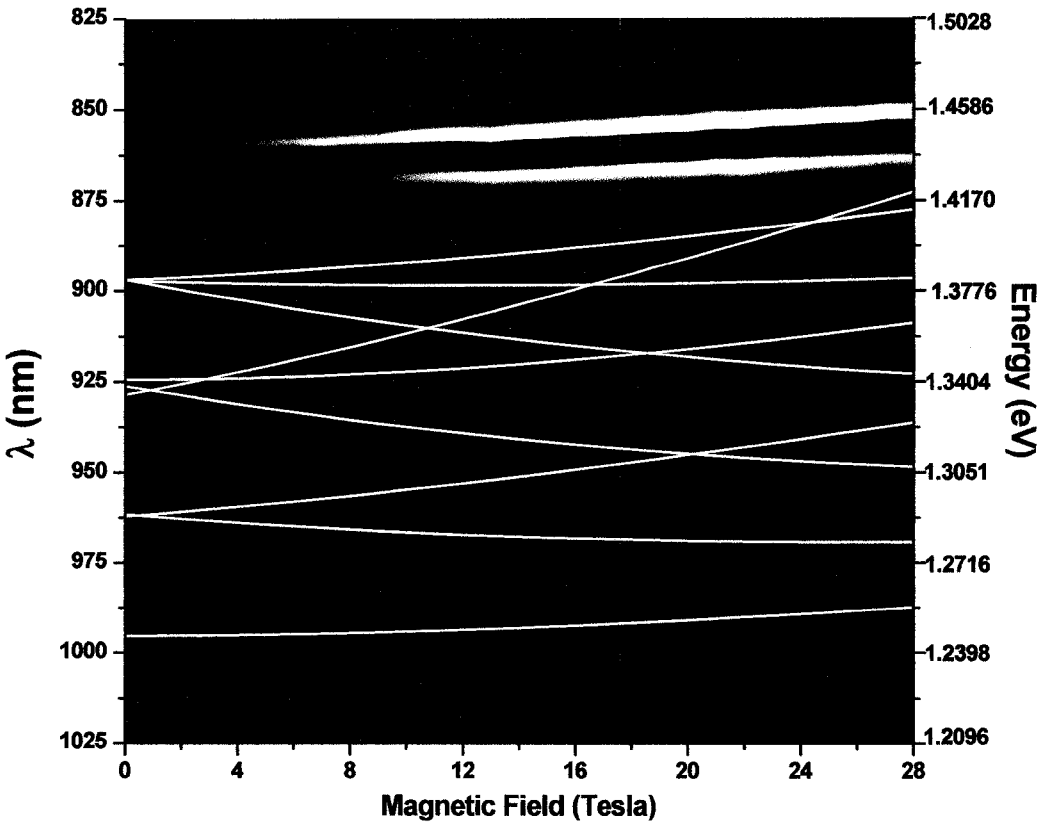

Figure 6.21: A simulation of the Fock-Darwin model showing the spectral evolution in a magnetic field (pink to red indicated the intensity of the PL peak)

A simulated evolution of the F-D lines is shown with white solid lines in Figure 6.21. The electron and hole in-plane effective masses for this are described in Table 6.2. In this Figure the (anti-)crossing points for both the experiment and the model occur at the same magnetic fields, but the simulated ones are at higher energies. For high energy states, the simulated emission intensities at zero magnetic field are somewhat offset from the experimental values. This deviation could be a result of the F-D model involving independent particles in two dimensions, while in PL, the interacting particles are produced during the laser excitation, where many-body interactions need to be considered.

Table 6. 2: Parameters for the fit of Figure 6.21

Energy level	Electron frequency $\omega_e \left(\frac{1}{s}\right)$	m_e^*	m_{hh}^*	$\frac{m_{hh}^*}{m_e^*}$
s(0,0)	6.306×10^{13}	$0.05287\, m_0$	$0.59775\, m_0$	11.31
p(0,1)	5.919×10^{13}	$0.06638\, m_0$	$0.45943\, m_0$	6.92
p(1,0)	5.419×10^{13}	$0.07189\, m_0$	$0.30019\, m_0$	4.18
p(0,2)	6.851×10^{13}	$0.05948\, m_0$	$2.33097\, m_0$	39.19
d(1,1)	7.142×10^{13}	$0.0579\, m_0$	$33.582\, m_0$	580
d(2,0)	6.543×10^{13}	$0.0553\, m_0$	$1.18793\, m_0$	21.48
f(0,3)	5.142×10^{13}	$0.07811\, m_0$	$0.22528\, m_0$	2.88
f(1,2)	2.531×10^{13}	$0.15841\, m_0$	$0.0915\, m_0$	0.58
f(2,1)	3.542×10^{13}	$0.1134\, m_0$	$0.11872\, m_0$	1.05

The estimated electron effective mass for the lower states is not far from that of InAs QDs ($\sim 0.04\, m_0$ - $0.055\, m_0$) [171-173], but is still closer to bulk GaAs ($0.063\, m_0$ [174])[85], which would mean an unrealistically high alloy proportion.

In M-PL, excitons are required to fill all the lower states in the QD up to the WL energy level in order to observe the splitting of the QD energy levels under the influence of magnetic fields. These electron-hole pairs in each QD energy levels might oscillate with different frequencies under a given magnetic field strength, which depended on the angular momentum and the energy eigenstate where the excitons are present.

The electrons and holes are localized in the dome-shaped QDs and correlated by a direct Coulomb interaction and the confinement potential. In the PL experiment, not only are these potentials important but also electron (hole) exchange and configuration interactions are significant too. The electron-electron exchange energies, spin-coupling configurations and screened Coulomb interactions are all many-body effects. Note that the electron-hole exchange and valence band mixing effects are discounted in current models [162].

Bayer [86] and Wojs [67, 140] described many excitons in SAQD through hidden symmetry, using a rule to determine the level structure of electron-hole complexes analogous to Hund's rules in atomic physics. Basically, Hund's rules determine that few electron configurations contribute dominantly to the ground state. By analogy, a few excitons are in the ground state configurations. In SAQD, two carrier species occupy the energy levels, and the excitonic ground-state can be treated by the dynamics of a polarization operator. Inter-level optical processes involve the polarization operator annihilating a photon and creating an electron-hole pair. Bayer has given examples of how the dynamics of hidden symmetry affect the emission spectra of excitonic artificial atoms in reference [86].

[85] InAs bulk electron effective mass is $0.0265\, m_0$ (Cf. Nakwaski [230).

M-PL has revealed valuable insights, but many interaction parameters need to be included for the analysis. In order to reduce the number of parameters, M-PLE was done instead. The simulated data are plotted as black dash lines in Figure 6.22 with the parameters detailed in Table 6.3.

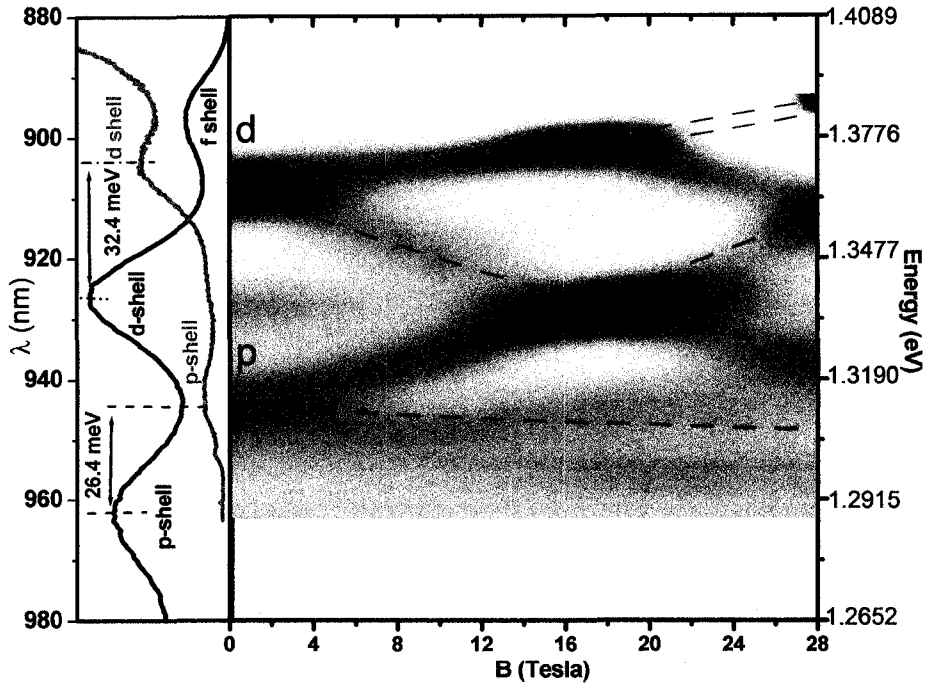

Figure 6.22: M-PLE overlaid with F-D simulation (black dashed lines)

In this figure, two p-branches and the lowest d-branch fit the experimental results quite well. The two higher d-branches appear to be degenerate states in the QD ($d\langle 1|1\rangle$ and $d\langle 2|0\rangle$) even in the presence of magnetic fields. These degenerate states are indicated with dash-lines for the highest branch in figure 6.22.

Table 6. 3: Simulated parameters for the M-PLE results shown in Figure 6.22

QD state	Electron frequency $\omega_e\left(\frac{1}{s}\right)$	m_e^*	m_{hh}^*	$\frac{m_{hh}^*}{m_e^*}$
$p\langle 0\|1\rangle$	$2.74\text{x}10^{13}$	$0.2695\,m_0$	$0.098\,m_0$	0.4
$p\langle 1\|0\rangle$	$1.24\,\text{x}10^{14}$	$0.0503\,m_0$	$0.166\,m_0$	3.3
$d\langle 0\|2\rangle$	$1.11\,\text{x}10^{14}$	$0.0578\,m_0$	$0.293\,m_0$	5.0
$d\langle 1\|1\rangle$	$1.13\,\text{x}10^{14}$	$0.0580\,m_0$	$0.298\,m_0$	5.1
$d\langle 2\|0\rangle$	$3.34\,\text{x}10^{13}$	$0.1925\,m_0$	$0.115\,m_0$	0.6

On inspection of the fitting parameters in Table 6.3, the electron frequencies in different QD energy levels differ but are of the same order of magnitude. As modeled, the lower p-branch electron oscillates at lower frequency than the higher branch. This is reflected in a raised electron effective mass for the lower branch, compared to the higher one. An opposite situation appears for the d-states, with higher branch electrons oscillating more slowly than lower ones. Especially at the crossing point, electrons in the $p\langle 1|0\rangle$ and $d\langle 0|2\rangle$ states oscillate with almost the same frequency.

From the foregoing estimates of diamagnetic shifts in Figure 6.12 and the in-plane exciton reduced-mass obtained from the M-PL and M-PLE, a determination of the mean square in-plane electron and hole separation can be made. It is obtained from [175]

$$\beta = \frac{e^2}{8\mu^*}\langle \rho^2 \rangle , \qquad \text{[EQ 6.4]}$$

where, as per Polimeni [175] the diamagnetic shift coefficient (β) of excitons confined in a QD is expressed by

$$\Delta E = \beta B^2 , \qquad \text{[EQ 6.5]}$$

where $\langle \rho^2 \rangle$ is the mean square of the in-plane electron and hole separation and μ^* is the in-plane reduced-mass. The relation in EQ [6.4] is not dependent on carrier wave functions in the growth direction; but using it, the mean square in-plane exciton extent is found by plotting the increase of the detection energy as a function of magnetic field squared. As shown in Figure 6.23, the fitted slope is ~0.00792 ± 0.00048 meV/T, which gives $\langle \rho^2 \rangle$ 1.841x10^{-17} m^2.

In weak fields, the lateral confinement in the QD is stronger than the Coulomb interaction energy, or $\langle \rho^2 \rangle$ is equivalent to the mean square of the distance between the electron and the hole $\langle \rho_{eh}{}^2 \rangle$. However, at high fields, which cause small carrier orbits, the lateral confinement is less important, and $\langle \rho^2 \rangle$ is equivalent to $\langle \rho_h{}^2 \rangle$ or $\langle \rho_e{}^2 \rangle$ and the e-h separation is reduced.

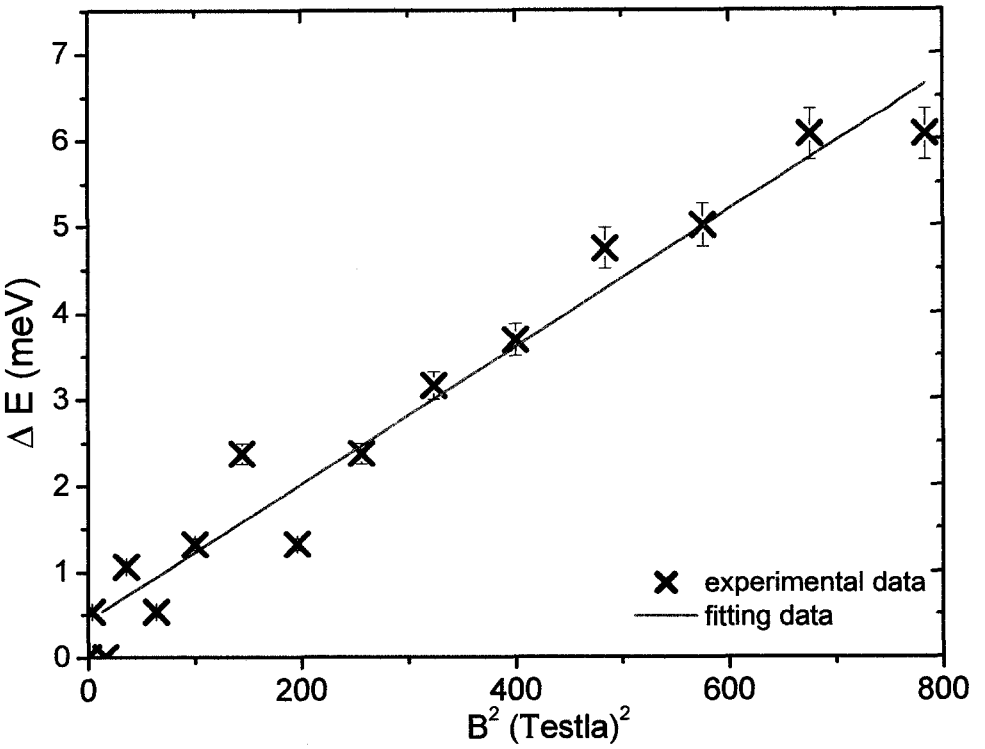

Figure 6.23: Energy shift of the ground-state emission as a function of squared magnetic field

This interpretation was confirmed by Cheng *et al* [163]. They described the electron-hole separation through the theory of excitonic artificial atoms as $(\ell_H)^2 \approx \frac{\hbar}{m^* \omega_H}$. Here the subscript H indicates a hybrid combination of the characteristic length of the QD confinement (quantum dot wave-function extension) and magnetic field-induced confinement (magnetic length). At zero magnetic field, the QD confinement length for electrons and holes is 3.156×10^{-17} m^2 when using the values in Table 6.1 with $m_e/m_h = 2.1$. Comparing with the experimental result (1.841×10^{-17} m^2), the modeled confinement is about double. As the external magnetic fields increase, the value of $(\ell_H)^2 \approx \frac{\hbar}{m^* \omega_H}$ tends to the magnitude of the magnetic length ($(\ell) = \left(\frac{\hbar}{eB}\right)^{1/2}$).

6.6 Summary

Photo-excited spectral lines of InAs SAQDs grown on a GaAs substrate are broadened by inhomogeneities. These SAQDs are dome-shaped with unique selection rules and electronic levels that are analogous to the two-dimensional harmonic oscillator. In-situ indium flush and ex-situ RTA at 825 °C for 30 seconds have been demonstrated in the foregoing experiments to reduce the broadening. After these treatments the PL spectra revealed well-resolved s, p, d and even f emission peaks which are modulated in intensity according to state-filling when the excitation power is changed.

PL spectra excited up to partially filled d and f levels were probed in an external magnetic field in order to lift (orbital angular momentum) degeneracies, but not the spin degeneracy. Ten (anti-)crossing regions were observed in this M-PL method, at ~10, 18 and 28 Tesla, with four of the crossings at ~18 Tesla. The simulated M-PL spectra were similar to the experimental ones, though with progressive offsets by many-body interactions not considered in the F-D model. These include screened Coulomb interactions, exchange between the top-most carriers in state N and those in filled states, as well as configuration interactions (CI). All of the interactions affect the chemical potential.

The many-body effects of the many excitons in PL or M-PL can also be described somewhat phenomenologically. Hidden symmetries discussed by Bayer [86] and Cheng [163] are used to described the observed behavior. Bayer described the situation with many excitons as a function of excitation power. As the excitation power was increased, the QD luminescence shifted because of the interaction of these many excitons. Cheng explained the multiple ground state configurations present at the merging (crossing) of two QD states such as the $|1,0\rangle$ and $|0,2\rangle$ states. In that case, relevant configurations could be filled with 5, 6, 7 or 8 excitons. This affects the crossing region by a displacement, and the two states do not actually cross but came very close to each other.

Comparing PL and PLE spectra in zero magnetic field, the PLE p and d lines were blue-shifted respectively 26.4 and 32.4 meV from PL positions. Two phonon peaks were observed at 36.4 meV and 31.9 meV above the s emission. These seem to correspond to GaAs bulk LO and InAs QD phonons, respectively engaged in resonant phonon-assisted luminescence. In M-PLE, two clear degenerate peaks branch off from the p and d lines although three d branches were expected: one line is presumed to remain doubly degenerate. The induced in-plane effective mass was found from the p branch splitting.

Chapter 7

The Influence of Doped Layer on InAs/GaAs SAQD

QD infrared photo detectors (QDIP) [176 - 179] now compete with QW-based ones, as QDIPs with normal light incidence [180] have lower dark current [181], greater quantum efficiency and higher operating temperature [182]. Greater grasp of how growth conditions bear on the electronic structure will facilitate the optimization for other applications. For instance QDIPs perform best when the QDs have high density and smaller size (with only one or two discrete energy levels).

In this chapter the electronic structure with doped capping layer is studied on layers of InAs/GaAs QDs. The influence of this doping on QDs in one and 25 layers is compared.

7.1 A Description of the Samples and Optical Measurements

Three InAs/GaAs SAQD samples grown by MBE via S-K growth mode were studied for the influence of the doping layer. The SAQD layer(s) were bounded by GaAs with a GaAs substrate on the bottom and a 100-nm capping layer on top. In-situ indium flush (~5-nm above the SAQD layer) and RTA [34] techniques were employed to minimize non-uniformities. As in the prior experiments improved uniformity could be observed through the reduced FWHM of the emission lines, reduced inter-line spacing and blue-shift of PLE absorption peak. In this set of experiments, the emission-line shifts away from the discrete QD energies which enable the study of the QD electronic structure. The features of each sample are listed in Table 7.1.

Table 7. 1: A summary of the properties of the samples investigated

Sample	*Layer of QD*	*Doping dose*	*Post growth annealing process.*
A	Single	No doping (Neutral)	RTA 875 °C for 30 sec
B	Single	p-doped ($2.5x10^{10}$ cm^{-2})	RTA 850 °C for 30sec
C	25 layers	p-doped ($4x10^{11}cm^{-2}$)	RTA 875 °C for 30 sec

Samples A and C were annealed at 875 °C with the same RTA conditions mentioned in Section 4.1. The samples[86] were reintroduced to vacuum after RTA and maintained at 77 K. In PL and PLE, 532-nm laser and tunable laser (~1.240 eV to ~1.393 eV) excitation sources were employed. The same optical equipment (spectrometer and detector) mentioned in Section 4.1 were used.

[86] Capped layer are exposed to an atmosphere before introducing to the optical vacuum chamber.

7.2 Results and Discussions

Figure 7.1 presents the PL spectra for sample A as a function of the annealing temperature. The s-p inter-level spacing was 53 meV, 39.8 meV, 33.3 meV and 30.8 meV for the as-grown (no RTA), RTA850, RTA875 and RTA900, respectively. The p-d inter-level spacing likewise decreases with the annealing temperature. Line-widths also decreased at higher anneals, and the lines blue-shifted slightly. The reduction of the inter-level spacing means that the gallium uptake and the uniformity of the SAQD increased due to the inter-diffusion across the barrier.

The inset in Figure 7.1 presents the peak positions as a function of the RTA temperature. The lower energy peaks blue-shifted dramatically for anneals from 875 °C to 900 °C and then stabilized. This result corresponds to an observation by Fafard [33], who suggested that the principal effects of the intermixing arise from diffusion in the vertical direction whereby the potential at the center of the QD increases with the inter-diffusion of gallium in and arsenic out. This intermixing shifts the thicker regions faster than the thin regions (which may already be homogenized), effectively making the potential of different QDs more alike. A.J. Williamson [183] noted the capping process induces the diffusion of the gallium into and the indium out of the dots, a process somewhat similar to the diffusion during the RTA anneals.

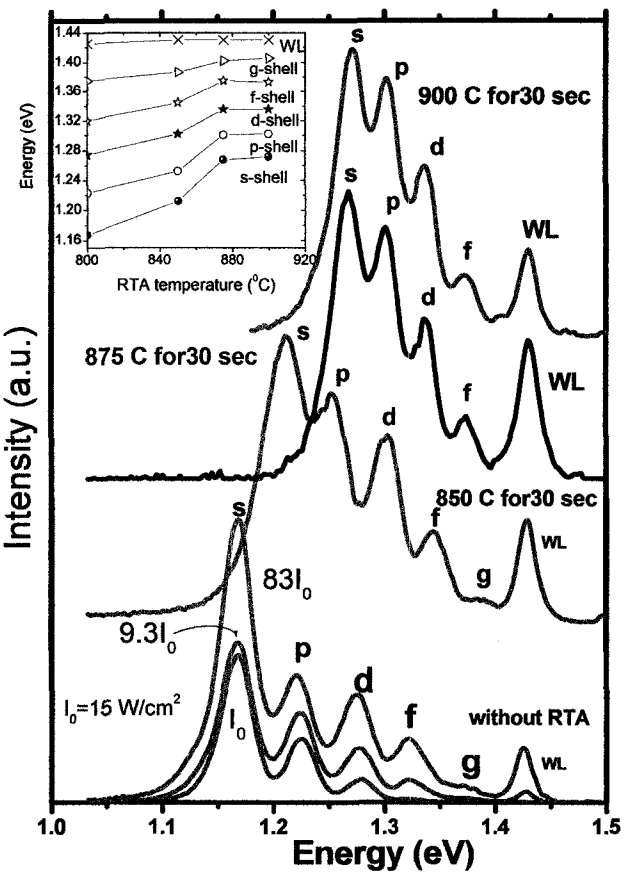

Figure 7.1: PL spectra as a function of the annealing temperature for sample A. Inset presents the peak position

The SAQD emission spectra as a function of excitation power for the untreated sample A (as-grown) appears at the bottom of Figure 7.1. Emissions of the s, p and d lines are observed at low excitation power (~15 W/cm^2); the f, g and WL lines appear only when power is increased 10-fold, and the overall intensity increases as the excitation power raises another order of magnitude, where the WL emission reaches about the same intensity as the f line. Nevertheless, a saturation of the lower state was not observed in this SAQD even at the high excitation power. This may suggest that the excitation profile was not uniform (Gaussian profile) or a different carrier dynamics for the intra-band and inter-band transitions. For example, Raymond *et al* [89-90, 104] also found that an optically excited density and a recombination lifetime are correlated.

The above results indicate that the sample A with an 875 °C annealing temperature is the best candidate for the PLE experiment in the range available: tunable from ~1.27 eV to 1.4 eV. The PL for this sample is presented in the top inset in Figure 7.2. The detected energy for PLE experiment is indicated with the red arrow in the inset. Only one PLE signature is observed in the spectrum at specific detection energy in this range.

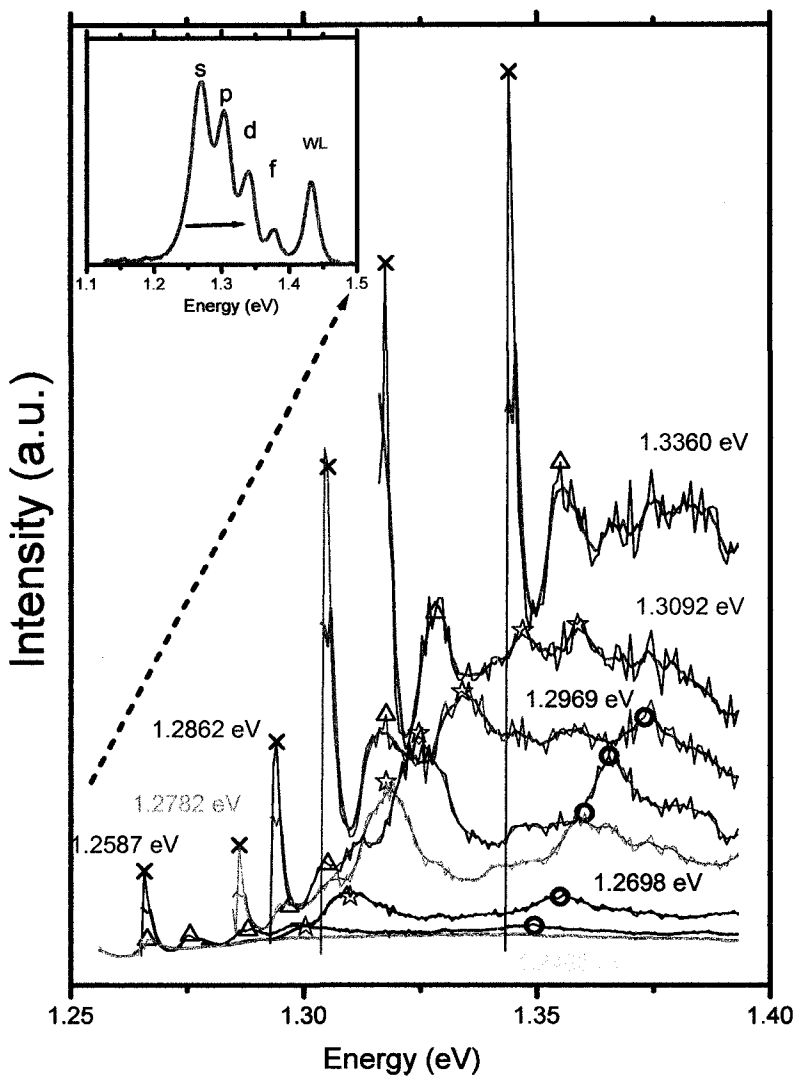

Figure 7.2: Sample A: PLE as a function of the ground-state detection energy without a magnetic field. Inset presents PL spectrum.

In PLE, the ground-state detection energy is set at a particular value for the low-end of the tuning range. With this ground-state sampling position fixed, the laser is tuned upwards in energy to map a spectrum of the intensity (emitted at the ground-state energy) as a function of excitation energy. The luminescence at the ground-state arises from those QD states selectively excited by the laser energy which then decay or thermalize non-radiatively to the ground-state and emit a photon at the ground state. In Figure 7.2 subsets of QDs are therefore probed from the ensemble s-line up to the p line[87]. The value labeling each spectrum is the detection energy[88] and vertical offset is included for clarity. The 1.297 eV spectrum reveals at least four peaks (1.305, 1.318, 1.335 and 1.373 eV), two of which may be a phonon assisted emission from other dots on the blue side of the GS energy. The other peaks are assigned to p (possibly also d) absorption.

Figure 7.2 shows the absorption in the p and d states blue-shifting with the various detection energies. The PLE spectra are dominated by the relaxation processes of the carriers from excited states, which involve multi-phonon and Auger scattering processes. The energy differences between the peak positions and the detection energy as a function of the latter are shown in Figure 7.3.

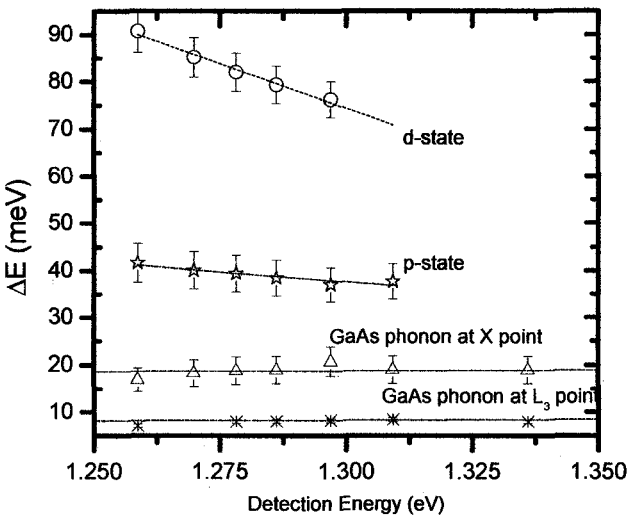

Figure 7.3: PLE peak positions of Fig. 7.2 as a function of various detection energies

The figure also shows the PLE line positions of some probable resonant phonons with the excited states in the SAQDs. The crosses and the open-triangles mark the peak positions at ~8 meV and ~18.8 meV respectively above the detection energy. These lines strongly suggest a phonon-assisted emission: the line at 8-meV corresponding to TA phonons in GaAs at the L_3 band center, with the line at 18.8-meV matching TA phonons in GaAs at X_1 band center [184]. The open-star and the crossing symbols mark the p and the d absorption lines.

[87] As the GS energies approach a PL p-line, their energy selections picks up the blue-shifted s-level emissions from a decreasing subset of QDs.

[88] The gray guide-lines are smoothed data using 5 adjacent points.

The p and d lines have a different behavior from that presented in Chapters 5 and 6. In those Chapters, the p and the d PLE peaks tend to be unchanged while the detected energies are tuned up to the higher energy. This may suggest that the QD energy levels are sensitive to the growth parameters. These QDs presented in Chapters 5 and 6 were formed within 26 seconds, with a 55-Å indium flush, and a 60 seconds annealing temperature at 500 °C on an n-doped GaAs substrate. However, here the peaks decrease with the blue-shifting of the detected energy, since the QDs in this chapter were formed within 27 seconds, within 50-Å indium flush, and a 60 seconds annealing temperature at 520 °C on an undoped GaAs substrate. The p and d signatures are relatively constant as shown in Figure 7.3 (i.e. more constant than the rising detection energy). This implies a relative invariance of these levels across the ensembles probed at the various detection energies. Such a result suggests that the ensembles detected at higher energy do not have a true round shape, and possibly include sharp corners. Conditions of diverse shapes are reasonable to expect in growth conditions at elevated temperatures or anticipate in variable strain, or compositional fluctuations.

It can be interpreted as if the QD electronic structure does not appear to be a constant relationship with the detection energy. The p- and the d-emission lines red-shift linearly with the detection energy, following $\Delta E_{p-state} = 149.98 - 86.45 E_{Det}$ and $\Delta E_{d-state} = 566.43 - 378.52 E_{Det}$, respectively. Consider for instance the detection energies of 1.2587, 1.2592 and 1.2597 eV; if the s-p inter-level (for all dots) were a constant 40 meV, the p lines would be expected at 1.2627, 1.2632 and 1.2637 eV, respectively. Similarly if the s-d difference were 90 meV, p lines at 1.3487, 1.3492 and 1.3497 eV would be anticipated. But this is not the case for sample A, meaning that the electronic structures of dot ensembles vary with the fluctuations in gallium/indium composition, strain, and dimensions (height and lateral size) from one ensemble to another.

Garcia [185] reported that a significant amount of gallium diffused into the pure InAs QDs during the growth process from all directions producing a dot with uniform gallium composition, while Fry [186] found that gallium could diffuse preferably up from the substrate into the QD. By performing the RTA, the uniformity of the gallium content was increased [33]. Williamson [183] stated that increasing the amount of gallium in the dots results in (i) a decrease the electron level spacing and increase the (s-s transition) excitonic band gap, (ii) a further reduction the electron energy, (iii) no effect on the hole energy. Therefore, the changing of the gallium composition has a large effect on the energy of the electron states and only a small effect on the hole states presumably because the unstrained valence band offset between GaAs and InAs is ~50 meV while the conduction band offset is ~1100 meV [187].

The QD gallium content (via the RTA or growth temperature) also has an effect on the dot shape as reported by Lee [188]. The TEM images showed that the lateral sizes and the density of the InAs QDs were not changed significantly up to 650 °C; but the lateral sizes increased and the dot density decreased when the QDs were annealed at 700 °C. Kim [189] and Jacobi [190] also reported changes in the size (height and lateral confinement) of SAQD. The TEM pictures clearly also show a wide selection of the lateral shapes, very few of them being perfect circles.

Williamson [183] states that decreasing the dot height or the lateral size (i) increasing the fundamental s-s gap (between electron and hole at lowest excited energy) and (ii) increasing the remaining inter level spacing. In short, reducing the dot volume increases the quantum confinement effects and the inter-level spacing without significantly the affecting wave-function shape (angular momentum nodes). But the more pronounced confinement arises from the vertical quantization of an electron and a hole: a change in height has a stronger effect on the energy levels than a change in the lateral confinement (the area at the base)[89].

7.3 Doped samples

Thus far the electronic structure of undoped sample A has been considered. The experiment was then extended to samples with a doped capping layer above the QDs. Sample B has the same QD structure as sample A, with a capping layer delta-doped with 2.5×10^{10} cm^{-2} of silicon. Figure 7.4 presents the PL spectra of an as-grown (non-annealed) sample B at three excitation powers.

With low excitation power (15 mW/cm^2), the emission from the ground and the first excited states are observed, whereas a d-line was observed in sample A. When the excitation power is increased 10 times, the emission from the s, p, d and f levels appear. No saturation for the lower states is obtained in this sample, similar to the result from sample A. The inter-level spacings for s-p, p-d and d-f emission peaks are 57 meV, 61 meV and 58 meV, respectively.

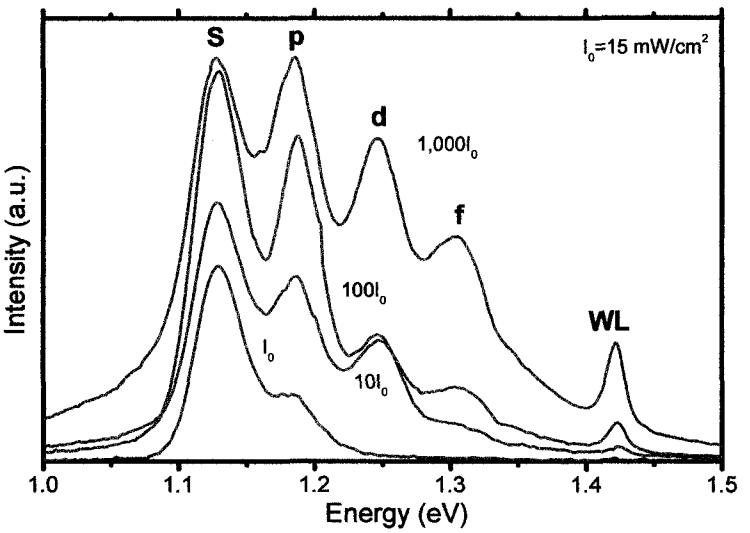

Figure 7.4: Sample B: PL spectra as a function of power with a cap doped at ~2.5×10^{10} cm^{-2}

As a preparatory step to the PLE experiments, the QD energy levels were adjusted by RTA to the range of the tunable excitation laser. Figure 7.5 shows PL spectra of sample B as a function of annealing temperature increasing in a step of 50 °C. As expected,

[89] This means that simply reducing dot height raises all of the electron levels and this change in height introduces effects at a different (higher) rate than changing lateral dimensions.

the emission lines blue-shifted and line FWHM narrowed while inter-level spacing dropped with the annealing temperature. Accordingly, sample B annealed at 850 °C was most suited to further investigations by PLE.

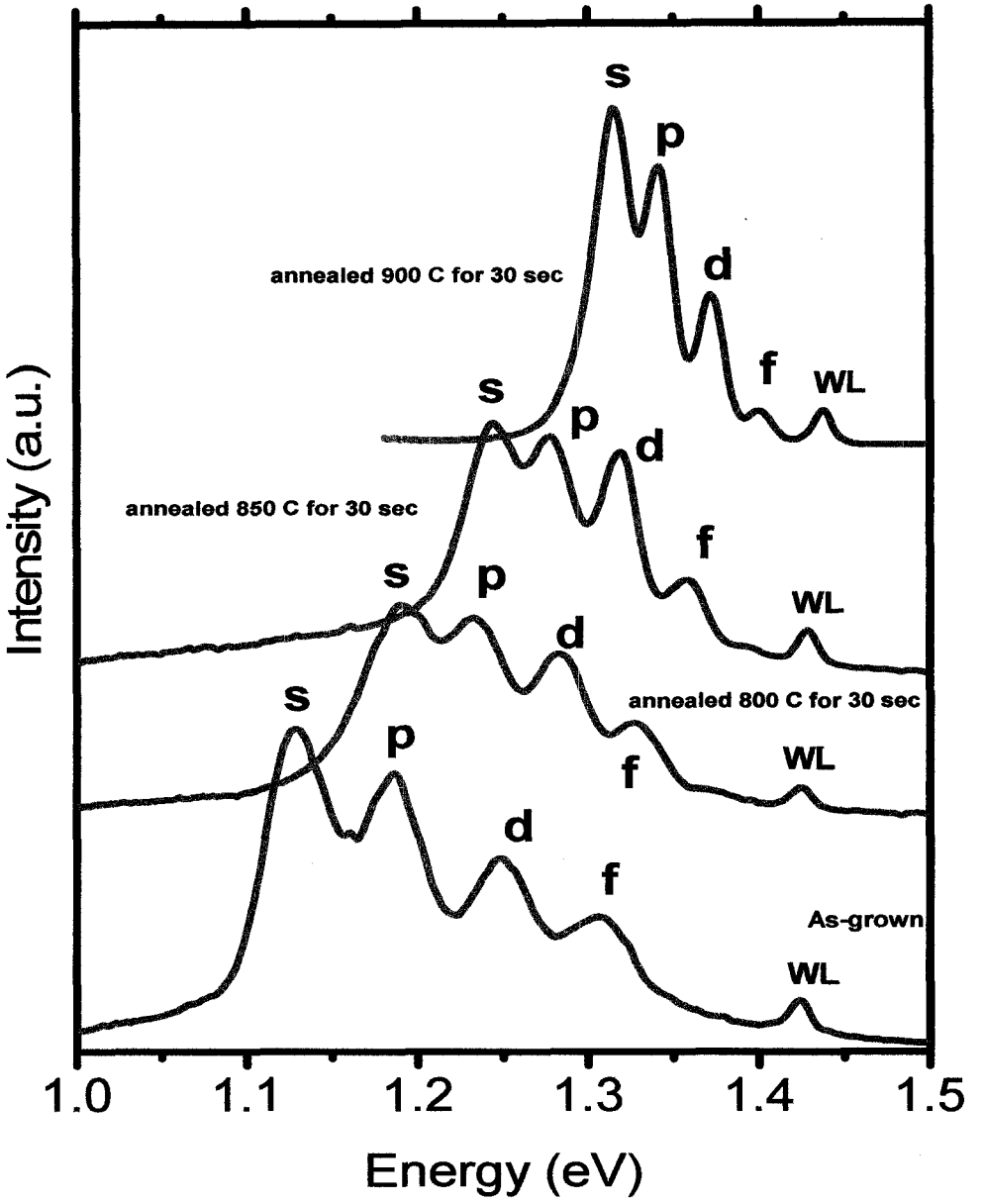

Figure 7.5: Sample B: PL spectrum as a function of the annealing temperature

Power-dependent PL was performed again after RTA, as shown in Figure 7.6. At a low power only the s and p lines appear. Higher state emissions are observed as the excitation power increases. State-filling is now evident, with p and d line intensities exceeding the s intensity, unlike the as-grown SAQD in Figure 7.4. The s-p, p-d and d-f inter-levels also changed to 29.3 meV, 41.9 meV and 38.7 meV, respectively. Thus after RTA, the inter-level spacing not only decreased but also varies in a different manner compared to the as-grown sample. The anneal process clearly changed the QD alloy composition and the dimensions affecting the carrier recombination rates from each level in the QD.

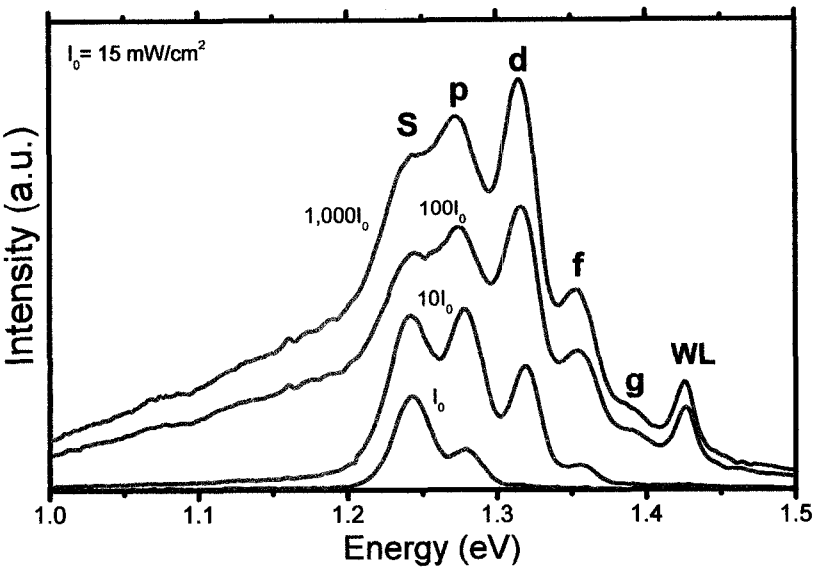

Figure 7.6: Power-dependent PL spectra for sample B annealed at 850 °C

The PLE for sample B was measured at 77 K. The ground-state detection energies were set in the PL s-line region as indicated at the bottom of Figure 7.7. The two detection energies were 1.254 and 1.2795 eV for these PLE spectra shown in dark and light lines respectively.

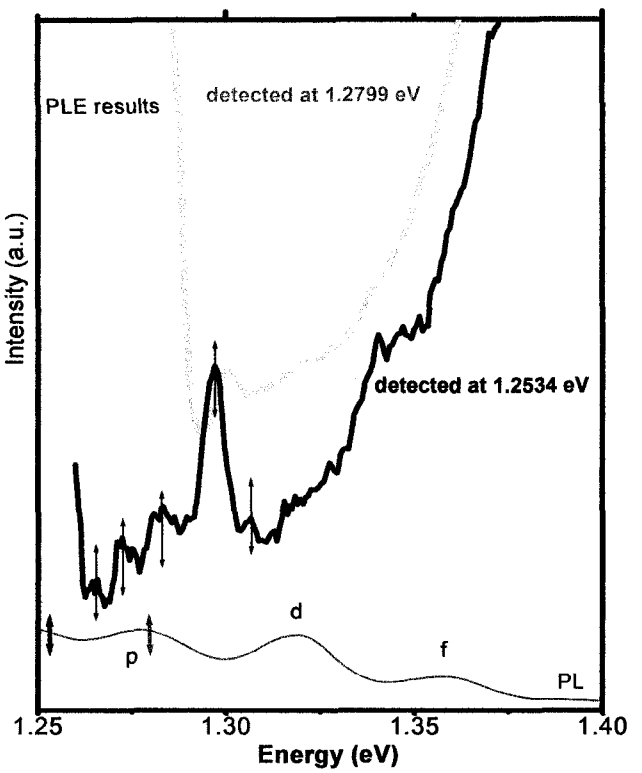

Figure7.7: Sample B: (bottom) PL; (top) PLE spectra at two GS detection energies. The uncertainty for each peak is ± 1 meV

As the excitation laser was tuned starting at ~ 8.7 meV above the GS detection energy up to the WL, no emission from the discrete energy states appeared for either detection settings. The resonant phonon lines were apparent for both PLE spectra[90]. The one at lower spectrum (dark) reveals five such peaks at 12, 19, 30, 43 and 53.5 meV respectively above the GS detection. The 19 meV emission corresponds to a GaAs LA phonon at the BZ X point [191]. The 54-meV peak may signify a combination of 30 meV phonon emission and either a multi-phonon emission with the 19 meV phonon or a combination of two 12-meV assisted phonon emissions. These estimations are based on the GaAs bulk phonon dispersions which do not exactly apply to the GaAs QDs. The 30 and 43 meV lines are possibly LO phonon-plasmon modes L^+ and L^- (at 31.1 and 46.7 meV [166, 192]). The higher GS spectrum (light) has one apparent phonon resonance at 21 meV above GS [91].

Fedorov and Baranov [192] describe that two LO phonon-plasmon modes L^+ and L^- involve the coupling between a QD electronic subsystem and a surface plasmon-phonon (SPPh) excitation of dopants in the cap/substrate layer via the electric potential produced by the excitation. Typically phonon-plasmons occur in a metal surface where a many-particle Auger-type process assists the transition from the excited to the ground states with emission of a surface plasmon. A similar energy transfer is evidently possible for QDs in the vicinity of doped semiconductor layers. This process implies the initial and final states in the QD are accompanied by absorption or emission of a low-energy surface plasmon or a SPPh excitation in the dopants, especially in the case of the direct contact between the QD and the doped region of the heterostructure.

Returning to PLE, the one hypothesis was that no PLE signatures would be observed with cap-doped QDs because the dopant atoms could diffuse into the QDs, especially when the laser source exciting on the SAQD, and the RTA process can enhance the possibility of the diffusion process. Thus dislocation-induced vacancies or substitials atoms in the QD will take up the dopants and act to trap the electron-hole pairs as bound exciton complexes (BEC)[92]. This BEC lacks a translational degree of freedom, and may accordingly be long-lived against non-radiative recombination, showing-up in luminescence and absorption spectra as extremely narrow peaks. The 1.29 eV peak detected at 1.253 eV in Figure 7.7 may be an example (which could be verified from lifetime experiments). Since the non-radiative recombination lifetime for BEC is shorter than at the QD radiative lifetime [193-194], the phonon emission tends to be enhanced, compared to the radiative recombination.

To complement this study, sample C was grown in conditions similar to samples A and B, but with 25 layers of quantum dots. The spectrum between the QD layers was ~ 30 nm [93] [195] and an indium flush was used to homogenize the QD heights. The final capping layer was delta-doped with silicon at a level of $4x10^{11}$ cm^{-2}. The sample's spectra were first measured with PL. At the bottom of the Figure 7.8, the PL spectra of the original sample C (as-grown wafer) are shown as a function of the excitation power. At very low excitation power, only s emission was detected, but as power increased the usual p, d, and f lines are observed.

---

[90] These would be proven phonons only if a magneric field had no effect on them.

[91] Which might still be the LA X phonon within experimental error: 19+1 overlaps 21-1.

[92] This BEC acts approximately like Frenkel excitons.

[93] The effect of coupling between two neighbor layers is expected to be very low, since the coupling distance between two vertical QDs is ~4 meV for 8-nm a spacing [35].

Sample C was cleaved into 5mm X 5mm pieces individually annealed for 30 seconds at 800, 850, 875 or 900 °C, with the corresponding PL spectra shown in Figure 7.8. A whole set as a function of the excitation power for sample RTA at 875 °C is included. Higher emission lines arose again as the excitation power increased. The inter-level energy separation was ~41 meV for the as-grown sample. As observed formerly, the FWHM and the inter-line spacing reduced at higher anneal temperature and the emission from each QD s-level blue-shifted by 13.5, 27, 30.5 and 73 meV respectively for the RTA800, RTA850, RTA875 and RTA900 samples.

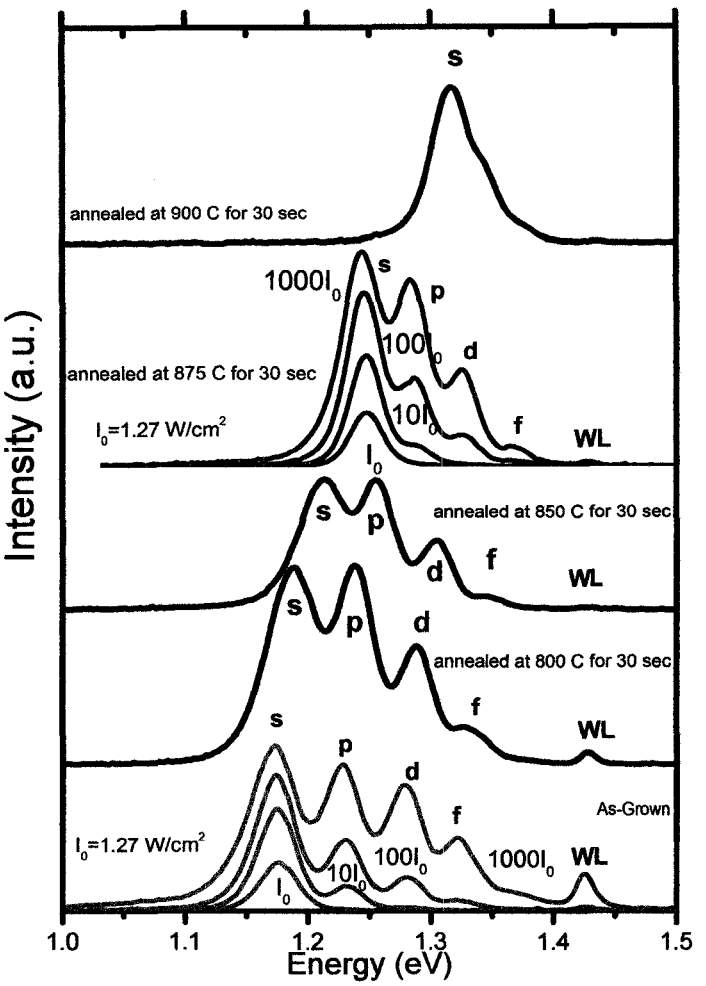

Figure 7.8: Sample C: PL spectra at different anneal temperatures

Sample C annealed at 875 °C was selected for the PLE experiments because its QD emission was in the available range tunable laser. The detection energy was set between ~1.211 eV and ~1.325 eV as shown with the arrow in the inset of Figure 7.9. The sample was doped in the capping layer atop the 25 QD-layer heterostructure. After the RTA, some of the dopant can diffuse into the QD layers beneath. It is expected that both the diffused dopant concentration and the SPPh coupling effects decrease with the distance from a cap layer. From Fick's law, the diffusion distance in time t is $\Delta = \sqrt{Dt}$, where D is the diffusion coefficient.

Dutt and Sharma [196] present the diffusion coefficient in the Arrhenius form: $D = D_0 \exp(\frac{-Q}{kT})$, with D_0 is an aerial velocity pre-factor and Q is the activation energy for the diffusion. The activation energy for silicon in GaAs material [197] is 8.617×10^{-5} eV/K and the pre-factor of aerial velocity 0.11 cm^2/sec, yielding 6.629×10^{-13} cm^2/sec for the diffusion coefficient[94] when temperature is 850 °C. Thus the diffusion distance after annealing for 30 seconds is 44 nm. This means diffused silicon can penetrate ~ 2 layers of SAQD while the excitation source can penetrate through 50 layers of QD, as shown by calculations using step-wise Beer's law. Therefore, the QD emission is to be expected from layers more than 50 nm from the cap.

The solid star and the sphere symbols in the following figure indicate the observed peak positions for the p and d states. To track these peaks, the relative peak energy (above the detection) is plotted in Figure 7.10.

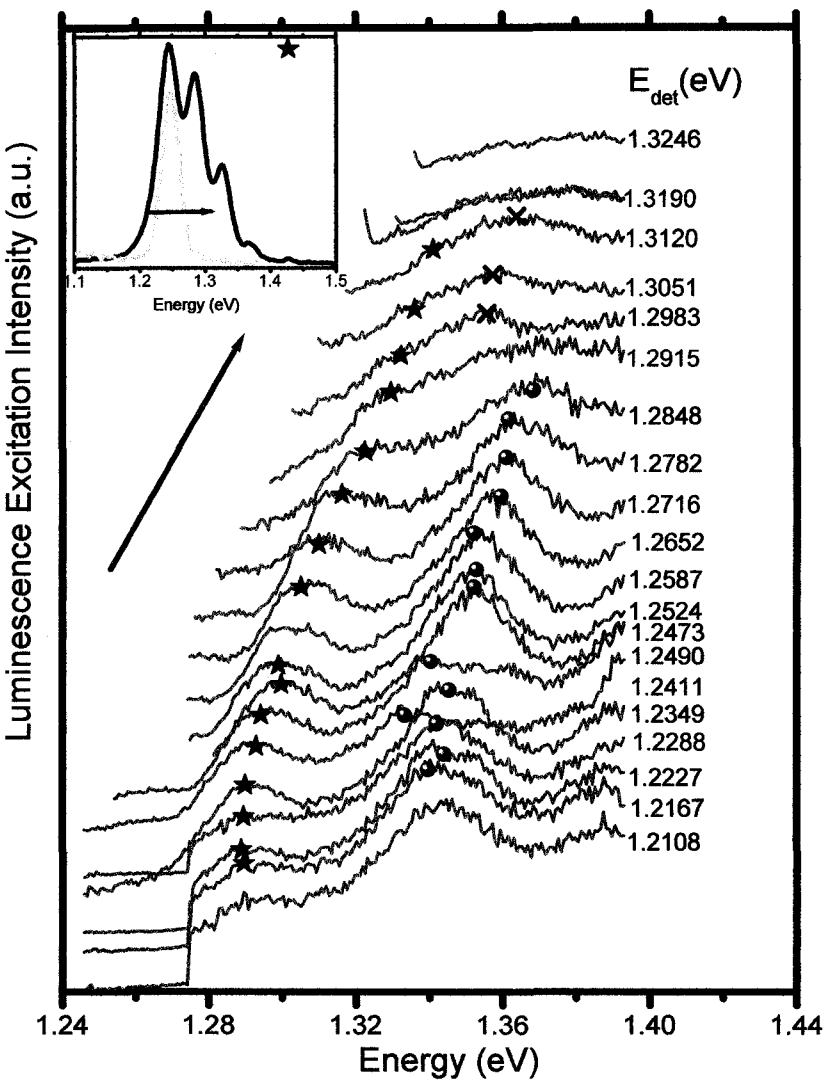

Figure 7.9: PLE spectra as a function of the detection energy: sample C annealed at 875 °C

[94] Using k, Boltzmann constant: 8.617×10^{-5} eV/K.

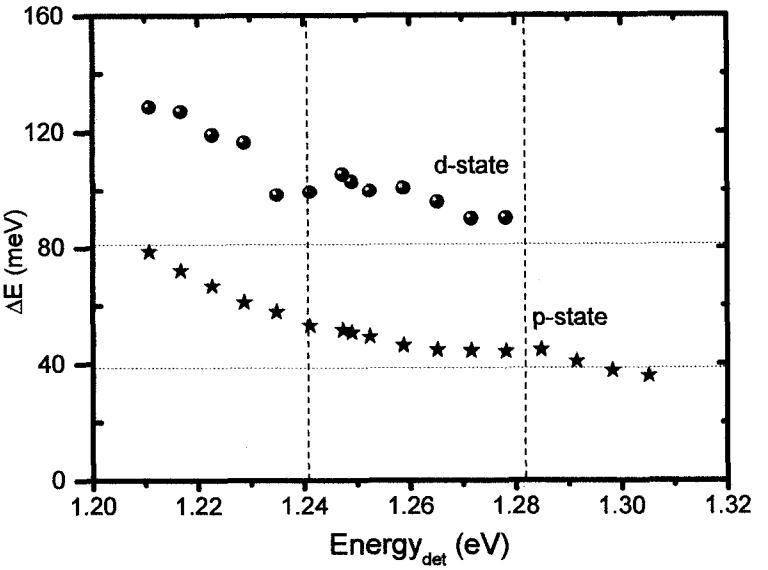

Figure 7.10: Measured relative peak positions from Fig. 7.9 vs detection energy

The abscissa may be partitioned into three regions. The first part defines the detection energies less than the lowest line (E_{det} <1.245 eV), the second in the s-p range (1.245 eV < E_{det} < 1.285 eV) and the third up to the d-line (1.285 eV < E_{det} < 1.326 eV). These partitions in energy are relative to the PL spectrum. In the first region, the PLE p and d lines strongly red-shift relative to the detection energy. This region represents an activated ensemble of QDs excited only in the GS region as it is unlikely to detect the excited states at the lower energy in this condition.

The second region represents the PLE emission detected from the nearby ground state of certain dots and some thermalized first-excited states from others. Here the p and d levels behave differently from the first region. The shift begins to decrease relative to the first region.

In the third region (detection beyond 1.285 eV), it is probable that these detection energies are not for excitation in the ground state energies of any QD. In this region only emission originating from p-level excitation is actually observed. As noted in Chapters 5 and 6, the PLE absorption lines tended to blue-shift, compared to PL peak. Thus d-line from smaller dots may have moved out of the discrete states into the WL continuum, causing d absorption peaks to vanish. Another explanation is that a direct recombination from the p-level suddenly dominates over the decay channels, leading to emission at the detection energy. This level remains mostly invariant across the dot ensembles detected

7.4 Conclusions

The spectra from the InAs/GaAs SAQD samples for both the un-doped (sample A) and the doped capping layer (sample B and C) reveal a broadened line width for the as-grown wafer because of inhomogeneities in the size of the QDs and the variation of composition The RTA reduced this broadening effect and shifted the PL peak positions, usefully to match the available tuning range of our PLE laser. Note that intermixing effects mainly occur in the vertical direction.

Sample A with no doping revealed the typical electronic structure of the discrete energy states in the QD, although the excited states are not always correlated to the ground state directly. In the PL experiment, the saturation of the lower state or the state filling was not observed even though the excitation power was high. This might be associated with the shorter lifetime (higher recombination rate) at the lower state although a widening of the line (as this hypothesis would suggest) was not clearly seen.

In PLE, two resonant phonons were observed in this sample at ~8 meV and ~18 meV, which respectively can correspond to phonons at the L point and X point of the BZ for bulk GaAs. The excited levels (p- and d-lines) separation tend to decrease with respect to the detection energy (GS level), especially the d-line with a characteristic difference from that studied in Chapters 5 and 6. The distinction may ensue from the dopants, and/or may implicate energy levels of various dot ensembles varying differently according to the shape, alloy composition, deposition temperature, or strain.

For sample B - a single layer of QDs with a doped capping layer - no resonant emission was observed in the PLE experiment. It is argued that this results from dopant atoms diffusing down in the QDs especially in the RTA process. The non-radiative channels (the phonon emission or the Auger scattering process) are then more probable, being enhanced by SPPh interactions and/or bound exciton complexes. In PL, the inter-level spacing between emission lines was a constant ~58 meV before RTA, which changed to an s-p, p-d and d-f spacing of 29, 42 and 39 meV respectively.

Sample C was grown in similar conditions to sample B, but with 25 layers of QDs and with adoped cap layer. After annealing at 875 °C, some excited-state PLE emission from QDs well beneath the capping layer was observed. As above, the dopant could diffuse down into the QD layers and the barriers beneath the capping layer. But the dopant density and a coupling decrease with a distance from the capping layer. The diffusion length of the silicon is ~44 nm. This means the silicon dopants will penetrate only a few QD layers at the top of the stack.

Chapter 8

Electrons in Doped InAs/GaAs QD Multiple Layers

As the carrier freedom is reduced to about 10 nm in all dimension, the SAQD inter-level spacing is in meV range. This is on the order of the phonon energies. Therefore, a control of the electron-phonon relaxation is desired to study the elastic or the 'on-level' processes such as the radiative transitions and the recombinations. Inelastic scattering channels arise including scatter mechanisms such as the multi-phonon relaxation [158, 197], the Auger scattering, the defect scattering [198-199] and the excited state absorption[95] [200-201]. Control of such relaxation in addition to the electronic structure of SAQDs can contribute to device improvements.

The carrier relaxation and electronic structure for SAQDs are commonly examined via PL, PLE and absorption techniques. PLE is the technique reported in this chapter, to further investigate the influence of the dopant dose. Many potential devices such as the single-electron transistors [202], the logic elements or the quantum bits [203], the memory cells [204], the infrared detectors and the quantum dot lasers are affected by doping. Since the carrier relaxation mechanisms are related to QD energy levels, the influence of the dot size (density of dots) at different doping levels is investigated.

8.1 Description of Samples and Optical Experiments

Seven InAs SAQD samples were MBE-grown using the S-K growth mode on GaAs substrates using Si δ-doping[96] at $1x10^{10}cm^{-3}$. Each sample comprised 50 layers separated by 30-nm GaAs[97] barriers δ-doped with the set doses as listed in Table 8.1, and capped with 100nm of GaAs. The estimated QD density from the structural observations (atomic force microscopy and plan-view TEM) and the average density of doping (in electrons per dots) surrounding a dot are included in this Table.

Table 8.1: The list of samples used to study the influence of the number of electrons per SAQDs

Sample	QD density (cm^{-2})	Doping doses (cm^{-2})[98]	Number of electrons per dot
2174	$0.5x10^{10}$	$1.0x10^{10}$	2
2505	$0.3x10^{10}$	$1.5x10^{10}$	5
2203	$0.5x10^{10}$	$3.5x10^{10}$	7
2504	$0.3x10^{10}$	$2.0x10^{10}$	7
2200	$0.5x10^{10}$	$6.0x10^{10}$	12
2506	$0.3x10^{10}$	$3.5x10^{10}$	12
2206	$0.5x10^{10}$	$11.0x10^{10}$	22

[95] By contrast in PLE, understood as excited-state absorption but detected only at a GS level, phonon relaxation is necessary. (cf. section 5.3)

[96] δ-doping means the introduction of a two-dimensional sheet of doping atoms during epitaxial growth. The concentration in the growth direction then has an almost δ-function-like profile.

[97] With a 30-nm GaAs barrier, the interaction between dots might exist, but is very weak [cf. Hinzer [206]]

[98] This is a combination of the background level from the GaAs substrate and the doping level in the GaAs barriers.

The samples comprised two series: at dot density $0.3x10^{10}$ cm^{-2} labeled 25xx, and $0.5x10^{10}$ cm^{-2} otherwise. The average diameter and height of the SAQDs was approximately 25 nm and 3-3.5 nm [92], respectively. The density and the size of the dots (height and lateral confinement) can be optically monitored and tailored through the growth parameters. For instance, Fafard *et al* [144] found that the layer thickness was associated with a reduction in the amplitude of the WL PL peaks and an increase in other QD peaks. They also reported greater inter-level spacings but a reduced PL peak resolution when the dot density was increased [205-206].

Reference [144] reported the deposition temperature as one mean of adjusting the optical inter-level spacing: raising the substrate temperature reduced the spacing and blue-shifted the emission or the absorption lines, not necessarily just a dimension effect. The amount of deposited InAs required to achieve well-defined electronic levels varied for different substrate temperatures: higher indium desorption rates and the kinetic suppression of the island formation occurred at a lower temperature. The peak positions are also affected by lateral strain fields within the QDs. About 1.6 ML of InAs promotes the spontaneous islands in the S-K growth mode, and increased InAs nucleation density favors the incorporation of relatively higher Ga concentration in the capping procedure, similar to raised deposition temperature.

After growth, the QD wafers were diced into 5mm X 5mm squares. Each square on a sample holder was inserted into a chamber cooled to 77 K. Samples were optically examined with the same experimental setup mentioned in Chapter 7.

8.2 Results and Discussion

Figure 8.1 presents non-resonant (black) and resonant (dark gray) PL spectra for the samples listed in table 8.1. From the lightly doped QD sample (2174), well-resolved luminescence peaks are observed at 1.199, 1.276, 1.325 and 1.373 eV respectively for s, p, d and f lines. The WL line is seen at 1.425 eV. Next, from the 22xx series s, p and d-lines occur at respectively 1.158, 1.216 and 1.296 eV with inter-level spacings s-p and p-d of 58 meV and 80 meV. Finally, from the 25xx series s, p and d lines appear at ~1.156 eV, ~1.229 eV and ~1.304 eV with a constant ~73 meV inter-level spacing. The s-p inter-level spacing of the 25xx series is wider than the 22xx series because the former is less dense with shorter height and greater lateral extent. The size of the dots is dependent on the growth temperature. Fafard [144] concluded that the higher temperatures produce larger dots (lower density) with a reduced inter-level spacing. This is due to the strain field caused by the lattice mismatch. Williamson [183] shown that reducing the dot height increases the quantum confinement and the inter-level spacings including the fundamental (GS) gap.

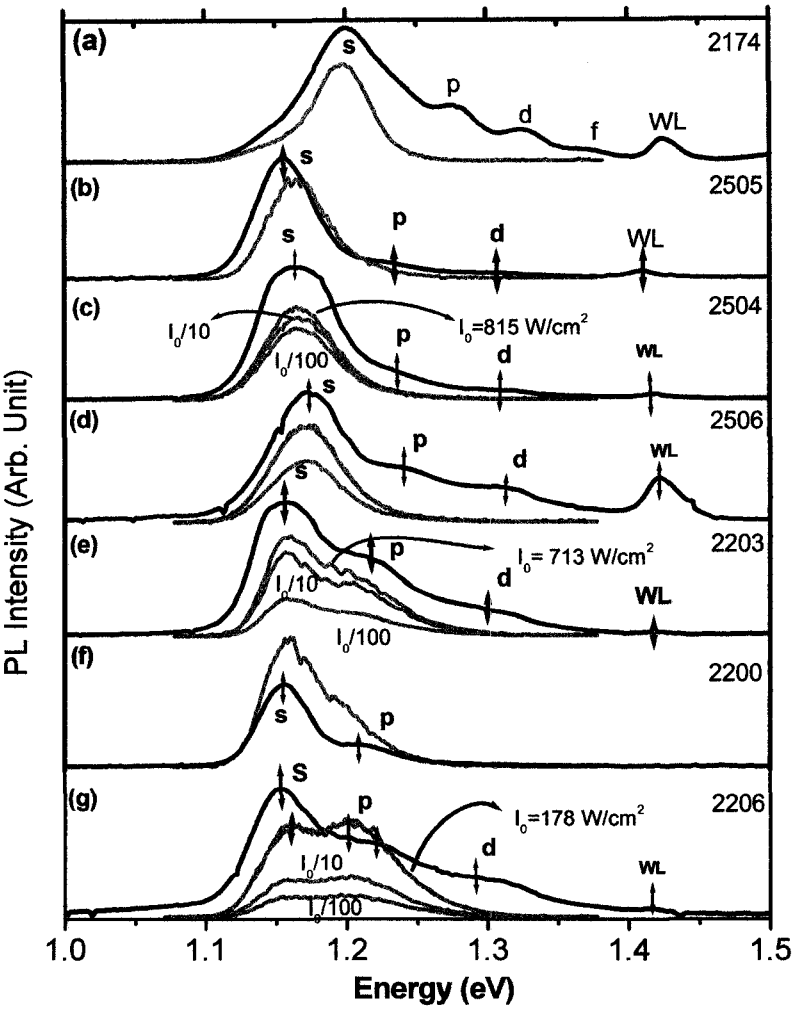

Figure 8.1: Non-resonant PL (black) and the resonant PL (gray lines) spectra excited with 2.3305-eV and 1.3931-eV laser lines, respectively

As described at the outset, SAQDs naturally form from the lattice mismatch between two semiconductors, but with size inhomogeneity their electronic structures vary. It is even more challenging to interpret the electronic structure with extra doping surrounding each dot[99]. Sample 2174, with two extra electrons injected in each dot[100], was studied in PLE. Some excitation photons promote valence electrons to a selected conduction level, and the created holes may thermalize (decay) to the ground-state energy via a phonon scattering and then recombine radiatively with the ground-state electrons (a phonon-assisted emission). This process is depicted in Figure 8.2.

[99] Silicon dopants has very little chance to diffuse into the QD since the diffusion coefficient of silicon at room temperature is negligible ($\sim 10^{-14}$ nm).

[100] These extra two electrons are from the δ-doping in the barrier layer or silicon defects which act as a donor. A donor is a shallow center which has an energy level just below the conduction band and can easily inject an electron by thermal ionization. Dopant ions are not electrically active but may still act as scattering or recombination centers (interstitials or substitutional ions).

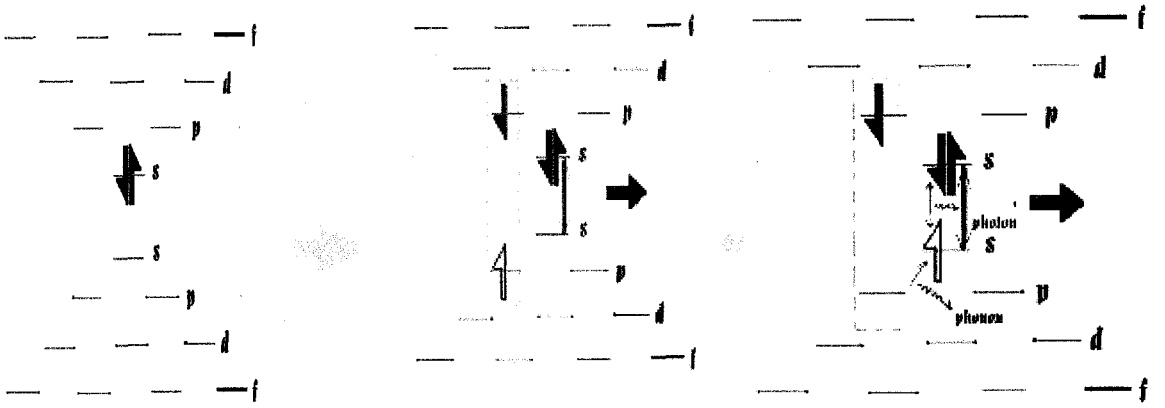

Figure 8.2: The energy level structure of sample 2174 showing a recombination process

Another possibility is that created electron-hole pairs simply recombine at the higher energy and emit a photon undetected in PLE. The Auger effect can also be involved: the energy released by a recombining electron is immediately absorbed by another electron which is then dissipated by emitting phonons.

Schmidt [207] *et al* claimed that the carrier relaxation process in a SAQD ensemble required the difference between QD levels to be an exact multiple of the available phonon energies, assuming that (i) the SAQD lack energy dispersion but instead have well-defined levels in k-space and (ii) the electrons and holes were localized in real space with strong Coulomb interaction making the electron and hole dependent of each other. In these conditions, the excitonic relaxation can be the dominant thermalization process: multiple phonon-assisted emissions may occur in small dots, but not in the larger ones because of the probable mismatch with available phonon energies. Therefore, the recombination processes associated with the confinement depend on dot size.

Figure 8.3 shows the PLE spectra for sample 2174 with detection energies selected in the range 1.179 eV to 1.324 eV. As the selected energy may lie between level s of one dot and p of another, the spectra revealed phonon-assisted p and s signatures.

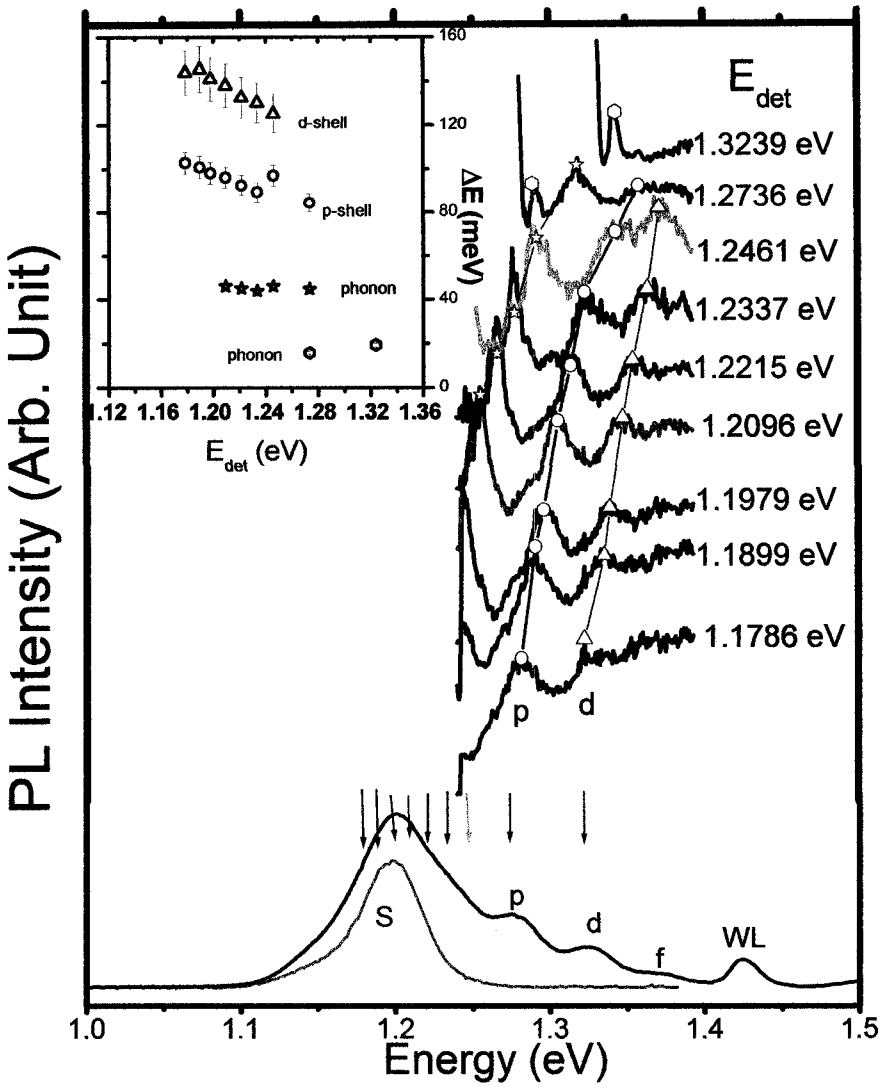

Figure 8.3: PLE spectra for Sample 2174 as a function of the detection energy

All the absorption peaks were tracked in the inset of Figure 8.3 plotting relative peak energies as a function of detection baselines. The open circles and the triangles trace p and d lines respectively, whose energies evidently decrease linearly with the detected energy, implying they are independent from the selected detection energy. Open stars and hexagons trace phonon-assisted emissions at ~46.6 meV and ~15 meV above the detection energy, respectively.

The 46.6-meV phonon close to the s-p transition energy can assist the excited electron-hole pairs produced in the p-level to jump down to the ground-state level and eventually recombine. Also this phonon energy corresponds to Raman scattering by coupled LO phonon-plasmon modes L^+ [166, 192]. Another possibility suggested by Feldmann *et al* [208] is that LA phonons make up the difference between LO phonons and the energy lost during relaxation, if so, there may be a combination of a bulk GaAs phonon (36.5 eV) and a 9-

meV LA phonon at the Γ point [209][101]. The 15-meV phonon may be the LA at the L point in the InAs bulk semiconductor [158].

Thus far, PLE is shown to be a more sensitive tool than PL to verify the quality of QD sample for building QD opto-electronic devices. Since the phonons offer decay channels competing with the direct recombination, a reduced sources of phonons (at a given temperature) should signify better quality of the QD opto-electronic devices.

PLE was also performed on sample 2505. It had an average of five doping electrons per dot, partly occupying the p level as illustrated in Figure 8.4. When the laser excites the sample, an e-h pair can be created in the first (p) excited level. The valence hole may decay and recombine with an electron in the lower state emitting a GS photon.

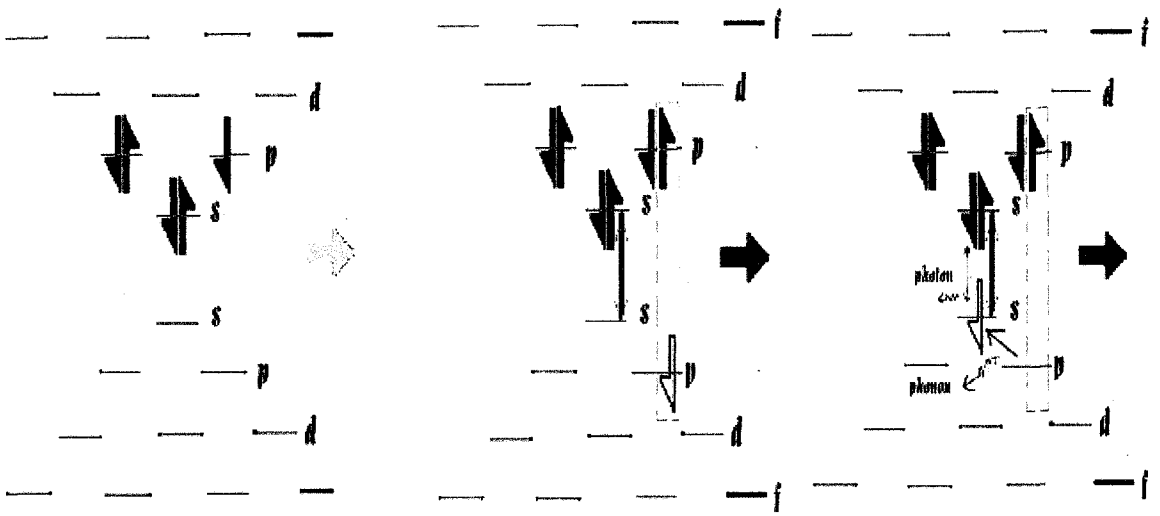

Figure 8.4: Electronic structure of sample 2505 along with proposed recombination process

Figure 8.5 presents PLE spectra for this sample with the detection energy selected from 1.1642 to 1.2461 eV. The excitation energy was tuned ~8 meV from the ground-state energy up to the WL. The excited p, d and f absorption peaks at respectively ~ 80, 160 and 230 meV above the ground-state detection energy are seen in the inset. Note that the level spacing for this sample is ~ 75 meV which is consistent with that observed in PL.

[101] The phonon dispersion relations in QDs still need to be studied because strain and acoustic boundaries have an effect. Thus LO, TO, LA and TA for QD should be expected to differ from bulk dispersion.

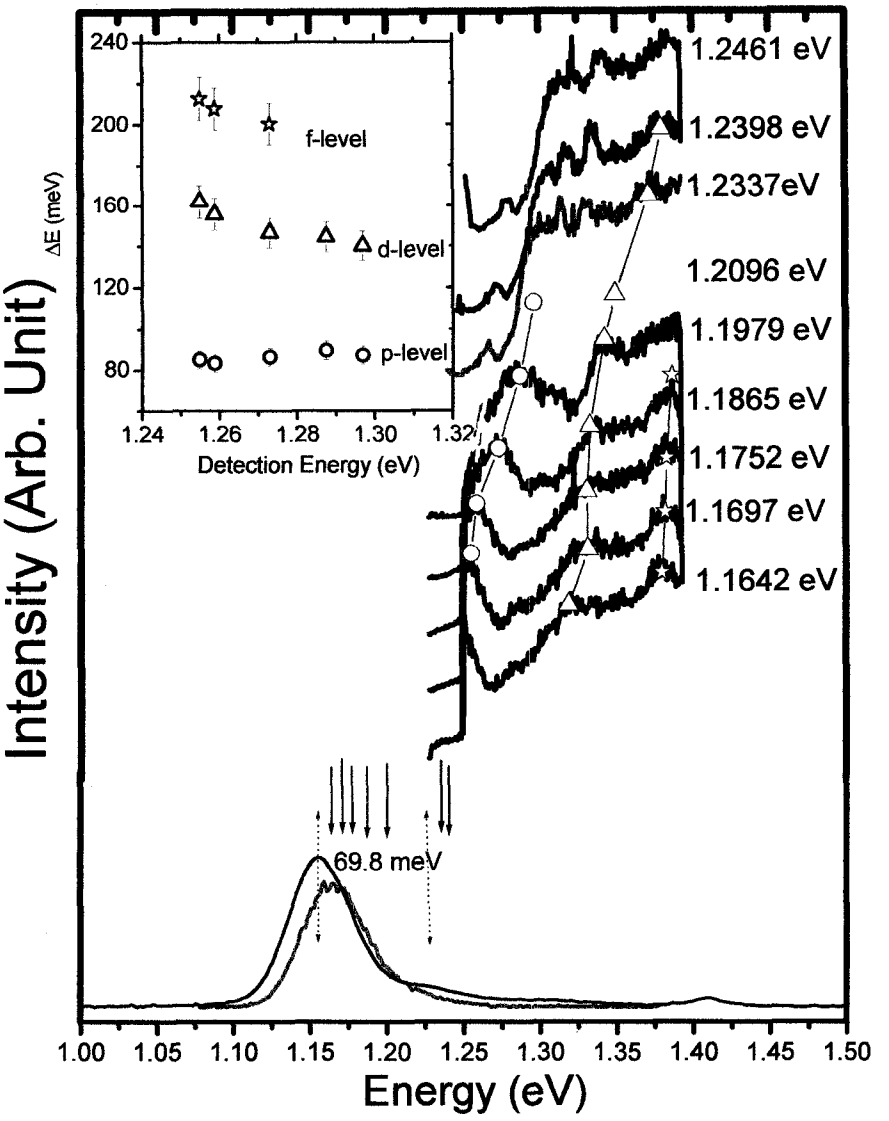

Figure 8.5: PLE spectra as a function of the detected energy for sample 2505

The PLE detects emissions only at the selected ground-state energy level. It is complicated to interpret the PLE spectra when the selected ground state matches (within a phonon) the s level of one dot and the p-level of another one, as it does in the 1.186 to 1.210 eV range. For the PLE detected in this range, clear signatures from d and f absorption levels are not expected because the detected energy are close to the continuum energy or WL energy. Quite a few phonon-assisted signatures appear at this detected energy and these phonon energies matching with the energy level spacing.

Sample 2203, with seven extra electrons per dot, was examined next. These injected electrons first occupy the lowest states in the QD as shown on the left of Figure 8.6. Electron-hole pairs are created in the QD as the excitation energy tunes away from the ground-state detection wavelength. When an ensemble's p-level is reached, the electron-hole pairs are not expected to be produced because the doping electrons completely fill this level. But pairs will be created when the excitation reaches the d-level of some QDs, as illustrated in the middle

panel. These excitons may recombine at this level and emit undetected photons; but other possibilities include ground-state emission after multi-level phonon-assisted hole decay as well as the Auger electron scattering[102].

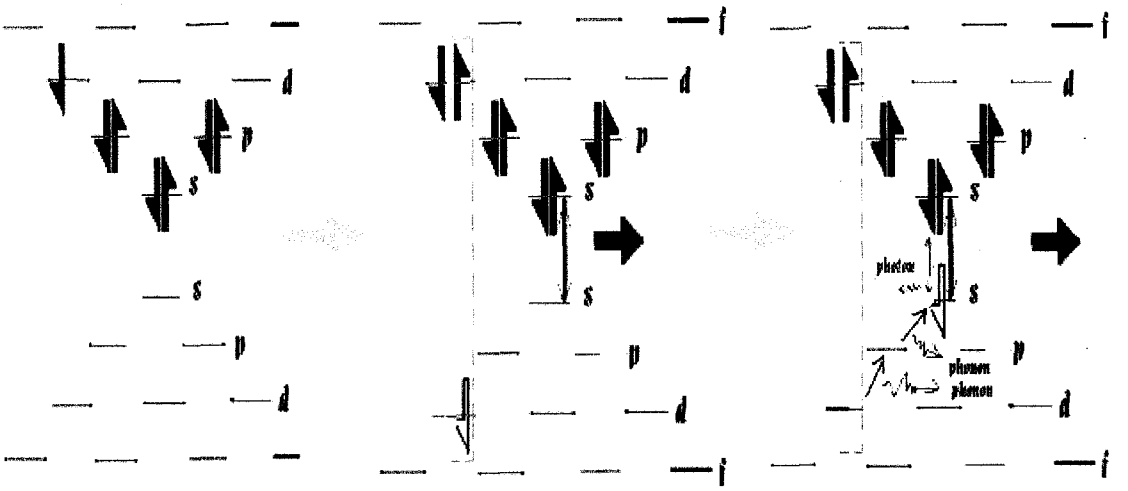

Figure 8.6: The electronic structure and proposed recombination process for samples 2203 and 2504.

Figure 8.7 presents the PLE spectra for various ground-state detection settings. The technique again selects dot ensembles at varying ground-state energies because of the inhomogeneities in height and diameter.

[102] cf. section 2.6 note that extra electrons from the doping make the Auger process feasible.

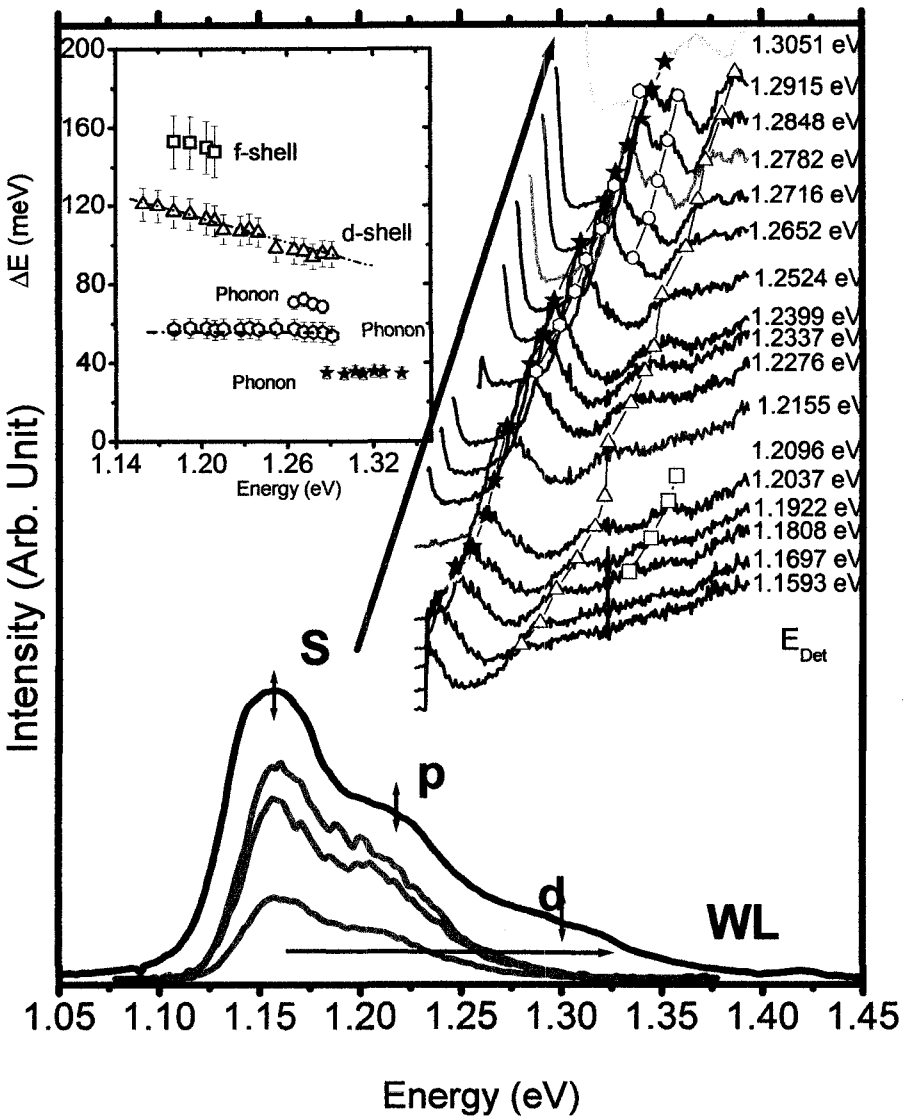

Figure 8.7: PLE spectra as a function of detected energy for sample 2203

The inset, as in the prior two cases, reveals three resonant phonon lines and two absorption peaks at the d and f levels. In this sample, many phonon-assisted emission channels are expected because electron-hole pairs are created only when the excitation energy is resonant with the d-level. One peak at 36.5 meV (solid stars) is associated to a bulk LO phonon at the BZ centre [76]. The ~60.5 meV (open hexagons) line may be phonon-assisted emission corresponding to an intermediate level between s and p states, involving multiple phonons [210]. For instance, Inoshita [211] states that longitudinal phonon emission via the Frohlich interaction is the dominant relaxation mechanism when the level separation equals to the LO phonon energy, as it does here (it equals the s-p transition energy). Accepting Inoshita's description means two phonons are playing a role in the recombination process: a LO phonon of the InAs WL (29.5 meV) and another bulk InAs phonon (31.9 meV) [212]. Finally, the last resonant phonon line occurs at ~73 meV (opened circles) and may result from two LO phonons of bulk GaAs at the zone center.

Two PLE signatures from the d- (triangle) and f- (square) levels tend to decrease with increasing detection energies. With the detection of less than 1.20 eV, peaks are likely to arise from the ground-state QD energy level. Spectra at a higher detection energy (> 1.20 eV) are more complex, where detection might be within a low-energy phonon of one dot's ground state but of another's first or second excited state. With higher detection energy, the picture simplifies to d and f signatures predominantly arising from d and f levels (followed by decay and recombination).

Sample 2504 might be thought to behave similar to sample 2203, as both have on average seven injected electrons per dot, but 2504 has a lower density with slightly bigger dots and a reduced inter-level spacing. Figure 8.8 presents PLE spectra for the latter sample at various detection energies. The PLE spectra are plotted here by varying the detection energies from the QD ground-state energy levels upto the second excited levels. The bottom plot of the Figure is the PL spectrum excited with 514.5-nm. The inset represents the difference between the detected PLE peak and the excitation energy as a functon of the latter.

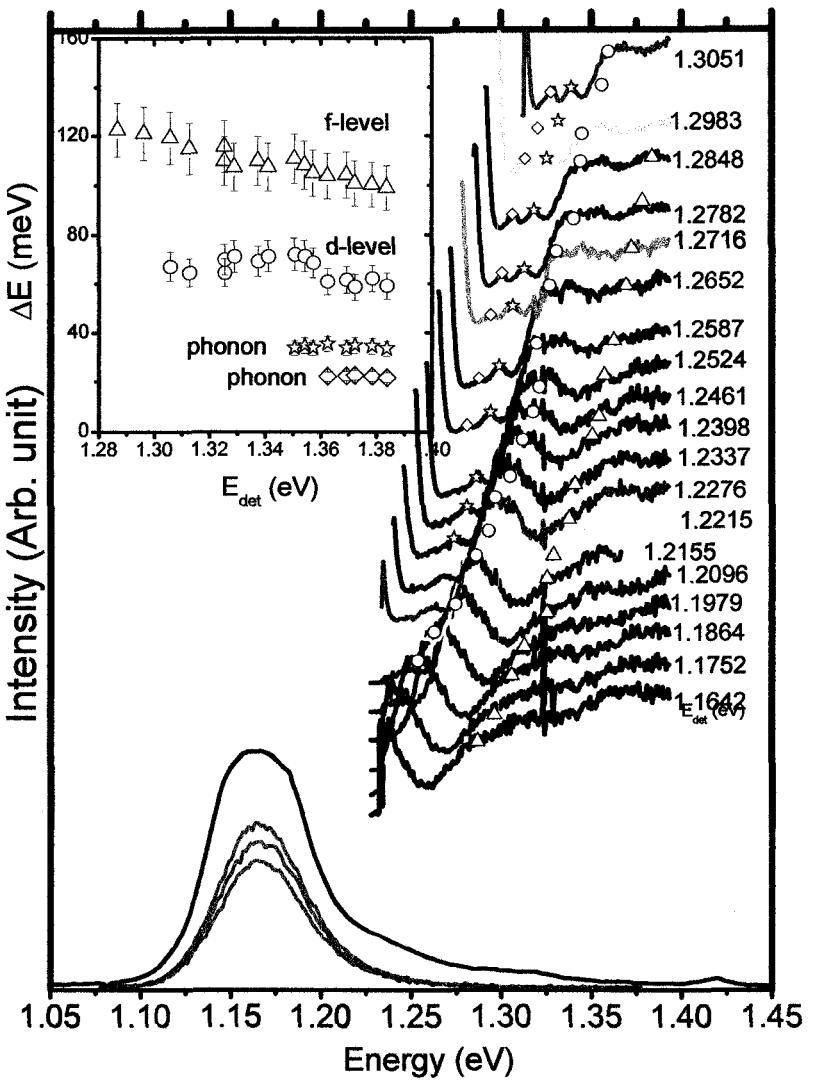

Figure 8.8: PLE spectrum for sample 2504

Again the inset is plotted as before, with two resonant phonon signatures at 22.5 meV (open diamonds) and 36.6 meV (open stars). The assisted-phonon emission at 22.5 meV may be coupling to LA phonons of InAs bulk at the X point [76]. The 36.5 meV corresponds to LO phonons of bulk GaAs at Γ point [76]. The open circles and the triangles are tracing respectively the d and f absorption peaks. They are red-shifted at about the same rate with the increase in the detection energy. This shift is however slower than the one in sample 2203, which has the same number of electrons from the doping.

This emphasizes that the revealed structure of the SAQD energy levels are sensitive to the PLE probing method. For example, samples 2203 and 2504 have the same number of injected electrons but with different QD densities. The PLE results show that the d and f peaks from the two samples behave differently.

As anticipated, if the number of extra electrons is further increased (filling up the d-level), only the f-level peaks are expected. Sample 2200 with 12 extra electrons per dot is a candidate to verify this assumption. As the excitation energy reaches the f-level, e-h pairs are produced, where the holes may thermalize by multi-level phonon emissions and eventually recombine with the ground-state electrons. This process is shown in Figure 8.9.

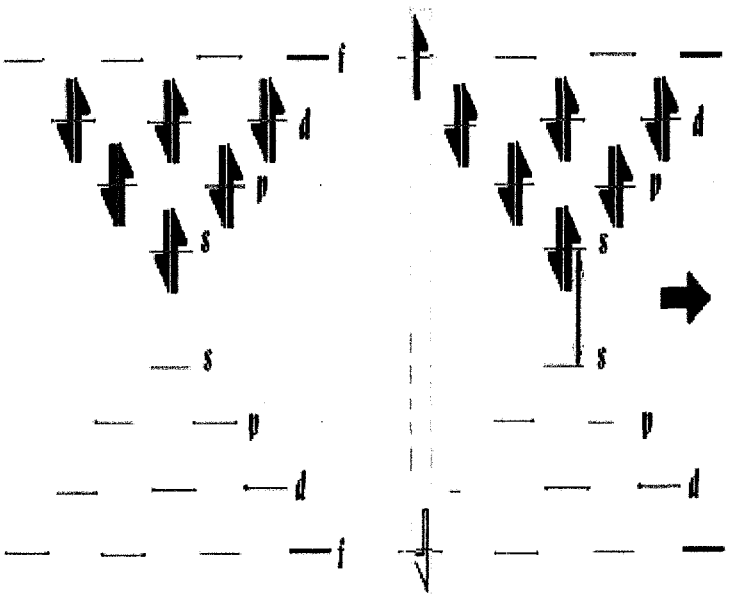

Figure 8.9: Electronic structure of sample 2200 with 12 extra electrons

In this figure, the left panel shows the energy structure of sample 2200 with 12 extra electrons populating the QD levels. The right panel depicts an electron-hole pair created by the excitation source and the subsequent emission after a hole 'thermalizes' to the ground-state level.

Figure 8.10 presents the PLE results of sample 2200. When the detection is set near the (PL) p peak, only an f-line is observed. As the detection wavelength enter the region of the excited states (i.e. d-level), some assisted phonon emission at ~52.6 meV above the detection energy is also observed. As the detection energy shifts to the blue toward the p peak, the f-line at about 120 meV above slowly decreases (see inset).

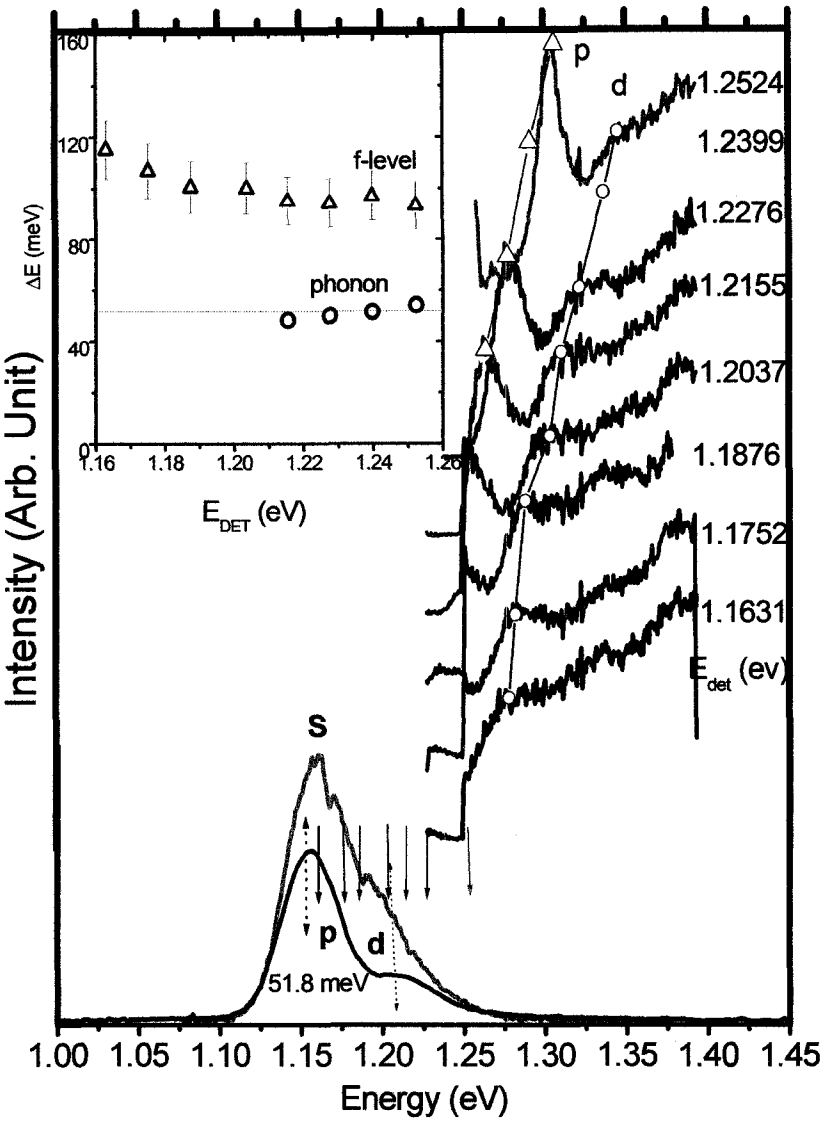

Figure 8.10: PLE spectra of sample 2200; bottom shows the PL with the selected ground-state energy indicated with arrows

Figure 8.11 presents the PLE results for sample 2506 with also 12 extra electrons per dot, but with a lower density than sample 2200. Here the f-lines (open stars in the inset, ~115 meV above the detection energy) are observed similar to sample 2200, but without significant changes with a change in the detection wavelength.

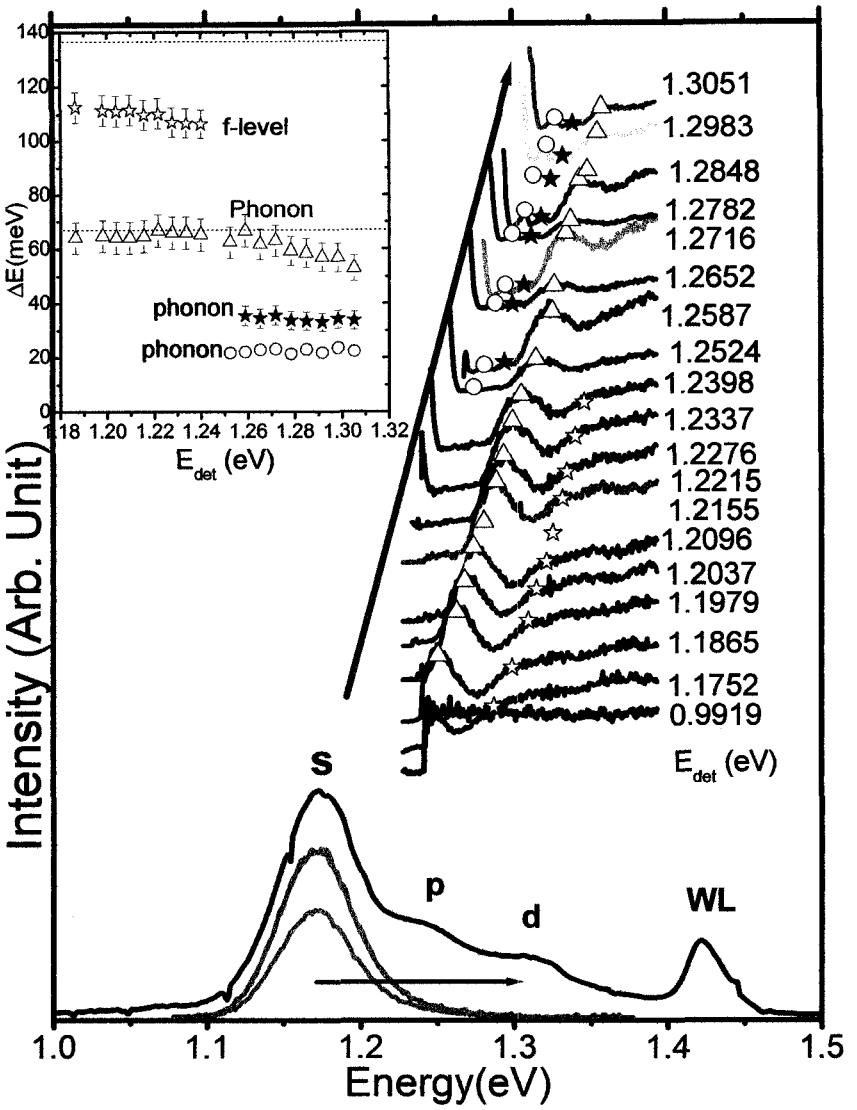

Figure 8.11: PLE spectra for sample 2506 with 12 extra electrons from doping

Three phonon-assisted emissions are observed with 67.1 meV (open triangles), 35 meV (closed stars) and 22.28 meV (opened circles) above the detection energy. The 67.1 meV phonon emission is consistent with the inter-level spacing for s-p and p-d. This suggests that phonons assist the electron or hole to recombine at the selective ground-state wavelength. Two others (35 meV and 22.28 meV) appear when the detection energy is set closer to WL energy. The former is a GaAs-InAs interface phonon [213-217]

As noted above, the PLE measurement – an absorption technique -- is sensitive to the electronic structure of the SAQD. The ensemble variations of the energy due to the height and the diameter for different dot density are observed in samples 2203 and 2504. For large numbers of doping electrons in the QD in samples with different dot densities (i.e. samples 2200 and 2506), the results differ noticeably. The energy level spacings for lower dot density (sample 2506) tend to match phonon energies, revealing many phonon-assisted emissions.

Thus, PLE may be used as a probing tool in the preparation of QD samples for opto-electronic devices.

For QDs with 22 extra electrons per dot, no absorption peaks are observed in PLE. Figure 8.12 shows the available conduction levels filled up to the f level and the electron-hole pairs can only be created in a g level if it exists; otherwise they are promoted to the WL. While the electrons in the lower level recombine with available hole, a higher state electron may release some energies (e.g. by Auger or phonon processes) to a second electron in the same level and the decay to a lower state. The second electron has a high chance to recombine with hole from the WL through additional Auger scattering [218 - 219].

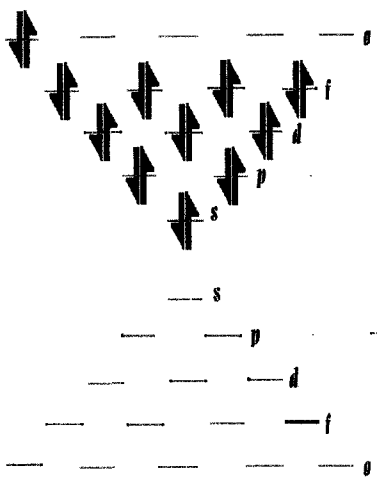

Figure 8.12: Schematic of the electronic energy structure of sample 2206 with extra 22 electrons per dot

Figure 8.13 presents the PLE results for sample 2206 as in the prior figures. Two peaks are dominant, at 52 meV and 104 meV above the detection energy, again suggesting phonons assisting the electron-hole pairs in order to recombine at the detection energy. Note that the s-p inter-level spacing for this sample is ~54 meV.

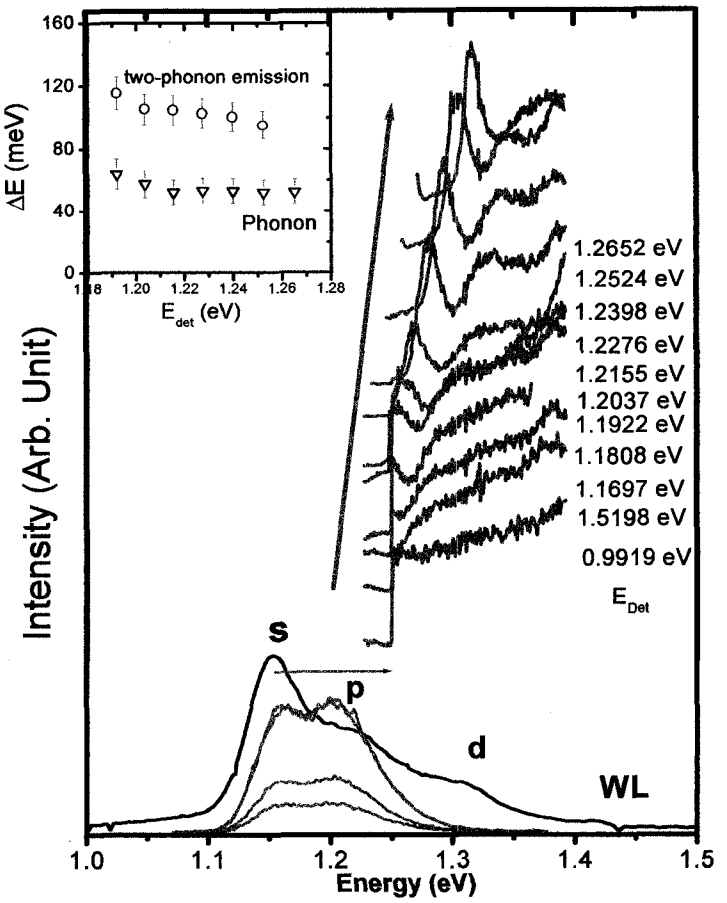

Figure 8.13: PLE result for Sample 2206 having 22 extra electrons per dot from the doping

8.3 Conclusions

A series of 50-layer InAs SAQD samples grown on GaAs substrate with various doping levels in the GaAs barriers was the central study of this chapter. Each sample had specific number of additional electrons per individual dots, varying from 2 to 22 electrons from doping. As the number of average conduction electrons increases, the electron-hole pairs aren't produced at the lower energy levels because doping electrons occupy the lower states. An increased number of phonon-assisted emission and Auger scattering processes follow in samples with more injected electrons.

The electronic structure of these SAQD samples with various electron occupancies is sensitive to the PLE probing. The PLE spectra reveal the non-radiative channels leading to emission of the QD ensembles, facilitated by thermalization from excited (absorption) states to near the detection energy with phonon-assisted emission. This sensitivity places PLE as a good tool to examine SAQD samples in fabrication of opto-electronic devices.

The PLE spectra for SAQD samples with the same number of doping electrons but with different dot densities have been studied. The results reveal that QD samples with low dot density have more non-radiative channels (multi-phonon-assisted emission or Auger scattering), suggesting that samples with low dot densities may be better candidates for engineering opto-electronic devices such as quantum dot infrared detectors.

Chapter 9

Conclusions and Future Work

QDs based on III-V compounds naturally (self-) assemble when there is enough lattice mismatch between adjacent layers of the heterostructure. The lateral diameter and height of individual dots vary as a result of strain, the amount of gallium, and indium content; but each individual dot produces a strong confinement for the carriers in three dimensions. The QD electronic energy levels are quantized in discrete states that can be modeled in sharp delta-function-like density of states.

To characterize the optical properties of SAQDs, PL and PLE techniques are the tools of choice. Most observations show that the inter-level energy differences among the QDs are approximately equal and are well-resolved. The optical transition rules of lens-shaped QDs allow electron-hole pairs to recombine only when the quantum numbers (n_+, n_-) between the initial and the final states are the same.

InAs SAQDs on GaAs can be considered as man-made atoms with energy levels that can be tagged with similar labels. Their electronic structure is a result of vertical and lateral confinement, which is similar respectively to a square well potential and a 2-D harmonic oscillator. This characteristic has allowed researchers to examine and interpret the electronic structure in a similar fashion to atomic spectra using the available spectroscopic facilities.

The energy-level structure of SAQDs as inferred from their optical emissions has been the central theme of this thesis. The study primarily addressed InAs/GaAs SAQDs grown at the National Research Council of Canada by Dr. Fafard. Initially, a single layer of InAs SAQD grown on a GaAs substrate was annealed at various temperatures for 30 seconds in order to reduce the spectral inhomogeneity and adjust their inter-level spacing. In this process, the increased diffusion of Ga into the InAs QD is evidenced by a strong blue shift. Subsequently the annealed samples were placed in an external magnetic field in the Faraday configuration to lift the degeneracies. The results are analogous to the spectra in the Fock-Darwin model. Fock-Darwin like spectra are most clearly obtained at the higher annealing temperatures because of the reductions in the inhomogeneity and the inter-level spacing.

An analysis of in-plane excitonic reduced-mass was obtained from the p level splitting with increasing magnetic field strengths. The results showed that the in-plane reduced-mass of the QD samples was in the range of $0.066 m_0 \pm 0.012 m_0$, slightly decreasing with increasing annealing temperatures. This suggests that the reduced-mass is only slightly dependent on the gallium content.

The eight-band k*p model predicted similar values only at the lowest Ga content (i.e. lowest anneal temperature) but twenty percent higher than the experimental findings at the highest anneal temperatures. The significant discrepancy may arise because the 8 band k*p calculation assumed that all the QDs are identical disks, and no spin-orbit interactions were

considered. Further studies of this discrepancy would evaluate the size, shape, composition and strain of QDs with annealing and how these are related to their optical electronic structure.

In M-PL optical characterization of InAs/GaAs SAQDs, the spectral peaks are red-shifted from the Fock-Darwin model. This is likely due to neglecting the many-body interactions among excitons such as exchange energy, configuration interaction energy, and the screened Coulomb interaction energy in the Fock-Darwin simulation. Interesting electronic structures were resolved in the spectra: ten level-crossings up to the f line, three of them at ~10 T, three more at ~28 T, and four at ~18 T.

The F-D model is based on a single (independent) particle picture, for bulk (not QD confinement), with e-h Coulomb interactions, and equal lateral extent for both the electron and the hole wave functions. At higher B fields, a certain degree of convergence between the bulk model and results on dots may be expected, because in both cases the carrier orbits (about magnetic field lines) are reduced in lateral dimension, so that latter barrier effects (in the dots) should diminish. However, the significant out-of-plane mobility from the size effects (vertical surface scattering) are not reduced by the magnetic field, and in fact the bulk model (which neglects vertical scattering) does not converge.

The PLE technique was employed to reduce the complexity or number of unknown interaction energies for the analysis. In this technique, the detected energy is set in the ground-state energy of SAQD but the exciting energy is tuned away from the detection energy up to WL. It was found that the electron-hole pairs are created only when the excitation energy is resonant with a QD energy level. One of exciton energies ensemble is therefore produced at a time and only the Coulomb interaction need to be taken into account. A comparison between the PL and PLE spectra at zero magnetic fields revealed that the PLE p-peak and d-peak positions were blue-shifted by 26.4 meV and 32.4 meV, respectively from the PL.

The M-PLE spectra resolved two clear branches from the degenerate p-level and d-level transitions. However *three* were expected from the d-level, this suggests that two degenerate states of the d-branch ($|1,1\rangle$ and $|2,0\rangle$) remain unresolved. Two resonant phonon-assisted emission peaks were observed 36.4 meV and 31.9 meV above the detection energy. These two phonon-assisted emissions correspond to GaAs bulk LO phonons and InAs QD phonons, respectively.

The reduced in-plane effective mass obtained from the p-branch energy-splitting was $\sim 0.072 m_0 \pm 0.010 m_0$ and $\sim 0.0058 m_0 \pm 0.010 m_0$ from the PLE and PL measurements, respectively. This value is in fair agreement with that obtained by other research groups. Surprisingly, the PLE reduced-mass is higher than the one obtained in PLE. It may imply that the electron is more mobile despite the number of interactions in M-PL. Alternatively, it is improbable that (coherent) interactions would *enhance* the mobility of carriers in PL measurements. On the other hand, the PLE spectra are difficult to interpret simply because the carrier recombination dynamic in PLE is more complex. Based on the ratio of two for the heavy hole to electron effective mass, the electron and heavy hole effective masses were

deduced to be at $0.1067\,m_0$ and $0.2241\,m_0$ in the PLE experiment but $\sim 0.0635\,m_0$ and $0.4814\,m_0$, respectively, in the PL measurement.

The InAs/GaAs SAQD properties of a multi-delta-function (comb) DOS has already been exploited [220] in low-threshold current and high-operating temperature quantum dot infrared photo detector (QDIP) usable at normal incidence (parallel to the growth direction). The optimization of the QDIP efficiencies requires a good understanding of the electro-optical properties of SAQDs, such as with doping layers.

Three SAQD samples were studied: a single layer of un-doped QD, a single layer of QD with modulated $\delta-$doping in the cap layer and a 25-layer of QD also with modulated doping in the cap layers. The un-doped QDs showed the typical well-resolved discrete spectrum and two resonant phonons at 8 meV and 18 meV above the detection energy. The p-level energy tends to remain constant above a changing detection energy, but the d line sharply red-shifts. This implies the energy levels of various dot ensembles vary differently according to different kinds of dispersion, whether gallium/indium alloy composition, strain or size parameters.

A single QD layer with a doped cap revealed no resonance from the QD itself. On the other hand, as anticipated discrete emissions re-appear in a 25-layer QD sample with doped cap. The dopant would diffuse down into QD layers and barriers beneath the capped layers, but the dopant density and coupling decreases with the distance from the capping layer.

The research was extended to further study the characteristics of SAQD comprising 50 layers of InAs QDs bounded by Si δ-doped GaAs barrier layers. Two series with different dot densities were examined and three different doping doses within each. By calculating the ratio of the number of dopant atoms and carriers to dot density, between two and twenty-two electrons were determined as surrounding the dots in each QD sample. As a result, emission from occupied energy states was observed, not directly, but through the Auger and multi-phonon scattering processes. As the average number of electrons occupying the conduction levels increased, direct recombination from the higher levels is reduced. For example if only two extra electrons occupied the energy states in the QD, then the p, d and f line emissions would be expected. On the other hand, if eight electrons occupy the available states, only the d and f lines are expected. This is essentially what was observed, recommending PLE as a sensitive probe of SAQD quality.

The research and analysis of this thesis has provided an awareness of possible future research projects. The InAs/GaAs SAQDs examined in Chapter 6 could be further pursued with single QD studies under M-PLE studies, including time-resolved spectroscopy. The study of a single InAs/GaAs quantum dot was also initiated with an interest in characterizing single QDs within mesa. Mesa patterns are effective in reducing the number of dots optically probed.

With Babinski *et al* [221], the electronic structure of mesa QDs in Faraday-configured magnetic fields was examined. Three prominent PL emission peaks appeared from the excitonic recombination in the single QD, interpreted as Wannier exciton, biexciton and charge-density wave (CDW). Meaningful conclusions may be drawn only when more detailed

experiments will be performed. Karlsson *et al* [222] began studying a single SAQD and found that the PL s-line intensity showed a dramatic dependence on excitation power.

Charged QDs on mesa patterns may be studied for the influence of the extra charges, again using the PL and PLE techniques. The outcomes of such study could contribute to the applications in Q-bit quantum computing, or transfer of quantized information from one place to another.

A related study would examine the single QD under the influence of an external electric field. An InAs QD embedded in a Schottky-based device can be examined under various parameters such as temperature, laser excitation power, and tunable laser excitation-energy (wavelength). This would contribute to the detailed understanding of exciton recombination, electronic structure, carrier escape and tunneling under an applied bias.

To sum up, the energy structure of InAs/GaAs SAQDs has been examined with the PL and PLE techniques with/without magnetic fields. It gave at least qualitative results similar to F-D spectrum model. As many interactions were neglected, several parameters are required to fit this F-D model. A reduced in-plane-exciton mass observed from p-state splitting from both M-PL and M-PLE measurements. This is in fair agreement with results from other research groups, yet the observed effective mass from PLE was higher than that of PL. It is suggesting a reduced mobility despite the reduced many-body interactions, but also calling into question the simplified interpretations of absorption spectra.

The influence of Si dopant on the electronic structure of SAQDs was also examined, with results suggesting that dopant atoms or carriers open further non-radiative recombination channels such as Auger scattering and phonon emission. Accordingly, no emission was observed from single doped SAQD layers. Further worthwhile study would include time-resolved spectroscopy of doped samples in order to study the lifetime of carriers in from each band-to-band transition.

Appendices

Appendix A

Properties of Bulk GaAs and InAs

Table A.1: Properties of bulk GaAs [223 - 224]

length of side of unit cube	A_{300}	5.65325 Å	
nearest- neighbor distance	$r_0 = \frac{\sqrt{3}A}{4}$	2.44793 Å	
unit cube volume	A^3	1.80674×10^{-22} cm^3	
primitive cell volume	$\frac{1}{4}A^3$	4.51689×10^{-23} cm^3	
Molecular density	$\frac{N}{2V} = \frac{4}{A^3}$	2.2139×10^{22} cm^{-3}	
Atomic density	$\frac{N}{V} = \frac{8}{A^3}$	4.4279×10^{22} cm^{-3}	
Molecular weight	M	144.642 amu	
calculated crystal density	ρ_{300}	5.3174 g/cm^3	
		At 4.2 K	**At 300 K**
effective mass for conduction band	$m_{eff(e)}$	$0.067\,m_0$	$0.063\,m_0$
effective mass for heavy hole band	$m_{eff(hh)}$	$0.51\,m_0$	$0.05\,m_0$
effective mass for light hole band	$m_{eff(lh)}$	$0.082\,m_0$	$0.076\,m_0$
effective mass for split of band	$m_{eff(so)}$	$0.0154\,m_0$	$0.145\,m_0$
Energy gap	E_g	1.52 eV	1.423 eV

Table A. 2: Summary of GaAs Dielectric Response for $\varepsilon < \varepsilon_i$ [225]

Parameter	Linear Form	300 K value
static dielectric constant	$K_0 = 12.40(1 + 1.20x10^{-4}T)$	12.85
High frequency dielectric constant (near bandgap dispersion)	$K_\infty = 10.60(1 + 9.0x10^{-5}T)$	10.88
Infrared refractive index	$(K_\infty)^{1/2} = n_\infty = 3.255(1 + 4.5x10^{-5}T)$	3.299
Long-wave TO phonon Energy	$\varepsilon_{TO} = 33.81(1 - 5.5x10^{-5}T)$	33.25 meV
Long-wave LO phonon Energy	$\varepsilon_{LO} = 36.57(1 - 4.0x10^{-5}T)$	36.13 meV
Ratio	$\frac{K_0}{K_\infty} = 1.170(1 + 3.0x10^{-5}T)$	1.181

Table A. 3: Band Parameters for InAs [64]

		At 4.2 K	At 300 K
Energy gap (eV)	E_g	0.42	0.35
effective mass for conduction band	$m_{eff(e)}$	$0.022\,m_0$	$0.022\,m_0$
effective mass for heavy hole band	$m_{eff(hh)}$	$0.41\,m_0$	$0.41\,m_0$
effective mass for light hole band	$m_{eff(lh)}$	$0.026\,m_0$	$0.026\,m_0$

Appendix B

FD non-Hamiltonian Ladder Operators

B.1 The Ladder Operators

Fock and Darwin [36 - 37] create new raising and lowering (ladder operators) in a magnetic field. The lowering or annihilation operators relating to positive and negative oscillation directions are:

$$a_+ = \frac{1}{\sqrt{2}}\left(a_x - ia_y\right) , \qquad \text{[EQ B.1]}$$

and

$$a = \frac{1}{\sqrt{2}}\left(a_x + ia_y\right) \text{ L,} \qquad \text{[EQ B.2]}$$

involving the lowering operators for the two-dimensional harmonic oscillator:

$$a_x = \sqrt{\frac{m^*\omega}{2\hbar}}\left(x + \frac{1}{m\omega} ip_x\right), \quad a_y = \sqrt{\frac{m^*\omega}{2\hbar}}\left(y + \frac{1}{m\omega} ip_y\right) . \qquad \text{[EQ B.3]}$$

Expanding a_+ and a_- therefore,

$$a_+ = \sqrt{\frac{m^*\omega}{4\hbar}}\left((x - iy) - \frac{i}{m\omega}(p_x) - ip_y\right). \qquad \text{[EQ B.4]}$$

Similarly,

$$a_- = \sqrt{\frac{m^*\omega}{4\hbar}}\left((x + iy) - \frac{i}{m\omega}(p_x) + ip_y\right) . \qquad \text{[EQ B.5]}$$

which are analogous to [EQ 2.33]

It is worthwhile to note that the commutators $\left[a_-, a_-^+\right] = 1$ and $\left[a_+, a_+^+\right] = 1$ as with the simpler commutators for a_x and a_y. The (mode) number operators that appear in these commutators are $a_+^+ a_+$ for the positive and $a_-^+ a_-$ for negative oscillation sense.

B.2 The F-D Hamiltonian

Now consider the F-D Hamiltonian in terms of the above number operators:

$$H = \hbar\Omega_+\left(a_+^+ a_+ + \frac{1}{2}\right) + \hbar\Omega_-\left(a_-^+ a_- + \frac{1}{2}\right), \qquad \text{[EQ 2.33]}$$

with $\Omega_\pm = \sqrt{\omega_\perp^2 + \left(\frac{\omega_c}{2}\right)^2} \pm \frac{\omega_c}{2}$. Here ω_c is the cyclotron frequency directly proportional to B field strength.

Expressed in term of in-plane reduced-mass $\mu_\perp^*$ and Ω_+ the creation and annihilation operators for the (+) mode become

$$a_+ = \frac{1}{2}\sqrt{\frac{m_\perp^* \Omega_+}{\hbar}}\left[(x-iy) - \frac{i}{\mu_\perp^* \Omega_+}(p_x - ip_y)\right], \qquad \text{[EQ 2.32a]}$$

$$a_+^+ = \frac{1}{2}\sqrt{\frac{m_\perp^* \Omega_+}{\hbar}}\left[(x+iy) + \frac{i}{\mu_\perp^* \Omega_+}(p_x + ip_y)\right], \qquad \text{[EQ B.6]}$$

having the product (mode number)

$$a_+^+ a_+ = \frac{1}{4}\left(\frac{m_\perp^* \Omega_+}{\hbar}\right)\left[(x+iy)(x-iy) + \left(\frac{1}{m_\perp^* \Omega_+}\right)^2 (p_x + ip_y)(p_x - ip_y) + \frac{i}{m_\perp^* \Omega_+}\left((p_x + ip_y)(x-iy) - (x+iy)(p_x - ip_y)\right)\right],$$

$$a_+^+ a_+ = \frac{1}{4}\left(\frac{m_\perp^* \Omega_+}{\hbar}\right)\left[\rho^2 + \left(\frac{1}{m_\perp^* \Omega_+}\right)^2 p_\perp^2 + \frac{(\ell_z - 2\hbar)}{m_\perp^* \Omega_+}\right], \qquad \text{[EQ B.7]}$$

$$a_- = \frac{1}{2}\sqrt{\frac{m_\perp^* \Omega_-}{\hbar}}\left[(x+iy) - \frac{i}{m_\perp^* \Omega_-}(p_x + ip_y)\right], \qquad \text{[EQ 2.32b]}$$

$$a_- = \frac{1}{2}\sqrt{\frac{m_\perp^* \Omega_-}{\hbar}}\left[(x-y) + \frac{i}{m_\perp^* \Omega_-}(p_x - ip_y)\right], \qquad \text{[EQ B.8]}$$

For (-) mode,

$$a_-^+ a_- = \frac{1}{4}\left(\frac{m_\perp^* \Omega_-}{\hbar}\right)\left[\rho^2 + \left(\frac{1}{m_\perp^* \Omega_-}\right)^2 p_\perp^2 - \frac{(\ell_z + 2\hbar)}{m_\perp^* \Omega_-}\right],$$

Combining terms,

$$\hbar\Omega_+(a_+^+ a_+) + \hbar\Omega_-(a_-^+ a_-) = \frac{1}{4} m_\perp^* \left(\Omega_-{}^2 + \Omega_+{}^2\right)\left[\rho^2 + \frac{p_\perp^2}{2m_\perp^*} - \frac{\hbar}{2}(\Omega_- + \Omega_+) + \frac{\ell_z}{2}(\Omega_- + \Omega_+)\right],$$

$$H = \hbar\Omega_+(a_+^+ a_+) + \hbar\Omega_-(a_-^+ a_-) + \frac{\hbar}{2}(\Omega_- + \Omega_+),$$

$$H = \frac{1}{2m_\perp^*}\vec{p}_\perp^2 + \frac{1}{2} m_\perp^* \Omega^2 \rho^2 + \frac{\omega_c}{2}\ell_z.$$

Appendix C

Selection Rule for Intra-Band Transition[103]

I. Bloch's Function for III-V Compound

Bloch's function represents in the $|J,M\rangle$ basis as shown in Table C.1.

Table C. 1: Bloch's function for conduction, heavy-hole and light-hole bands[104]

	u_i	$\|J,M\rangle$	
C.B.	u_1	$\left\|\frac{1}{2},\frac{1}{2}\right\rangle$	$i\|s\uparrow\rangle$
	u_2	$\left\|\frac{1}{2},-\frac{1}{2}\right\rangle$	$i\|s\downarrow\rangle$
Hh	u_3	$\left\|\frac{3}{2},\frac{3}{2}\right\rangle$	$\frac{1}{\sqrt{2}}\|(x+iy)\uparrow\rangle$
	u_4	$\left\|\frac{3}{2},-\frac{3}{2}\right\rangle$	$\frac{1}{\sqrt{2}}\|(x-iy)\downarrow\rangle$
Lh	u_5	$\left\|\frac{3}{2},\frac{1}{2}\right\rangle$	$-\sqrt{\frac{2}{3}}\|z\uparrow\rangle+\frac{1}{6}\|(x+iy)\downarrow\rangle$
	u_6	$\left\|\frac{3}{2},-\frac{1}{2}\right\rangle$	$-\sqrt{\frac{2}{3}}\|z\downarrow\rangle-\frac{1}{6}\|(x-iy)\uparrow\rangle$

II The dipole matrix element between Bloch functions: $\left\langle u_{v_h}\left|\vec{\varepsilon}\cdot\vec{p}\right|u_{v_e}\right\rangle$

$\vec{q}$ \ $\vec{\varepsilon}$	**x**	**y**	**z**
x	**0**	$\frac{\Pi}{\sqrt{2}}$	**0**
y	$\frac{\Pi}{\sqrt{2}}$	**0**	**0**
z	$\frac{\Pi}{\sqrt{2}}$	$\frac{\Pi}{\sqrt{2}}$	**0**

where $\Pi=\frac{-i}{m_0}\langle s|p_x|x\rangle=\frac{-i}{m_0}\langle s|p_y|y\rangle=\frac{-i}{m_0}\langle s|p_z|z\rangle$

[103] This summary is from page 243-260 of reference [73].
[104] This is from page 44 of reference [73].

Appendix D
The Number of Available States and Absorption Coefficient

D.1. An Example of Calculating the Number of Available States for Each Energy Level

Recall: The number of available state from [EQ 3.1]

$$N(\varepsilon) = \int d\varepsilon (g(\varepsilon)),$$

and density of states for QD from [EQ 2.9]

$$g_{Qdot}(\varepsilon) = 2\sum \delta(\varepsilon - \varepsilon_{n_x,n_y,n_z}),$$

Therefore, the number of available states for QD is

$$N(\varepsilon) = \int d\varepsilon \left(2\sum \delta(\varepsilon - \varepsilon_{n_x,n_y,n_z})\right).$$

For example, the lowest energy level has the number of available states for <u>only one dot</u> is

(s level): $$N(\varepsilon) = \int d\varepsilon \left(2\delta(\varepsilon - \varepsilon_{0,0,j_z})\right) = 2,$$

(p-level): $$N(\varepsilon) = 2\int d\varepsilon \left(\delta(\varepsilon - \varepsilon_{0,1,j_z}) + \delta(\varepsilon - \varepsilon_{1,0,j_z})\right) = 4,$$

(d-level): $$N(\varepsilon) = 2\int d\varepsilon \left(\delta(\varepsilon - \varepsilon_{2,0,j_z}) + \delta(\varepsilon - \varepsilon_{1,1,j_z}) + +\delta(\varepsilon - \varepsilon_{0,2,j_z})\right) = 6,$$

(f-level): $$N(\varepsilon) = 2\int d\varepsilon \left(\delta(\varepsilon - \varepsilon_{3,0,j_z}) + \delta(\varepsilon - \varepsilon_{2,1,j_z}) + \delta(\varepsilon - \varepsilon_{1,2,j_z}) + \delta(\varepsilon - \varepsilon_{0,3,j_z})\right) = 8,$$

Accordingly the number of available states for $5\text{x}10^{10}$ dots per cm^2 is

s level	$1\text{x}10^{11}$ cm^{-2}
p level	$2\text{x}10^{11}$ cm^{-2}
d level	$3\text{x}10^{11}$ cm^{-2}
f level	$4\text{x}10^{11}$ cm^{-2}

D.2 Reflection Index and Absorption Coefficient

Reflection at normal incidence [225] can be calculated by

$$R = \frac{(n-1)^2 + k^2}{(n+1)^2 + k^2}, \qquad [D.1]$$

where n and k are real and imaginary part of the refractive index. k also represents the rate of light extinction in the material. According to data from Adachi [226] as shown in Fig. D.1, n and k are about 4.2 and 0.43 at 514.5-nm excitation wavelength for GaAs semiconductor. Substituting these two values in [EQ D.1]; the reflective coefficient at the surface of GaAs is 0.383. This means that 61.7% of the incident light intensity is transmitted into the sample, where it is progressively absorbed or re-radiated.

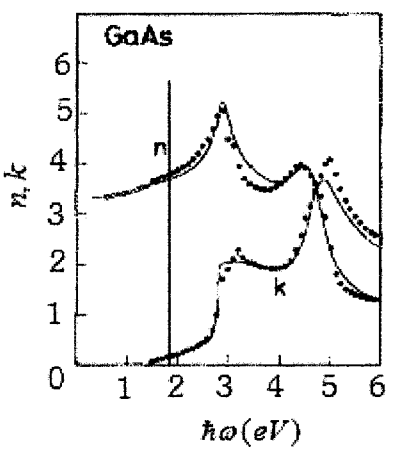

Figure D. 1: A plot of (n) and (k) imaginary parts of the complex index of refraction as a function of wavelength for GaAs from ref [226].

Since the single QD lies 100 nm below the sample surface, some of the light is absorbed in this layer. The relation of absorbed light and incident light are given by

$$I = I_0 \exp[-\alpha z] \qquad [D.2]$$

where α is the absorption coefficient and z is the thickness layer. According to Casey [227], the absorption coefficient for GaAs is ~ $6\text{x}10^4$ cm^{-1}(166 nm). With all of this in mind, the net transmitted light intensity right before hitting on the QD is ~ 0.3387 as detailed,

$$I = 0.6171 I_0 \exp[-(6\text{x}10^4\ \text{cm}^{-1})(100nm)] = 0.3387 I_0$$

or about 33.9 percent

To estimate the maximum distance light propagate before it could all be absorbed through the layer of InAs QD, is roughly estimate to be ~135 nm, where the absorption coefficient for InAs is $8x10^4\ cm^{-1}$.

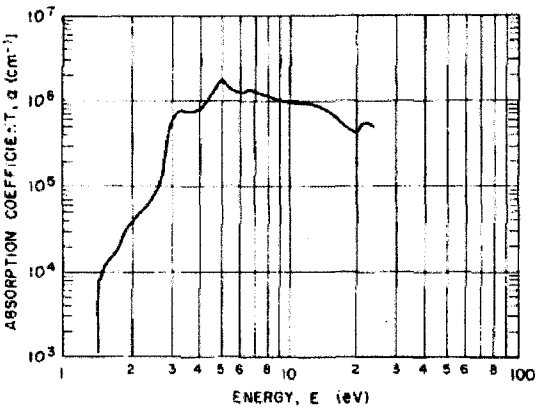

Figure D. 2: A Graph of absorption coefficient of GaAs [227]

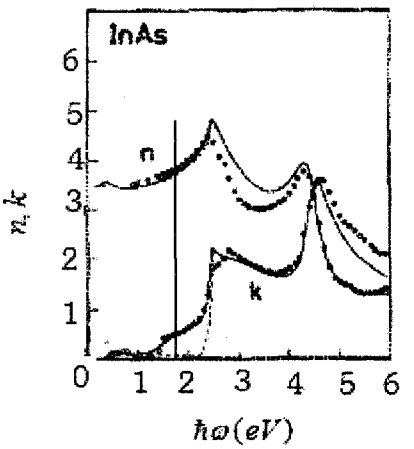

Figure D. 3: A plot of (n) and (k) imaginary parts of the complex index of refraction as a function of wavelength for InAs (after Adachi[226]).

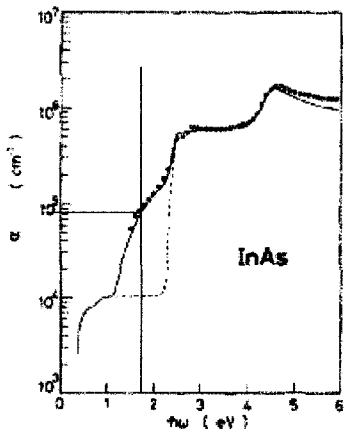

Figure D. 4: A Graph of absorption coefficient of InAs (after Adachi[226]).

References

[1] G. Grosskopf *et al.*, "Optical Millimeter-Wave Generation and Wireless Data Transmission Using a Dual-Mode Laser," IEEE Photonics Technology Letters ***12*** (12), 1692-1694 (2000).

[2] M. Francesco *et al.*, "Photonic Access Concentrator for ATM Gigabit Switching Fabrics," Journal of Lightwave Technology ***13*** (11), 2142-2151 (1995).

[3] R. A. Nordin *et al.*, "A Systems Perspective on Digital Interconnection Technology," Journal of Lightwave Technology ***10*** (6), 811-827 (1992).

[4] K. D. C. Trapp, "What You Can Expect from Tunable Lasers," Photonics Spectra ***35*** (9), 167-171 (2001).

[5] L. Wosinska, "Reliability Study of Fault-Tolerant Multi-Wavelength Non-Blocking Optical Cross Connect Based on InGaAsP/InP Laser-Amplifier Gate-Switch Arrays," IEEE Photonics Technology Letters ***5*** (10), 1206-1209 (1993).

[6] W. H. Knox, "Ultra-Fast Technology in Telecommunications," IEEE Journal of Selected Topics in Quantum Electronics ***6*** (6), 1273-1278 (2000).

[7] Y. I. Alivov *et al.*, "Forward-Current Electroluminescence from GaN/ZnO Double Heterostructure Diode," Solid-State Electronics ***49*** (10), 1693-1696 (2005).

[8] A. A. Allerman *et al.*, "Growth and Design of Deep-UV (240-290 nm) Light Emitting Diodes Using AlGaN Alloys," Journal of Crystal Growth ***272*** (1-4 SPEC. ISS.), 227-241 (2004).

[9] T. N. Danilova *et al.*, "Light-Emitting Diodes Based on GaSb Alloys for the 1.6-4.4 μm Mid-Infrared Spectral Range," Semiconductors ***39*** (11), 1235-1266 (2005).

[10] A. J. Fischer *et al.*, "Device Performance of AlGaN-Based 240-300 nm Deep UV LEDs," Proceedings of SPIE - The International Society for Optical Engineering ***5530***, 38-47 (2004).

[11] S. Suchalkin *et al.*, "Electrically Tunable Cascaded Mid-IR Type II Light Source," Progress in Biomedical Optics and Imaging - Proceedings of SPIE ***5738***, 130-137 (2005).

[12] R. Q. Yang, "Mid-Infrared Inter-band Cascade Lasers Based on Type-II Heterostructures," Microelectronics Journal ***30*** (10), 1043-1056 (1999).

[13] B. Zhurtanov *et al.*, "High-Efficiency 3.4-4.4 μm Light-Emitting Diodes Based on a p-AlGaAsSb/n-InGaAsSb/n-AlGaAsSb Heterostructure Operating at Room Temperature," Technical Physics Letters ***27*** (3), 173-175 (2001).

[14] R. Tsu, "Challenges in Nano-Electronics," Nanotechnology ***12***, 625-628 (2001).

[15] I. Hayashi and M.B. Panish, "GaAs-$GaAs_xAl_{1-x}$ As Heterostructure Injection Lasers which Exhibit Low Thresholds at Room Temperature," Journal of Applied Physics ***41*** (1), 150-163 (1970).

[16] S. Kurtin, T. Mcgill and C.A. Mead, "Fundamental Transition in the Electronic Nature of Solids," Physical Review Letters **22** (26), 1433-1436 (1969).

[17] K. Brunner *et al.*, "Photoluminescence from a Single GaAs/AlGaAs Quantum Dot," Physical Review Letters **69**, 3216-3220 (1992).

[18] D. Leonard *et al.*, "Direct Formation of Quantum-Sized Dots from Uniform Coherent Islands of InGaAs on GaAs Surfaces," Applied Physics Letters **63**, 3203-3206 (1993).

[19] O.G. Schmidt *et al.*, "Novel Nanostructure Architectures," Physica E: Low-Dimensional System & Nanostructures **25**, 280-287 (2004).

[20] A. Forchel *et al.*, "Optical Studies of Free-Standing Single InGaAs/GaAs Quantum Dots," Semiconductor Science and Technology **11**, 1529-1533 (1996).

[21] Y.C. Stephen and R.K. peter, "Imprint Lithography with sub-10 nm Feature Size and High Throughput," Microelectronic Engineering **35**, 237-240 (1997).

[22] J. Martin-Sanchez *et al.*, "Ordered InAs Quantum Dots on Pre-Patterned GaAs (001) by Local Oxidation Nanolithography," Journal of Crystal Growth **284**, 313-318 (2005).

[23] V. C. Elarde *et al.*, "Controlled Fabrication of InGaAs Quantum Dots by Selective Area Epitaxy MOCVD Growth," Journal of Crystal Growth **272**, 148-153 (2004).

[24] X. Mei *et al.*, "Highly-Ordered GaAs/AlGaAs Quantum-Dot Arrays on GaAs (001) Substrates Grown by Molecular-Beam Epitaxy using Nanochannel Alumina Masks," Applied Physics Letters **82**, 967-969 (2003).

[25] K. W. Sun *et al.*, "Selective Growth and Photoluminescence Studies of InAs Self-Organized Quantum Dot Arrays on Patterned GaAs (001) Substrates," Nanotechnology **13**, 576-580 (2002).

[26] E. T. Batteh *et al.*, "Coherent Nonlinear Optical Spectroscopy of Fluctuation Quantum Dots: Evidence for Coupling between Quantum Dots," Physical Review B **71**, 155327 (2005).

[27] A. Zrenner *et al.*, "Quantum Dots Formed by Interface Fluctuations in AlAs/GaAs Coupled Quantum Well Structures," Physical Review Letters **72** (21), 3382-3385 (1994).

[28] Q. D. Zhuang *et al.*, "Growth of Self-Organized InAs Quantum Dots on InP by Solid-Source Molecular Beam Epitaxy," Journal of Crystal Growth **216**, 57-61 (2000).

[29] F.A. Zhao *et al.*, "InAs Nanostructure Grown with Different Growth Rate in InAlAs Matrix on InP (001) Substrate," Physica E: Low-Dimensional System & Nanostructures **23**, 31-35 (2004).

[30] J. Brault *et al.*, "Strained InAs Nanostructures Self-Organised on High-Index InP (113)B," Applied Surface Science **166**, 326-331 (2000).

[31] J. Ahopelto *et al.*, "Selective Growth of InGaAs on Nanoscale InP Islands," Applied Physics Letters **65**, 1662-1664 (1994).

[32] N. Perret *et al.*, "Origin of the Inhomogeneous Broadening and Alloy Intermixing in InAs/GaAs Self-Assembled Quantum Dots," Physical Review B **62**, 5092-5099 (2000).

[33] S. Fafard and C. Ni, Allen, "Intermixing in Quantum-Dot Ensembles with Sharp Adjustable Shells," Applied Physics Letters **75**, 2374-2376 (1999).

[34] S. J. Xu *et al.*, "Effect of Rapid Thermal Annealing on Structure and Luminescence of Self-Assembled InAs/GaAs Quantum Dots," Applied Physics Letters **72**, 3335-3337 (1998).

[35] K. Hinzer *et al.*, "Optical Spectroscopy of a Single $Al_{0.36}In_{0.64}As/Al_{0.33}Ga_{0.67}As$ Quantum Dot," Physical Review B **63**, 075314 (2001).

[36] V. Fock, "Bemerkung Zur Quantelung Des Harmonischen Oszillators im Magnetfeld": Zeitshrift fur Physik **47**, 446 (1928).

[37] C.G. Darwin, "The Diamagnetism of the Free Electron," Proceeding Cambridge Philosophy Society **27**, 86 (1930).

[38] D. O'Brien *et al.*, "Feedback Sensitivity of 1.3 μm InAs/GaAs Quantum Dot Lasers," Electronic Letters **39** (25), 1819-1820 (2003).

[39] O. Qasaimeh, "Linewidth Enhancement Factor of Quantum Dot Lasers," Optical and Quantum Electronics **37** (5), 495-507 (2005).

[40] K. W. Su *et al.*, "InAs/GaAs Quantum-Dot Saturable Absorber for a Diode-Pumped Passively Mode-Locked Nd: YVO_4 Laser at 1342 nm," Optical Letters **30** (12), 1482-1484 (2005).

[41] J. Tatebayashi *et al.*, "Low Threshold Current Operation of Self-Assembled InAs/GaAs Quantum Dot Lasers by Metal Organic Chemical Vapour Deposition," Electronics Letters **39** (15), 1130-1131 (2003).

[42] V. M. Ustinov and A. E. Zhukov, "GaAs-Based Long-Wavelength Lasers," Semiconductor Science and Technology, **15** (8), 41-54 (2000).

[43] N. N. Ledentsov *et al.*, "QD Lasers: Physics and Applications," Proceeding of SPIE - Semiconductor and Organic Optoelectronic Material and Devices **5624**, 335-365 (2005).

[44] C. Munakata and H. Shimizu, "Fixed Oxide Charge in n-Type Silicon Wafers Studied by ac Surface Photo-Voltage Technique," Semiconductor Science and Technology **15**, 40-43(2000).

[45] E. Pazy *et al.*, "Spin-Based Optical Quantum Computation via Pauli Blocking in Semiconductor Quantum Dots," Europhysics Letters **62** (2), 175-181 (2003).

[46] D. Loss and D. P. Divincenzo, "Quantum Computation with Quantum Dots," Physical Review A **57**, 120-127 (1998).

[47] V. N. Golovach and D. Loss, "Electron Spins in Artificial Atoms and Molecules for Quantum Computing," Semiconductor Science and Technology **17**, 355-366 (2002).

[48] M. Kroutvar *et al.*, "Optically Programmable Electron Spin Memory Using Semiconductor Quantum Dots," Nature **432**, 81-84 (2004).

[49] P. Recher, E.V. Sukhorukov and D. Loss, "Quantum Dot as Spin Filter and Spin Memory," Physical Review Letters **85**, 1962-1965 (2000).

[50] M. Geller *et al.*, "Hole Storage in GaSb/GaAs Quantum Dots for Memory Devices," Physica Status Solidi (B) Basic Research **238**, 258-261 (2003).

[51] S. M. Kim and J. S. Harris, "Multispectral Operation of Self-Assembled InGaAs Quantum-Dot Infrared Photodetectors," Applied Physics Letters **85**, 4154-4156 (2004).

[52] S.M. Landi *et al.*, "InAs/InGaAs/InP Structures for Quantum Dot Infrared Photodetectors," Physica Status Solidi (C) **2**, 3171-3174 (2005).

[53] John H. Davies, The Physics of Low-Dimensional Semiconductors, Reprinted in 2000, (The University of Cambridge Press, USA, 1998).

[54] D. Bimberg, M. Grundmann and N. N. Ledentsov, Quantum Dot Heterostructures, (John Wiley & Sons Ltd., USA, 1999): Eugen Merzbacher, Quantum Mechanics, 5th Reprinting (John Wiley and Sons, Inc, 2000), p 3-7.

[55] V. N. Lutskii, "Quantum Size Effect, Present State and Perspectives of Experimental Investigations," Physics Status Solidi (A) **1**, 199-220 (1970).

[56] E. Kapon, D. M. Hwang and R. Bhat, "Stimulated Emission in Semiconductor Quantum Wire Heterostructure," Physical Review Letters **63**, 430-434 (1989).

[57] O. Brandt *et al.*, "Direct Synthesis of InAs Quantum Dots in Single-Crystalline GaAs Matrix by Molecular Beam Expitaxy," Surface Science **267**, 204-208 (1992).

[58] P. M. Petroff and S. P. Denbaars, "MBE and MOCVD Growth and Properties of Self-Assembling Quantum Dot Array in III-V Semiconductor Structures," Superlattices and Microstructures **15** (1), 15- 21 (1994).

[59] J. Y. Marzin, J. M. Gerard, A. Izrael, D. Barrier and G. Bastard, "Photoluminescence of Single InAs Quantum Dots Obtained by Self-Organized Growth on GaAs," Physical Review Letters **73** (5), 716-719 (1994).

[60] J. Y. Lim *et al.*, " Optical Properties of Quantum Dot Infrared Photo-Detector with Dot in an Asymmetric Well Structure," in Infrared and Photo-electronic Imagers and Detector Devices, Jul 31-Aug 1 2005, Anonymous (International Society for Optical Engineering, Bellingham WA, WA 98227-0010, United States, San Diego, CA, United States, 2005) pp. 1-6.

[61] J. C. Shin *et al.*, "Modification of the Optical and Electrical Properties of Quantum Dot Infrared Photo-Detector (QDIP) by Thermal Treatment," in Infrared and Photo-electronic Imagers and Detector Devices, Jul 31-Aug 1 2005, Anonymous (International Society for Optical Engineering, Bellingham WA, WA 98227-0010, United States, San Diego, CA, United States, 2005) pp. 1-6.

[62] O. G. Schmidt *et al.*, "InAs/GaAs Quantum Dot Lasers," in Proceedings of the 1996 8th International Conference on Indium Phosphide and Related Materials, Apr 21-25 1996, Anonymous (IEEE, Piscataway, NJ, USA, Schwabisch Gmund, Ger, 1996) pp. 727-730.

[63] N. N. Ledentsov *et al.*, "QD Lasers: Physics and Applications," Semiconductor and Organic Optoelectronic Materials and Devices, Nov 9-11 2004, Anonymous (International Society for Optical Engineering, Bellingham, WA 98227-0010, United States, Beijing, China, 2004) pp. 335-344.

[64] I. Vurgaftman; "Band Parameters for III-V Compound Semiconductors and Their Alloys," Journal of Applied Physics ***89***, 5815 (2001).

[65] S. Fafard, H.C. Liu *et al.*; "Quantum Dot Devices," Proceeding of the SPIE – The International Society for Optical Engineering, ***4078***, 100 (2000).

[66] H. S. Kim *et al.*, "Structure and Thermal Stability of InAs/GaAs Quantum Dots Grown by Atomic Layer Epitaxy and Molecular Beam Epitaxy," Journal of Crystal Growth ***285***, 137-145 (2005).

[67] A. Wojs *et al.*, "Electronic Structure and Magneto-Optics of Self-Assembled Quantum Dots," Physical Review B ***54***, 5604- 5608(1996).

[68] Claude Cohen-Tannoudji, Quantum Mechanics Vol. 2, (Published by Wiley Infer-Science, printed in Canada (1997).

[69] L. Jack, P. Jawrylak and A. Wojs, Quantum Dot, (Springer 1997).

[70] W. Sheng, M. Korkusinski and P. Hawrylak, "Microscopic Approach to Many-Exciton Complexes in Self-Assembled InGaAs/GaAs Quantum Dots," Physica E: Low-Dimensional Systems & Nanostructures ***26***, 267-270 (2005).

[71] W. Sheng, S-J Cheng and P. Hawrylak, "Multi-Band Theory of Multi-Exciton Complexes in Self-Assembled Quantum Dots," Physical Review B ***71***, 035316 (2005).

[72] J. J. Sakurai, Modern Quantum Mechanics, Revised edition (Addison-Wesley Publishing Company, Printed in USA, 1994).

[73] G. Bastard, Wave Mechanics Applied to Semiconductor Hetero-Structures, (Halsted Press, a Division of John Wiley & Sons Inc., printed in USA 1988).

[74] A. V. Uskov *et al.*, "Auger Carrier Capture Kinetics in Self-Assembled Quantum Dot Structures," Applied Physics Letters ***72***, 58 (1998).

[75] N. Peyghambarian, Introduction to Semiconductor Optics, (Prentic Hall, printed in USA 1993).

[76] J. L. T. Waugh and G. Dolling; "Crystal Dynamics of Gallium Arsenide": Physical Review ***132***, 2410-2412 (1963).

[77] S. Fafard, "Near-Surface InAs/GaAs Quantum Dots with Sharp Electronic Shells," Applied Physics Letters ***76***, 2703-2705 (2000).

[78] G. Saint-Girons *et al.*, "Photoluminescence Probing of Non-Radiative Channels in Hydrogenated In(Ga)As/GaAs Quantum Dots," Journal of Crystal Growth ***264***, 334-338 (2004).

[79] D. B. Roitman *et al.*, in Proceedings of the 1998 Conference on Organic Light-Emitting Materials and Devices II, Jul 21-23 1998, Anonymous (Society of Photo-Optical Instrumentation Engineers, Bellingham, WA, USA, San Diego, CA, USA, 1998) pp. 232-242.

[80] M. P. Ulmer *et al.*, in UV, X-Ray, and Gamma-Ray Space Instrumentation for Astronomy XIV, Aug 1-3 2005, Anonymous (International Society for Optical Engineering, Bellingham WA, WA 98227-0010, United States, San Diego, CA, United States, 2005) pp. 1-10.

[81] K. Yamanaka *et al.*, "Light Emission from Individual Self-Assembled InAs/GaAs Quantum Dots Excited by Tunneling Current Injection," Applied Physic Letters ***73*** (11), 1460-1462 (1998).

[82] M. Arzberger *et al.*, "Electroluminescence Studies of Stacked Self-Assembled InAs/GaAs-Quantum Dots Embedded in a Bragg Resonator," Physica E: Low-Dimensional Systems & Nanostructures ***2*** (1-4), 594-598 (1998).

[83] N. V. Baidus *et al.*, "1.3-1.5 μm Electroluminescence from Schottky Diodes Made on Au-InAs/GaAs Quantum-Size Heterostructures," Semiconductor Science and Technology ***19***, 469-471 (2004).

[84] D. L. Huffaker *et al.*, in 2002 IEEE/LEOS Annual Meeting Conference Proceedings: 15th Annual Meeting of the IEEE Lasers and Electro-Optics Society, Nov 10-14 2002, Anonymous (Institute of Electrical and Electronics Engineers Inc, Glasgow, United Kingdom, 2002) pp. 614-615.

[85] C. Nì Allen, P. Finnie, S. Raymond, Z.R. Wasilewski and S. Fafard, "Inhomogeneous Broadening in Quantum Dots with Ternary Aluminum Alloys," Applied Physics Letters ***79***, 2701-2703 (2001).

[86] M. Bayer *et al.*, "Hidden Symmetries in the Energy Levels of Excitonic Artificial Atoms," Nature ***405***, 923-926 (2000).

[87] Eugen Merzbacher, Quantum Mechanics, 3rd edition (John Wiley and Sons Inc., Printed in Singapore, 2000), p 543.

[88] Y. M. Park *et al.*, "State Filling Phenomena in Modulation-Doped InAs Quantum Dots," Journal of Crystal Growth ***271***, 385-390 (2004).

[89] S. Raymond *et al.*, "State-filling and Magneto-Photoluminescence of Excited States in InGaAs/GaAs Self-Assembled Quantum Dots," Superlattices and Microstructures ***21***, 541-559 (1997).

[90] S. Raymond *et al.*, "State Filling and Time-Resolved Photoluminescence of Excited States in $In_xGa_{1-x}As$/GaAs Self-Assembled Quantum Dots," Physical Review B ***54***, 11548 - 11554 (1996).

[91] S. Fafard *et al.*, "Visible Photoluminescence from N-dot Ensembles and the Line-Width of Ultra-Small $Al_yIn_{1-y}As/Al_xGa_{1-x}As$ Quantum Dots," Physical Review B ***50***, 8086(1994).

[92] J.P. Mccaffrey *et al.*, "Determination of the Size, Shape, and Composition of Indium-Flushed Self-Assembled Quantum Dots by Transmission Electron Microscopy," Journal of Applied Physics ***88***, 2272-2278 (2000).

[93] S. Fafard *et al.*, "Evolution of the Energy Levels in Quantum Dot Ensembles with Different Densities," Applied Physics Letters ***75***, 1866-1888 (1999).

[94] H. Saito *et al.*, "Influence of GaAs Capping on the Optical Properties of InGaAs/GaAs Surface Quantum Dots with 1.5 micron Emission," Applied Physics Letters ***73***, 2742-2745 (1998).

[95] S. Fafard *et al*, "Self-Assembled Quantum Dots: Five Years Later," Superlattices and Microstructures ***25***, 87-97 (1999).

[96] Z.R. Wasilewski *et al.*, "Size and Shape Engineering of Vertically Stacked Self-Assembled Quantum Dots," Journal of Crystal Growth ***201/202***, 1131-1135 (1999).

[97] Z. Mi and P. Bhattacharya, "Molecular-Beam Epitaxial Growth and Characteristics of Highly Uniform InAs/GaAs Quantum Dot layers," Journal of Applied Physics ***98***, 023510 (2005).

[98] W. Guo *et al.*, "Growth of Highly Ordered Relaxed InAs/GaAs Quantum Dots on Non-Lithographically Patterned Substrates by Molecular Beam Epitaxy," Journal of Crystal Growth ***287***, 509-513 (2006).

[99] B. A. Joyce *et al*, "In Situ Studies of III-V Semiconductor Film Growth by Molecular Beam Epitaxy," Journal of Crystal Growth ***201/202***, 106-112 (1999).

[100] M-C Chen *et al.*, "Self-Organized InAs/GaAs Quantum Dots Grown on (100) Misoriented Substrates by Molecular Beam Epitaxy," Journal of Crystal Growth ***188***, 383-386 (1998).

[101] B.J. Riel *et al.*, "InAs/GaAs(100) Self-Assembled Quantum Dots: Arsenic Pressure and Capping Effects," Journal of Crystal Growth ***236***, 145-154 (2002).

[102] K. Iizuka, K. Mori and T. Suzuki, "Effects of Growth Interruption During the Formation of InAs/GaAs Self-Assembled Quantum Dots Grown by Molecular Beam Epitaxy," Microelectronics Journal ***34***, 611-613 (2003).

[103] G. M. Guryanov *et al.*, "Formation of InGaAs/GaAs Quantum Dots by Sub-Monolayer Molecular Beam Epitaxy," Surface Science **331-333**, 414-418 (1995).

[104] S. Raymond, X. Guo, J. L. Men, and S. Fafard, "Excited-State Radiative Lifetime in Self-Assembled Quantum Dots Obtained from State-Filling Spectroscopy," Physical Review B **59**, 7624 (1999).

[105] W. Seifert *et al.*, "In-Situ Growth of Quantum Dot Structures by the Stranski-Krastanow Growth Mode," Progress Crystal Growth and Characterization **33**, 423-471 (1996).

[106] K. I. Shiramine *et al.*, "Size, Density, and Shape of InAs Quantum Dots in Closely Stacked Multilayers Grown by the Stranski-Krastanow Mode," Journal of Vacuum Science and Technology B **21**, 2054-2060 (2003).

[107] D. Leonard *et al.*, "Critical Layer Thickness for Self-Assembled InAs Islands on GaAs," Physical Review B **50**, 11687-11697 (1994)

[108] P.D. Wang *et al.*, "Luminescence Spectroscopy of InAs Self-Assembled Quantum Dots," Superlattices and Microstructures **21**, 259-265 (1997).

[109] C. K. Chia *et al*, "Group-V Intermixing in InAs/InP Quantum Dots," Applied Physics Letters **86**, 051905 (2005).

[110] P. Lever, H. H. Tan and C. Jagadish, "Impurity Free Vacancy Disordering of InGaAs Quantum Dots," Journal of Applied Physics **96**, 7544-7548 (2004).

[111] D. Bhattacharyya *et al.*, "Selective Control of Self-Organized $In_{0.5}Ga_{0.5}As$/GaAs Quantum Dot Properties: Quantum Dot Intermixing," Journal of Applied Physics **88**, 4619-4622 (2000).

[112] K. Asakawa and Y. Sugimoto, "Dry Etching Nanofabrication Technology Perspective for Novel Optical Devices/Components," Proceedings of SPIE – The International Society for Optical Engineering **4532**, 300-313 (2001).

[113] M. Henini, "Quantum Dot Nanostructures," Materials Today **5**(6), 48-53 (2002).

[114] U. Mariti *et al*, "Fabrication of Buries GaAlAs NM-Structures by Deep UV Holographic and MBE Growth on Finely Channeled Substrates," Microelectronic Engineering **13**, 391-394 (1991).

[115] S. Fafard, K. Hinzer, S. Raymond, M. Dion, J. McCaffrey, Y. Feng and S. Charbonneau, "Red-Emitting Semiconductor Quantum Dot Lasers," Science **274**, 1350-1353 (1996).

[116] K. Asakawa *et al.*, "Nanotechnologies of Photonic Crystals and Quantum Dots for Ultra-Small and Ultra-Fast all Optical Switches," Proceeding of SPIE – The International Society for Optical Engineering **5926**, 1-13 (2005).

[117] R. Pasanth *et al.*, " All-Optical Switching Due to State Filling in Quantum Dots," Applied Physics Letters **84**, 4059-4061 (2004).

[118] M. Sugawara *et al*, "Recent Progress in Self-Assembled Quantum-Dot Optical Devices for Optical Telecommunication: Temperature-Insensitive 10 Gb/s^{-1} Directly Modulated Lasers and 40 Gb/s^{-1} Signal-Regenerative Amplifiers," Journal of Physics D: Applied Physics **38**(13), 2126-2134 (2005).

[119] S. Bischoff *et al.*, "Ultrafast Gain Recovery and Modulation Limitations in Self-Assembled Quantum-Dot Devices," IEEE Photonics Technology Letters **13**(6), 541-543(2003).

[120] H. Jiang and J. Singh, "Self-Assembled Semiconductor Structures: Electronic and Optoelectronic Properties," IEEE Journal of Quantum Electronics **34**(7), 1188-1196 (1998).

[121] Y. Arakawa, "Progress in Quantum Dots for Optoelectronics Applications," Proceedings of SPIE – The International Society for Optical Engineering **4598**, 106-112 (2001).

[122] A.J. Shields *et al.* "Optoelectronic Devices for Single Photon Generation," Proceedings of SPIE - The International Society for Optical Engineering **5722**, 1-14 (2005).

[123] D.J. Mowbray *et al.*, "InAs-GaAs Self-Assembled Quantum Dot Lasers: Physical Processes and Device Characteristics," Physica E: Low-Dimensional Systems & Nanostructures **7**(3), 489-493 (2000).

[124] Y. Arakawa, "Progress and Prospect of Quantum Dot Lasers," Proceedings of SPIE - The International Society for Optical Engineering **4580,** 179-185 (2001).

[125] J. Martinez-Pastor *et al*, "Exciton Recombination in Self-Assembled InAs/GaAs Small Quantum Dots Under an External Electric Field," Physica Status Solidi (A) Applied Research **190(** 2), 599-603(2002).

[126] G. Ortner *et al.*, "Experimental Demonstration of Coherent Coupling of Two Quantum Dots," Physica E: Low-Dimensional Systems & Nanostructures **26**, 281-285 (2005).

[127] Z. Yuan, B. E. Kardynal, R. M. Stevenson, A. J. Shields, C. J. Lobo, K. Cooper, N.S. Beattie, D. A. Ritchie and M. Pepper, "Electrically Driven Single-Photon Source," Science **295,** 102-105 (2002).

[128] M. Ciorga, A. Sachrajda, P. Hawrylak, C. Gould, P. Zawadzki, S. Jullian, Y. Feng and Z. Wasilewski, "Addition Spectrum of a Lateral Dot From Coulomb and Spin-Blockade Spectroscopy," Physical Review B **61**, R16315(2000).

[129] L.P. Kouwenhoven, T. H. Oosterkamp, M.W. Danoesastro, M. Eto, D.G. Austing, T. Honda, S. Tarucha, "Excitation Spectra of Circular Few-Electron Quantum Dots," Science **278**, 1788 -1792 (1997).

[130] P.G. Eliseev *et al*, "Gain in Ultra-Low-Threshold InAs/InGaAs Quantum Dot Lasers," Conference Digest - IEEE International Semiconductor Laser Conference, 65-66 (2000).

[131] M. Ishida *et al.*, "Photon Lifetime Dependence of Modulation Efficiency and K Factor in 1.3 μm Self-Assembled InAs/GaAs Quantum-Dot Lasers: Impact of Capture Time and Maximum Modal Gain on Modulation Bandwidth," Applied Physics Letters ***85***(18), 4145-4147 (2004).

[132] K. Mukai *et al.*, "Low Threshold and High Output Power Lasing of Columnar - Shaped Self-Assembled InAs/GaAs Quantum Dots," Conference Digest - IEEE International Semiconductor Laser Conference, 213-214 (1998).

[133] V. Tokranov *et al*, "InAs Quantum Dot Laser Diodes: Structure, Characteristics and Temperature Dependence," Proceedings of SPIE - The International Society for Optical Engineering ***4656***, 79-88 (2002).

[134] H. Saito *et al.*, "Room-Temperature Ground-State Lasing Using Long-Wavelength InAs Quantum Dots on InAlGaAs/InP (311)B," Conference Proceedings - International Conference on Indium Phosphide and Related Materials, 83-86 (2001).

[135] S. Malik, C. Roberts, R. Murray and M. Paty, "Tuning Self-Assembled InAs Quantum Dots by Rapid Thermal Annealing," Applied Physics Letters ***71***, 1987-1989 (1997).

[136] R. Leon, Y. Kim, C. Jagadish, M. Gal, J. Zou and D. J. Cockayne, "Effects of Inter-Diffusion on the Luminescence of InGaAs/GaAs Quantum Dots," Applied Physics Letters ***69***, 1888-1890 (1996).

[137] S. Raymond and *et al.*, "Exciton Droplets in Zero Dimensional Systems in a Magnetic Fields," Solid State Communications ***101***, 883-889 (1997).

[138] S. Menard, J. Beerens, D. Morris, V. Aimez, J. Beauvais and S. Fafard, "Magneto-Photoluminescence Study of Intermixed Self-Assembled InAs/GaAs Quantum Dots," Journal of Vacuum Science Technology B ***20***, 1501 (2002).

[139] P.P. Paskov, P.O. Holtz, B. Monear, J. M. Gareia, W.V. Schoenfeld and P. M. Petroff, "Magnetoluminescence of Highly Excited InAs/GaAs Self-Assembled Quantum Dots," Physical Review B. ***62***, 7344 – 7349 (2000).

[140] A. Wojs and P. Hawrylak, "Exciton-Exciton Interactions in Highly Excited Quantum Dots in a Magnetic Field," Solid State Communications ***100***, 487-491 (1996).

[141] C. Ni. Allen *et al.*, "Quantum Dot Intermixing with Thermal and Laser Annealing," Applications of Photonic Technology 4, Proceedings of SPIE ***4087***, 1188-1193 (2000) .

[142] GD Knight, *Transport and Optical Response in Cu Damascene Lines with Grain and Texture*, Ph.D. dissertation (U. Ottawa, 2006).

[143] K. Hinzer *et al.*, "Widely Tunable Self-Assembled Quantum Dot Lasers," Journal of Vacuum Science and Technology, Part A: Vacuum, Surfaces and Films ***18*** (2), 578-581 (2000).

[144] S. Fafard, Z. R. Wasilewski *et al.* "Manipulating the Energy Levels of Semiconductor Quantum Dots," Physical Review B ***59***, 15368-15373 (1999).

[145] T. M. Hsu, Y.S. Lan, W.H. Chang, N.T. Yeh and J.I. Chyi, "Tuning the Energy Levels of Self-Asembled InAs Quantum Dots by Rapid Thermal Annealing," Applied Physics Letters ***76***, 691(2000).

[146] A.R. Goni, H. Born, R. Heitz, A. Hoffmann, C. Thomsen, F. Heinrichsdorff, and Bimberg, "Magnetoluminescence Study of Annealing Effects on the Electronic Structure of Self-Organized InGaAs/GaAs Quantum Dots," Japanese Journal of Applied Physics ***39***, 3907(2000).

[147] S. Raymond, S. Studenikin, A. Sachrajda, Z. Wasilewski, S. J. Cheng, W. Sheng, P. Hawrylak, A. Babinski, M. Potemski, G.Ortner and M. Bayer, "Excitnic Energy Shell Structures of Self-Assembled InGaAs/GaAs Quantum Dots," Physical Review Letters ***92***, 187402 (2004).

[148] T. Bahder, "Eight-Band k*p Model of Strained Zinc-Blende Crystals," Physical Review B ***41***, 11992-12000 (1990).

[149] A. Rastelli *et al*, "Self-Assembled Quantum Dots for Single-Dot Optical Investigations," Superlattices and Microstructures ***36***, 1810191 (2004).

[150] T. Yang *et al*, "Highly Uniform Self-Assembled InAs/GaAs Quantum Dots Emitting at 1.3 micron by Metalorganic Chemical Vapor Deposition," Physica E: Low-Dimensional Systems & Nanostructures ***26***, 77-80 (2005).

[151] T. Yang *et.al*, "Narrow Photoluminescence Linewidth (<17 meV) from Highly Uniform Self-Assembled InAs/GaAs Quantum Dots Grown by Low-Pressure Metalorganic Chemical Vapor Deposition," Applied Physics Letters ***84***, 2817-2819(2004).

[152] S. Fafard, "Quantum Dot Structures and Devices with Sharp Adjustable Electronic Shells," Physica E: Low-Dimensional Systems & Nanostructures ***8***, 107-116 (2000).

[153] A. Babinski, S. Awirothananon *et al.*, "Photoluminescence Excitation Spectroscopy of InAs/GaAs Quantum Dots in High Magnetic Field," Physica E: Low-Dimensional Systems & Nanostructures ***22***, 603-606 (2004).

[154] S.Fafard, M. Spanner, J.P. McCaffrey, Z. R. Wasilewski, "Coupled InAs/GaAs Quantum Dots with Well-Defined Electronic Shells," Applied Physics Letters ***76***, 2268 (2000).

[155] D. Leonard, S. Fafard, K. Pond, Y.H. Zhang, J.M. Merz, and P.M. Petroff, "Structural and Optical Properties of Self-Assembled InGaAs Quantum Dots," Journal of Vacuum Science and Technology B ***12***, 2516 (1994).

[156] S. Fafard, D. Leonard, J.M. Merz, and P.M. Petroff, "Selective Excitation of the Photoluminescence, and the Energy Levels of Ultrasmall InGaAs/GaAs Quantum Dots," Applied Physics Letters ***65***, 1388 (1994).

[157] Eougenious L. Ivchenko, Optical Spectroscopy of Semiconductor Nano-Structures, (Alpha Science International Ltd. Harrow, Printed in UK, 2005), p. 205.

[158] R. Heitz *et al.* "Energy Relaxation by Multiphonon Process in InAs/GaAs Quantum Dots," Physical Review B ***56***, 10435-10445 (1997).

[159] S. Fafard *et al.* "Phonon and Radiative Recombination in Self-Assembled Quantum Dots," Physical Review B ***52***, 5752-5755 (1995).

[160] L.R. Wilson *et al.*, "Magneto-Optical Studied of Self-organized InAs/GaAs Quantum Dots," Physical Review B ***57***, 2073-2076(1998).

[161] S. Awirothananon *et al*, "Electronic and Structural Properties of Inter-diffused Self-Assembled Quantum Dots from Magneto-Photoluminescence," Japanese Journal of Applied Physics: Part 1 ***43***, 2088-2092 (2004).

[162] S. J. Cheng *et al.*, "Electron-Hole Complexes in Self-Assembled Quantum Dots in Strong Magnetic Fields," Physica E: Low-Dimensional System & Nanostructures ***21***, 211-214 (2004).

[163] S. J. Cheng *et al.*, "Theory of Excitonic Artificial Atoms: InGaAs/GaAs Quantum Dots in Strong Magnetic Fields," Physical Review B ***68***, 235330 (2005).

[164] K. H. Hellwege, O. Madelung, M. Schulz, and H. Weiss, Landolt-Bronstein, Numerical Data and Functional Relationships in Science and Technology, New Series, Group III, Volume 17a (Springer, Berlin, 1982).

[165] M. Grundmann, O. Stier, and D. Bimberg, "InAs/GaAs Pyramidal Quantum Dots: Strain Distribution, Optical Phonons, and Electronic Structure," Physical Review B ***52***, 11969 (1996).

[166] A. V. Baranov, V. Davydov, H. –W Ren, S. Sugou and Y. Masumoto, "Phonon-Enhanced Intraband Transition in InAs Self-Assembled Quantum Dots," Journal of Luminescence ***87-89***, 503-505 (2000).

[167] R. Rinaldi, P. V. Giugno, R. Cingolani, H. Lipsanen, M. Sopanen and J. Tulkki, "Zeeman effect in Parabolic Quantum Dots," Physical Review Letters ***77***, 342-345 (1996).

[168] K. Kuldova *et al*, "Magneto-Photoluminescence Study of Electronic Transitions in InAs/GaAs Quantum Dot Layers," Material Science and Engineering B ***88***, 247-251 (2002).

[169] S. Hameau, Y. Guldner, O. Verzelen, R. Ferreira, G. Bastard, J. Zeman, A. Lemaitre and J. M. Gerard, "Strong Electron-Phonon Coupling Regime in Quantum Dots: Evidence for Everlasting Resonant Palarons," Physical Review Letters ***83***, 4152 (1999).

[170] Th. Wimbauer *et al.*, "Zeeman Splitting of the Excitonic Recombination in $In_xGa_{1-x}As$/GaAs Single Quantum Wells," Physical Review B ***50***, 8889 (1994).

[171] I. E. Itaskevich, M. Henini, H. A. Carmona, L. Eaves, P.C. Main, D. K. Maude and J.C. Portal, "Photoluminescence Spectroscopy of Self-Assembled InAs Quantum Dots in Strong Magnetic Field and Under High Pressure," Applied Physics Letters ***70***, 505 (1997).

[172] G. Janssen, E. Goovaerts, A. Bouwen, B. Partoens, B. Van Daele, N. Zurauskiene, P. M. Koenraad and J. H. Wolter, "Observation of Cyclotron Resonance in an InAs/GaAs Wetting Layer with Shallowly Formed Quantum Dots," Physical Review B ***68***, 045329 (2003).

[173] E. Deleporte *et al.* "Strong Electron-Phonon Coupling Regime in Self-Assembled Quantum Dots," Physics State Solid (C) ***1***, 1391-1396 (2004).

[174] B. Srocka, H. Scheffler, and D. Bimberg, "Rhodium- and Iridium-Realted Deep Levels in $In_{0.53}Ga_{0.47}As$," Applied Physics Letters ***64***, 2679 (1994).

[175] A. Polimeni *et al.*, "Magneto-Photoluminescence and Electroluminescence Spectroscopy of Self-Assembled (In)GaAs Quantum Dots on High Index Planes," Physica E: Low Dimensional Systems & Nanostructures ***2***, 662-666 (1998).

[176] K. W. Berryman, S. A. Lyon, and Mordechai Segev, "Mid-Infrared Photoconductivity in InAs Quantum Dots," Applied Physics Letters ***70***, 1861 (1997).

[177] D. Pan, E. Towe, and S. Kennerly, "Normal-Incidence Intersubband (In,Ga)As/GaAs Quantum Dot Infrared Photodetectors," Applied Physics Letters ***73***(14), 1937(1998).

[178] L. Chu, A. Zrenner, G. Bohm, and G. Abtreiter, "Normal-Incident Intersubband Photocurrent Spectroscopy on InAs/GaAs Quantum Dots," Applied Physics Letters ***75***(23), 3599 (1999).

[179] A. D. Stiff, S. Krishna, D. Bhattacharya and S. Kennerly, "High-Detectivity Normal-Incidence, Mid-Infrared InAs/GaAs Quantum-Dot Detector Operating at 150 K," Applied Physics Letters ***79(3)***, 421 (2001).

[180] A. Weber *et al.*, "Strong Normal-Incidence Infrared Absorption in Self-Organized InAs/InAlAs Quantum Dots Grown on InP (001)," Applied Physics Letters ***74***, 413 (1999).

[181] V. Ryzhii, "The Theory of Quantum-Dot Infrared Phototransistors," Semiconductor Science and Technology ***11***, 759 (1999).

[182] J. Urayama, T.B. Norris, J. Singh, and P. Bhattacharya, "Observation of Phonon Bottleneck in Quantum Dot Electronic Relaxation," Physical Review Letters ***86***, 4930 (2001).

[183] Andrew J. Williamson, "Energy States in Quantum Dots," International Journal of High Speed Electronics and Systems ***12***(1), 15-43(2002).

[184] Otfried Madelung, Semiconductors: Data Handbook, 3rd edition (Spinger-Verlag Berlin Heidelberg, 2004).

[185] J. M. Garcia, *et al.*, "Intermixing and Shape Changes During the Formation of InAs Self-Assembled Quantum Dots," Applied Physics Letters ***71***, 2014- 2016(1997).

[186] P. W. Fry *et al.*, "Inverted Electron-Hole Alignment in InAs-GaAs Self-Assembled Quantum Dots," Physical Review Letters ***84***, 733 (2000).

[187] Y. Tang *et al*, "Self-Assembled InAs/GaAs Quantum Dots Studied with Excitation Dependent Cathodoluminescence," Journal of Applied Physics ***84***, 3342 (1998).

[188] K.H. Lee *et al.*, "Effect of Thermal Annealing in the Microstructural and the Optical Properties of Uncapped InAs Quantum Dots Grown on GaAs Buffer Layers," Solid State Communications ***133***, 65-70 (2005).

[189] J. S. Kim, C-R Lee, J. I. Lee and J-Y Leem, "Shape-Dependent Optical Properties of Self-Assembed InAs/GaAs Quantum Dots," Journal of Crystal Growth ***289***, 68-71 (2006).

[190] K. Jacobi, "Atomic Structure of InAs Quantum Dots on GaAs," Progress in Surface Science ***71***, 185-215 (2003).

[191] R. Carles, N. Saint-cricg, J.B. Renucci, M.A. Renucci and A. Zwick, "Second-Order Raman Scattering in InAs," Physical Review B ***22***, 4804 (1980).

[192] A. V. Fedorov and A. V. Baranov, "Intraband Carrier Relaxation in Quantum Dots Mediated by Surface Plasmon-Phonon Excitations," Optics and Spectroscopy ***97***, 63-74 (2004).

[193] T. S. Shamirzaev *et al.*, "Strong Sensitivity of Photoluminescence of InAs/AlAs Quantum Dots to Defects: Evidence for Lateral Inter-Dot Transport," Semiconductor Science and Technology ***21***, 527-531 (2006).

[194] J. Siegert *et al.*, "Carrier Dynamics in Modulation-Doped InAs/GaAs Quantum Dots," Physical Review B ***72,*** 085316 (2005).

[195] K. Hinzer *et al.*, "Optical Spectroscopy of Electronic States in a Single Pair of Vertically Coupled Self-Assembled Quantum Dots," Physics State Solid (B) ***224,*** 385-392 (2001).

[196] M. B. Dutt and B. L. Sharma, Diffusion in Semiconductors and Non-Matallic Solids, Edited by D.L. Beke (Springer-Verlag, Berlin, 1998), p 3-1.

[197] R. Heitz *et al.* "Enhanced Polar Exciton-LO-Phonon Interaction in Quantum Dots," Physical Review Letters ***83***, 4654-4657 (1999).

[198] P. C. Sercel, "Multiphonon-Assisted Tunneling Through Deep Levels: A Rapid Energy-Relaxation Mechanism in Nonideal Quantum Dot Hetero-structures," Physical Review B ***51***, 14532 (1995).

[199] P. Altieri *et al.* "Resonant Quenching of Photoluminescence in $In_xGa_{1-x}As/Al_yGa_{1-y}As$/GaAs Self-Assembled Quantum Dots," Material Science and Engineering B ***88***, 252-254 (2002).

[200] Q. Xie *et al.*, "Realization of Optically Active Strained InAs Island Quantum Boxes on GaAs(100) via Molecular Beam Epitaxy and the Role of Island Induced Strain Fields," Journal of Crystal Growth ***150***, 357-363 (1995).

[201] R. Heitz *et al.*, "Excited States and Energy Relaxation in Stacked InAs/GaAs Quantum Dots," Physical Review B ***57***, 9050-9060 (1998).

[202] L. Guo, E. Leobandung and S. Y. Chou, "A Silicon Single-Electron Transistor Memory Operating at Room Temperature," Science ***275***, 649 (1997).

[203] A. Khaetskii, D. Loss and L. Glazman, "Electron Spin Evolution Induced by Interaction with Nuclei in a Quantum Dot," Physical Review B ***67***, 195329 (2003).

[204] K. Yano *et al.*, "Single-Electron Memory for Giga-to-Tera Bit Storage," Proceedings of the IEEE – the International Society for Optical Engineering ***87(4)***, 633(1999)

[205] R. Leon, S. Marcinkevicius, X.Z. Liao, J. Zou, D. J. H. Cockayne and S. Fafard, "Ensemble Interaction in Strained Semiconductor Quantum Dots," Physical Review B ***60(12)***, 8517-8520 (1999).

[206] R. Leon and S. Fafard, "Structural and Radiative Evolution in Quantum Dots Near the $In_xGa_{1-x}As/GaAs$ Stranski-Krastanow Transformation," Physical Review B ***58(4)***, 1726-1729(1998).

[207] K. H. Scmidt, G. Medeiros-Ribeiro, M. Oestreich, G. H. Dohler and P.M. Petroff, "Carrier Relaxatin and Electronic Structure in InAs Self-Assembled Quantum Dots," Physical Review B ***54(16)***, 11346-11353 (1996).

[208] J. Feldmann, S.T. Cundiff, M. Arzberger, G. Bohm and G. Abstreiter, "Carrier Capture into InAs/GaAs Quantum Dot via Multiple Optical Phonon Emission," Journal of Applied Physics ***89***, 1180-1183 (2001).

[209] W. Hackenberg and G. Fasal, "Determination of the LO-phonon and $\Gamma \rightarrow L$ Intervalley Scattering Time in GaAs from Hot Electron Luminescence Spectroscopy," Solid State Electronics ***32(12)***, 1247-1251 (1989).

[210] T. Inoshita and H. Sakaki, "Multi-Phonon Relaxation of Electrons in a Semiconductor Quantum Dot," Solid State Electronics ***37***, 1175-1178(1994).

[211] T. Inoshita and H. Sakaki, "Electron Relaxation in a Quantum Dot: Significance of Multi-Phonon Processes," Physical Review B ***46***, 7260-7263 (1992).

[212] M. V. Maximov *et al.*, "Carrier Relaxation Mechanisms and Fermi Versus Non-Fermi Carrier Distribution in Quantum Dot Arrays Formed by Activated Alloy Phase Separation," Nanotechnology ***11***, 309-313 (2000).

[213] A. W. e. Minnaert *et al*, "Frohlich Interaction in InAs/GaAs Self-Assembled Quantum Dots," Physical Review B ***63***, 075303 (2001).

[214] C. Kanyinda-Malu, R. Maria Dela Cruz, "Interface Phonon Modes in Truncated Conical Self-Assembled Quantum Dots," Surface Science ***529***, 503-514 (2003).

[215] J. I. Climente *et al*, "Phonon-Induced Electron Relaxation in Correlated Quantum Dots," Physics State Solid (C), **3**(11), 3660 (2006).

[216] D. J. Jang *et al*, "Carrier Relaxation in Multi-Stacked InAs/GaAs Quantum Dots," Physics State Solid (C) **3**(11), 3664 (2006).

[217] P. A. Knipp *et al*, "Coupling Between LO Phonons and Electronic Excitations of Quantum Dots," Physical Review B **56**(3), 1516(1997).

[218] P. P. Paskov *et al.*, "Auger Processes in InAs Self-Assembled Quantum Dots," Physica E: Low-Dimensional System & Nanostructures **6**, 440-443 (2000).

[219] P. Hawker, A.J. Kent and M. Henini, "Energy Relaxation by Photonexcited Carriers in the InAs/GaAs Quantum Dot System: Bolometric Detection of Strong Acoustic-Phonon Emission," Applied Physics Letters **75(24)**, 3832 – 3834 (1999).

[220] H. C. Liu *et al.*, "Quantum Dot Infrared Photodetectors," Applied Physics Letters **78**, 79(2001).

[221] A. Babinski, S. Awirothananon, J. Lapointe, Z. Wasilewski, S. Raymond and M. Potemski, "Single-Dot Spectroscopy in High Magnetic Fields," Physica E: Low-Dimensional System & Nanostructures **26**, 190-193 (2005).

[222] K. F. Karlsson *et al.*, "The Influence of Carrier Diffusion on the Formation of Charged Exciton in InAs/GaAs Quantum Dots," Physica E: Low-Dimensional Systems & Nanostructures **13**, 101-104 (2002).

[223] J. S. Blakemore, "Semiconducting and Other Major Properties of Gallium Arsenide," Journal of Applied Physics **53** R123-R 181 (1982).

[225] C. Kittel, Introduction to Solid State Physics, 7th edition (John Wiley & Son, Inc., New York, USA. 1996). p 330.

[226] S. Adachi, "Optical Dispersion Relations for GaP, GaAs, GaSb, InP, InAs, InSb, $Al_xGa_{1-x}As$ and $In_{1-x}Ga_xAs_yP_{1-y}$," Journal of Applied Physics **66**(12), 6030 (1989).

[227] H. C. Casey Jr., D. D. Sell and K. W. Wecht, "Concentration Dependence of the Coefficient for n- and p-Type GaAs Between 1. 3 and 1. 6 eV," Journal of Applied Physics **46** (1), 250-257 (1975).

[228] Jackques I. Pankove, Optical Processes in Semiconductors, (Dover Publications Inc., New York, USA 1971).

[229] C. Klingshirm, Semiconductor Optics, 2nd edition (Springer 2005) p 129-130.

[230] W. Nakwaski, "Effective Masses of Electrons and Heavy Holes in GaAs, InAs, AlAs and Their Ternary Compounds," Physica B **210**, 1-25 (1995).